PARTICLE CONFINEMENT AND MAGNETIC FLUCTUATIONS IN TOKAMAK DISCHARGES WITH GAS PUFFING

Thesis by

Bruce Stephen Levine

In Partial Fulfillment of the Requirements

for the Degree of

Doctor of Philosophy

California Institute of Technology

Pasadena, California

1980

(Submitted May 8, 1980)

ACKNOWLEDGMENTS

The author wishes to express his appreciation to his advisor, Professor Roy W. Gould, for his suggestion of these research topics, numerous helpful comments, and direct contributions to the realization of these experiments.

It is a sincere pleasure to thank Mark A. Hedemann for his generous cooperation, especially with the maintenance and modification of the Caltech Tokamak hardware and the loan of his magnetic probes, and Eric D. Frederickson for many helpful discussions concerning the theory of tearing modes. The electronic wizardry of Frank Cosso is profoundly appreciated, as is the introduction to the operation of the Caltech Tokamak by Dr. Randall L. Kubena.

Helpful suggestions regarding the operation of gas-puffing systems were made by Dr. Keith Burrell of the General Atomic Company and Dr. Ronald Parker of MIT. Useful software for the Vector 1+ microcomputer was written by Natalie Gluck and David Feinstein. The contributions to the typing of this manuscript by Michelle Schroeder and Ruth Stratton are gratefully acknowledged.

Finally, the author wishes to thank his family for their love and support.

ABSTRACT

An experimental investigation has been made of particle confinement and magnetic fluctuations associated with short (< 1 msec) gas pulses into a Tokamak discharge. The fluctuations are measured with movable pairs of magnetic probes, each containing a poloidal and radial coil and inserted into the outer regions of the plasma.

When neutral gas is added and the current channel contracts, the fluctuation spectra are dominated by an $m = 2$ mode that grows with the classical tearing-mode rate. When the gas feed is terminated, much broader spectra of modes with m up to 15 are observed. The modal frequencies are nearly integer multiples of 11 kHz. The $m = 2$ mode dominates the poloidal spectra, while the radial spectra have numerous modes of appreciable amplitude. Time-delay measurements suggest that many of the higher-order ($m > 3$) modes originate in deformation of the $m = 2$ and $m = 3$ magnetic islands. A strong $m = 7$ is found to be localized near the limiter in $q(a) = 3.8$ discharges, hence this mode is identified as an $m = 7$, $n = 2$. It is found that the $m = 2$ mode becomes destabilized for discharges for which the peak puff density approaches the upper limit given by the Murakami scaling relation. The $m = 2$ mode grows at a rate much slower than the classical tearing-mode rate. The threshold in peak puff density for this destabilization coincides with a degradation in particle confinement.

TABLE OF CONTENTS

I. INTRODUCTION

The Tokamak remains one of the most promising devices under consideration for future generation of power by controlled thermonuclear reaction. Briefly, it is a toroidal chamber on which is wound a solenoid providing a large, static (over the duration of the discharge) toroidal field which constrains charged particles to move about it in Larmor orbits (Fig. 1). A simple toroidal solenoid has a magnetic field varying as 1/R, where R is the radial coordinate in cylindrical geometry. There is thus associated with this field a gradient drift perpendicular to the plane of symmetry of the torus that has an opposite sense for the two signs of charge. Were there no helicity to the magnetic field there would be no neutralization of this charge build-up and the resulting $\underset{\sim}{E} \times \underset{\sim}{B}$ drift would cause outward motion of the plasma into the wall. A toroidal current is driven through the plasma by making it the secondary of an air-core transformer. This current has the dual effect of ohmically heating the plasma as well as creating a poloidal magnetic field, that is, a field consisting of closed lines enclosing a convex surface in an azimuthal plane within the Tokamak. Superimposed on the toroidal magnetic field, the net effect of the poloidal field is a twisting around the torus that permits neutralization of the above-mentioned charge separation. A vertical magnetic field is added to counteract outward movement of the plasma due to the excess of magnetic pressure on the inner side of the plasma. This field is curved slightly towards the toroidal axis of symmetry to provide a $\underset{\sim}{J} \times \underset{\sim}{B}$ force towards the plane of symmetry should the plasma stray upwards or downwards. Finally, a horizontal field is provided to compensate for errors in the toroidal winding. The ohmic-heating, vertical, and horizontal fields are provided by sets of windings external to the torus and toroidal field coil.

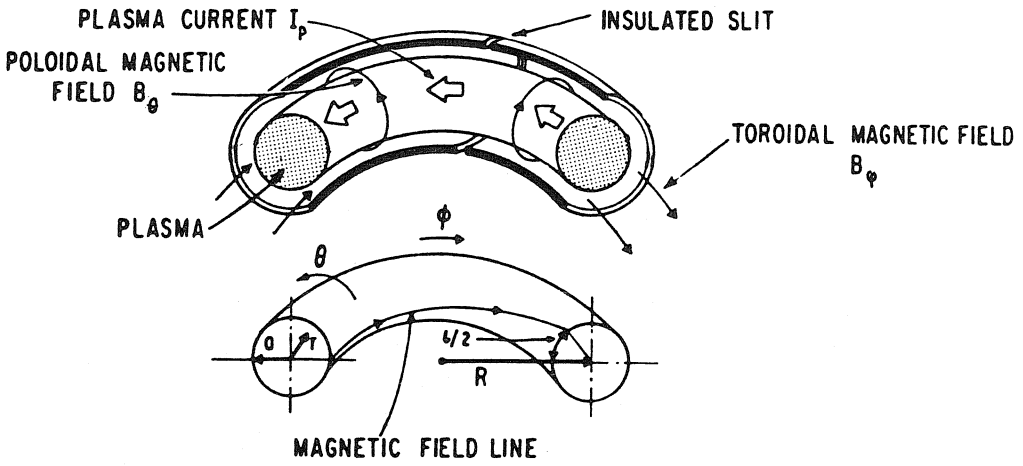

Figure 1. Tokamak geometry. The angles θ and ϕ are, respectively, the poloidal and toroidal angles, r is the radial coordinate, a and R are, respectively, the toroidal minor and major radii. This convention is observed throughout this thesis.

Referring to Fig. 1 once again, the quantity q may be defined at a point as the ratio of the number of times a field line winds the long way around the torus to the number of times it winds the short way around the torus in the limit of an infinite number of circuits. If a field line lies on a mode-rational surface, that is, if it closes on itself after n times around the long way and m times the short way then q = n/m. Alternatively, in toroidal geometry at a point $\underset{\sim}{x} = (r, \theta, \phi)$

$$q(\underset{\sim}{x}) = \frac{B_\phi}{B_\theta} \cdot \frac{r}{R} \tag{1.1}$$

where B_ϕ is the toroidal field, B_θ the poloidal field, R the toroidal major radius, and r the minor radius of the toroidal surface with major radius R upon which $\underset{\sim}{x}$ sits. Call this surface S. Approximating the plasma locally as a cylinder (neglecting toroidal inductance) gives

$$B_\theta(r) \simeq \frac{\mu_o I}{2\pi r} \tag{1.2}$$

where I is the current enclosed by the surface S. Hence, evaluated at the outer radius of the plasma, a,

$$q(a) \simeq \frac{2\pi a^2 B_\phi}{\mu_o I_p R} \tag{1.3}$$

where I_p is the total plasma current. Small values of q are desirable since one would rather invest one's available energy resources in ohmically heating the plasma ($I_p^2 R$) than in the magnetic field ($B_\phi^2/2\mu_o$). However, q, often called the plasma safety factor, and its spatial derivatives (magnetic shear) enter the theory of magnetohydrodynamic (MHD) modes, and in practice q must be kept greater than about 2.5 for macroscopic stability.

Efforts in Tokamak research are, of course, aimed towards the goal of sustaining a thermonuclear discharge. A calculation of the energy required to create and sustain a fusion discharge radiating energy and losing particles whose energy is recovered with an efficiency not greater than 33% was carried out by J. D. Lawson.[1] The result, known as the Lawson Criterion, is that the product of the electron density and energy confinement time, $n\tau_E$, must exceed a value of about $10^{14}cm^{-3}$-sec for deuterium-tritium reactions in which the ion temperatures exceed about 2.6 keV; $n\tau_E$ must exceed a value of about $10^{16}cm^{-3}$-sec to sustain a thermonuclear burn with deuterium-deuterium reactions in which the ion temperatures exceed about 17 keV.

The confinement of Tokamak plasmas is considerably degraded by diffusion via collisional and convective mechanisms. These make attainment of the Lawson conditions even more difficult than one might anticipate. The particle diffusion coefficient due to stochastic Coulomb scattering may be described by $D \sim (\Delta x)^2/\Delta t$ where Δx is the mean spatial step size and Δt the mean step time associated with a charged-particle Coulomb-scattering event. In a homogeneous magnetic field (straight field lines) the mean step size is the Larmor radius ρ and the mean time is the reciprocal of the Coulomb collision frequency

$$\nu_{ei} \simeq \frac{1.6 \times 10^4 Z_{eff}(n_e/10^{13}cm^{-3})}{(T_e/1\ keV)^{3/2}}\ (Hz) \qquad (1.4)$$

where $Z_{eff} \equiv \sum_i n_i Z_i^2 / \sum_i n_i Z_i$ is the effective atomic number of the plasma made up of electrons and ions of the i^{th} species having number density n_i and atomic number Z_i, the sums being taken over all ion species present. For a typical Caltech Tokamak discharge, $n_e \simeq 10^{13} cm^{-3}$, $T_e \simeq 100eV$, $B_\phi \simeq 4.1kG$, and Z_{eff} is assumed to be about 1.5 (the filling gas being hydrogen and the remaining ion species being impurities of much larger mass); the Larmor radius is thus $\rho \simeq 5.8 \times 10^{-3} cm$ and $\nu_{ei} \simeq 7.6 \times 10^5 Hz$, hence the classical diffusion coefficient for Coulomb collisions is about $26 cm^2/sec$.

The complexities of Tokamak plasmas considerably enhance the classical diffusion value. Figure 2 shows the graph of the diffusion coefficient due to Coulomb collisions and modified by geometric and trapped-particle effects versus the Coulomb collision frequency. The lower dashed line represents the value $\rho^2 \nu_{ei}$ discussed in the foregoing. Enhancement of diffusion comes about at small values of ν_{ei}, the "collisionless regime", by the trapping of charged particles into so-called banana orbits. The previously mentioned excess of toroidal magnetic field on the inside of a toroidal solenoid with respect to the field on the outside of the solenoid ($B_\phi \sim (R + r \cos \theta))^{-1}$ in the geometry of Fig. 1) creates a magnetic mirror which may reflect particles toward the outside of the torus thus preventing the completion the short way around the torus of closed drift orbits. These trapped (in the magnetic mirror) particles execute drift orbits that have a banana-like shape when projected onto an azimuthal plane (Fig. 3). The mean radial step size for trapped particles is the width of the banana orbit, $\Delta r_T \simeq 2q(r)\, \rho / \sqrt{r/R}$, where the safety factor q is evaluated at the mean minor radius of the banana orbit. This mean step size is on the order of 10 times the Larmor radius in most Tokamaks. Additionally, those

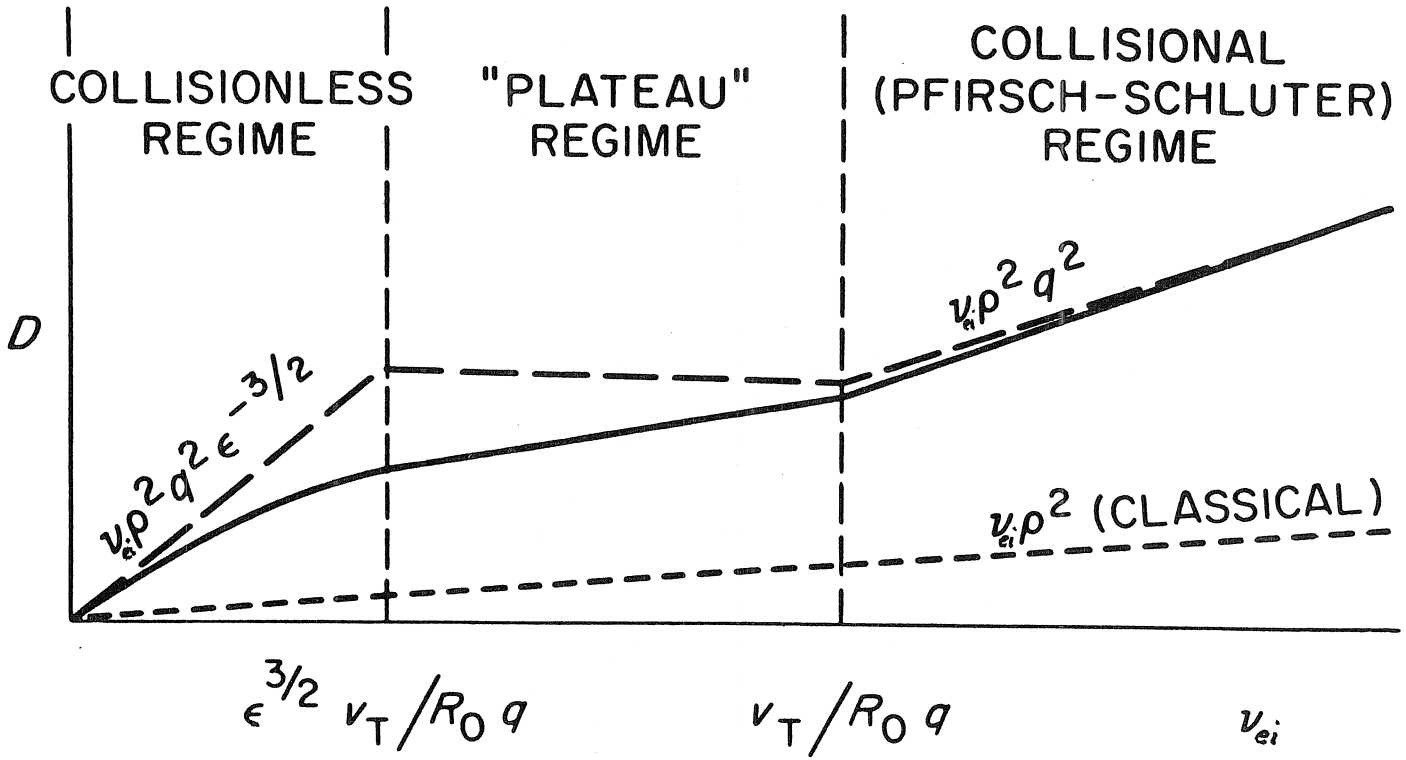

Figure 2. (Adapted from ref. (2)). Collisional diffusion coefficient vs. Coulomb collision frequency ν_{ei}. v_T is the thermal velocity of electrons, $(kT_e/M_e)^{1/2}$, and R_0 is the major radius, $\epsilon = r/R_0$ and $q = q(r)$ at a radius r within the plasma.

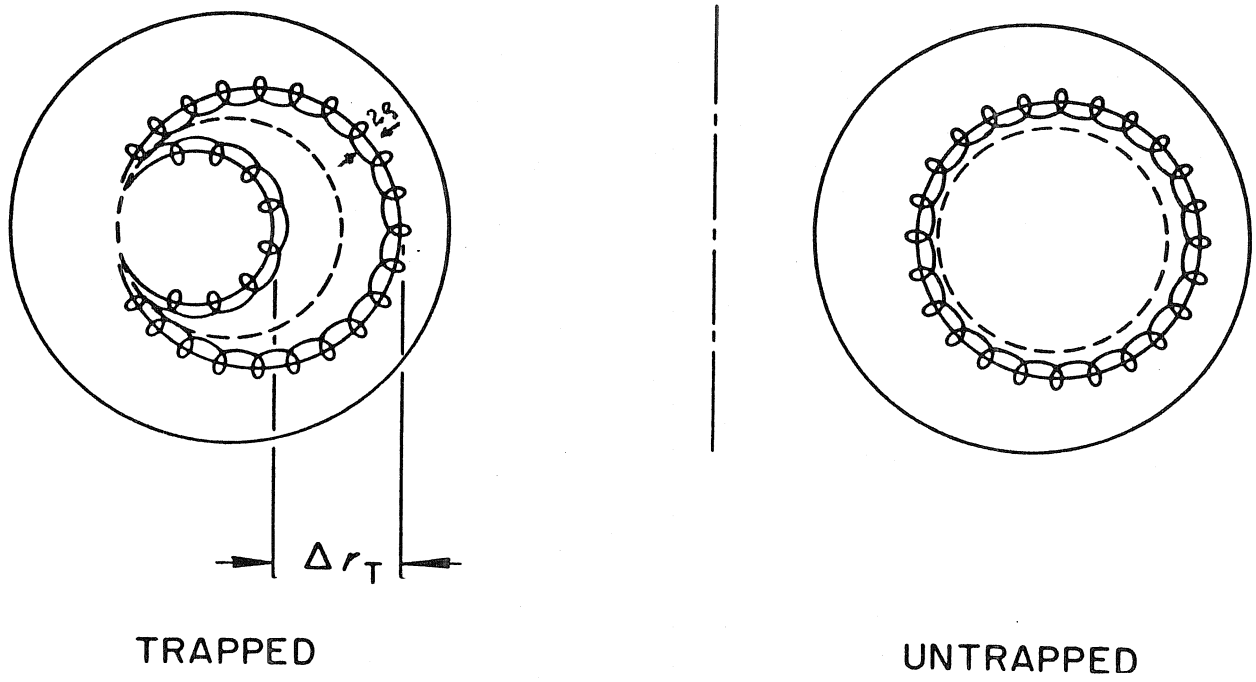

Figure 3. (Adapted from ref. (2)).

Left: Trapped particle executing a banana trajectory. The random walk step size Δr_T is considerably larger than the Larmor radius ρ.

Right: Trajectory of a particle not confined by the magnetic mirror.

Both: Dashed lines represent flux surfaces (q = constant).

particles with poloidal velocities sufficient to avoid entrapment have their step sizes enhanced by a factor q ($\lesssim 4$) by the effects of toroidal geometry.

At higher collision frequencies trapped particles may scatter before they can completely trace out their banana orbits. If the collision frequency is high enough that motion along the magnetic field is impeded by diffusive resistance to the flow the collisionality is said to be in the "plateau regime". This is the regime into which the Caltech Tokamak falls. If the collision frequency is high enough that motion along the magnetic field is impeded by diffusive resistance to the flow the collisionality is said to be in the collisional or Pfirsch-Schluter regime[3] and $D \sim \nu_{ei}\rho^2 q^2$. The advantage to low-q operation is obvious.

Particle loss rates from Tokamaks are larger by several orders of magnitude than those predicted by collision theory. Further enhancement of diffusion may take place via so-called anomalous transport. The phenomenology of anomalous transport is generally divided into two sections: microinstabilities, which result from kinetic effects, and macroinstabilities which result from fluid effects. Among the latter are the kink-tearing mode MHD instabilities. These instabilities are believed to be responsible for the creation of structures called magnetic islands (Fig. 4) that have associated with their growth fluid convection cells. Particularly worrisome is the possibility of non-linear destabilization of these modes which theory predicts will permit the growth of the magnetic islands to widths of one-third to one-half the plasma radius. It is confirmed experimentally that magnetic-fluctuation activity of the type thought to be caused by tearing modes, particularly the m = 1 and m = 2 poloidal mode

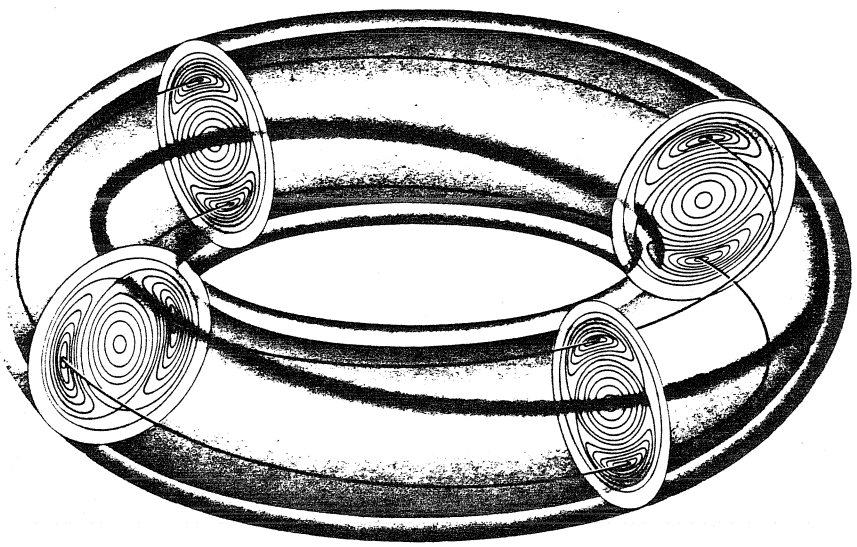

Figure 4. (From ref. (4)). m=2 (n=1) magnetic islands. The islands are really a set of nested flux tubes resulting from the superposition of a radial magnetic field perturbation with the proper helicity, i.e., varying as $\exp[i(m\theta+n\phi)]$, upon a static toroidal field B_ϕ and sheared poloidal field B_θ, i.e., $\partial B_\theta/\partial r \neq 0$. The widths of the islands are exaggerated with respect to those deduced from experimental measurements.

number oscillations, precedes the so-called disruptive instability. This phenomenon is not a fluid instability derived from MHD theory but rather a collection of phenomena that has so far defied theoretical analysis. A disruption is characterized by simultaneous inward jumps in the plasma major radius and outward jumps in the plasma minor radius and the appearance of negative spikes on the loop voltage (that is, the voltage that drives ohmic heating). The outward jumps in minor radius can severely damage the apparatus normally shielded within the shadow cast by refractory metal "limiters" (there are no such limiters in the Caltech Tokamak, hence a reference to a limiter shall henceforth mean the terminus of the plasma, that is, the vacuum vessel itself). The plasma may recover from mild disruptions but severe disruptions may actually prematurely terminate the duration of the discharge.

To return to the contribution to diffusion by transport across magnetic islands, theoretical efforts to obtain a simple expression for this term have been frustrated by a lack of a concise expression for the radial excursion associated with the fluid convection; in fact, there are stagnation points in the flow and portions of the fluid make hardly any excursions. Nonetheless field lines near the inside edge of the islands connect to near the outside edge, hence transport across these structures is widely believed to be rapid.

Recent experiments in the Alcator Tokamak[5] have shown linear scaling of energy confinement time with electron density in all but the most extreme cases of high-density discharges (the Caltech Tokamak cannot reach this extreme parameter regime). These experiments also demonstrated linear scaling of particle confinement time with electron density.

Daughney[6] has proposed a scaling law for the average electron energy confinement time

$$\tau_{Ee} \propto \frac{n_e T_e^{3/2}}{Z_{eff}^{1/2} I^{3/2}} a^3 \qquad (1.5)$$

which is based on data from experiments in the ST, ATC, TFR, and Ormak Tokamaks. Since it appears the $n\tau_E \propto n^2$ Tokamaks are intentionally operated with the highest densities achievable. There is an upper limit[7] on the filling pressure, and thus the particle density, which may be broken down with currently employed techniques of gas pre-ionization and subsequent application of ohmic-heating power.[8-10] It has been found experimentally that addition of neutral gas during a Tokamak discharge can increase the charged-particle density beyond the level of full ionization of the filling gas. This procedure is called gas puffing.

There is a further reason for wishing to add neutral gas during the Tokamak discharge that has just recently had its importance revealed. The major contribution to energy loss due to radiation comes from acceleration of electrons by nuclei, that is, bremsstrahlung. The power density radiated by all electrons (in watts/m^3) from a neutral hydrogen plasma is given by

$$w_x = 4.8 \times 10^{-37} n^2 T_e^{1/2} \qquad (1.6)$$

where n is the electron density in particles/m^3 and T_e the electron temperature in keV.[11] Enhancement of the radiated power by a factor

$$\sum_\xi (Z_\xi n_{i\xi}) \sum_\zeta (Z_\zeta^2 n_{i\zeta} / Z_1 n_{i1}^2)$$

occurs when impurity ions of atomic number Z_ξ are added to a plasma with ion density n_{i1} and atomic number Z_1. Even low-Z impurities such as oxygen may substantially increase energy loss by bremsstrahlung, which at thermonuclear temperatures is in the x-ray range of wavelengths. The TFR group calculates 40% of the power input to their experiment is lost by low-Z bremsstrahlung.[12] Theoretical calculations suggest domination of bremsstrahlung over such mechanisms as diffusion and heat conduction as the principal cause of energy loss in the larger Tokamaks planned for the future.[13,14] Purity of substances entering the discharge is thus of crucial importance in progress toward power generation.

A substantial amount of impurities may be present within a Tokamak in the form of gas adsorbed on the walls. In particular, discharges in the Caltech Tokamak are commonly run at initial neutral (i.e., filling) hydrogen pressures of 1.35×10^{-4} Torr, or roughly 9×10^{12} hydrogen atoms per cm^3, whereas a single monolayer of monatomic gas desorbed from the walls and distributed uniformly throughout the volume would provide roughly 4×10^{14} atoms per cm^3. It is important to note that the walls are under continuous bombardment by the plasma throughout the duration of the discharge. Particle confinement times in Tokamaks are generally of the order of one to a few tenths of the duration of the discharge, hence on the average each plasma particle makes several trips to the wall each shot. In the Caltech Tokamak the average electron temperature measured by means of the plasma conductivity is in excess of 100eV, and this is certainly enough energy to knock adsorbed atoms off the wall and to ionize them. Hence gas adsorbed on the walls is certain to figure prominently as a source of particle influx. Evaporation of titanium onto Tokamak walls

prior to each discharge has been demonstrated to effectively inhibit oxygen influx;[15] this is, however, a costly, awkward, and time-consuming process.[16] Within the last few years wall conditioning by exposure to a low-temperature audio-frequency hydrogen discharge has been demonstrated to limit the oxygen and carbon available for such influx. Oren and Taylor have shown that discharge cleaning removes oxygen and carbon by converting them to water vapor and methane which may be pumped out, reducing the residual amount of oxygen in the Microtor Tokamak to nearly 10^{10} atoms per cm^3.[17] Implementation of discharge cleaning is discussed in the body of this thesis.

While discharges in Tokamaks with clean walls radiate less energy in the form of x-rays and although discharge cleaning extends substantially the parameter range in which the Caltech Tokamak can be operated without premature termination of discharges, a deleterious effect on the electron density subsequent to breakdown is observed. In the Caltech Tokamak this manifests itself as a monotonic decay from the full-ionization value of roughly 9×10^{12} electrons/cm^3 to roughly 3×10^{12} electrons/cm^3 at four milliseconds into the shot. Thereafter the decay is still monotonic but less severe (Fig. 5). No such decay has been reported in Tokamaks that do not employ discharge cleaning. Addition of neutral hydrogen by gas puffing recovers the lost electron density, the pure gas substitutes for an influx of impure gas atoms knocked off the walls by a discharge in a dirty Tokamak.

There exists an upper limit on the amount of neutral hydrogen that may be incorporated into the plasma without disruption. The peak achievable electron density scales linearly with the ratio of toroidal magnetic field to the major radius of the torus or equivalently with the product of

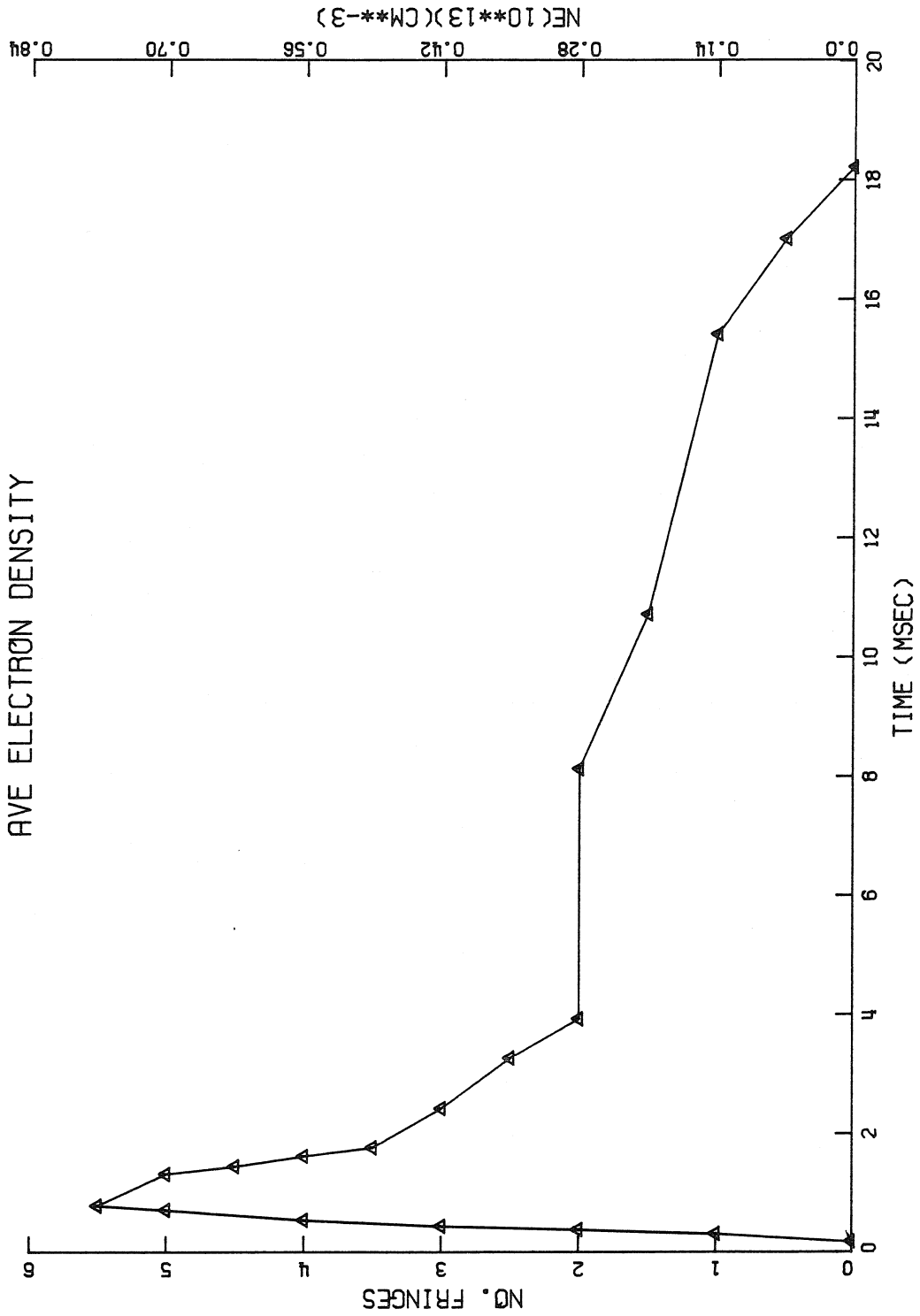

Figure 5. Typical line-averaged electron density trace for a Caltech Tokamak discharge without gas-puffing (filling pressure p_o = 1.3 x 10^{-4} Torr, ohmic-heating fast-bank (OHFB) at 1 kV, slow-bank (OHSB) at 310v, vertical-field fast-bank (VFFB) at 120v, slow-bank (VFSB) at 49v, toroidal-field bank at 3.8 kV (4.0 kG peak) and horizontal-correction current (I_{HC}) at 100 A).

on-axis current density, J(0), and safety factor, q(0), (the latter quantity is close to 1).[18] Such disruptions are generally believed to be related to the cooling of the outside of the plasma by the neutral gas feed and to the shrinking of the current channel.

In the body of this thesis a series of experiments is described that demonstrates that while particle confinement in the Caltech Tokamak is relatively unaffected by manipulation of those parameters that alter (within the normal range of operation) the plasma safety factor, q, changing those parameters that are believed to alter the magnetic shear, $\partial q/\partial r$, in such a way as to increase the shear strongly degrades particle confinement. The phase relation between magnetic fluctuation components measured with pairs of probes is shown to be consistent with the formation of magnetic island structures rotating within, and with, the plasma. In the case of increasing particle density the degradation in particle confinement is shown to coincide with destabilization of an m = 2 fluctuation mode the growth time of which is an order of magnitude larger than the classical tearing-mode growth time. The phenomenology of the magnetic fluctuations is shown to be consistent with classical tearing-mode theory in the growth rate of the m = 2 mode and the stabilization of higher m-number modes during neutral gas feed to the discharge (when the magnetic shear is believed to be largest) and in the appearance of higher m-number modes upon cessation of gas puffing (when the shear is believed to relax to a smaller value). Additionally, the nature of these high-order modes is explained: both harmonic distortion products resulting from deformation of the m = 2 and m = 3 magnetic-island and the m = 7, n = 2, mode are present during the density decay of a short gas puff.

II. EXPERIMENTAL APPARATUS

A. Introduction

In this chapter the Caltech Tokamak system will be described. The section following this one deals with the sources of energy and method of implementation for the generation of the toroidal, vertical, and horizontal fields, and the ohmic-heating current which heats the plasma and provides the poloidal field. The next section describes the pumping and discharge cleaning systems. This is followed by a discussion of the implementation of gas puffing. The final two sections describe the systems of diagnostic measurements and data acquisition.

B. Ohmic Heating and Confinement Field Generation

The short duration ($\lesssim$ 20 msec) of Caltech Tokamak discharges and the fact that the energy required to create and sustain the discharges is stored in large banks of capacitors mandates the mode of operation be a cycle of discharges followed by longer ($\sim$ 1 min) intervals during which the banks are recharged, data are transferred to permanent storage, and operating parameters may be adjusted. The various energy supplies are discharged and the data acquisition and gas-puffing systems are set into operation by a system of digital timing units. Each timing unit produces an output voltage pulse after a settable delay from reception of an input voltage pulse. The triggering of the entire system is summarized in Figure 6. Two time scales appear in this figure: timing unit time which begins ($t = 0$) with the triggering of the toroidal field while shot time begins ($t = 0$) with the simultaneous application of the ohmic-heating fast-bank and triggering of the data acquisition system. The toroidal bank is discharged first because of the slow rise to full value of the toroidal field;

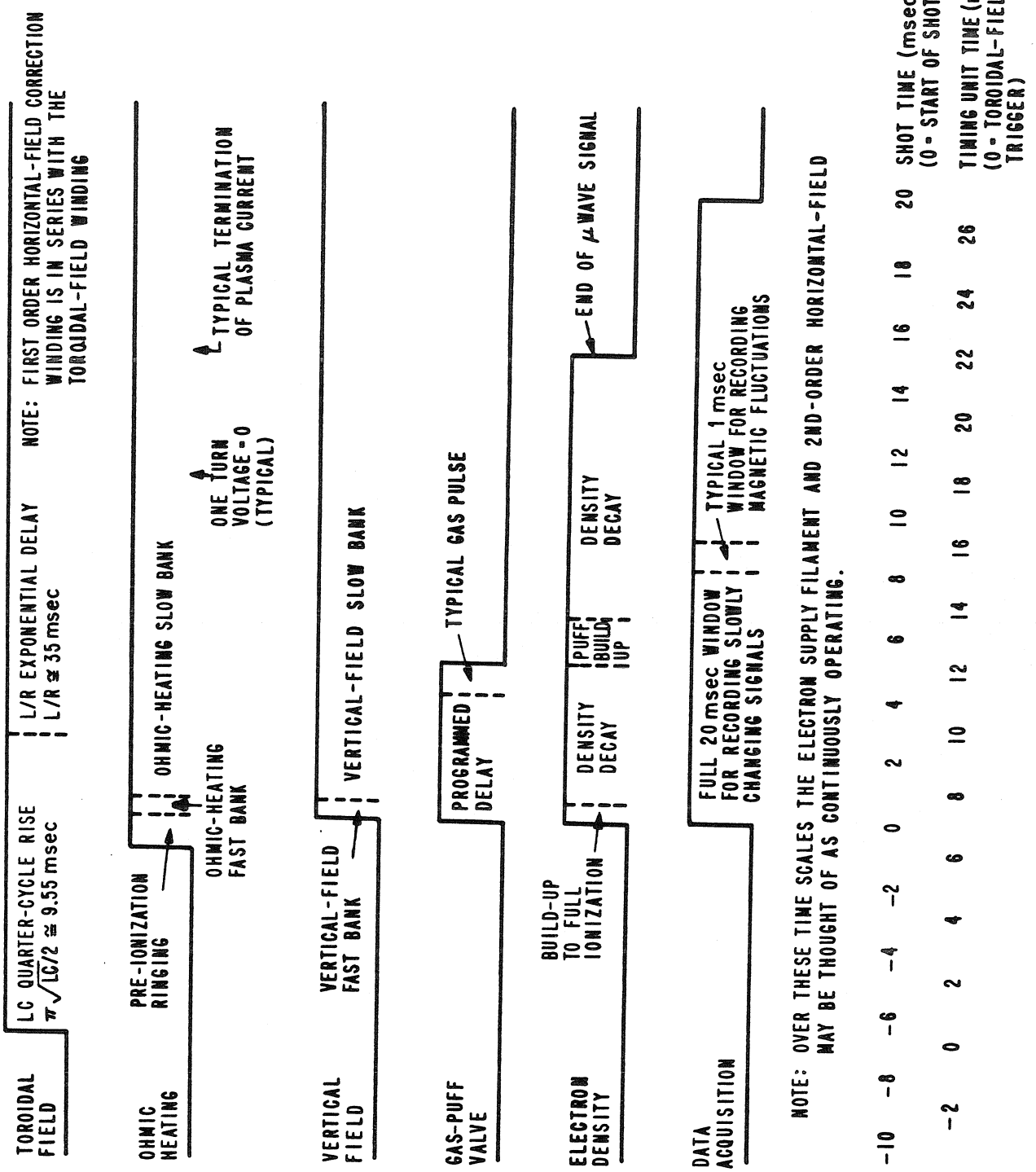

Figure 6. Timing diagram for discharging of supply banks and initiating gas puffing and data acquisition. The timing unit time scale refers to the actual settings on the pulse generating units. Shot time refers t=0 to the application of the ohmic-heating fast-bank which causes the filling gas to be fully ionized. This time scale is the one used in the discussion of experimental results.

the other systems are triggered for the most part 6-7 msec after the toroidal field is triggered. The toroidal field timing unit also triggers the 60 sec delay to the next shot, a warning beeper that sounds 2.5 sec before the next shot, and the d.c. horizontal field and filament source of electrons that are turned on 4 sec before the following shot and off 6 sec later. Hence, these latter two systems are on for the entire time span of Fig. 6. The timing unit system requires a manual trigger pulse to start it cycling. The reader may find it convenient to consult Fig. 6 as the various systems are discussed. To be included in the discussion of diagnostic signals are plasma current, loop voltage, microwave interferometer, and position-coil traces. These signals are the basis upon which the experimenter selects his operating parameters.

The vacuum vessel is comprised of four non-magnetic stainless-steel elbows (Fig. 7) flanged and pairwise bolted together. Bakelite spacers outside viton o-ring vacuum seals isolate the two halves electrically so that the vessel itself does not form the secondary winding for the ohmic-heating air-core transformer. The assemblage forms a torus of 15 cm minor radius and 46 cm major radius. Access to the plasma is gained via several small circular ports and four long, thin, vertically-oriented ports. The toroidal solenoid is wound directly on the torus, the shape and number of ports having been chosen to minimize error fields which might cause the magnetic field lines to intersect the wall rather than to "close upon themselves" (in practice it is only necessary that particle loss due to outward spiraling be smaller than replacement by recycled particles, that is, those ions that are neutralized at the walls and that re-enter the plasma where they are re-ionized). Energy to power the toroidal windings

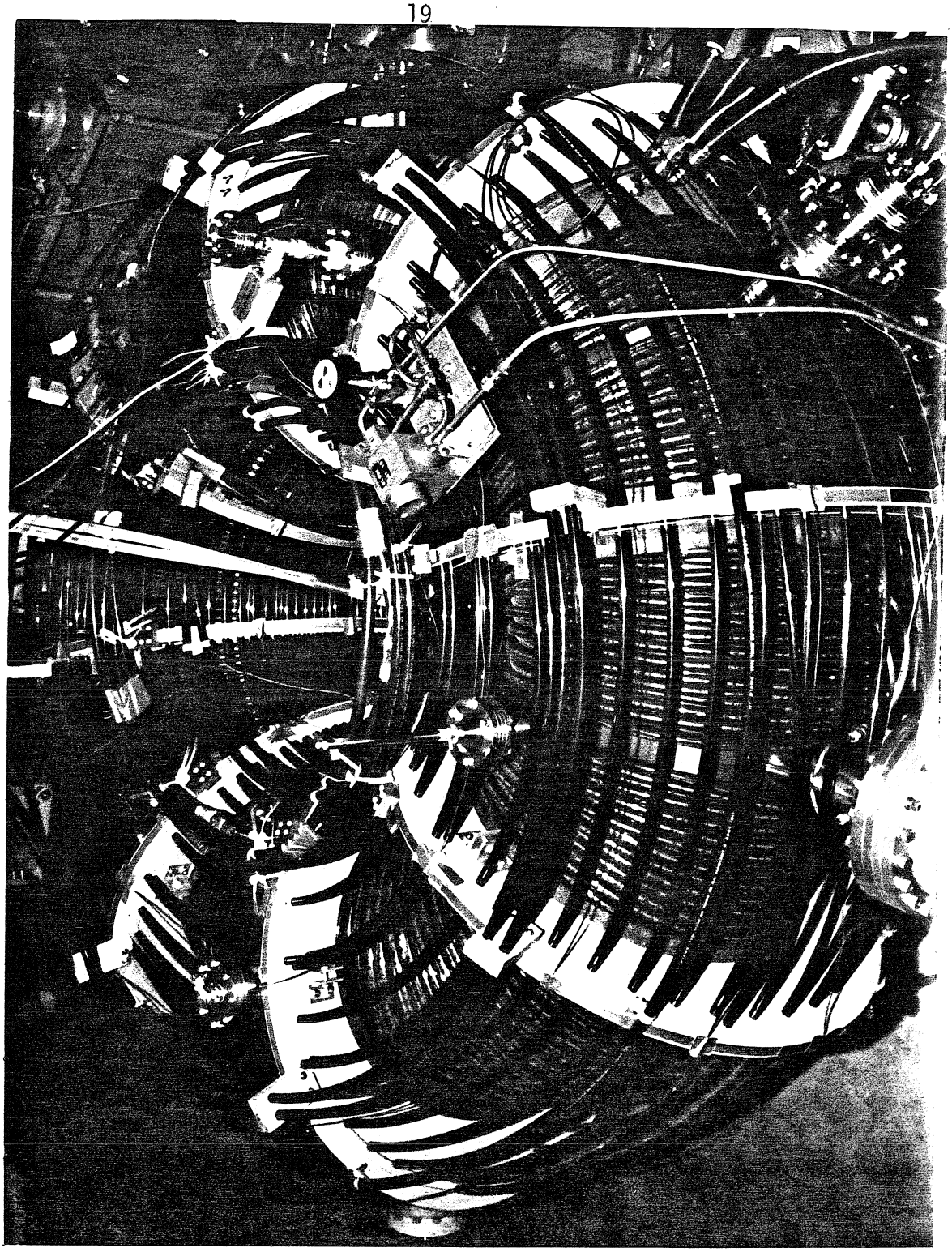

Figure 7. The Caltech Tokamak.

comes from a 4.8 μf, 10 kV (250 kJ) capacitor bank. The bank is discharged into the winding, the current rising as a quarter-sinusoid of a quarter-period $\pi/2\sqrt{LC}$ (≈9.55 msec), and when the current reaches its peak the bank is crowbarred by two shunt ignitrons. The current in the winding then decays with e-folding time L/R (≈35 msec) where R is the resistance of the winding.

Wooden collars serve as coil forms for the ohmic-heating, vertical and horizontal-field windings. The ohmic-heating winding consists of 40 turns located primarily on the inside of the torus and spaced so that the ohmic-heating coil itself is a flux surface. The flux induced by the coil is thus external to the torus except for errors due to the discrete nature of the winding. The coil is energized in a three-step process. At 5.91 msec after initiation of the toroidal bank discharge the pre-ionization capacitor is discharged into the winding. This is a 1 μf, 10 kV (generally charged to 7-9 kV) capacitor whose small capacitance in series with the winding creates a slowly decaying audio-frequency (4 kHz) acceleration voltage for the free electrons in the torus. This signal is the major source of noise in the system. After four or more cycles sufficient numbers of hydrogen molecules have been dissociated and ionized that application of a rather high voltage (typically, 1 kV) to the winding from the ohmic-heating fast bank of capacitors accelerates the electrons several times around the torus to create an avalanche breakdown of the filling gas. This bank has 432 μf capacitance and a $\pi/2\sqrt{LC}$ quarter-cycle rise-time much smaller than the ohmic-heating slow-bank of capacitors. The latter is a 208 mF, 450 V bank which is crowbarred across the winding when a zero-crossing circuit determines that the fast-bank voltage has

fallen to that of the slow bank. The slow bank thus maintains the ohmic-heating current for the major portion of the discharge.

It is appropriate to note at this point that the pre-ionization circuit is guaranteed a supply of free electrons to accelerate by a tungsten filament source recessed in a port. This filament is heated with 60 Hz current for 4 seconds prior to the discharge. The filament is placed at a lower DC potential than the torus, the potential controlling the emission current. The ohmic-heating fast-bank is triggered 7.00 msec after initiation of the toroidal bank discharge. The number of pre-ionization cycles is a function of the characteristics of the particular ignitron which switches the capacitor into the circuit. This turns out to be quite random and ignitrons must be selected and occasionally replaced.

The vertical magnetic-field supply also consists of slow and fast banks of capacitors, the capacitances (1.92 μf at 450 V for the fast bank, 396 μf at 100 V for the slow bank) being chosen so that the shape of the vertical field signal follows that of the plasma current. The ohmic-heating slow-bank voltage is chosen to provide the desired plasma current while the vertical-field slow-bank voltage is chosen, on the basis of this current, to keep the plasma centered during the discharge. The ohmic-heating fast-bank voltage is chosen primarily to provide full-ionization of the filling gas for a variety of pressures. The vertical-field fast-bank voltage is chosen for good centering once the ohmic-heating fast-bank voltage is chosen. Gas-puffing requires re-adjustment of the vertical field slow bank to slightly smaller voltages.

The horizontal-field winding originally comprised two turns on the top and two turns on the bottom of the torus in series with the toroidal

winding. The horizontal field corrects errors in magnetic field believed to be caused by asymmetries in the toroidal winding. These asymmetries arise from the excursions the winding makes around the diagnostic and pumping ports. These errors should scale linearly with the toroidal field, hence the series arrangement. In scaling the ohmic-heating and vertical-field supplies upwards to create longer discharges it was determined that the horizontal correction was insufficient. A second set of correction coils was wound next to the first and is energized by a Hewlett-Packard Model 6453A 200-ampere, 15-volt supply simultaneously with the filament. The desired correction scales linearly with the toroidal field lending credence to the preceding theory of error origin.

C. The Pumping and Discharge Cleaning Supplies

A system base pressure of roughly 1×10^{-7} Torr is maintained with a pumping stack consisting of a Leybold-Heraeus turbomolecular pump, zeolite trap, and Sergeant-Welch forepump. No cryobaffle is used. High purity hydrogen gas is leaked in between the turbo-pump and zeolite trap to provide the filling gas for Tokamak shots or discharge cleaning. Since the turbo-pump pumps heavy molecules faster than light ones, the heavy impurity molecules have greater difficulty making their way across the pump, hence further purification of the filling gas is realized.

Each day, before the Tokamak is ready for experimental work, a pulsed audio-frequency discharge is run. Neutral hydrogen at a filling pressure of 2.5 to 3.5×10^{-4} Torr (c f. typical Tokamak shot filling pressures of 1.35×10^{-4} Torr) is broken down by 5 kV at 38 kHz pulsed on the ohmic-heating winding for 70-90 msec of each 1.0 second period. A steady d.c. toroidal magnetic field of 146 gauss is provided by running

70 amps d.c. through the toroidal field windings. This weakly confines the plasma.

As Oren and Taylor maintain, the most abundant low-Z impurities, oxygen and carbon, are knocked off the wall and ionized by the discharge, the toroidal field keeps these ions away from the wall long enough that between pulses they may combine with the filling hydrogen to form gaseous H_2O and CH_4 which are subject to being pumped out of the torus. A quadrupole gas analyzer (Varian Model 978-1000) and strip chart recorder monitor the composition of the gas present in the Tokamak. The analyzer is programmed to sweep through atomic masses 10 to 20 each 5 minutes; inspection of the strip chart shows the evolution of such lines as H_2O and CH_3 (methane radical). After a short ($\sim$ 20 min) period of discharge cleaning the water vapor line becomes the dominant peak on the chart; its magnitude falls off roughly as 1/t. One finds that after about 5 hours of continuous discharge cleaning the water vapor line reaches a level that diminishes so slowly as to make further cleaning intolerable. Fortunately, this level is sufficiently small to eliminate the most obvious effect associated with dirty walls: less than optimal shot duration. One finds that operating with parameters that produce 20 msec long discharges with very clean walls may produce shots lasting $\sim$ 16 msec with dirtier walls. Equivalently, discharges in a dirty Tokamak require more ohmic-heating power to sustain them for a given period of time. Exposure of the vessel interior to the atmosphere during alteration of experimental equipment or contamination of the walls due to accidental introduction of pump oil or chemical solvents may make mandatory 24 hours or more of discharge cleaning to restore clean wall conditions.

D. The Gas-Puffing System

The gas-puffing system (Figure 8) consists of a separate source of high-purity hydrogen gas which, via regulator and leak valves, fills a reservoir consisting of a length of stainless-steel tube connected to the Veeco PV-10 piezoelectric valve and thence via pyrex tube to one of the small circular ports on the underside of the Tokamak. The reservoir may be evacuated and then filled to the desired pressure.

The valve itself consists of a machined valve seat and a viton disk cemented to a bimorph piezoelectric crystal. A voltage of the proper amplitude and sign applied across the crystal opens the valve. When no voltage is applied the mechanical forces are such as to close the valve. The valve presents a nominal 30 nf load to the source driving it. The manufacturer specifies that the valve opens in less than 2 msec, presumably if a voltage step from fully closed (0 V.) to fully open (100 V.) is applied. Since the duration of the plasma shot is $\lesssim$ 20 msec it is desirable to open the valve in less than the rated time. To this end the valve is biased to a voltage just below significant opening. In practice this is chosen to be the level that increases base pressure to 5×10^{-6} Torr (roughly 34 V). The voltage steps to 125 V rather than 100 V, this value being chosen to increase opening speed without decreasing valve lifetime. This procedure reduces to less than one msec the delay between the voltage step and the increase of electron density as determined by microwave interferometry. Day-to-day variation of valve characteristics are noticed. The valve sometimes fails to seat reproducibly. The tendency of the valve to stick shut when first used after several hours of remaining closed is lessened by keeping the valve

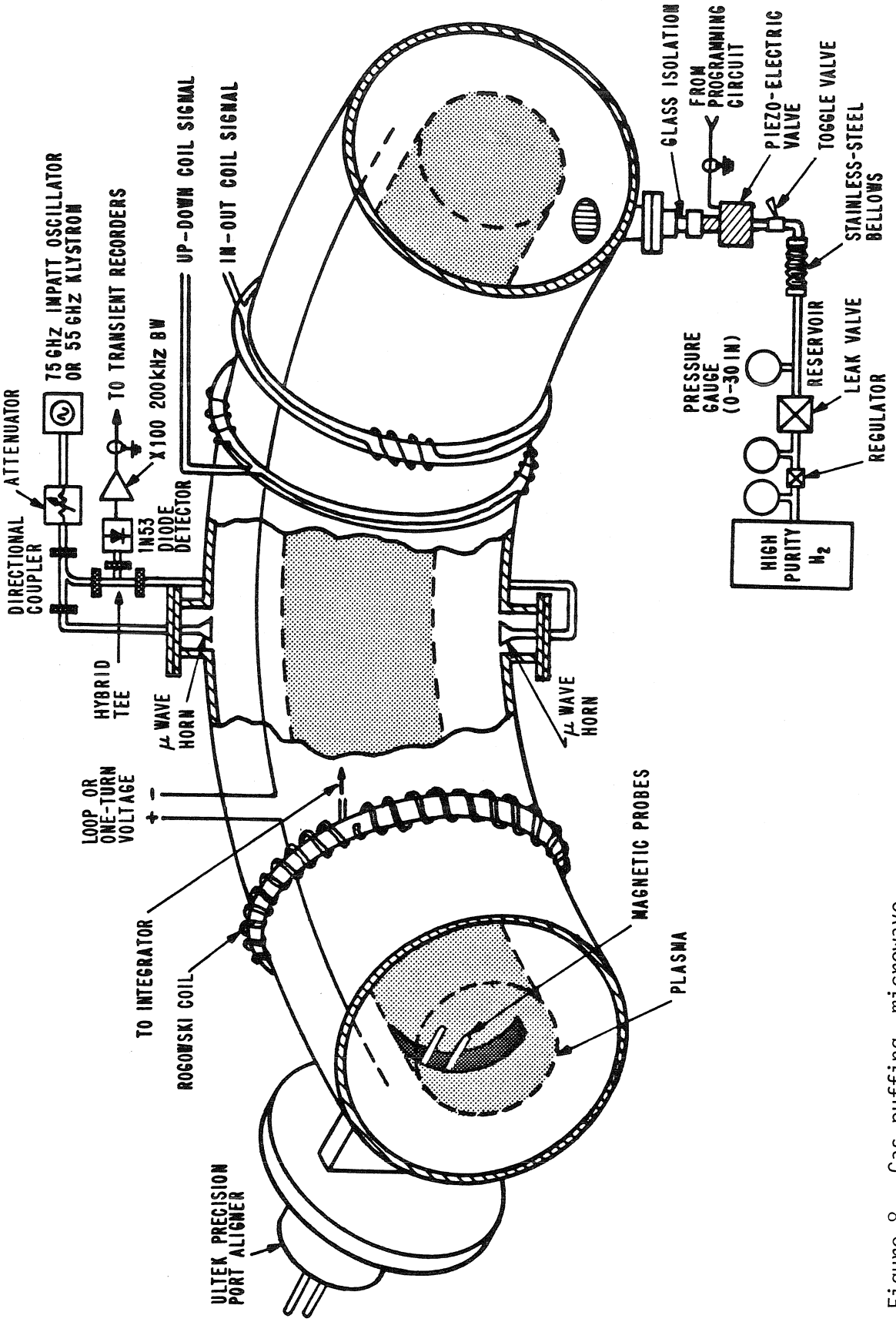

Figure 8. Gas puffing, microwave, and diagnostic systems.

fully opened during discharge cleaning and the interval between cleaning and firing the Tokamak. Nevertheless, initial pulsing is always erratic and requires frequent bias adjustment. Adjustment of bias does, however, allow maintenance of constant filling pressure.

The toroidal field timing unit is used to trigger other timing units that provide on and off pulses at presettable delays to the gas-puffing valve voltage-programming circuit shown schematically in Appendix I. A pair of on and off pulses trigger a D-type flip-flop, the output of which may be variably attenuated. Up to four of these pulses may be summed so that a relatively complex waveform may be generated if so desired. The final stages provide offset and amplification to the voltage levels discussed above.

The motivation for gas-puffing was described in some detail in the introduction. Briefly, auxiliary neutral gas is needed to substitute for the rather impure wall influx in a dirty Tokamak, and energy confinement is believed to increase linearly with the particle density. Hence gas-puffing creates conditions closer to those required by the Lawson Criterion to reach thermonuclear breakeven. It will be shown in the next chapter that if one puffs in gas and allows the elevated density to decay by cessation of the gas feed then the time-evolution of the particle density yields useful information about the containment of particles. Figure 9 shows the microwave interferometer-derived particle density for a shot for which the valve, with 970 Torr hydrogen reservoir pressure, was opened with a 0.32 msec long, 125 V pulse beginning 3.4 msec into the shot (cf. Fig. (5)).

The throughput of the puffing valve for a typical gas pulse is

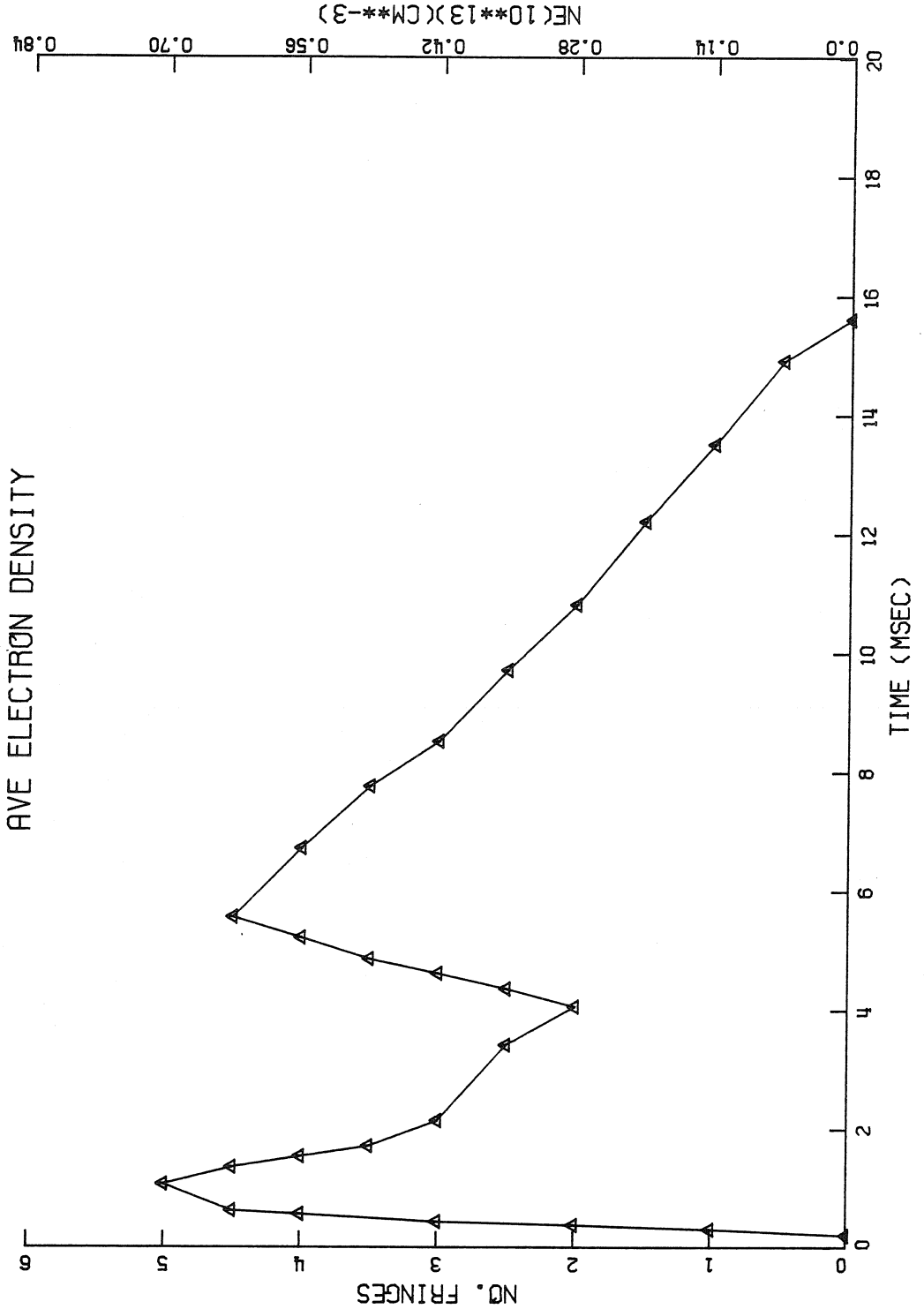

Figure 9. Line-averaged electron density trace with gas-puffing. The shot parameters are identical to those of Figure 5. The voltage pulse was applied from 3.40 to 3.72 msec with 970 Torr pressure behind the valve.

estimated in the following way. Enough gas was puffed in to increase the line-averaged particle density by three microwave fringes (the interferometer measurement is discussed in the following section). The experiment was then shut down and the Tokamak valved off from the pumping stack. Averaging over 30 pulses it was found that 8.1×10^{-5} Torr of hydrogen was added to the Tokamak volume of 204 liters for a 0.56 msec, 125 V pulse applied to the valve (the reservoir pressure was 970 Torr). The estimated valve throughput is

$$Q = \frac{V\Delta P}{\Delta t} \simeq 30 \frac{\text{Torr-}\ell}{\text{sec}}$$

Burrell[19] assembled a gas-feed system also using a Veeco PV-10 valve but deliberately employed Poiseuille flow through a tube 75 cm long and 0.7 mm diameter between the valve and the ISX-A Tokamak. The throughput of this system was 41 Torr-ℓ/sec but the flow had a 10% to 90% rise time of about 8 msec.

The gas flow through the puffing system is non-steady and the effects of viscosity (the gas pulse travels down a tube 28 cm long and 0.95 cm in diameter between the valve and the Tokamak; this tube consists of the Tokamak port, flanges, and the glass electrical-isolation section) and compressibility are likely not negligible. It is probable that the large pressure ratio across the valve (970 Torr to 1.35×10^{-4} Torr) causes a shock wave to appear in the flow subsequent to opening the valve. However, the sluggish time-response of the valve suggests that following application of the 125 V the flow from the valve is initially an isentropic compression that eventually forms a shock wave weaker than the $M_s = 5.2$ obtainable from the normal shock relations and a pressure ratio of 7.2×10^{6}. If a shock wave does form then no fluid may leave the

puffing system until the shock reaches the Tokamak end of the 28 cm tube. Since the shock speed is $c_s = M_s a$ where $a = (\gamma RT)^{1/2} = 1.306 \times 10^{5}$ cm/sec is the speed of sound in hydrogen at 293° K and M_s is the Mach number of the shock (≤ 5.2), the fastest the gas could enter the Tokamak is about

$$t_f \simeq \frac{28 \text{ cm}}{5.2 \times 1.306 \times 10^{5} \text{ cm/sec}} = 0.04 \text{ msec},$$

while the slowest it could take is about

$$t_f \simeq \frac{28 \text{ cm}}{1.306 \times 10^{5} \text{ cm/sec}} = 0.21 \text{ msec},$$

which is the time sound takes to travel the 28 cm.

There is a time delay from the leading edge of the valve voltage pulse to the start of the density-rise portion of the microwave signal of about 0.65 msec for the above pulses. Thus, it takes about 0.44 to 0.61 msec from the time the gas begins to enter the torus until the interferometer detects a density increase. The gas-puffing and microwave ports are separated by 105° in toroidal angle, hence it is estimated that it takes about 1.7 times as long to travel 180°, or 0.75 to 1.05 msec for the ionized gas to get half-way around the torus. Relating this to the microwave signal means that the ionized gas pulse travels around the torus in approximately the first 0.10 to 0.40 msec of the roughly 1 msec long density rise.

It should be noted that the large mass fluxes associated with these gas pulses imply the flow into the Tokamak is a well collimated jet. Langmuir probe temperature measurements in the Caltech Tokamak indicate that the plasma electrons have energy >14 eV beyond 1 cm into the torus. Thus, it is expected that the gas pulse is ionized in a small region of the plasma near the puffing orifice.

E. Diagnostics

1. The microwave interferometer

The reader has already been exposed, in Figs. 5 and 9, to particle density versus time graphs and, perhaps, has been convinced of their utility but wonders how they are obtained.

In a cold (T = 0), magnetized plasma the wave which propagates perpendicular to and decoupled from the static magnetic field is called the ordinary wave. The dispersion relation for this wave is given by

$$\omega^2 = \omega_{pe}^2 + k^2c^2 \tag{2.1}$$

where $\omega_{pe}^2 = n_e e^2/m_e\varepsilon_o$, n_e = electron density, m_e = electron mass, and ion terms have been neglected since they are of order m_e/m_i. This wave is evanescent for $n_e > n_c$ where $n_c = \omega^2\varepsilon_o m_e/e^2$. If an ordinary wave is launched in a plasma in which $n_e < n_c$ the wave is shifted in phase with respect to a wave simultaneously launched in a vacuum region. This phase shift, over a path of length L, is given by

$$\Delta\phi = \int_o^L \frac{\omega}{c}\left[1-\frac{n_e}{n_c}\right]^{\frac{1}{2}} dx \simeq \frac{\omega}{c}L - \frac{\omega}{2cn_c}\int_o^L n_e dx \tag{2.2}$$

$$\Delta\phi \simeq \frac{\omega L}{c} - \frac{\omega L}{2cn_c}\langle n_e\rangle \text{ where } \langle n_e\rangle = \frac{1}{L}\int_o^L n_e dx \quad \text{and} \tag{2.3}$$

the approximation is valid provided $n_e << n_c$. Thus the chordal average electron density of a plasma may be determined by launching an ordinary wave of known frequency.

The microwave interferometry system (Figure 8) consists of a 60 GHz Klystron or 75.0 Hughes Impatt Oscillator source (the latter coming into use after the former became gassy) feeding two 4 mm waveguide paths.

One path remains external to the plasma, the second feeds a waveguide horn just outside the plasma wall (i.e., recessed in a port) and continues with a similar horn diametrically opposed to the first. A hybrid junction gives an output that is a linear combination of the two signals and a 1N53 diode detector on the junction output gives an output voltage which varies as the cosine of the phase difference of the two input signals. The 1N53 is selected for good output at the source frequency. The detector output is fed via a short length of coaxial cable to a gain 100 amplifier consisting of two LF356 op-amps ac-coupled and each in a times-10 configuration feeding a LM310 line-driving op-amp. Recording of the signal is done on the transient recorders described subsequently. The same signal is recorded on 2, 5, 10 and 20 msec time scales and transferred to floppy diskette via the Vector 1+ microcomputer. Each channel is stored in an array of 1024 eight-bit bytes (i.e., as an integer between 0 and 255). Figure 10 shows the 2 and 20 msec full-scale traces corresponding to Fig. 9 . In general, the fringes are fairly regular but have noise superimposed on them. The noise is believed to arise mainly from plasma density fluctuations. As an aid to interpretation of the fringes some of the noise is removed by Gaussian averaging, that is, given an array n_i: $0 \le i \le 1023$, the averaged array $\bar{n}_i$ consists of values

$$\bar{n}_i \equiv \frac{1}{K} \sum_{j=i-n}^{i+n} c_j n_j$$

where $c_j = \exp[-(j/N)^2]$ and $K = \sum_{-N}^{N} c_j$. (2.4)

Hence the averaging includes those samples NT either side of a given sample, where 1/T is the sampling rate. Figure 11 shows the data of

Figure 10. Raw microwave signals corresponding to Figure 9. Vertical scale is 1 volt full scale. Lower trace is inverted with respect to upper by transient recorder electronics. Spectral analysis shows that over the last half-millisecond of the upper trace the microwave fluctuations are predominantly of frequency 25 kHz.

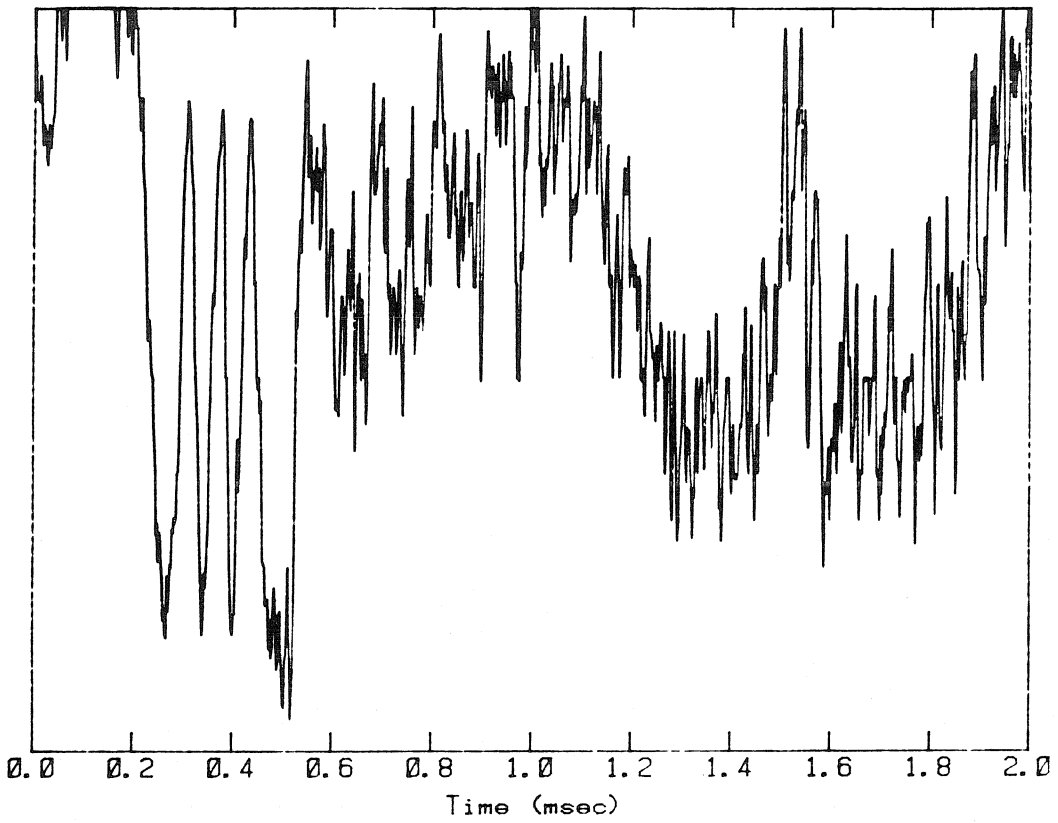
0.0
0.2
0.4
0.6
0.8
1.0
1.2
1.4
1.6
1.8
2.0
Time (msec)

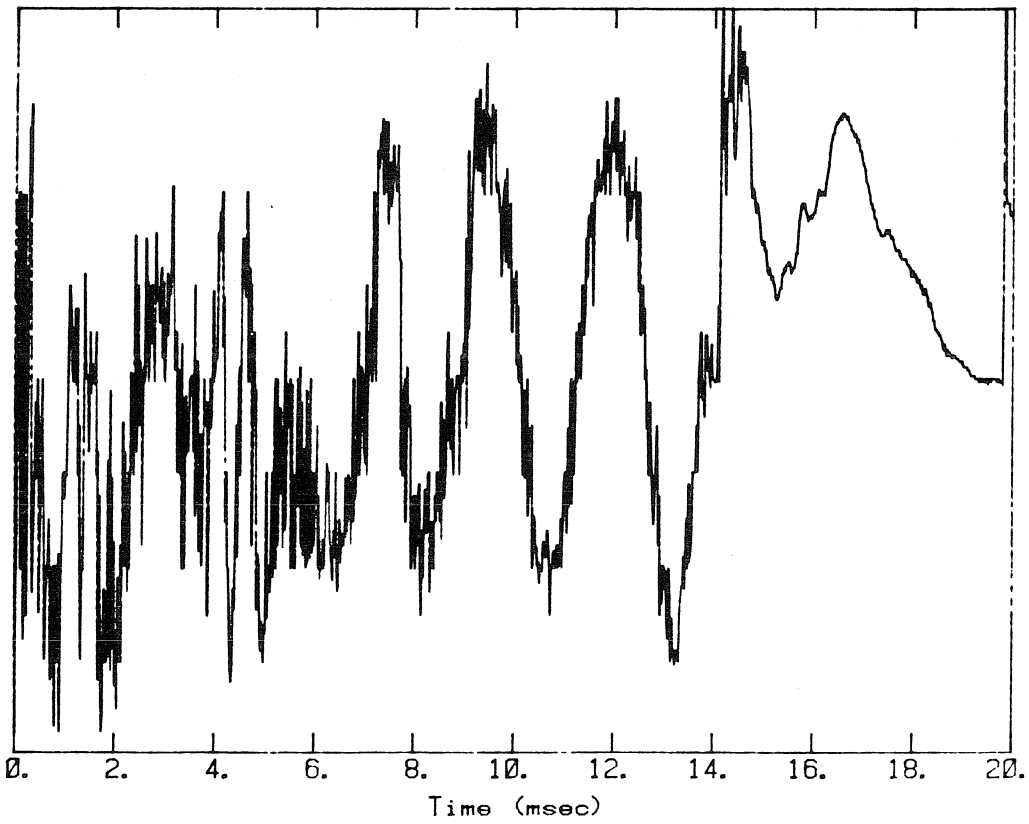
0.
2.
4.
6.
8.
10.
12.
14.
16.
18.
20.
Time (msec)

Figure 10.

Figure 11. Gaussian averaged (see text) traces corresponding to Figure 40. Gaussian half-widths are: top, NT = 60 μsec; bottom, NT = 60 μsec (or FWHM = 10 μsec, 100 μsec, resp.). The density build-up comes between 0.2 and 1.0 msec of the upper trace.

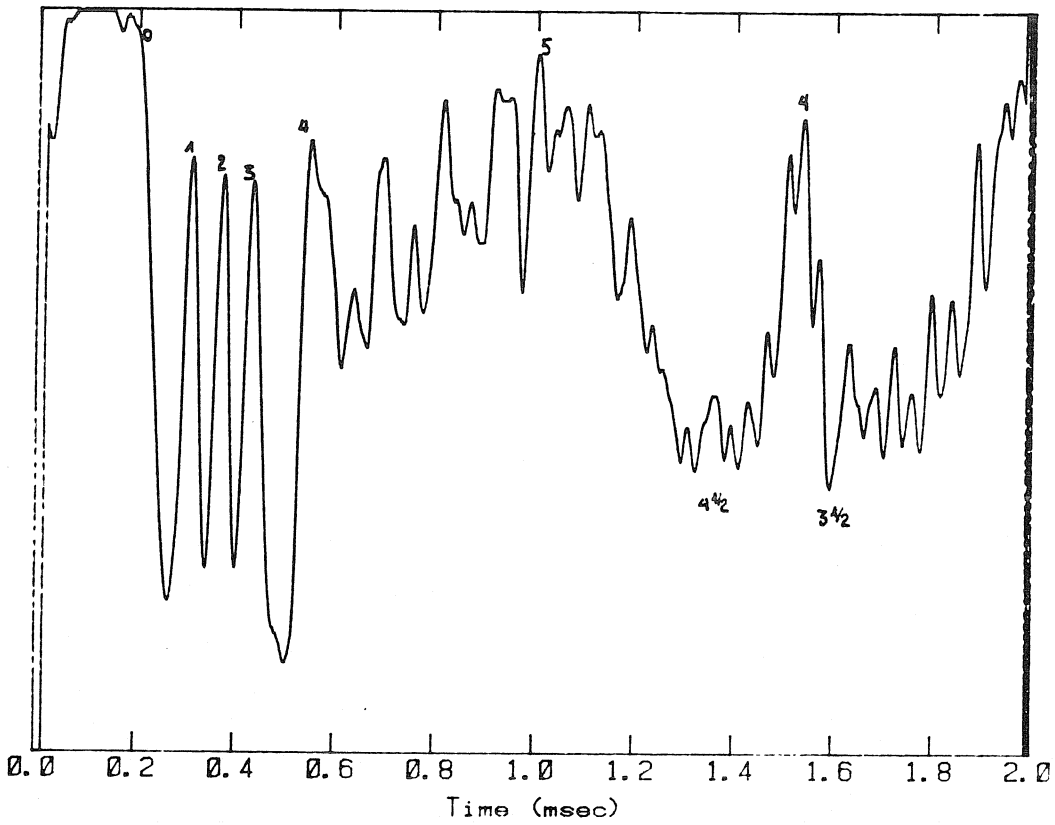
0
1
2
3
4
5
4½
3½
0.0
0.2
0.4
0.6
0.8
1.0
1.2
1.4
1.6
1.8
2.0
Time (msec)

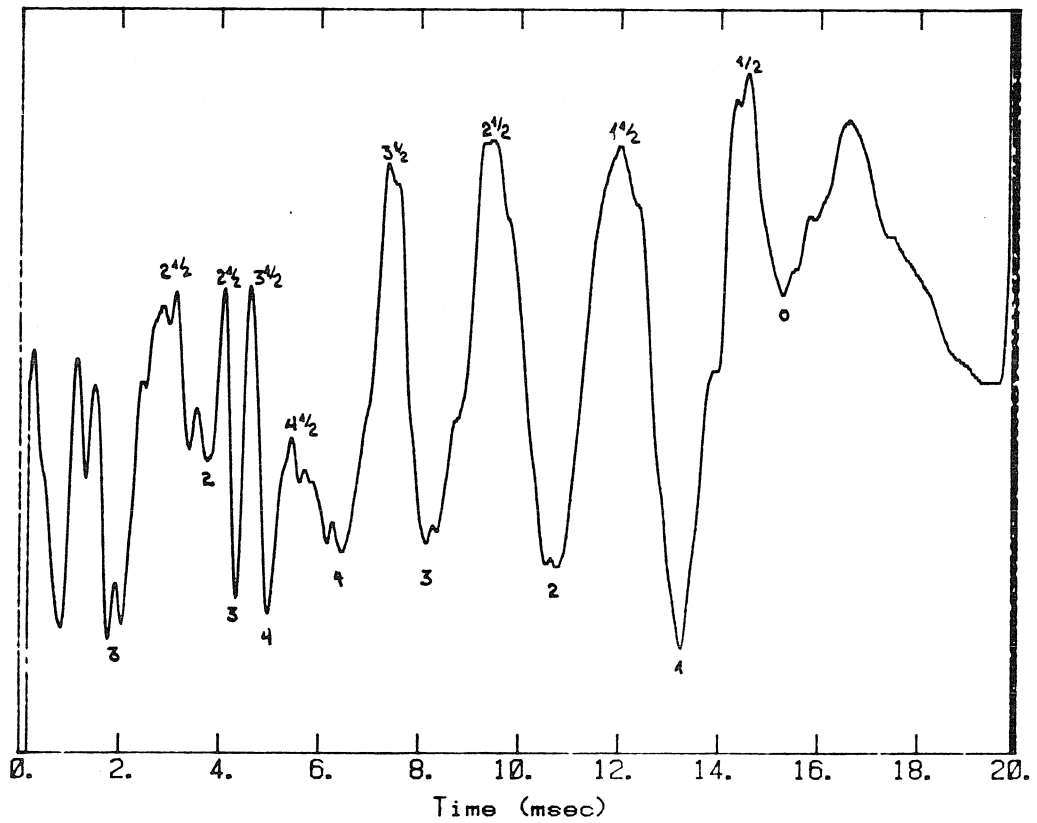
2½
2½
3½
4½
3½
2½
1½
½
0
0.
2.
4.
6.
8.
10.
12.
14.
16.
18.
20.
Time (msec)

Figure 11.

Fig. 10 smoothed by Gaussian averaging with a half-width N = 3. These fringes are the ones used to obtain Fig. 9, the half-integral values marked on Fig. 11 correspond to the "number of fringes" axis of Fig. 9. For the range of electron densities considered herein, a linear approximation to the phase relation, equation (2.2), works quite well; one recorded microwave fringe corresponds to a change in density of 1.4×10^{12} particles-cm^{-3} for a 60 GHz source (i.e., the klystron) and to a change in density of 1.8×10^{12} particles-cm^{-3} for a 75.0 GHz source (i.e., the Impatt oscillator). However, since the output of the detector is proportional to the cosine of the phase shift, this technique gives no information as to whether a fringe represents an increase or decrease in density. When single pulses are applied to the gas-puffing valve, the density evolution is rather simple and the interpretation of the fringes is straightforward. Difficulties in interpretation often arise from drift in the detector or klystron outputs, i.e., poor signal-to-noise ratio, and during the second millisecond of the discharge from noise that is believed to have its origin in strong density fluctuations.

To generate plots like Figs. 5 and 9, pairs of values of particle density and time from the extreme of averaged microwave traces like those of Fig. 11 are entered into a FORTRAN program. This program also sorts the data into subarrays consisting of the ordered pairs of particle density and time for the monotonically increasing and decreasing density versus time segments. For example, the gas-puff density decay segment lasting from 5 to 15.5 msec in Fig. 9 would be placed into one such subarray. The program fits a straight line in the least-squares sense to

such subarrays to give numerical values of the time-rate of density decay or growth. The result of this computation will be shown in the following chapter to be a useful measure of particle confinement.

The relation between the line-averaged density determined from the microwave phase shift along a minor diameter and the average density over the entire plasma volume is dependent on the spatial distribution of plasma density. Consider, for example, the density distributions given by $n(r) \sim (1 - r^2/a^2)^p$; $p = 0$ gives a uniform density distribution, $p = 1$ gives a parabolic distribution, etc. Denoting the line-averaged particle density by $\langle n \rangle$ and the volume-averaged density distribution by N/V where $N = \int_V n \, dV$ and V is the Tokamak volume, then it follows that $(N/V)/\langle n \rangle = 1.00, 0.85, 0.75$ for $p = 0, 0.5, 1$, respectively. That is, on-axis peaking of the density profile causes the line-averaged density to be larger than the volume-averaged density.

Returning to the measurement of the throughput of the puffing valve discussed in the previous section, it was mentioned that addition of 8.1×10^{-5} Torr hydrogen to the 204 liter Tokamak volume adds three full microwave fringes to the interferometer signal. From the perfect gas law 8.1×10^{-5} Torr corresponds to 5.34×10^{12} atoms-cm^{-3} hydrogen. With a microwave source frequency of 75.0 GHz the line-averaged particle density corresponding to three microwave fringes is 5.4×10^{12} particles-cm^{-3}. For density profiles varying as $(1 - r^2/a^2)^p$ this result corresponds to 100, 85, and 75 percent ionization for $p = 0, 0.5$, and 1, respectively. Judging from the results reported from Tokamaks with spatial density resolution, a parabolic profile ($p = 1$) is fairly realistic for discharges without gas

puffing. Gas puffing tends to broaden the density profile but never to a uniform density ($p = 0$). It seems plausible, then, that on the order of 80 to 90 percent of the added gas is ionized.

2. One-turn voltage

It would be useful to know the loop voltage driving the plasma current ($\oint_C \underset{\sim}{E} \cdot d\underset{\sim}{\ell}$ about a closed circular loop C down the major circumference of the plasma) as well as the plasma current, so that the resistance of the plasma would be known, since the electron temperature, in principle, may be deduced from the plasma resistance. It is obviously impractical to try to suspend a loop inside the torus; instead, a single circular turn is placed just outside the toroidal field winding in the doughnut hole (Fig. 8) and the voltage across this loop is recorded. This loop, or one-turn voltage differs from $\oint_C \underset{\sim}{E} \cdot d\underset{\sim}{\ell}$ driving the plasma current by the poloidal magnetic flux linking the area A between the one-turn loop and the loop C. Figure 12a shows the one-turn voltage trace inverted. One may see in this figure the tail end of the final pre-ionization ring, followed a fraction of a millisecond later by the application of the ohmic-heating fast bank which saturates the trace. The low-voltage portion of the curve corresponds to discharge of the ohmic-heating slow bank following the crowbarring at a loop voltage of roughly 6.2 V.

A relation based on the flux linking the one-turn loop that takes into account the flux through area A but ignores the mechanical work required to move the plasma if its internal inductance L_{int} changes with time[20] is given by

$$V_l I_p = R_p I_p^2 + \frac{d}{dt}\left(\frac{1}{2} L_{int} I_p^2\right) \qquad (2.5)$$

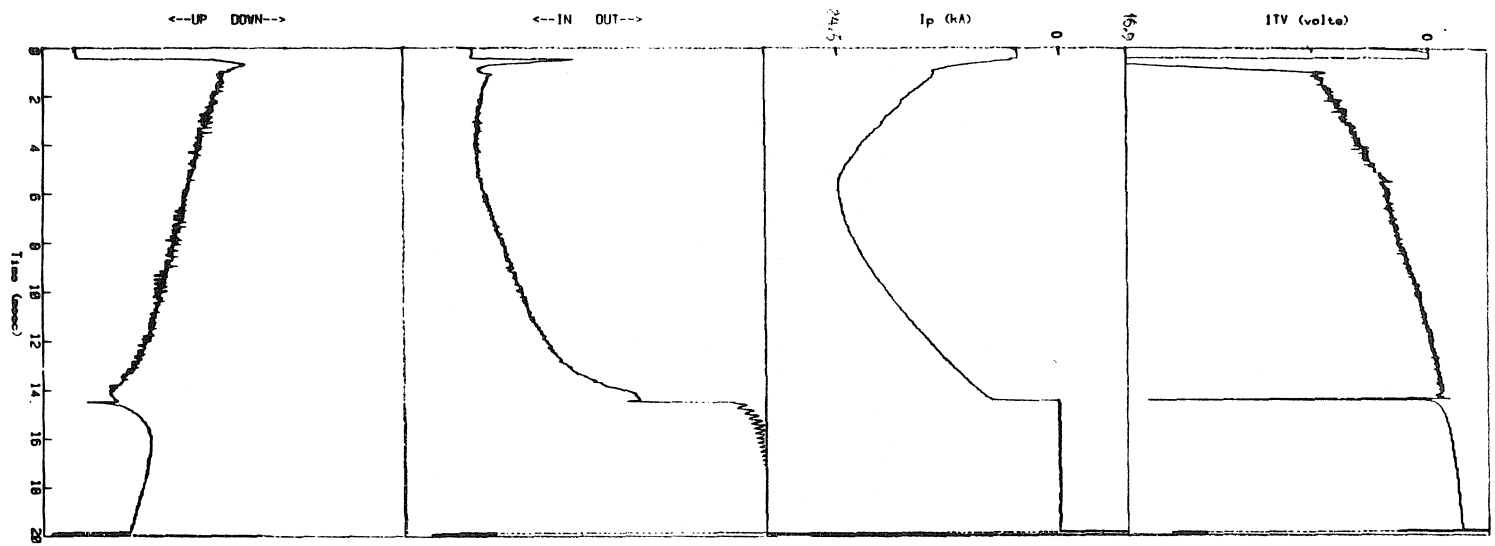

Figure 12. (a) One-turn, or loop, voltage. The transient recorder inverts the signal.

(b) Plasma current from integrated Rogowski coil voltage, also inverted.

(c) In-out trace, oscillation at end is spurious signal from transient recorder itself. Full scale is 50 cm, because of offset error the position information is not accurate at small I_p.

(d) Up-down trace, full scale is 20 cm, again, position information is not accurate at small I_p.

To display the tail of the last preionization ring and the firing of the ohmic heating fast-bank the transient recorders were triggered 0.5 msec earlier than usual.

where v_1 is the one-turn voltage, I_p the plasma current, and R_p the plasma resistance.[21,22] The inductive term takes into account the flux through A. The internal inductance of a plasma with a parabolic current profile is given by[20]

$$L_{int} = \frac{11\mu_o R}{24} = 0.265\ \mu h \tag{2.6}$$

The plasma resistance, often called the Spitzer resistance, is given by

$$R_p = \frac{2\pi R}{\pi a^2}\eta = 4.21 \times 10^{-3}\ Z_{eff}\ (\log \Lambda)\ T_e^{-3/2}\ (\text{ohms}) \tag{2.7}$$

where $\Lambda = 1.54 \times 10^{10}\ T_e^{-3/2}\ n_e^{-1/2}$ (T_e in eV, n_e in cm^{-3}),[25] and Z_{eff} was defined in connection with equation (1.4). If equation (2.5) can be solved for R_p, then equation (2.7) can be solved for T_e. Integrating equation (2.5) with respect to time gives

$$\langle R_p \rangle \equiv \frac{\int_{t-\varepsilon/2}^{t+\varepsilon/2} R_p I_p^2\, dt}{\int_{t-\varepsilon/2}^{t+\varepsilon/2} I_p^2\, dt} = \frac{1}{\int_{t-\varepsilon/2}^{t+\varepsilon/2} I_p^2\, dt}\left[\int_{t-\varepsilon/2}^{t+\varepsilon/2} v_1 I_p\, dt - \frac{1}{2} L_{int}\left(I_p^2(t+\varepsilon/2) - I_p^2(t-\varepsilon/2)\right)\right] \tag{2.8}$$

Equation (2.8) is easily evaluated numerically and yields electron temperatures for discharges without gas puffing between 100 and 170 eV for that portion of the shot in which gas puffing is usually employed. Gas puffing decreased the conductivity temperature about 22% when the electron density was increased from 2.7 to $8.1 \times 10^{12}\ cm^{-3}$. The electron temperatures determined in this fashion become suspect at small values of the one-turn

voltage when the inductive term is comparable to the ohmic-heating term in equation (2.5), since L_{int} is not known accurately without knowledge of the plasma current density distribution. Dimock[21] reports that the conductivity temperature is typically correct to within ±50% of Thomson-scattering values.

3. Rogowski coil

Plasma current is measured by a coil that is sensitive only to the poloidal magnetic field (Fig. 7). The coil is formed by winding a solenoid on a piece of flexible tubing of length slightly greater than the minor circumference of the toroidal-field solenoid winding. The Rogowski winding doubles back on itself so that when put around the torus no voltage is induced by the net toroidal field current passing through the azimuthal planar section enclosed by the Rogowski loop. The integrated voltage induced on this coil is proportional to the plasma current. A typical integrated voltage trace is shown in Fig. 12b.

4. In-out and up-down coils and plasma centering

Two other coils are wound on flexible tubing and placed linking the torus in an azimuthal plane (Fig. 7). The in-out coil is wound with greatest turns density on the inside and outside of the torus. The sense of the winding reverses itself at the top of the torus. Thus a circular filamentary current I in the plane of symmetry of the torus would produce a voltage depending in sign on its distance from the inner and outer walls and in magnitude on dI/dt. To remove the latter dependence, the integrated voltage is divided by the plasma current with a Burr-Brown 4291H analog divider chip. The output voltage of the divider increases as the

plasma moves outwards (Fig. 12c). The up-down coil detects vertical motion by the same mechanism (Fig. 12d). Since the exact distribution of current within the plasma is not known, these signals do not give exact positioning information, but are vital to optimizing the plasma position by trimming the vertical and horizontal fields.

As mentioned in the introduction, the vertical magnetic field exerts a $\underset{\sim}{J} \times \underset{\sim}{B}$ force in the inward direction (toward the toroidal axis of symmetry) to counteract the excess of poloidal magnetic field pressure on the inner side of the plasma with respect to the outer side. And, as discussed earlier in this chapter, this vertical field is realized by the discharge of capacitor banks, hence it is a programmed field with a limited number of variable parameters, namely the capacitance and charging voltage of the slow and fast banks. It has been established through variation of these parameters that maximization of the duration of the discharge with minimization of the interaction between the plasma and the wall is best achieved by holding the plasma steady in lateral (in-out) position until the last few milliseconds of the discharge when the plasma is allowed to drift outward. This accounts for the shape of the in-out trace in Fig. 12c. Discharges of the greatest duration are obtained with extremely small vertical field voltages which cause the plasma to sweep outward and ride against the wall. As documented by S. O. Dean et al.,[2] if the major radius of the plasma increases to the point of interaction with the wall, then impurities are injected into the plasma, plasma current and energy are lost, and the plasma is restored to a more well-centered position. This phenomenon is detected in the Caltech Tokamak as a distortion of the

microwave interferometer trace towards the end of the discharge and a simultaneous loss of plasma current from the integrated Rogowsky coil voltage. Extremely large slow-bank voltages prematurely terminate the discharges. Between these extremes, widely separated in vertical-field slow-bank voltage, the discharges are most reproducible. Thus, the in-out trace of Fig. 12c represents the best achievable centering of the plasma and the vertical field is trimmed to maintain the in-out trace qualitatively the same.

As mentioned in the introduction, the horizontal magnetic field exerts a $\underset{\sim}{J} \times \underset{\sim}{B}$ force in the downward direction (toward the Earth) to counteract the horizontal field having origin in toroidal field errors. The former field, as previously discussed, is generated with a d.c. current supply. In practice precise setting of the horizontal field is not critical; it seems not to be within the capability of the d.c. supply to push the plasma into the lower wall and interaction with the upper wall is obtained only at very small supply currents.

To maintain good plasma centering in the above sense, the vertical magnetic field must be increased as the plasma current is increased. Extreme variations in the toroidal field or plasma current may require small adjustments in the horizontal correction field to keep the traces qualitatively the same.

5. Data acquisition and transferral system

Figure 13 shows the block diagram of the data acquisition and transferral system and the peripheral data storage and analysis devices. Timing unit pulses (Fig. 6) trigger a bank of 16 digital transient

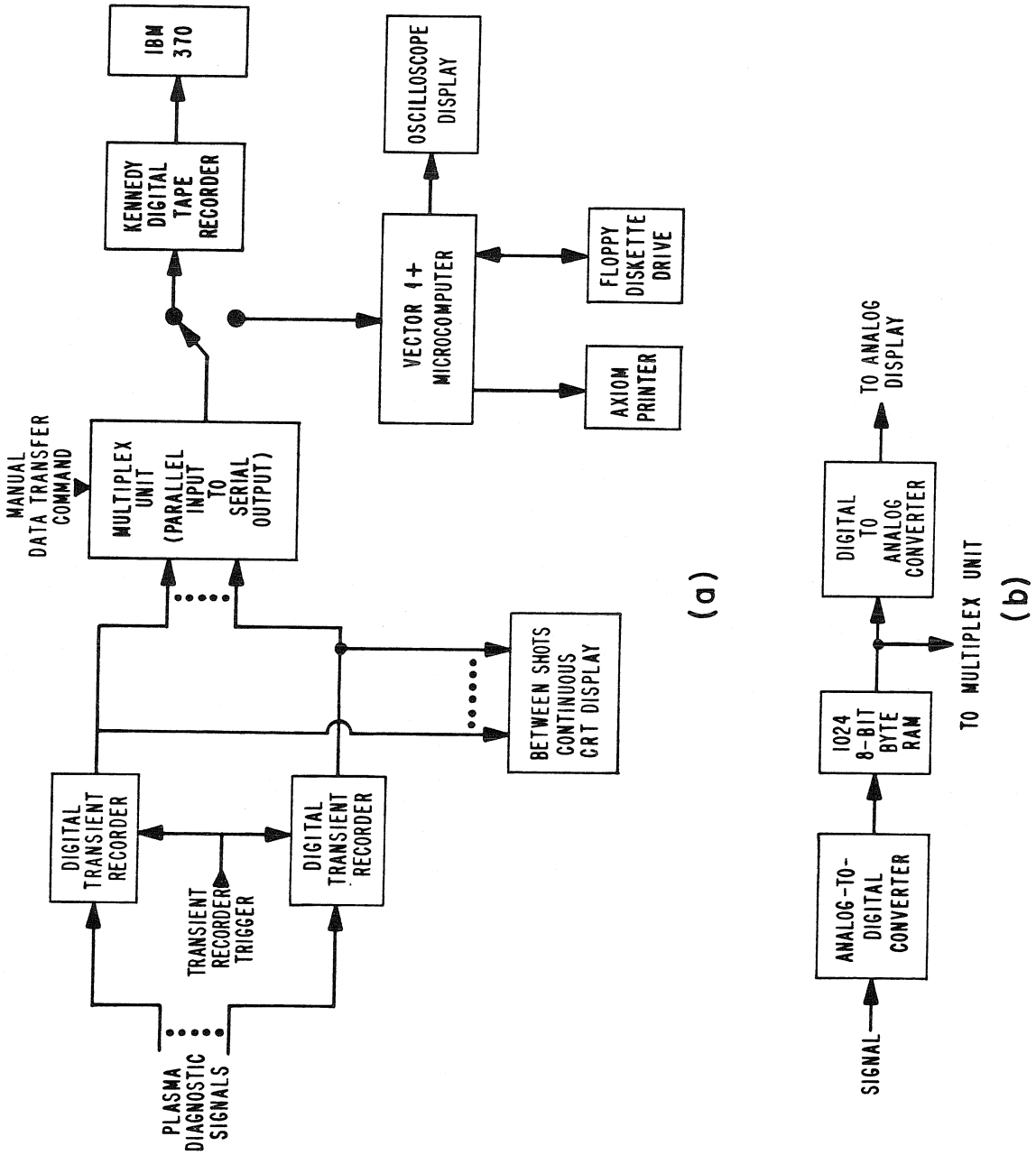

Fig. 13 a) Data acquisition, display, and reduction system block diagram.

b) Single digital transient recorder module block diagram.

recorder units. While each transient recorder is independently triggerable, it is convenient to trigger all units simultaneously with the exception of those units devoted to recording fluctuation signals. One millisecond sampling windows are used for the latter, and a delay is needed to move this window across the 20 msec shot length. Four of the transient recorders have the capability of 1.0 μsec analog-to-digital conversion times, the others have 5 μsec conversion time capability; the faster units are dedicated to the wider bandwidth diagnostic signals, specifically fluctuation signals and the first two milliseconds of the microwave signal. Each converted signal is stored in a 1024 byte memory, each byte being 8 bits (i.e., each byte represents an integer between 0 and 255). Between shots the memories of the transient recorders are continuously interrogated, converted to analog voltages, and displayed on Tektronix model 604 monitors. On manual command the recorded signals are multiplexed, that is, memories one through sixteen are interrogated in order, and these serial data are made available for transfer onto magnetic tape in a Kennedy model 1400 incremental tape recorder or onto floppy diskette via a Vector Graphics model Vector 1+ microcomputer, an 8080-based system. The tapes are taken to the Booth Computing Center IBM-370 computer for analysis, while the floppy diskettes are available for analysis on the Vector 1+ with the North Star BASIC language. Hard copy is available on an Axiom EX820 thermal printer.

One persistent and random problem with the transient recorders was their failure to trigger on the same (1 MHz) clock cycle. If one unit drops a byte from the beginning, i.e., starts recording after one byte

has already been recorded on another unit, then there is an apparent frequency-dependent phase shift between these channels. For example, if the conversion rates are 1 byte per μsec, then a one byte error in recording a sine wave of angular frequency ω results in a phase shift $\psi(\omega) = \omega \times 1$ μsec. Byte-dropping has been established by recording a sine wave from a signal generator on two units simultaneously and comparing the memories by computing the normalized cross-correlation amplitude.

6. Fluctuation measurement system

Probes sensitive to magnetic fluctuations have been built by M. A. Hedemann. These probes are simply two small 10-turn coils oriented so that the axis of symmetry of the poloidal coil is parallel to the poloidal unit vector and the axis of symmetry of the radial coil is parallel to the radial unit vector; the coils are enclosed in a 0.64 cm diameter pyrex envelope sealed to a Cajon glass-to-metal transition. In each probe the coils share the same center; the coil form is such that the cross-section of the radial coil is circular with a 0.32 cm diameter and the poloidal coil has a square cross-section 0.32 cm on a side. The probes are placed in O-ring feedthroughs welded to an Ultek Precision Port-Aligner (Fig. 8); the angle between probes is variable in the poloidal direction, thus measurements sensitive only to the poloidal phase difference may be made. If the probes are placed close together then rotation of one of the poloidal probes through 180° reverses the phase of the signal with respect to that of the other probe, hence the signals originate in magnetic phenomena rather than in capacitive coupling to electrostatic modes. Signals recorded on tape are analyzed on the

Booth Computing Center IBM-370 with a program, the original version of which was written by R. L. Kubena. Details of the computations and the application to the experiments to be described are given in the following section.

III. Computational Methods and Their Application to Magnetic Fluctuations

A. Introduction

The following material will discuss the principal spectral and temporal analysis techniques applied to the magnetic probe data. The three numerical functions to be described are the root-mean-square magnetic field, the cross-power spectral density, and the normalized cross-correlation amplitude. The principal applications to be described are mode-number determination and the measurement of the apparent poloidal rotational velocity.

B. RMS Magnetic Field

Since the voltage across one of the poloidal (radial) coils described previously is proportional to the poloidal (radial) component of $\dot{B}$ averaged over the area enclosed by the coil, it is a trivial matter to integrate numerically the magnetic probe signals to obtain the poloidal (radial) component of B and the root-mean-square value of this quantity over the 1024 samples comprising the contents of a single transient recorder memory for a particular shot; that is,

$$B_n = \sum_{i=0}^{n} \dot{B}_i \quad , \qquad n = 0,1,2,\cdots,1023$$

and

$$B_{rms} = \left[\sum_{n=0}^{1023} B_n^2\right]^{1/2} / \sqrt{1024} \quad . \tag{3.1}$$

C. Cross-Power Spectral Density

Strictly speaking, the cross-power spectral density (cpsd) function is defined as an average over an ensemble $\{x_k\}$ of stationary functions of

time $x_k(t)$. An ensemble $\{x_k\}$ is stationary provided its mean value $\mu_x(t)$, autocorrelation function $R_x(t,t+\tau)$, and an infinite collection of higher moments are time-invariant; that is, defining

$$\mu_x(t) \equiv \lim_{N\to\infty} \frac{1}{N} \sum_{k=1}^{N} x_k(t) ,$$

$$R_x(t,t+\tau) \equiv \lim_{N\to\infty} \frac{1}{N} \sum_{k=1}^{N} x_k(t)\, x_k(t+\tau) , \quad \text{etc.}, \tag{3.2}$$

then $\{x_k\}$ is a stationary ensemble if $\mu_x(t)$, $R_x(t,t+\tau)$, etc. do not depend on t. Given two sample functions $x_k(t)$ and $y_k(t)$ from stationary random processes $\{x_k(t)\}$ and $\{y_k(t)\}$, the cpsd is given by

$$G_{xy}(f) = \lim_{T\to\infty} \frac{1}{T} E\left[X_k^*(f,T)\, Y_k(f,T)\right] \tag{3.3}$$

where

$$X_k(f,T) \equiv \int_0^T x_k(t)\, e^{-i2\pi ft}\, dt , \qquad Y_k(f,T) \equiv \int_0^T y_k(t)\, e^{-i2\pi ft}\, dt$$

the * denotes complex conjugation, and E denotes ensemble average.

Of course the magnetic fluctuation data considered here do not arise from stationary processes; for example, the mean-square value of the magnetic fluctuation field varies with time. Further, the data are obtained by sampling a signal over a finite interval of time, hence the limit $T \to \infty$ in equation (3.3) may not be taken. Additionally, since

$$x_k(f,T) = \int_0^T x_k(t)\, e^{i2\pi ft}\, dt = \int_{-\infty}^{\infty} x_k(t)\, u_T(t)\, e^{i2\pi ft}\, dt$$

where

$$u_T(t) \equiv \begin{cases} 1 & 0 < t < T \\ 0 & \text{elsewhere} \end{cases} , \tag{3.4}$$

it is required that Fourier transforms be computed. These must be approximated in a reasonable amount of time in the case of sampled data. For these purposes a 1024-point Fast Fourier Transform (FFT) routine contained in the Booth Computer Center IBM-370 library is used. Since this routine provides output only at nonnegative frequencies, the approximation is made

$$\text{cpsd}[x(t),y(t)] \simeq \frac{2}{T} X(f)^* Y(f) \tag{3.5}$$

where $x(t)$ and $y(t)$ are two sampled functions, T is the total sampling time (number of samples times interval between samples), and $X(f)$ and $Y(f)$ are the FFT's of x and y. The factor 2 comes from the requirement $0 \leq f < \infty$.

As a practical consideration, the magnetic signals are always sampled at 1 μsec intervals, the fastest rate selectable. This maximizes the Nyquist frequency, f_c, which is the frequency above which aliasing, or erroneous mapping of high frequency into low frequency components by the sampling process may occur:

$$f_c = \frac{1}{2\Delta t} = 500 \text{ kHz} \tag{3.6}$$

All magnetic signals are low-pass filtered with corner frequencies at 300 kHz to inhibit aliasing. Additionally, the frequency resolution, Δf, of the FFT program is determined by the total sampling time, T = 1024 x 1 μsec = 1.024 msec by

$$\Delta f = \frac{1}{T} = 977 \text{ Hz} . \tag{3.7}$$

The FFT routine outputs spectral amplitudes and phases at discrete frequencies $n\Delta f$, $n = 0,1,2,\cdots,1023$.

Since the amplitude and phase of the computed cpsd of magnetic fluctuation signals are not smooth functions of frequency, it is convenient to Gaussian average them (see microwave interferometer discussion). A Gaussian half-width of N = 4 is used, hence $N\Delta f$ = 3.8 kHz and the full width at half maximum of the Gaussian is 6.5 kHz. Some averaging of the cpsd is a consequence of the finite total sampling time T. The FFT routine computes an approximation to

$$\int_{-T/2}^{T/2} x(t)\, e^{i\omega t}\, dt = \int_{-\infty}^{\infty} x(t)\, u(t)\, e^{i\omega t}\, dt$$

$$= X(f) \otimes T\,\mathrm{sinc}(Tf) \qquad (3.8)$$

where

$$u(t) = \begin{cases} 1 & -T/2 < t < T/2 \\ 0 & \text{elsewhere} \end{cases}, \quad \mathrm{sinc}(Tf) = \frac{\sin(\pi Tf)}{\pi Tf},$$

$X(f)$ is the Fourier transform of $x(t)$, and $\otimes$ denotes the convolution operation. Since the sinc function has rather large amplitude, and alternately negative sign, side lobes the FFT computation for equally weighted data will suffer from some undesirable frequency-averaging effects. If the data are weighted by a Hanning window function

$$h(t) = \begin{cases} \frac{1}{2}\left(1 + \cos\frac{2\pi t}{T}\right) & -T/2 < t < T/2 \\ 0 & \text{elsewhere} \end{cases}, \qquad (3.9)$$

so that $\int_{-T/2}^{T/2} x(t)\, h(t) e^{i\omega t}\, dt$ is approximated, the situation is much improved, since the Fourier transform of the Hanning function, H(f), has

much smaller amplitude side lobes than the sinc function. The main lobe of H(f) has zero value at ±1.1 kHz and the full width at half maximum is 1.3 kHz. This is a much narrower bandwidth of averaging than that of the Gaussian averaging.

D. Applications of the CPSD

1. Determination of mode numbers

Experiments with poloidal magnetic coils distributed about a minor circumference of a Tokamak (ϕ = constant, r = a) show that subsequent to the breakdown of the filling gas such coils detect fluctuation components varying as $\cos(m\theta - \omega t)$. Integer values of m from 2 to 6 have been reported.

Assuming the existence of a magnetic disturbance varying in phase as $(m\theta + n\phi - \omega t)$ since the magnetic probes in the Caltech Tokamak (Fig. 8)) lie in a plane $\phi = \phi_0$, a poloidal probe would see a field varying as $\cos(m\theta - \omega t)$, while a radial probe at the same point, since $\nabla \cdot \underset{\sim}{B} = 0$, would see a field varying as $\sin(m\theta - \omega t)$. Then it is straightforward to show that if two probes are separated in poloidal angle by θ_0, the argument (phase) of the cpsd is that given in Table I.

Table I

Probe 1	Probe 2	Angle of separation	arg(cpsd)
poloidal	poloidal	θ_0	$m\theta_0$
poloidal	radial	θ_0	$m\theta_0 - \pi/2$
radial	radial	θ_0	$m\theta_0$
radial	poloidal	0	$-\pi/2$

Then, in principle, the poloidal mode number m is determinable from a cpsd phase measurement. The last row is relevant to signals originating from the radial and poloidal windings in a single probe.

2. Rotation of magnetic islands

The cross-power spectral density ($\frac{2X^*(f)Y(f)}{T}$) and auto-power spectral density ($2|X(f)|^2/T$) of experimental data from the Caltech Tokamak will be shown to display peaks at frequencies that are nearly integer multiples of a fundamental frequency on the order of 11 or 12 kHz. Strong, static magnetic structures having m-fold poloidal symmetry (varying as $e^{im\theta}$) and rotating in the poloidal direction with angular frequency ω_0 would show up in such spectra as frequency peaks at $\omega = m\omega_0$. One theoretical explanation of the origin of such structures is found in tearing modes. In the resistive (i.e., non-infinite conductivity) magnetohydrodynamic (MHD) model, a toroidal plasma is unstable with respect to the growth of magnetic perturbations $B_{r,\theta} \sim \psi_{r,\theta}(r) \exp[\Upsilon t + i(m\theta + n\phi)]$ about the surfaces $q(r) = m/n$ and provided there is magnetic shear at these surfaces ($\partial q/\partial r \neq 0$ at $r = q^{-1}(m/n)$). Such structures are called magnetic islands and one was sketched schematically in Fig. 4 . As will be shown in Chapter IV, tearing mode theory predicts real values for Υ, hence the magnetic perturbations are stationary, that is, they have zero phase velocity. However, it is known from experiments that Tokamak plasmas rotate. If magnetic islands are somehow convected along with the plasma, then the tearing-mode theory may be reconciled with experimental fact. In this section the attempts by theorists to effect this reconciliation will be

summarized. Then it will be shown that the phase of the cpsd of fluctuation quantities yields some information about the apparent rotational velocity. Finally, experimental results from other Tokamaks will be summarized.

In the zero resistivity approximation, MHD theory requires magnetic field lines be convected with the fluid mass velocity which, since plasma ions are so much more massive than electrons, is approximately the net ion velocity. A source of fluid mass velocity is to be found in the experimentally observed radial electric field in Tokamak plasmas; Langmuir probe measurements in the Caltech Tokamak show that $\underset{\sim}{E}_r$ points inward. The cross product of $\underset{\sim}{E}_r$ with the toroidal field $\underset{\sim}{B}_\phi$ gives a net fluid drift velocity in the poloidal (θ) direction with the sense of the electron diamagnetic drift, i.e., along $\nabla n_e \times \underset{\sim}{B}_\phi$ since ∇n_e also points inward radially.

However, Ware[25,26] has shown that in the nonzero resistivity approximation to the MHD theory if the electron kinetic pressure is much larger than the ion kinetic pressure, then the field lines are convected with the net electron velocity. It is believed that the electron pressure is larger than the ion pressure in the Caltech Tokamak; however, Ware maintains that even when $p_i \gg p_e$ is a poor approximation, the Hall-effect terms introduced by nonzero resistivity are sufficient to tie magnetic field lines to the electron fluid. Since the plasma current is carried for the most part by the electrons, the net electron fluid velocity is primarily in the toroidal (ϕ) direction. Further, the magnetic island structure is helical so toroidal rotation would be detected with poloidally distributed probes as in Fig. 8 as poloidal

rotation (it may be helpful to visualize a screw lying horizontally viewed through a vertical slot; then both translation along the screw's axis and rotation about this axis appear as vertical motion of the threads). It is readily verified that whether the current flows along or against the direction of the toroidal field, this toroidal rotation would appear as poloidal rotation in the electron diamagnetic drift direction to poloidally distributed probes.

The probe geometry of Fig. 8 is ideal for measuring the magnitude and sense of the poloidal component of magnetic fluctuation velocity. Referring once again to Fig. 1 in which toroidal coordinates were defined, it is possible to separate the probes in the poloidal (θ) direction by placing the centers of the coils in one probe of (r,θ,ϕ) and the centers of the coils in the other probe at $(r,\theta+\theta_0,\phi)$ by adjustment of the port-aligner. If one measures the same component, e.g., B_θ, in each probe, takes the Fourier transforms, and compares the phases of the spectral components corresponding to a particular frequency, then one may compute the time delay of this component between the probes as the difference in phase divided by the angular frequency of the spectral peak. The difference in phase is just the argument of the cross-power spectral density of the probe signals for this particular frequency. When experimental results are discussed in the following, the time delay shall be computed in this manner, that is,

$$\tau(\omega) = (\arg(\text{cpsd}))/\omega \quad . \tag{3.10}$$

To return to the status of the experimentally observed direction of rotation of magnetic fluctuations in Tokamaks in general, it should

be pointed out that the usual experimental measurement configuration is an array of poloidally sensitive coils distributed about a minor circumference of the torus (these are called Mirnov coils). Thus, only poloidal phase information about the poloidal component of fluctuations is available for analysis. Bateman[27] has surveyed the observations from various Tokamaks and finds, in general, that in hot Tokamaks ($T_e \gtrsim 100$ eV) the sense of rotation appears to be that of the electron diamagnetic drift and that in cold Tokamaks ($T_e < 100$ eV) it is the opposite. The reader is reminded that conductivity measurements show that in the Caltech Tokamak $T_e \gtrsim 100$ eV. The next section will discuss experimental determination of the sense of the apparent poloidal rotation.

E. Normalized Cross-Correlation Amplitude

The normalized cross-correlation amplitude of two functions x(t) and y(t) is defined by

$$R_{xy}(\tau) \equiv \lim_{T\to\infty} \left\{\frac{1}{T}\int_0^T x(t)\, y(t+\tau)\, dt \Big/ \left[\frac{1}{T}\int_0^T x^2(t)dt\right]^{\frac{1}{2}}\left[\frac{1}{T}\int_0^T y^2(t)dt\right]^{\frac{1}{2}}\right\} . \tag{3.11}$$

When x and y are interchanged,

$$R_{yx}(\tau) \equiv \lim_{T\to\infty} \left\{\frac{1}{T}\int_0^T y(t)\, x(t+\tau)\, dt \Big/ \left[\frac{1}{T}\int_0^T x^2(t)dt\right]^{\frac{1}{2}}\left[\frac{1}{T}\int_0^T y^2(t)dt\right]^{\frac{1}{2}}\right\}$$

$$= R_{xy}(-\tau) \quad , \tag{3.12}$$

the last step following from a change of variable $t' = t+\tau$. Given two transient-recorder records $\{x_n = x(n\Delta t)\}$ and $\{y_n = y(n\Delta t)\}$, where $n = 0,1,2,\cdots,1023$ and Δt = time interval between samples, R_{xy} may be approximated by

$$R_{xy}(r\Delta t) = \frac{1}{1024 - r} \sum_{n=0}^{1023 - r} x(n\Delta t)y[(n+r)\Delta t] \Big/$$

$$[\frac{1}{1024} \sum_{n=0}^{1023} x^2(n\Delta t) \frac{1}{1024} \sum_{n=0}^{1023} y^2(n\Delta t)]^{1/2}$$

$$= \frac{1024}{1024 - r} \sum_{n=0}^{1023 - r} x_n y_{n+r} \Big/ [\sum_{n=0}^{1023} x_n^2 \sum_{n=0}^{1023} y_n^2]^{1/2}$$

$$\text{for } r = 0,1,2,\cdots,1023 \qquad (3.13)$$

and $R_{yx}(r\Delta t)$, hence $R_{xy}(-r\Delta t)$, is obtained from equation (3.13) by interchanging x and y.

The normalized cross-correlation function may be used to determine the apparent poloidal angular velocity of rotation of the plasma. As pointed out previously, solid-body poloidal or toroidal rotation (or a combination of both) of a magnetic structure having the form $f_{mn}(r)\, e^{i(m\theta+n\phi)}$ would cause a voltage $v_{mn} = f_{mn}(r)\cos(\omega_m t - m\theta - n\phi)$ to appear, where $\omega_m = m\omega_o$, and ω_o is the apparent poloidal angular velocity of rotation. Equation (3.11) will now be evaluated for an arbitrary number of these rotating structures.

Separating the poloidal magnetic probes by poloidal angle θ_o (probes at $\underset{\sim}{x}_1 = (r,\theta,\phi)$ and $\underset{\sim}{x}_2 = (r,\theta+\theta_o,\phi)$ in the probe geometry of Fig. 8 would cause the fluctuation signals

$$x(t) = \sum_{m,n} f_{mn}(r)\cos(\omega_m t - m\theta - n\phi)$$

and

$$y(t) = \sum_{m,n} f_{mn}(r)\cos(\omega_m t - m(\theta+\theta_o) - n\phi) \qquad (3.14)$$

to be seen at $\underset{\sim}{x}_1$ and $\underset{\sim}{x}_2$, respectively. Then,

$$R_{xy}(\tau) = \lim_{T\to\infty} \int_0^T x(t)y(t+\tau)dt \Big/ \left[\int_0^T x^2(t)dt \int_0^T y^2(t)dt\right]^{1/2}$$

$$= \lim_{N\to\infty} \int_0^{2N\pi/\omega_o} x(t)y(t+\tau)dt \Big/ \left[\int_0^{2N\pi/\omega_o} x^2(t)dt \int_0^{2N\pi/\omega_o} y^2(t)dt\right]^{\frac{1}{2}}$$

$$= \frac{\lim_{N\to\infty} \sum_{k=1}^{N} \int_{2(k-1)\pi/\omega_o}^{2k\pi/\omega_o} x(t)y(t+\tau)dt}{\left[\sum_{k=1}^{N} \int_{2(k-1)\pi/\omega_o}^{2k\pi/\omega_o} x^2(t)dt \sum_{k=1}^{N} \int_{2(k-1)\pi/\omega_o}^{2k\pi/\omega_o} y^2(t)dt\right]^{1/2}}$$

$$= \lim_{N\to\infty} \sum_{m,n} f_{mn}^2(r)\cos m(\theta_o - \omega_o\tau) \Big/ \sum_{m,n} f_{mn}^2(r) \quad . \tag{3.15}$$

Thus, $R_{xy}(\tau)$ takes a maximum value of unity at $\tau_{peak} = \theta_o/\omega_o$. Therefore, the apparent poloidal angular velocity of rotation may be determined from the time delay τ_{peak} at the peak normalized cross-correlation amplitude and the poloidal angle of separation of the probes θ_o by

$$\omega_o = \theta_o/\tau_{peak} \quad . \tag{3.16}$$

The sign of the time delay τ_{peak} at the peak normalized cross-correlation amplitude gives the sense of the apparent poloidal rotation. In the experiments reported in this thesis it was found that the plasma <u>always</u> appeared to rotate in the direction of <u>electron</u> diamagnetic drift.

IV. Particle Confinement Experiments

A. Introduction

As was discussed in the introduction, confinement in Tokamaks is not well understood. In particular, collisional diffusion coefficients scale linearly with the electron density, n_e, hence one would expect a degradation in confinement as n_e is increased; in fact, the Alcator scaling result mentioned previously is that particle and energy confinement times increase linearly with increasing n_e (the particle confinement time was found to be a factor of 4 times larger than the energy confinement time by the Alcator group). Most important, confinement times are several orders of magnitude smaller than those predicted by the theory of Coulomb collisions.

In the section to follow it will be shown that a simple particle conservation model and the Alcator scaling relation predict that the particle density resulting from a short (< 1 msec valve voltage pulse) gas puff as in Fig. 7 ought to exhibit a linear time-rate of decay following cessation of neutral gas feed. The reader may have been struck by this feature of Fig. 9. The time-rate of decay is shown, in this model, to depend on the fraction of particles recycled at the wall and the coefficient of proportionality between the particle confinement time and the particle density. It is conceivable that this coefficient might have dependences on such parameters as the toroidal field, electron temperature, plasma current, and minor radius as does the coefficient between the electron energy confinement time and particle density given by the Daughney empirical scaling relation, equation (1.5) of the

introduction, so it is natural to investigate how the variation of discharge and gas-puff parameters affects the particle confinement as determined by the time-rate of gas-puff density decay. The discharge parameters readily controlled are the toroidal field and plasma current, and the gas-puff parameters subject to manipulation are the pulse length (hence the amount of gas admitted), the throughput of the puffing system via the gas reservoir pressure (hence the rate at which gas is admitted) and the delay of the pulse from the initiation of the shot (hence when gas is admitted). These experiments have been performed and the results will be discussed along with a comparison to the results expected from the theory of convective diffusion across magnetic islands created by tearing modes. It is also, perhaps, instructive to compare the results to the predictions of collision theory, even though the actual diffusion is anomalously large, and the Daughney scaling law, even though this result describes electron energy confinement (the energy confinement time enters the Lawson relation, so considerable effort has gone into computing this scaling and negligible effort into computing the scaling of the particle confinement time). Finally, a section has been added that summarizes the current state of the theory of particle influx and density build-up during gas puffing.

B. Alcator scaling and time-rate of density decay

The Alcator group reported[5] in 1976 the observation that both particle and energy confinement times scale linearly with average electron density. These results have come to be known collectively as "Alcator scaling." It was also observed that the average electron

density following cessation of external neutral gas feed decayed linearly with time. This result is consistent with Alcator scaling; let the equation of particle conservation be

$$\dot{n} + \frac{n}{\tau_p} = Q + R_W \tag{4.1}$$

where n is the average density of electrons, or ions, since the plasma is charge neutral, τ_p is the particle confinement time, Q represents an external source of particles, namely the gas-puffing supply, and R_W represents the contribution due to wall-recycling. The latter term includes those particles that are lost by the discharge and that reenter at a later time. In particular, an escaped ion may be neutralized at the wall, or an adsorbed neutral may be freed from the wall by a collision, and not being restrained by the magnetic field, may enter the discharge and be ionized subsequently. After termination of neutral gas feed Q = 0. The wall recycling term may be modeled as some fraction of the second term in equation (4.1), namely

$$R_W = \gamma \frac{n}{\tau_p} \quad , \qquad 0 < \gamma < 1 \tag{4.2}$$

Alternatively, the Pulsator group[28] views the same conservation process as determined by

$$\dot{n} + \frac{n}{\tau} = Q \tag{4.3}$$

which differs from (4.1) in that τ is the <u>observed</u> particle confinement time. Wall-recycling means $\tau > \tau_p$, and if all particles are recycled there should be no decay ($\dot{n} = 0$ and $Q = 0 \Longrightarrow \tau = \infty$), hence the Pulsator group models τ as

$$\tau = \tau_p/(1 - \gamma) \tag{4.4}$$

where γ is the fraction of particles recycled. These views are, of course, equivalent. Then combining (4.3) and (4.4) with Q = 0 and Alcator scaling, $\tau_p = \alpha n$, one has

$$\dot{n} = \frac{-(1 - \gamma)}{\alpha} \tag{4.5}$$

and if γ and α are constant in time, then $\dot{n}$ is constant in time, hence the time-rate of density decay should be linear. This is in fact what the Alcator group observed and what is observed on the Caltech Tokamak when the density elevated by short gas puffs in a well-centered plasma decays (Fig. 9, etc.).

The time-rate of change of the average electron density in the decay of a gas puff, then, is a measure of the particle confinement coefficient provided the wall-recycling coefficient is known. The Alcator group finds the parameter γ to be between 0.2 and 0.4 for various types of discharges. Additionally, the decay rate yields empirical information about the diffusion coefficient.[29] The flux of ions, $\Gamma_{i\perp}$, crossing a given toroidal surface S of minor radius just smaller than the limiter radius is given by $\Gamma_{i\perp} = D_\perp \nabla_\perp n_i$ where n_i is the ion density. The number of ions crossing this surface is given by $\Gamma_i A = n_i V_s/\tau$ where V_s is the volume enclosed by S and A is the area of the surface S. Thus

$$D_\perp = \frac{n_i V_s}{\nabla_\perp n_i A \tau} = \frac{V_s(1 - \gamma)}{\nabla_\perp n_i A \alpha} = \frac{-\dot{n} V_s}{\nabla_\perp n_i A} \tag{4.6}$$

where $\nabla_\perp n_i$ is averaged over the surface S. Thus, the cross-field diffusion

coefficient is proportional to the measured rate of decay of the average electron density. Scaturro and Kusse[29] have measured $\nabla_\perp n_i$ at the edge of the Alcator Tokamak with Langmuir probes and used equation (4.6) to compute $D_\perp$. This value was found to be roughly three times the Bohm diffusion coefficient ($D_{Bohm} = \frac{1}{16}\frac{\kappa T_e}{eB}$).

In the following the data will be presented in the form of $-1/(dn/dt) = \alpha/1-\gamma$ versus a given parameter so that an <u>increasing</u> value represents <u>improved</u> particle confinement time for a given average electron density and improved cross-field diffusion.

C. Parameter Variation Experiments

1. General comments

As the reader may have gathered from Fig. 12, the plasma current does not stay constant throughout the duration of the discharge. Unless otherwise indicated, the gas pulses were timed so that the peak density was attained approximately at the time the plasma current was a maximum, assuring that the current was as constant as possible over the duration of the puff. The limiter q has been calculated on the Vector 1+ using the current trace of Fig. 12 and a model of the toroidal field (quarter-cycle sine wave followed by exponential decay with the measured time constants) using equation (1.3); this is shown in Fig. 14. The bulk of the duration of this discharge has q(a) between 4 and 5. At the end of this discharge (about 14.5 msec into the shot) the plasma current is zero or very small and q(a) is off the scale of Fig. 14. The q(a) versus time traces are indistinguishable from shot to shot and qualitatively the same (i.e., the same shape) when toroidal field and plasma current are varied.

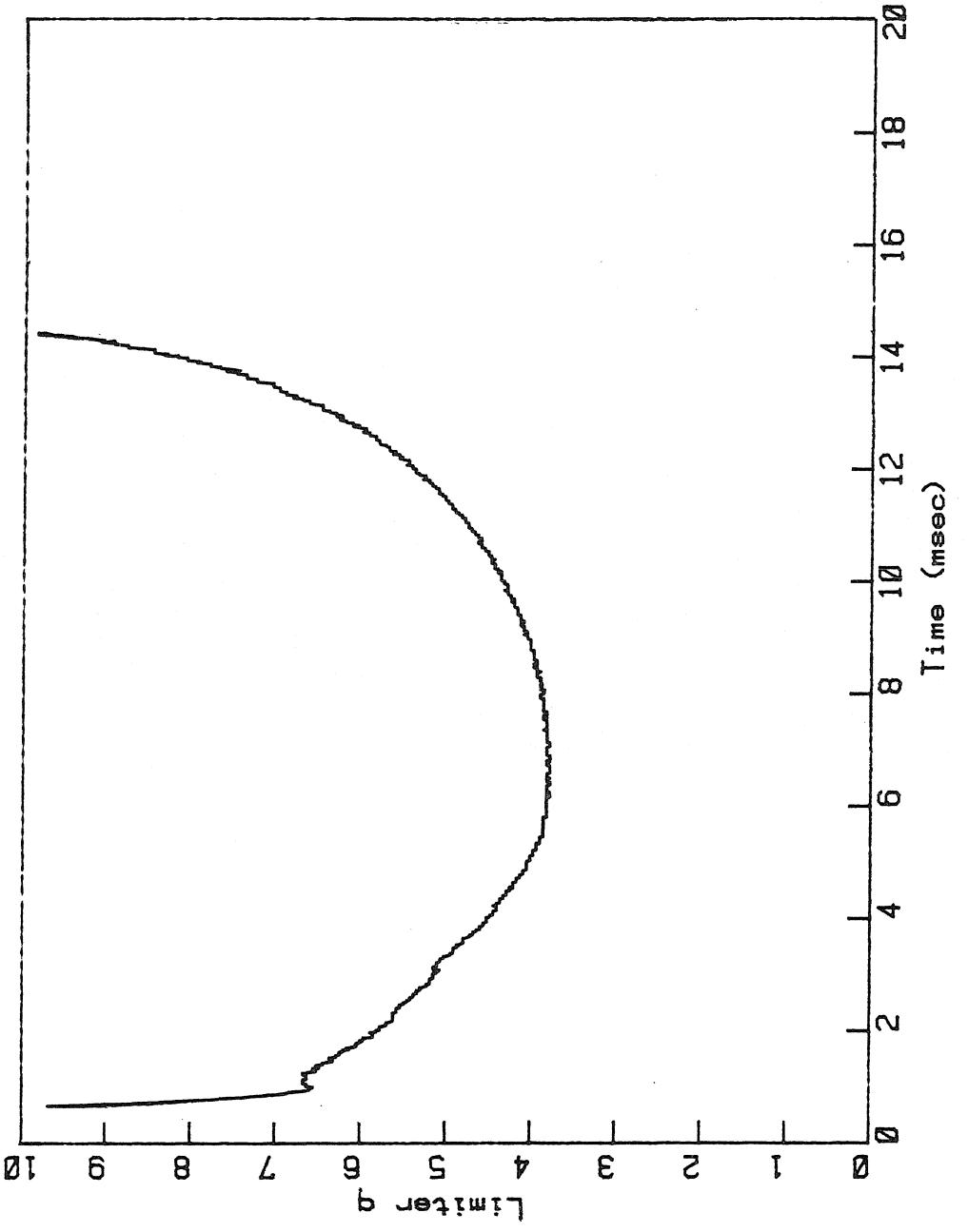

Figure 14. Limiter q (q(a)) versus time deduced from the current trace of Figure 12.

When in the following, plasma current and limiter q values are given for a particular discharge they shall represent the respective quantities evaluated at the time of peak puff particle density. When toroidal field values are given they represent the peak value attained during the shot. This comes (Fig. 6) about 2.7 msec into the shot.

Before doing these experiments the vertical and horizontal fields and the plasma current were independently varied throughout the full range of available values to assure that the decay of gas puff particle density was fully due to particle transport and not to the scraping off of plasma against the wall. Riding of the plasma against the outer wall is detected by a departure from a linear time-rate of gas-puff density decay to a slower rate of decay and a corresponding loss of plasma current during the last few milliseconds of the discharge.

It was found that when gas was puffed during the initial portion of the density decay (1-4 msec in Fig. 5) the noise on the microwave interferometer signal became comparable in amplitude to the density change fringes, making it impossible to follow the evolution of the density. This problem is circumvented by waiting until 3-1/2 to 4 milliseconds into the shot before adding gas. It will be shown that gas puffing tends to destabilize low-order magnetic fluctuation modes, and it is well known from numerous experiments that in the early portion of a Tokamak discharge, while the current is increasing, strong low-order (small m-number) magnetic oscillations are seen with magnetic probes. It is speculated here that gas-puffing during the first few milliseconds of a Caltech Tokamak discharge may drive these modes to

amplitudes large enough to mask the microwave signal with noise. Recent publications from other Tokamak experiments show a similar delay of the commencement of puffing to a time well into the initial density decay.

2. Reservoir pressure

The puffing system (Fig. 7) throughput is found empirically to increase monotonically as the pressure in the reservoir volume between the leak valve and piezoelectric valve is increased. Rapid density rise rates, hence high throughput values, are desirable because of the relatively short duration of the discharge (about 12-16 msec with gas puffing) and since the puff density decay region (lasting $\lesssim$ 7 msec) is of interest. Figure 15 shows density traces for a sequence of shots in which both the valve voltage pulse length t and the reservoir pressure P_{res} are varied in such a way that the puff attains approximately the same peak density (it turns out that these values scale as $t \sim P_{res}^{1.4}$ for $P_{res} < 1$ atm) while ohmic-heating voltages, toroidal field, filling pressure, etc. are held constant at the values in the figure caption. Figure 16 shows the time-rate of density rise $d\langle n\rangle/dt$ determined from a least-squares fit to the data of Fig. 15 plotted against the reservoir pressure. The rise is faster with increasing pressure up to roughly 800 Torr beyond which either the throughput of the system saturates, or the plasma cannot incorporate the extra gas quite as quickly. These saturated density rise rates are sufficiently rapid that the density rise occupies little of the shot time. Figure 17 plots $-1/(d\langle n\rangle/dt)$ determined from a least-squares fit to the density decay segments of the traces of Fig. 15. The particle confinement is unaffected by the reservoir pressure; in essence, the plasma appears to have no memory of how fast the gas was added.

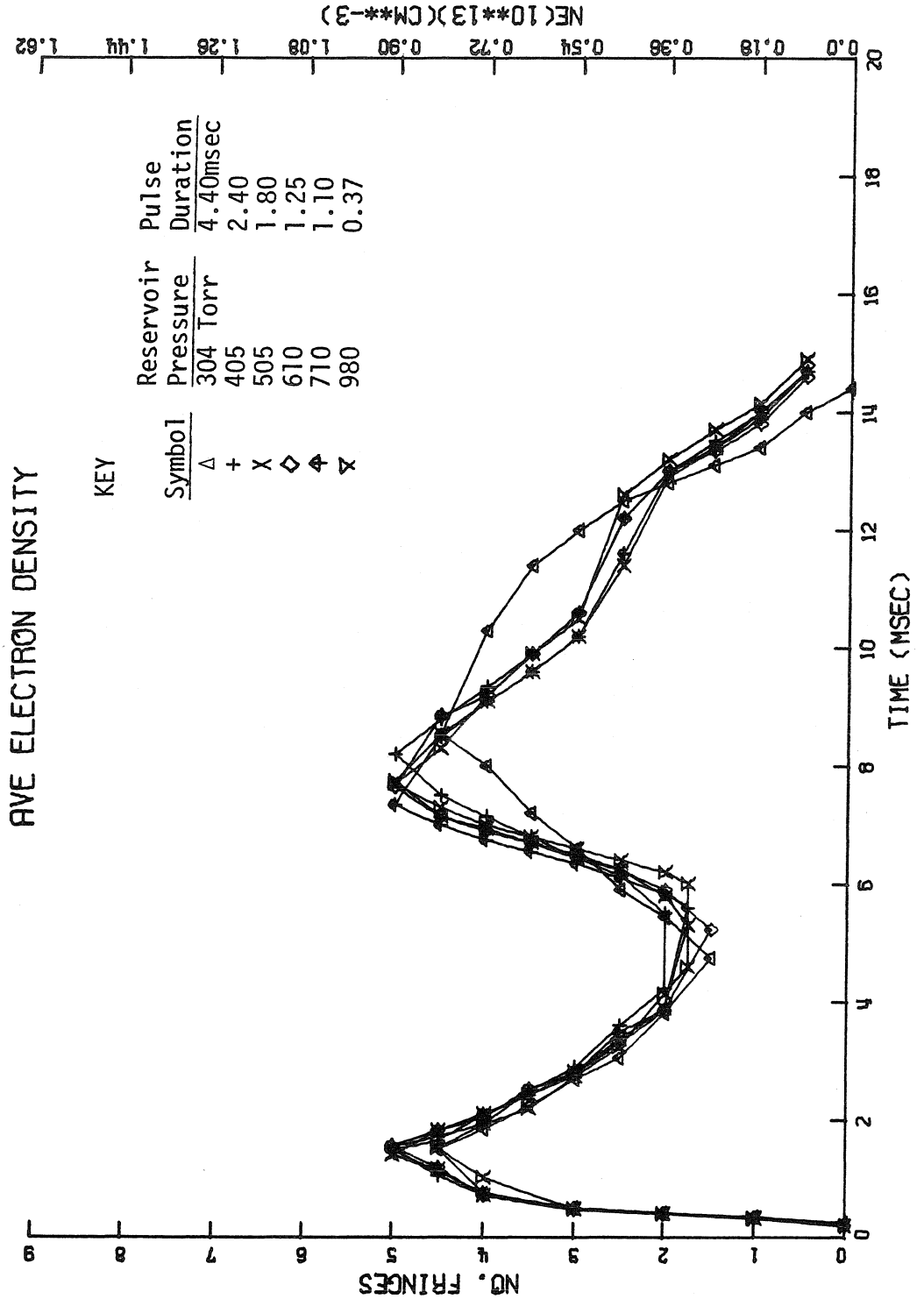

Figure 15. Variation of pulse duration and reservoir pressure while keeping peak density roughly constant. Other parameters: B_ϕ = 4.1 kG, OHFB = 1 kV, OHSB = 360v, VFFB = 120v, VFSB = 47v, filling pressure 1.35 x 10^{-4} Torr H_2.

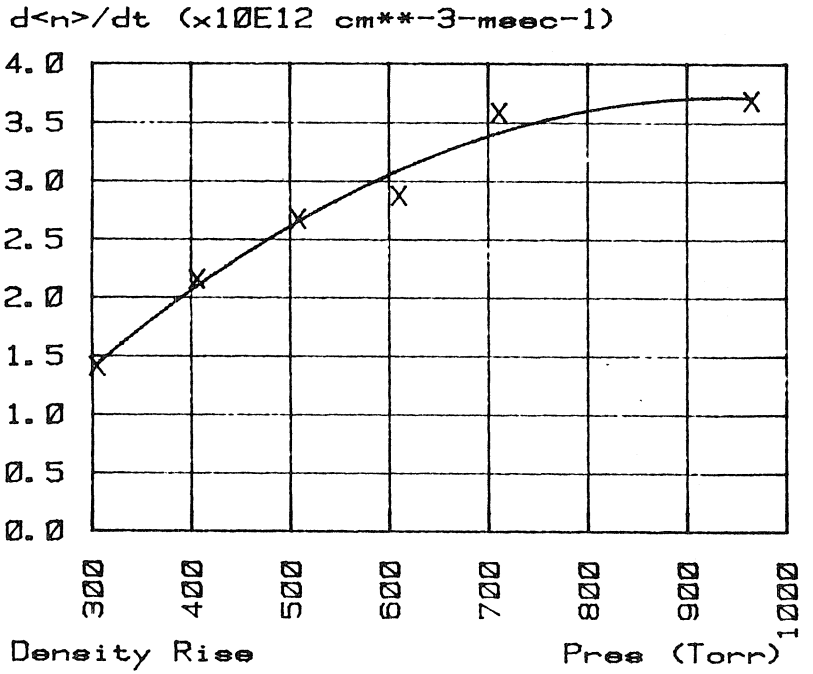

Figure 16. Least-squares fit time-rate of density rise of gas puffs of Figure 15 versus the reservoir pressure P_{res}. <n> is the line-averaged density (Eqn. (2.3)).

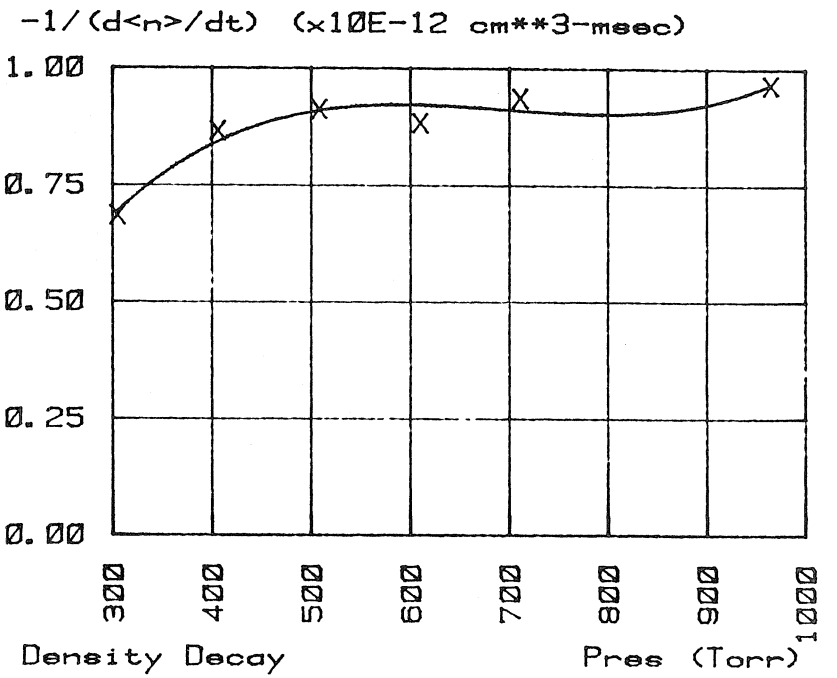

Figure 17. -1/(d<n>/dt) from least-squares fit to the density decay segments of Figure 45 versus the reservoir pressure P_{res}. Particle confinement appears to be independent of rate at which gas is introduced.

3. Toroidal field

The density traces in Fig. 18 are derived from microwave traces obtained from a sequence of shots in which the toroidal field B_ϕ was varied while the other discharge and the gas-puffing parameters were held constant at the values specified in the figure caption. The toroidal field was varied from 3.0 to 4.7 kGauss corresponding to limiter q's at the time of peak puff density of 2.9 to 4.6. The upper limit on the toroidal field is set by mechanical considerations; the magnetic energy in the toroidal winding varies as the square of B_ϕ and stresses on the solenoid become quite visible at the higher B_ϕ settings. The lower (Kruskal-Shafranov) limit on B_ϕ is determined by the safety factor q ; when q(r) becomes less than unity within the plasma the m = 1 kink mode is destabilized causing a catastrophic disruption of the discharge. Tokamaks with Thomson-scattering electron temperature measurement systems capable of radial resolution infer current-density and safety-factor profiles as follows: since $J = E/\eta$, E being approximated from the loop voltage and the major circumference of the torus, and the Spitzer resistivity (eq. (2.7)) $\eta \sim T_e^{-3/2}$, the profile of J is inferred, and from equation (1.1) the profile of q. These measurements show that once the discharge has established itself, the current-density J(r) decreases monotonically with increasing radius, hence q(r) increases monotonically with increasing radius. The exact current-density distribution in the Caltech Tokamak is not known; however, it is quite reasonable to assume that it monotonically decreases with increasing radius, hence the value of q at the center of the discharge is the minimum q over the entire torus. It was found experimentally that shots with B_ϕ = 2.5 kG (cor-

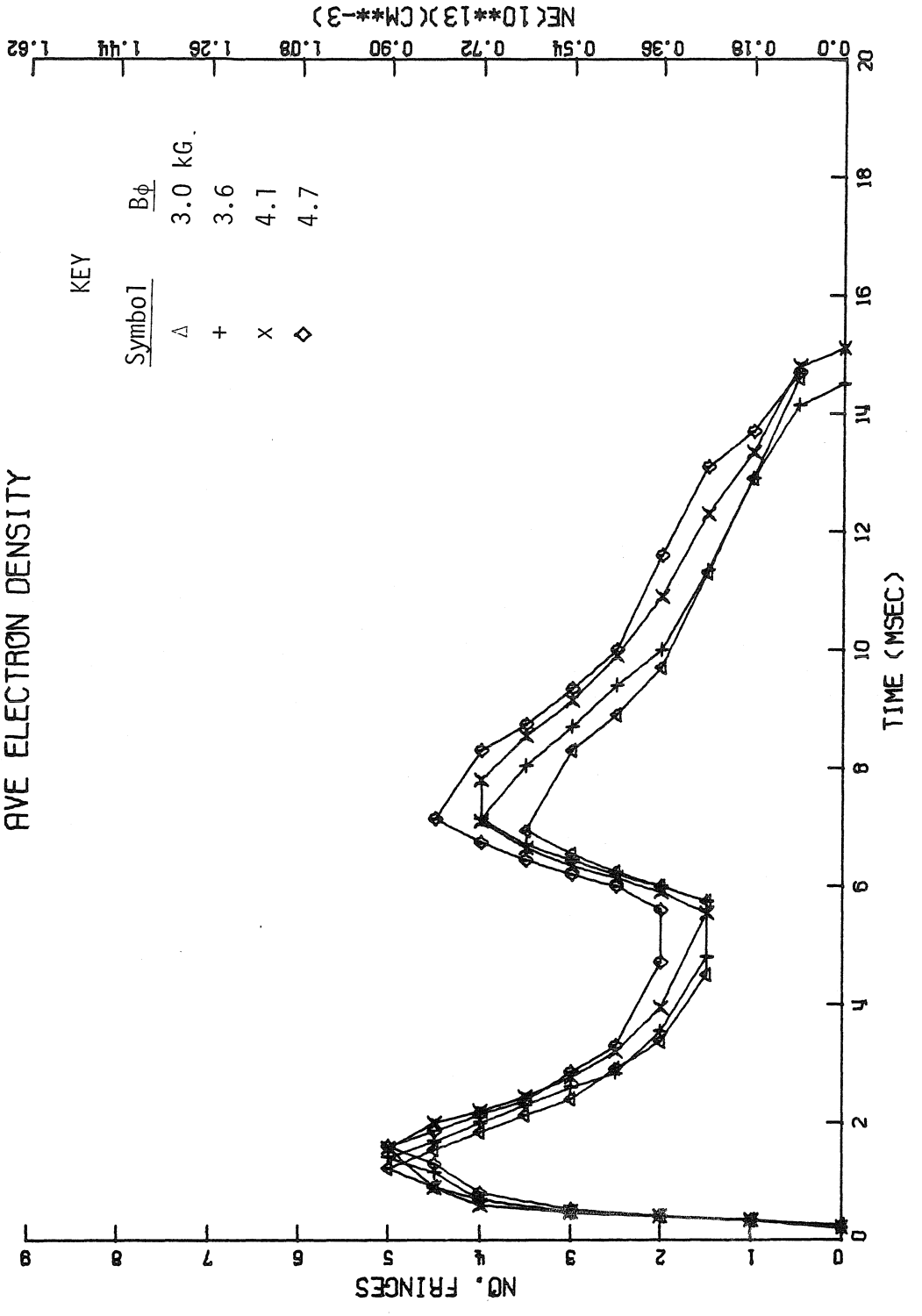

Figure 18. Variation of toroidal field B_ϕ while keeping other discharge and puffing parameters constant: OHFB = 1 kV, OHSB = 120v, VFSB = 49v, filling pressure 1.35 x 10^{-4} Torr H_2, puff reservoir pressure 970 Torr, puff voltage pulse on at 5.04 msec and off at 5.38 msec.

responding roughly to q(a) = 2.3) disrupted, presumably because q(0) dipped below unity.

Figures 19 and 20 present the least-squares fit rate of change of density information corresponding to Figure 18. There is no dramatic change in the density growth rate or particle confinement as B_ϕ is varied in the manner described above.

According to tearing-mode theory those modes with poloidal mode-number m and toroidal mode-number n may be unstable only about mode rational surfaces of minor radius $r < a$ such that $m/n = q(r)$ (and $q(r) < q(a)$ for $r < a$ from the above argument). Hence, raising the limiter q increases the number of modes that may contribute to anomalous diffusion. Figure 20 would seem to indicate that if such modes actually are destabilized in the Caltech Tokamak, they do not seriously affect particle confinement in the usual mode of operation ($q(a) \sim 3.8$).

The Daughney scaling law, equation (1.5), states that the electron energy confinement time is independent of B_ϕ. The collisional diffusion coefficient (Fig. 2) is proportional to $\rho^2 q^2$ where ρ, the Larmor radius, is inversely proportional to B_ϕ and q is proportional to B_ϕ, hence it has no dependence on B_ϕ. It is perhaps useful to compute the confinement time expected from this coefficient. From Fig. 2, $D \propto \nu_{ei}\rho^2 q^2$, and

$$\nu_{ei} = 3.62 \times 10^{-6}\, n_i T_e^{-3/2} \log \Lambda\, Z_{eff}$$

$$= \begin{cases} 6.99 \times 10^4 \text{ Hz}, & n_i = n_e = 10^{12}\text{cm}^{-2} \\ 6.52 \times 10^5 \text{ Hz}, & n_i = n_e = 10^{13}\text{cm}^{-3} \end{cases}$$

$$\text{where } \Lambda = \frac{1.23 \times 10^7\, T_e^{3/2}}{n_e^{1/2}\, Z_{eff}} \Longrightarrow \log \Lambda = \begin{cases} 16.1, & n_e = 10^{12}\text{cm}^3 \\ 15.0, & n_e = 10^{13}\text{cm}^{-3} \end{cases}$$

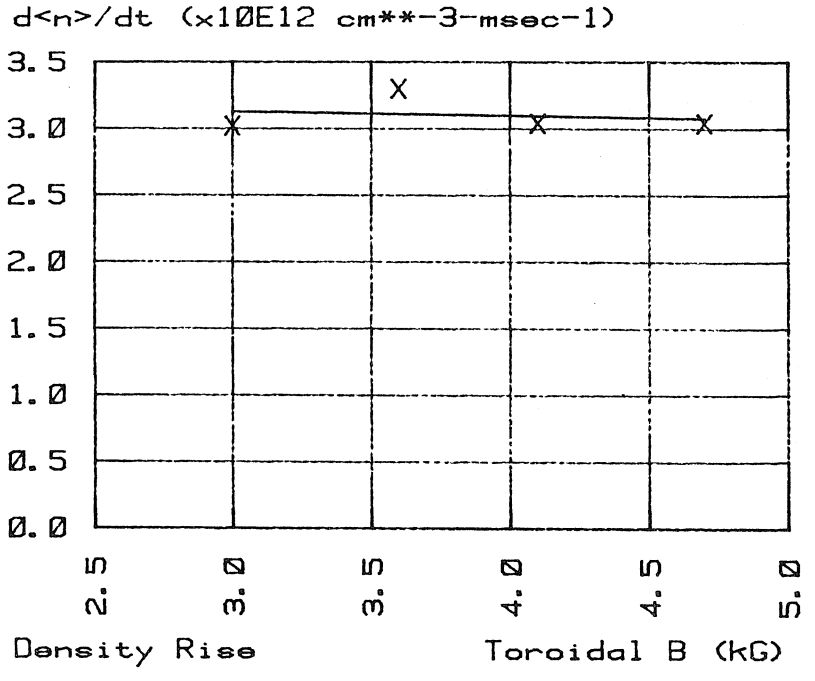

Figure 19. Least-squares fit time-rate of density rise of gas puffs of Figure 18 versus the toroidal field.

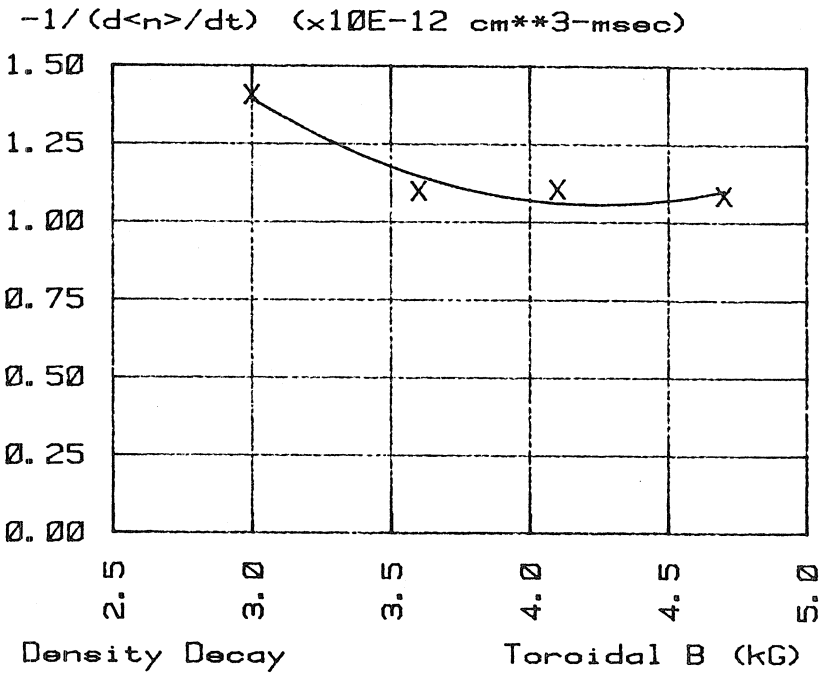

Figure 20. -1/(d<n>/dt) from least-squares fit to the density decay segments of Figure 18 versus the toroidal field. The particle confinement appears to be insensitive to the toroidal field (limiter q's varies from 2.9 to 4.6).

and

$$Z_{eff} = 1.5 \text{ (assumed)}, \quad T_e = 100 \text{ eV}$$

Since $$\rho = v_{th}/\omega_{ce} = \sqrt{\frac{\kappa T_e}{m_e}} \Big/ \frac{eB_\phi}{m_e} = 5.84 \times 10^{-3} \quad \text{where} \quad B_\phi = 4.08 \text{ kG}$$

and $q = 3.8$ typical value at peak puff density (see Fig. 14)

thus $$D \propto \nu_{ei} \rho^2 q^2 = \begin{cases} 34.5 \text{ cm}^2/\text{sec} , & n_e = 10^{12}\text{cm}^{-3} \\ 321 \text{ cm}^2/\text{sec} , & n_e = 10^{13}\text{cm}^{-3} \end{cases}$$

Then the collisional particle confinement time τ_c is of the order

$$\tau_c \sim \frac{a^2}{D} = \begin{cases} 6.5 \text{ sec} , & n_e = 10^{12}\text{cm}^{-3} \\ 0.7 \text{ sec} , & n_e = 10^{13}\text{cm}^{-3} \end{cases} ,$$

where a = 15 cm (toroidal minor radius of vacuum vessel)

From Fig. 20, $\alpha/1-\gamma = -1/(d\langle n\rangle/dt) \simeq 1.1 \times 10^{-12}\text{cm}^3\text{-msec}$

If $\gamma \sim .3$ (Alcator result) $\Longrightarrow$ $\alpha \sim 7.7 \times 10^{-13}\text{cm}^{-3}\text{-msec}$

$$\Longrightarrow \tau_p \sim \begin{matrix} 0.8 \text{ msec} , & n_e = 10^{12}\text{cm}^{-3} \\ 8.0 \text{ msec} , & n_e = 10^{13}\text{cm}^{-3} \end{matrix}$$

hence the claim that the observed confinement time is "anomalously small."

4. Plasma current

The interpretation of the variation of plasma current, I_p, is less straightforward than that of B_ϕ because of certain side effects. Although q is inversely proportional to I_p, it is also true that increasing I_p increases the ohmic-heating power, hence T_e increases with I_p. Changing I_p conceivably changes the energy balance of the plasma as well,

hence $\partial T_e/\partial r$ and the magnetic shear $\partial q/\partial r$ may both also depend on I_p. Daughney[6] maintains that the average electron temperature in an ohmically-heated Tokamak scales as $T_e \sim I_p^{.5}$; the same set of Tokamak data was used to derive this relation as was used to derive equation (1.5). From conductivity measurements in the Caltech Tokamak, it is found that increasing I_p by a factor of about 1.72 increases T_e by a factor of about 1.45, hence $T_e \sim I_p^{.7}$. This exponent is within the error of the experiment of Daughney's value. Variation of the magnetic shear is important to the theory of tearing-mode stability (this will be discussed in detail in the following). In summary, I_p cannot be varied without changing other parameters.

Figure 21 shows density traces from a sequence of shots in which I_p was varied from 16.5 kA to 28.4 kA keeping other variables constant at the values in the figure caption. The corresponding limiter q's at the peak puff density were 3.2 to 5.4; the smallest (largest) I_p corresponding to the largest (smallest) q(a). The least-squares fit to the density rise and fall data is presented in Figs. 22 and 23. From the former figure one sees that increasing the plasma current seems to slightly inhibit the incorporation of auxiliary gas into the plasma. The latter figure shows that with the exception of very small currents the particle confinement is relatively unaffected by a change in I_p. This parallels the result obtained when B_ϕ was varied. The particle confinement does not appear to be significantly altered by variation of limiter q, since $q \sim B_\phi/I_p$. This should not come as a surprise since, from Fig. 14, q(a) rises toward the end of the shot, while $d\langle n\rangle/dt$ is nearly constant.

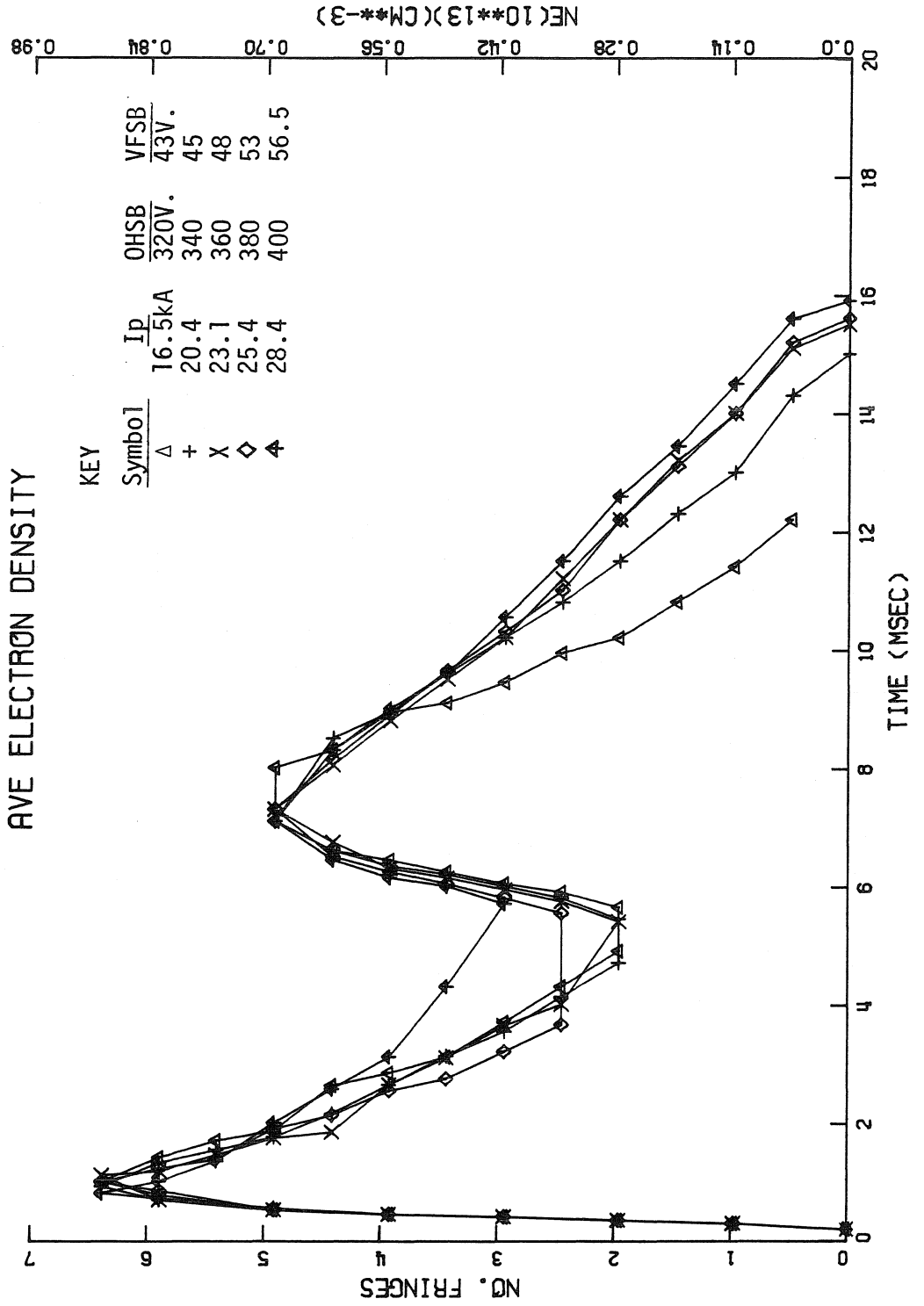

Figure 21. Variation of plasma current while keeping other discharge and puffing parameters constant: OHFB = 1 kV, VFFB = 120v, filling pressure 1.40 x 10^{-4} Torr H_2, puff reservoir pressure 970 Torr, puff voltage pulse on at 4.90 msec and off at 5.22 msec.

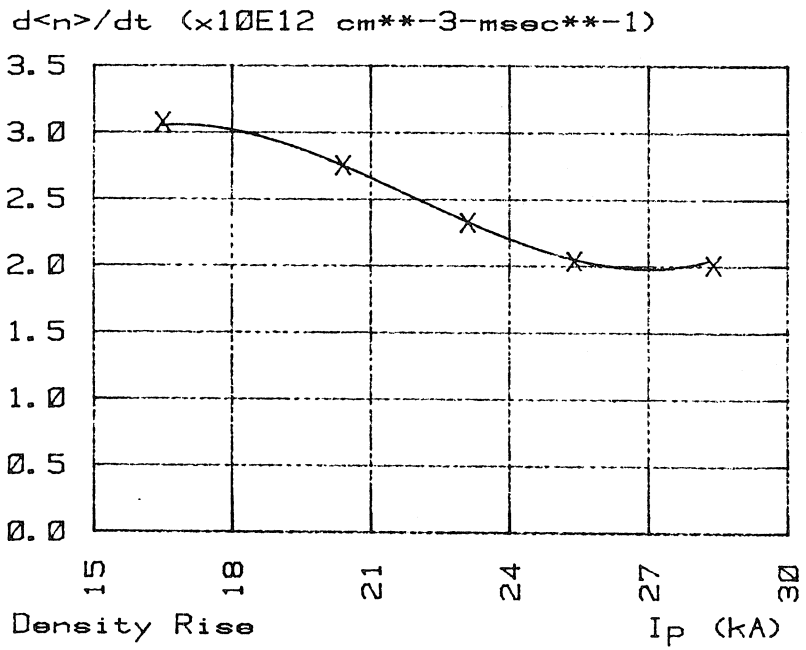

Figure 22. Least-squares fit time-rate density rise of gas puffs of Figure 21 versus the plasma current. Incorporation of the puffed gas is slightly slower at the higher currents.

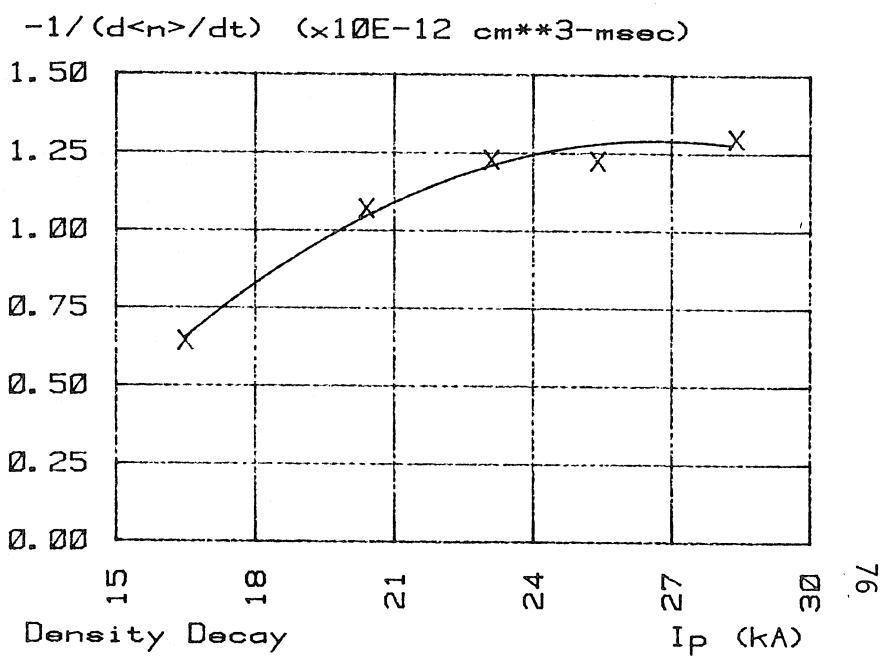

Figure 23. -1/(d<n>/dt) from least-squares fit to the density decay segments of Figure 21 versus the plasma current. The particle confinement is insensitive to the plasma current except at very small values of this parameter.

Daughney's two scaling laws, $\tau_{eE} \sim \frac{n_e T_e^{3/2}}{Z_{eff} I_p^{3/2}} a^3$ and $T_e \sim I_p^{.5}$ suggest that $\tau_{eE} \sim I_p^{-3/4}$ hence increasing the plasma current is expected to make the electron energy confinement time poorer. The collisional diffusion coefficient is $D \sim \nu_{ei} \rho^2 q^2$ where $\nu_{ei} \sim T_e^{-3/2}$, $\rho^2 \sim T_e$, and $q^2 \sim I_p^{-2}$, hence $D \sim T_e^{-1/2} I_p^{-2}$. Using either Daughney's scaling law $T_e \sim I_p^{.5}$ or the observed Caltech Tokamak scaling $T_e \sim I_p^{.7}$, the collisional diffusion should decrease, hence particle confinement improve, as I_p increases.

5. Temporal development of particle confinement

Delay of the beginning of the gas pulse from the beginning of the shot permits determination of the time evolution of the particle confinement time. Figure 24 presents a series of density traces obtained from a sequence of shots in which a standard gas pulse (0.32 msec duration, reservoir pressure 970 Torr and, as always, pulse voltage 125 V) was delayed 1 msec from one trace to the next. In contrast to Figures 15, 18, and 21 in which the density decay regions were qualitatively similar, the decay segments of Fig. 24 show a progressive steepening as the pulse is further delayed. This is quantified in Fig. 25, in which least-squares fit data deduced from the decay segments are plotted against the time at which each puff attains its maximum particle density. There is clearly a degradation in particle confinement more severe than the divagations at the extremes of Figs. 17, 20, and 23.

The toroidal field and plasma current decrease and the limiter q increases as each shot develops (see Figs. 12 and 14), however, from

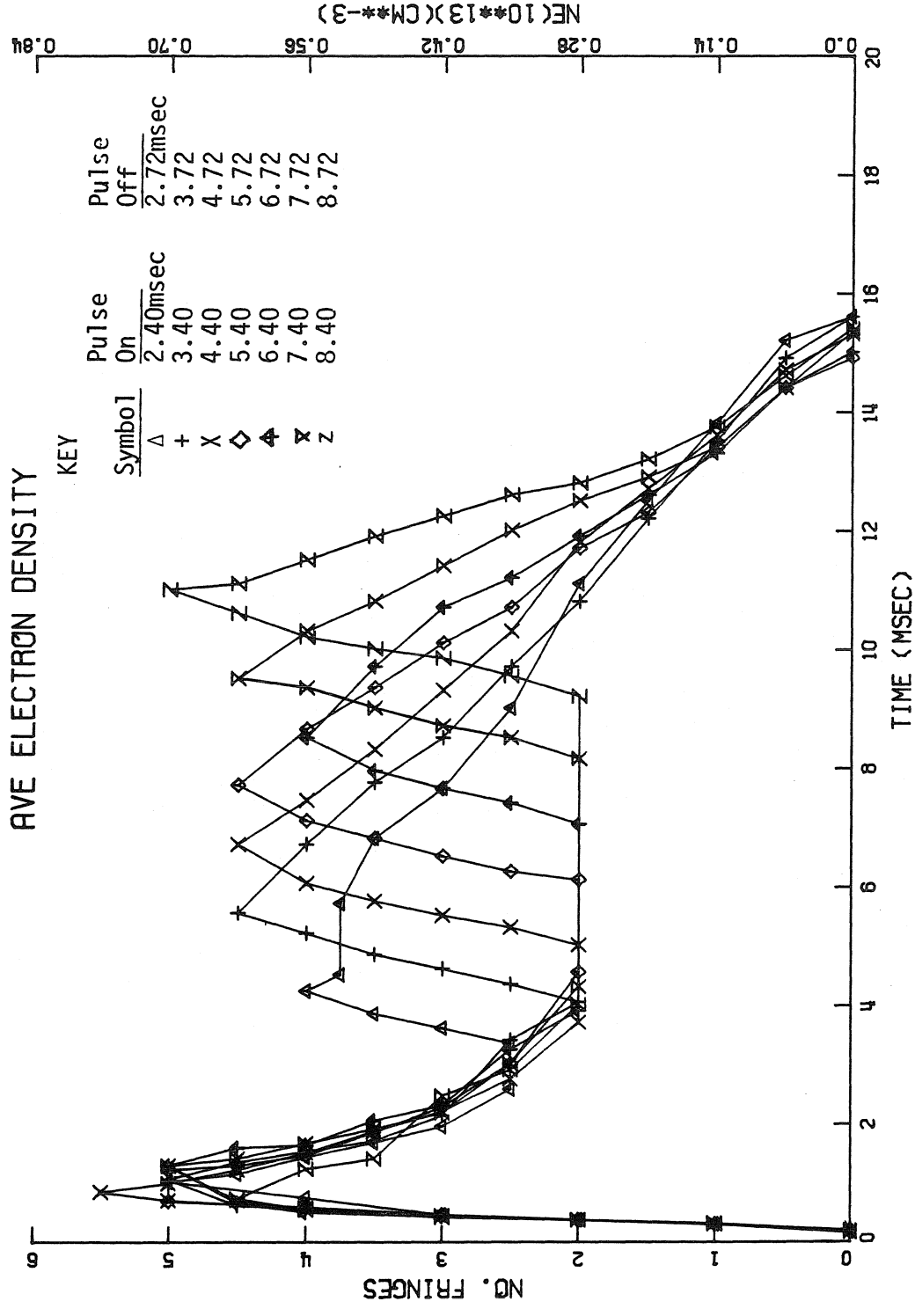

Figure 24. Variation of the delay from the beginning of the shot to the opening of the valve. Reservoir pressure and voltage pulse duration are kept constant at P_{res} = 970 Torr and 0.32 msec; other fixed quantities: filling pressure p_o = 1.30 x 10^{-4} Torr, OHFB = 1 kV, OHSB = 30v, VFFB = 120v, VFSB = 53v, B_ϕ = 4.0 kG.

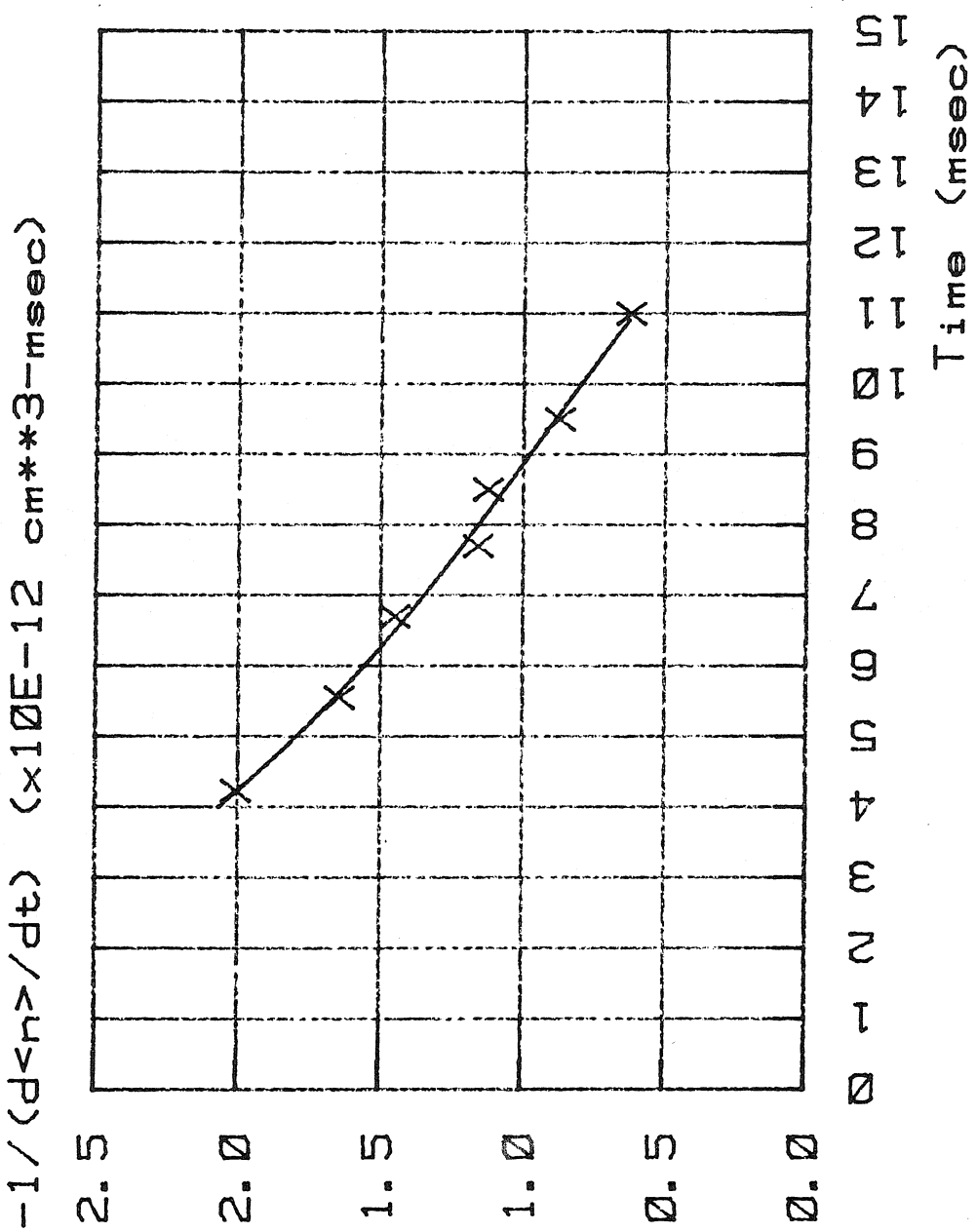

Figure 25. -1/(d<n>/dt) from least-squares fit to the density decay segments of Figure 24 versus the time at which the peak puff particle density was attained. Particle confinement degrades steadily as the shot nears its end.

the previous two sections this cannot account for the observed degradation in particle confinement. One is led to consider thermal effects for the origin of this degradation. Since the radial distribution of temperature is not known, the following discussion is of necessity speculative.

The shrinkage of the current channel, or steepening of the current density profile with time, is a well-known characteristic of ohmically-heated Tokamak discharges. Furth, Rosenbluth, Rutherford, and Stodiek[30] numerically evaluated the energy balance of a Tokamak discharge and found a series of thermal instabilities that led to the gradual contraction of the plasma minor radius as the discharge evolved. The lowest-order thermal eigenfunction could be stabilized by maintenance of a constant plasma current, while the higher-order thermal modes required for stability that $T_i/T_e \gtrsim 2/3$, where T_i and T_e are the ion and electron temperatures, respectively. Neither can the plasma current in the Caltech Tokamak be held constant nor can this temperature ratio criterion be met presently (auxiliary heating of the plasma ions through neutral-beam injection or radio-frequency excitation of ion resonances could create a more favorable ratio). Additional mechanisms cited by the authors that may lead to current-channel shrinkage and that were not accounted for in this computation include contraction due to space-dependent neutral-gas density and impurity-associated cooling processes. It seems very likely that the current-channel must shrink in the Caltech Tokamak as the discharge evolves.

The Daughney scaling relation shows that the electron energy confinement time has a strong dependence on toroidal minor radius:

$\tau_{eE} \sim a^3$. It is conceivable that τ_p, hence α, could have a strong dependence on minor radius. Daughney collected his data from Tokamaks with different vacuum-vessel minor radii as well as from ST and TFR Tokamak discharges in which the minor radii were varied, presumably with movable refractory metal limiters. The presumed shrinkage of the current-channel in the Caltech Tokamak might be equivalent to the stopping down of the plasma aperture with movable limiters, and lead to the observed decrease in particle confinement time.

6. Gas-puff intensity

a. Experimental results: The variation of the duration of the auxiliary gas-feed voltage pulse permits the study of the dependence of particle confinement on the peak particle density achieved, or the gas-puff intensity. Figure 26 presents density traces for a sequence of shots in which the valve voltage pulse was successively prolonged so that, for ease of interpretation of the microwave signal, the number of density rise fringes was a multiple of one-half. The figure caption lists the quantities held constant from shot to shot. The reader's attention is called to the rapid time-rate of particle loss for the puffs attaining the highest densities. Figure 27 presents the customary least-squares fit data derived from the density decay segments of Fig. 26. In order to bring out the degradation in particle confinement at the higher densities, the data of Fig. 27 were multiplied by peak puff particle densities to produce Fig. 28. This latter datum may be regarded as a pseudo-peak particle confinement time; that is, the peak particle confinement time divided by $1 - \gamma$ since $-1/(dn/dt) = \alpha/(1 - \gamma)$ and $\tau_p = \alpha n$. Alcator values of γ are on the order of 0.2 to 0.4, hence

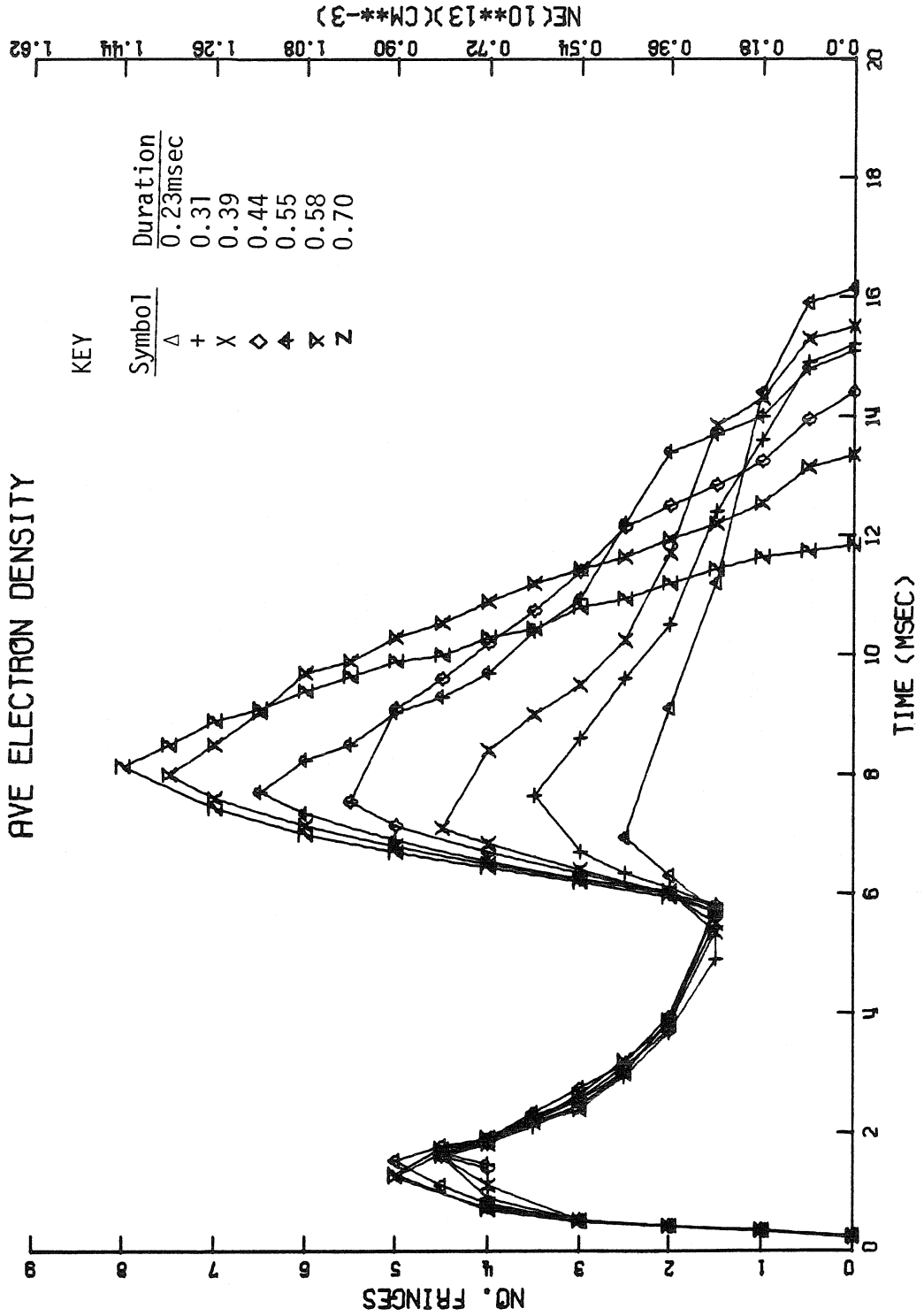

Figure 26. Variation of the pulse duration. Reservoir pressure and start of pulse kept at 970 Torr and 5.15 msec; other fixed quantities: filling pressure 1.35 x 10^{-4} Torr, OHFB = 1 kV, OHSB = 360v, VFFB = 120v, VFSB = 48v, B_ϕ = 4.1 kG.

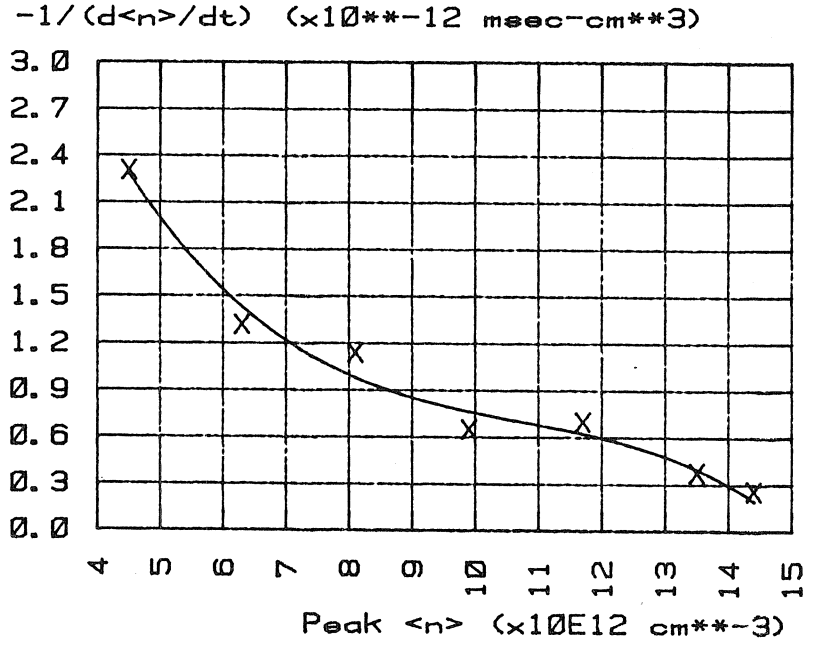

Figure 27. -1/(d<n>/dt) from least-squares fit to the density decay segments of Figure 26 versus the peak particle density attained by the puff.

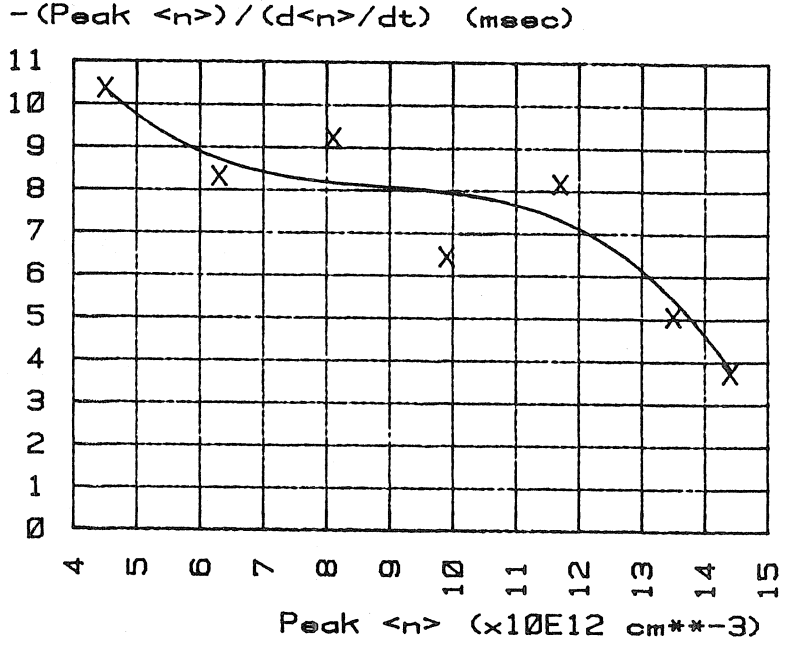

Figure 28. The data of Figure 27 are multiplied point-by-point by the peak particle density attained to give a pseudo-peak confinement time (see text).

the true peak particle confinement times are probably a fraction of those presented here. Figure 28 shows two features worth discussing at length, the lack of the improvement in particle confinement as the puff is prolonged that one would expect from Alcator scaling and a density threshold beyond which particle confinement is severely degraded.

b. Gas-puff intensity and Alcator scaling: The observed linearity of the time-rate of decay of the particle density (i.e., $d\langle n\rangle/dt = \text{constant}$) following termination of the neutral gas feed of any Caltech Tokamak gas puff has been shown to be consistent with the Alcator scaling relation $\tau_p = \alpha n$. One would expect, then, that the data of Fig. 28, pseudo-peak particle confinement time (peak particle confinement time divided by $1 - \gamma$) versus peak particle density, should show a monotonic increase of $-\text{peak}\langle n\rangle/(d\langle n\rangle/dt)$ with increasing peak n ; that is, the decay rate of higher-intensity (longer pulse-length) gas puffs should be slower than that of lower-intensity (shorter pulse-length) gas puffs. The data of Fig. 28 therefore appear to be inconsistent with Alcator scaling.

It is conceivable that τ_p may have a parametric dependence on discharge quantities other than n. Once again, by analogy with the Daughney scaling relation

$$\tau_{eE} \sim \frac{n_e T_e^{3/2} a^3}{Z_{eff}\, I_p^{3/2}}$$

it is possible that α may depend in a similar fashion on T_e, I_p, and a. In the following section it will be argued that gas puffing shrinks the plasma current channel and cools the plasma. If one identifies the current-channel dimension with the quantity a in the Daughney scaling relation,

then the diminishing of T_e and a might balance an increase in n_e to keep -peak<n>/(d<n>/dt) from increasing with peak<n>. However, this is highly speculative and the inconsistency between the measurements summarized in Figs. 27 and 28 and the Alcator scaling relation remains unresolved.

c. Particle-confinement degradation threshold: The severe degradation of particle confinement for gas puffs attaining peak average electron densities in excess of $1.3 \times 10^{13} cm^{-3}$ is accompanied by the appearance of simultaneous negative-going spikes on the one-turn voltage, "inward" jumps on the in-out signal, steps on the integrated Rogowski signal, in other words, minor- (in the sense that they do not terminate the discharge) or mini-disruptions. These occur during the later few milliseconds of the decay of the gas puff. This density threshold is consistent with the Murakami[18] scaling relation, that is, that the maximum attainable line-averaged electron density of Tokamaks is proportional to the ratio of toroidal magnetic field to major radius. Figure 29 is taken from Murakami's work and altered to include the point (0.89 T/m, $1.3 \times 10^{13} cm^{-3}$) for the Caltech Tokamak. As mentioned in the preceding discussion, this density threshold will be shown in the following (Chapter VI) to correspond to the nonlinear growth of an m = 2 magnetic fluctuation mode. Since the magnetic shear determines the stability of tearing modes in both the linear and nonlinear resistive MHD theory, it is appropriate to discuss what happens to this quantity during gas puffing.

It has been reported by Tokamak groups[5,31] possessing spatially resolvable electron-temperature diagnostics that the current-density profile steepens, or the current-channel shrinks, while auxiliary gas is

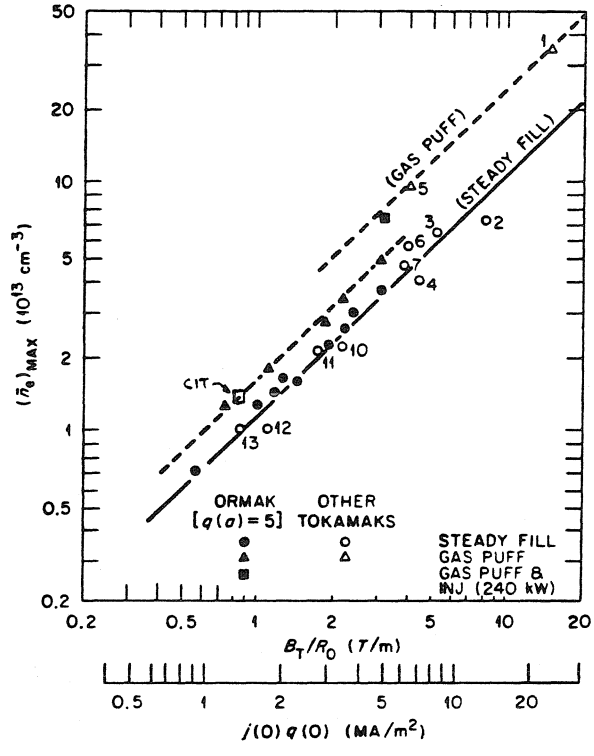

Fig. 29 (adapted from Ref. 18)

The points on this figure represent the maximum density data reported by Tokamaks such as Alcator and Ormak, while the CIT point represents the threshold density beyond which minor disruptions appear.

fed to the plasma. The explanation of this steepening is that the presence of the neutral gas at the edge of the plasma cools the outside of the discharge by virtue of the energy used up in ionizing the gas and bringing the added ion and electrons into thermal equilibrium with the plasma species. Since these same Tokamaks sustain constant plasma-current discharges with feedback between the Rogowski coil and the ohmic-heating generators, and since the cooling at the edge increases the resistivity there, the current in the center of these discharges increases. Again, lacking spatial temperature resolution in the Caltech Tokamak, it must be assumed that the gas feed at the edge of the plasma cools the outside with respect to the inside of the discharge and thus shrinks the current channel. It will now be shown that gas puffing in the Caltech Tokamak does not significantly change the plasma current but does cool the plasma.

The gas puffs of Fig. 26 have minimal effect on the plasma current. Table II compiles measurements of the plasma current just before the

Table II

SYMBOL	PEAK DENSITY	I_p JUST BEFORE DENSITY RISE	I_p IN MIDDLE OF DENSITY RISE	I_p AT END OF DENSITY RISE
Δ	2.5 fringes	24.9 kA	25.1 kA	24.8
+	3.5	25.3	24.9	23.7
x	4.5	25.9	25.6	24.8
◇	5.5	24.8	24.6	23.7
♠	6.5	25.3	24.5	22.9
▽	7.5	23.7	22.6	21.3
z	8.0	23.5	22.3	21.0
	Average	24.8 kA	24.2 kA	23.2 kA
	Std. Dev.	0.9 kA	1.3 kA	1.5 kA

density rise segments, that is, before the gas puff can exert an influence, in the middle of the density rise segment, and at the end of these segments. There is no dramatic change in plasma current as the gas puffs are successively prolonged; in fact, from the standard deviations it would seem that most of the spread in values in a particular column is due to shot-to-shot randomness. The resolution of the measurement is approximately 0.2 kA (= 40 kA full scale/255 dynamic range of transient recorder analog-to-digital converter).

Strictly speaking, comparisons should not be made between conductivity temperature measurements from discharges for which it is felt that the current-density distributions may differ because of the internal inductance term in equation (2.5). The more peaked the current density profile, the larger the internal inductance. However, the conductivity temperature was computed for two discharges, one without gas puffing and one with relatively mild gas puffing, i.e., enough gas was added to increase the particle density by 3 microwave fringes or $5.4 \times 10^{12} cm^{-3}$ above the $2.7 \times 10^{12} cm^{-3}$ prior to the density rise. Evaluating each conductivity temperature at the time corresponding to the peak of the density rise segment of the shot with gas puffing, it was found that the auxiliary gas cooled the plasma from 115 eV without puffing to 90 eV with puffing (roughly -22%). It seems plausible, then, that gas puffing cools the plasma considerably without changing the plasma current very much (for purposes of comparison the plasma current declined by 2.6% from the 115 eV shot to the 90 eV shot). This is consistent with the supposition that gas puffing steepens the current-density profile. It will now be shown that current-channel shrinking at constant plasma

current causes an increase in the magnetic shear at a mode-rational surface ($r = r_s$ such that $q(r_s) = m/n$, where m and n are integers).

Magnetic shear is said to exist at a point $\underset{\sim}{x} = (r,\theta,\phi)$ if there is a variation with the radial coordinate r of the pitch ι of the helical magnetic field lines, where

$$\iota(\underset{\sim}{x}) = \iota(r) = \frac{1}{2\pi} \frac{B_\theta}{B_\phi} \frac{R}{r} \tag{4.7}$$

and, as usual, θ and ϕ are respectively the poloidal and toroidal coordinates and B_θ and B_ϕ are respectively the poloidal and toroidal components of the magnetic field. Since the pitch, or rotational transform, is related to the safety factor q by $q = 2\pi/\iota$, one may define the magnetic shear as $\partial q/\partial r$; thus, there is zero magnetic shear if $\partial q/\partial r = 0$, which implies $\partial \iota/\partial r = 0$. In a cylindrical plasma

$$q(r) = \frac{r}{R} \frac{B_\phi}{B_\theta} \simeq \frac{r}{R} \frac{B_\phi \, 2\pi r}{\mu_o \int_0^r dr' 2\pi r' J(r')} = \frac{r^2 B_\phi}{\mu_o R \int_0^r dr' r' J(r')} \tag{4.8}$$

Steepening of the current-density profile at constant plasma current implies an increase in magnetic shear at a particular flux surface q(r) = constant. This happens for the following reasons:

1. On-axis peaking of the current-density profile lowers q(r) in the vicinity of r = 0.
2. q(a) is constant for a given plasma current, i.e., it is independent of the functional dependence of J on r.
3. A current-density profile that decreases monotonically with increasing radius (the experimentally observed case in other

Tokamaks) implies a q profile that increases with increasing radius.

Hence, with the exception of $r = 0$, the $q(r)$ versus r curve steepens as the current-density profile steepens. Further,

4. As the current-density profile steepens, the radius r_o at which $q(r)$ takes a particular value q_o moves outward, which in practice means r_o moves toward increasing $\partial q/\partial r$.

Figure 30 illustrates this phenomenology. The current-density profiles of Fig. 30a are derived from a set of realistic electron temperature profiles $T = T_0(1 - \alpha \frac{r^2}{a^2})^p$, where $\alpha = .9$ (this allows for the experimentally observed nonzero temperature at the edge of the Caltech Tokamak) and p successively takes on values 1, 1.5, and 2, and the relation $J \sim T^{3/2}$. The plasma current is 24 kA for each profile. The extreme values of p represent fairly flat and peaked temperature profiles compared to those reported from various experiments in other Tokamaks. Figure 30b shows plots of $q(r)$ versus r deduced from the J profiles. Notice that the radius associated with a particular value of q, e.g., $r = q^{-1}(2)$, moves outward as successively steeper current-density profiles are considered, and thus $\partial q/\partial r$ at $r = q^{-1}(2)$ increases.

In conclusion, although the current-density profile in a Caltech Tokamak plasma is not accurately known, there is good reason to assume that gas puffing shrinks the current channel and thus increases the magnetic shear at a given flux surface $q(r) =$ constant (in particular, at mode-rational surfaces). Further, as the gas puff is intensified (as the gas pulse is prolonged) the magnetic shear at a given mode-rational surface

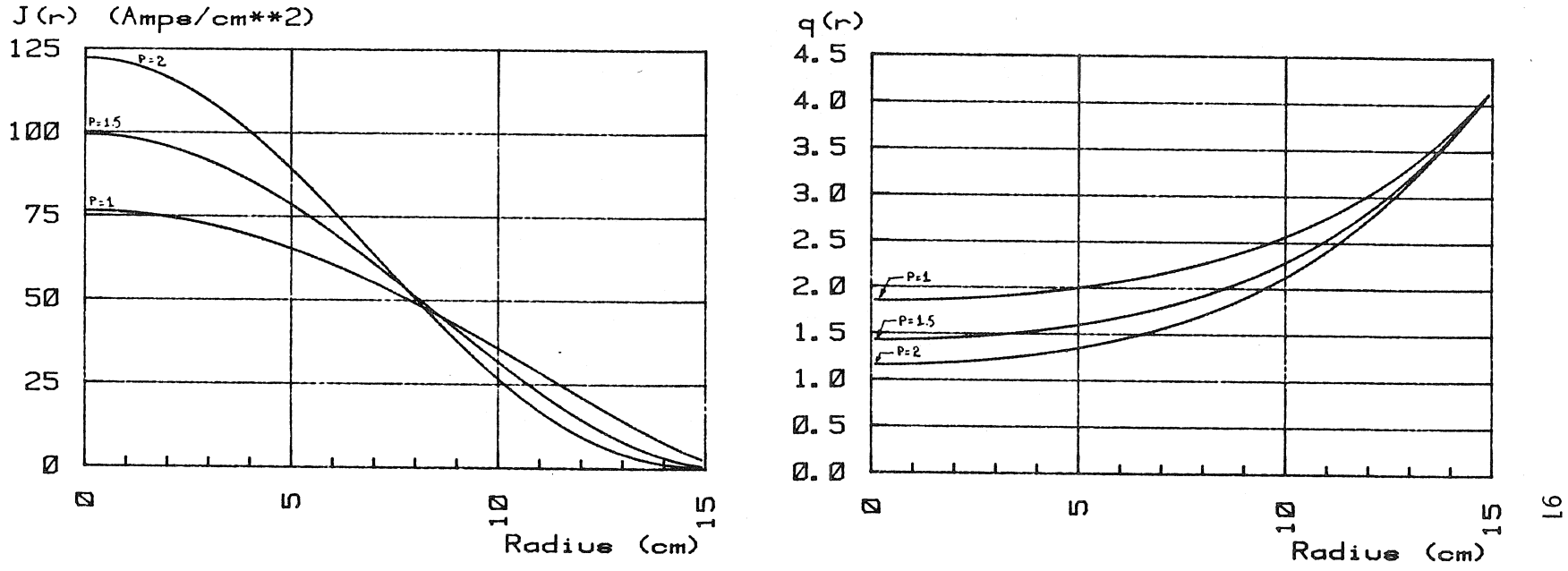

Figure 30. (a) Current-density profiles deduced from $J \sim T^{3/2}$ and $T = T_o (1-\alpha r^2/a^2)^p$, where $\alpha = .9$, $a = 15$ cm, $I_p = 24$ kA, $p = 1, 1.5, 2$.

(b) Safety factor q profiles corresponding to the current density profiles of (a). $B_\phi = 4.1$ kG. At a particular mode-rational surface (e.g., $r = r_s$ such that $q(r_s) = 2$) the magnetic shear $\partial q/\partial r$ increases as the current-density profile steepens (p increases).

should increase. Thus, the peak density threshold of $1.3 \times 10^{13} cm^{-3}$ may in fact be a threshold in magnetic shear.

It is also noted that if the current channel shrinks due to thermal instabilities as the discharge evolves, this too will increase the level of magnetic shear at the mode-rational surfaces.

D. Theory of Particle Influx and Density Build-Up

While not of pivotal interest in these researches, the two principal explanations of why gas puffing works merit a brief summary. The Oak Ridge numerical simulation group found that their transport code for ORMAK Tokamak discharges failed to yield a temporally growing central particle density; in fact, the code predicted hollow electron-density profiles. This is in sharp contrast to the behavior of all Tokamaks employing gas puffing. Successful simulation followed inclusion of a term due to the Ware Pinch.[32,33] This phenomenon consists in the drift toward the magnetic axis of trapped particles, that is, those particles caught in the magnetic mirror formed by the excess of toroidal magnetic field near the toroidal axis of symmetry compared to the field at the outside of the plasma. The temperature threshold for this effect is given by

$$T_e^2 = 6.7 \times 10^{-13} \, nqR \qquad (7.9)$$

where n is the average electron density, R is the toroidal major radius, and q is the plasma safety factor $q(a) = (a/R)(B_\phi/B_\theta)$ where a is the toroidal minor radius, B_ϕ the toroidal magnetic field, and B_θ the poloidal magnetic field evaluated at the limiter. The critical temperatures in the Caltech Tokamak for $n = 10^{12}$ and 10^{13} cm^{-3} and $q = 3.8$ are,

respectively, 11 and 34 eV. The electron temperature measured by plasma conductivity is in excess of 100 eV, hence the Caltech Tokamak has plasma parameters well within the regime of validity for the Ware Pinch.

Numerical simulation of transport by collisional processes alone in the Alcator Tokamak performed by the MIT group also obtained hollow particle-density profiles for gas-puffed discharges. Inclusion of the Ware Pinch did not obviate this defect. Coppi and Spight[34] were led to consider the effect of the gas-puff-driven steepening of the ion-temperature gradient (due to cooling of the edge of the plasma) and broadening of the charged particle density gradient. They maintained that, for sufficient steepening and broadening, electron temperature fluctuations driven by ion drift modes induce a net inflow of electrons and ions. These gradient-driven electrostatic fluctuations are called ion mixing modes. Inclusion of the corresponding terms into the Alcator transport code brought the simulations into qualitative agreement with the experimental results. Subsequent elaboration by Antonsen, Coppi, and Englade[35] includes quasilinear effects and successfully predicts the experimentally observed expulsion of impurity ions; these authors maintain that the driving mechanism of the quasilinear transport in the collisional limit is ion mixing mode fluctuations in the presence of finite electron thermal conductivity along the magnetic field. It is well beyond the scope of the experiments reported herein to ascertain the presence of these electrostatic modes or to weigh the relative importance of collisional, Ware Pinch, and ion-mixing mode processes.

V. Magnetic Fluctuations: Theoretical and Experimental Background

A. Introduction

The first measurements of magnetic fluctuation activity in Tokamaks were made in the T-3 Tokamak by Mirnov and Semenov[36,37] in 1971. These experiments consisted of observations of poloidal magnetic fluctuations by means of coils arranged around a minor circumference of the Tokamak. The salient result was that during the rise of the plasma current following initiation of the discharge, magnetic fluctuations of considerable intensity occur. The mode numbers of these fluctuations were observed to drop continuously from $m = 6$ to $m = 3$ or 2, presumably as the current channel contracted, and the intensity of the fluctuations became negligible as the current became relatively constant in time. In Tokamak terminology such poloidally sensitive coils have come to be called Mirnov coils and the strong low-frequency magnetic fluctuations, Mirnov oscillations.

Long before Mirnov and Semenov's experiments, pinch and stellarator plasmas were seen to display instability in configurations for which the infinite conductivity magnetohydrodynamic (MHD) model predicted stability. In particular, in a cylindrical or toroidal geometry kink-mode solutions may only be unstable on mode-rational surfaces (that is, on $r = r_s$ where $q(r_s) = m/n$ and m and n are integers) in a vacuum shell which surrounds a zero-resistivity plasma and which itself is enclosed by conducting walls. Since the common experimental configuration is that of a plasma having finite conductivity and extending to the plasma limiter (in the Caltech Tokamak the plasma extends out to the vacuum

vessel) kink-mode theory has a dubious physical foundation. In 1963 Furth, Killeen, and Rosenbluth[38] (FKR) included nonzero resistivity into a MHD instability calculation for the first time. The principal result was the elucidation of the resistive mode analogous to the kink mode, the so-called tearing mode. Like the kink mode, the tearing mode is a long wavelength magnetic oscillation and is considered a likely candidate for the source of Mirnov oscillations.

This chapter contains a simplification due to Bateman[27] of the FKR theory. The principal results to be derived are the growth rate of the tearing mode, the spatial distribution of the tearing-mode magnetic-field components, i.e., magnetic island formation, and the spatial distribution of fluid-velocity components, i.e., the convection cells associated with this model. A simple expression for the width of a magnetic island is derived and recent theoretical work on tearing-mode theory is summarized.

B. Preliminary Material

Before reproducing the derivation of the growth rate of tearing modes and so on, it is necessary to create a framework for the boundary layer calculation that gives this rate and to point out the mathematical and physical differences between the kink and tearing modes. FKR solved the tearing-mode problem in a semi-infinite magnetized plasma, or slab geometry. An important feature of this solution is that the resistivity ($\sim 7 \times 10^{-5}$ ohm-cm in the Caltech Tokamak) is only important near the planar surface determined by $\underset{\sim}{k} \cdot \underset{\sim}{B} = 0$, where $\underset{\sim}{k}$ is the tearing-mode wave vector and $\underset{\sim}{B}$ is the static magnetic field. FKR modeled the plasma as having infinite conductivity except in a thin resistive layer surrounding

the $\underset{\sim}{k}\cdot\underset{\sim}{B} = 0$ surface. The solution within this (boundary) layer must be matched to the zero-resistivity solutions in the surrounding plasma.

The extension of the FKR theory to a geometry closer to that of Tokamaks was made by Furth, Rutherford, and Selberg[39] (FRS) who, in 1973, solved the tearing-mode problem in cylindrical geometry following Shafranov's[24] example of considering a non-uniform current density distribution within the plasma. The argument is often made that the extensions from a slab geometry to a cylindrical geometry and thence to a toroidal geometry follow simply, because the cylindrical and toroidal radii of curvature are much larger than the resistive layer width. The importance of considering realistic current-density profiles and geometries (a Tokamak plasma is, after all, closer to a cylinder than a semi-infinite slab) is, as Shafranov demonstrated, to be found in the determination of the stability conditions for the various tearing-mode solutions. The salient features of the FRS problem are these: radial magnetic-perturbation fields of the form $B_r^p = i\psi(r)\exp[\gamma t + i(m\theta - kz)]$ are solutions of a second-order differential equation identical to the zero-resistivity eigenmode equation used to derive kink modes except near the singular points of this differential equation, r_s, where $\underset{\sim}{k}\cdot\underset{\sim}{B}(r_s) = -kB_z + \frac{m}{r}B_\theta(r_s) = 0$. (In toroidal geometry

$$\underset{\sim}{k}\cdot\underset{\sim}{B}(r_s) = \frac{m}{r}B_\theta(r_s) - \frac{n}{R}B_\phi(r_s), \quad \text{hence}$$

$$\underset{\sim}{k}\cdot\underset{\sim}{B} = 0 \Longrightarrow \frac{m}{n} = \frac{r}{R}\frac{B_\phi(r_s)}{B_\theta(r_s)} = q(r_s)\ ,$$

i.e., mode rational surfaces) At these points a more exact fourth-order differential equation incorporating the effects of nonzero resistivity

must be used. The solution proceeds by solving the second-order differential equation for $\psi_1(r)$ and $\psi_2(r)$ in the respective ranges $0 < r < r_s$ and $r_s < r < a$ with the appropriate boundary conditions at the wall ($\psi_2(a) = 0$) and on the magnetic axis ($\psi_1(r) \sim r^{m-1}$ as $r \to 0$). There will, in general, be a discontinuity in the derivative of ψ at $r = r_s$. Define

$$\Delta' \equiv \frac{d}{dr}(\psi_2 - \psi_1)\Big|_{r_s} \Big/ \psi(r_s) \tag{5.1}$$

Analysis of the fourth-order differential euqation shows that Δ' must be positive for growth of the tearing mode ($\gamma > 0$). FRS computed Δ' for several current-density profiles. The result of these calculations is that as the current-density profile becomes more peaked (i.e., as the magnetic shear increases) the higher m-number modes are stabilized in descending order of m. The m = 2 mode was found to be unstable over a very wide range of limiter q's with every profile considered. The m = 3 mode was found to be unstable with even a quite peaked current density profile, but then only within a narrow range of high ($\gtrsim 5$) limiter q's; the trend was clearly toward stabilization of the m = 3 mode with increasing magnetic shear. The $m \geq 4$ modes became absolutely stabilized (i.e., regardless of limiter q) with what would be considered a moderate amount of shear from an experimental viewpoint.

Figure 31 shows radial distributions of $\psi(x)$ for m = 2 where $x = r/r_o$ and r_o is a characteristic dimension of the current density profile. The parameter varied is the location of the resistive layer $x_s = r_s/r_o$. The dashed vertical lines connect the values of x_s on the x-axis with their proper eigenmodes. The boundary layer is modeled as being so thin that one sees only the discontinuity in the derivative of

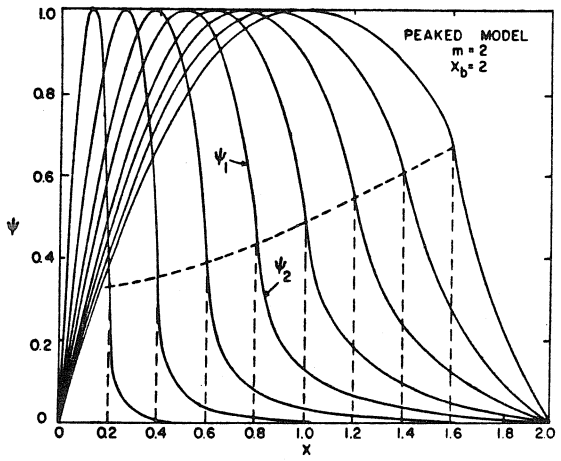

Fig. 31 (adapted from Ref. 39)

The radial dependence of the m = 2 tearing mode plotted against the normalized radius. The dashed vertical lines connect the value of the normalized mode rational radius ($q^{-1}(2)$) with the corresponding eigenmode. A fairly peaked current-density profile was used.

ψ at x_s rather than a smooth matching over the layer. This approximation now appears to be rather poor in light of estimates of the magnetic island width based on fluctuation measurements.

The mathematical difference between the kink and tearing modes is to be found in the matching condition at the $\underset{\sim}{k}\cdot\underset{\sim}{B} = 0$ layer. The tearing-mode assumption is that ψ varies smoothly, but ψ' jumps across this layer and the kink-mode assumption is that both ψ and ψ' are continuous across $r = r_s$. Another important difference between these modes is that the growth rate of the kink mode takes place on the rapid hydromagnetic time scales whereas the resistivity in the boundary layer slows the growth of the tearing mode. Further, introduction of dissipation creates states of lower potential energy for the plasma as a whole, by allowing the tearing and reconnection of magnetic field lines within the boundary layer to produce the magnetic island topology shown in Fig. 4. Zero resistivity mandates the magnetic field lines be "frozen" into the fluid obviating such a rearrangement.

C. Boundary Layer Dynamics

It is now time to proceed with Bateman's simplification of the FKR derivation. The aim of this calculation is to solve for the resistive layer width and growth rate in terms of Δ' and the hydromagnetic and resistive parameters. The derivation starts with the MHD equations to set up the basic framework and then uses the balance of forces and rate at which work is done on a fluid element within the resistive layer to determine the growth rate of the tearing mode. On a first reading of this thesis the reader might prefer to skip to the solution, equation (5.22),

taking note of Fig. 32.

It will be shown that the magnetic island topology is the result of the superposition of the tearing-mode magnetic perturbation field upon that part of the magnetic field $\underset{\sim}{B}$ near the mode-rational surface $r = r_s$ having shear. The shearless part of the field contributes the helical twisting around the torus seen in Fig. 4. To this end one computes a magnetic field $\underset{\sim}{B}_q(r)$ having zero shear and constant safety factor q ($=q(r_s)$ of the field $\underset{\sim}{B}$) across the plasma. Then the shear field $\underset{\sim}{B}_*(r)$ is defined as

$$\underset{\sim}{B}_*(\underset{\sim}{r}) \equiv \underset{\sim}{B}(\underset{\sim}{r}) - \underset{\sim}{B}_q(\underset{\sim}{r}) \tag{5.2}$$

For example, in a cylindrical plasma of length L, let the magnetic field be

$$\underset{\sim}{B}(r) = B_\theta(r)\hat{e}_\theta + B_z(r)\hat{e}_z \Longrightarrow q(\underset{\sim}{B}(r)) = (2\pi r/L)(B_z(r)/B_\theta(r))$$

Let

$$\underset{\sim}{B}_q(r) = \frac{r}{r_s} B_\theta(r_s)\hat{e}_\theta - B_z(r_s)\hat{e}_z$$

$$\Longrightarrow q(\underset{\sim}{B}_q(r)) = \frac{2\pi r}{L} \frac{B_z(r_s)}{\frac{r}{r_s} B_\theta(r_s)} = \frac{2\pi r_s}{L} \frac{B_z(r_s)}{B_\theta(r_s)} = q(\underset{\sim}{B}(r_s)) \quad \text{for all } r$$

Hence $\underset{\sim}{B}_q$ has no shear ($\partial q(B_q(r))/\partial r \equiv 0$).

To approximate a toroidal plasma with magnetic field $\underset{\sim}{B} = B_\theta(r)\hat{e}_\theta + B_\phi\hat{e}_\phi$ (Fig. 1) by a slab of plasma extending infinitely in the y- and z-directions, one makes the respective identifications of the θ- and ϕ-coordinates with the y- and z-coordinates and the r-direction with the x-direction. Then the appropriate magnetic field

in the slab has only y- and z-components and the y-component must of necessity have only an x-dependence. By the above one considers a y-directed, static, sheared magnetic field $B_*(x)$ where $B_* = 0$ when $x = 0$, that is, $x = 0$ is chosen to be at the mode-rational layer (Fig. 32). Expressing B_* in a series expansion about $x = 0$ and considering a single harmonic component of the x-directed magnetic-field perturbation, one has

$$B_x = B_x^p \sin ky + B_*' x + O(x^2) \tag{5.3}$$

in the vicinity of $x = 0$. The superscript p denotes perturbation quantities. The perturbation is assumed uniform in the z direction.

The x-component of Faraday's Law is then

$$\frac{\partial}{\partial t} B_x^p = - \frac{\partial}{\partial y} E_z^p \tag{5.4}$$

and Ohm's law gives

$$E_z^p = -v_x^p B_* + \eta_o J_z^p \tag{5.5}$$

where $\eta_o = \eta_o(x)$ is the resistivity. For purposes of this derivation it is assumed that η_o is large only in a small neighborhood of $x = 0$. The balance of forces on the fluid gives

$$\rho_o \frac{\partial}{\partial t} v_x^p = -J_z^p B_* \tag{5.6}$$

where ρ_o is the fluid density. Finally, all motion is assumed to be incompressible

$$\nabla \cdot \underset{\sim}{v}^p = 0 \tag{5.7}$$

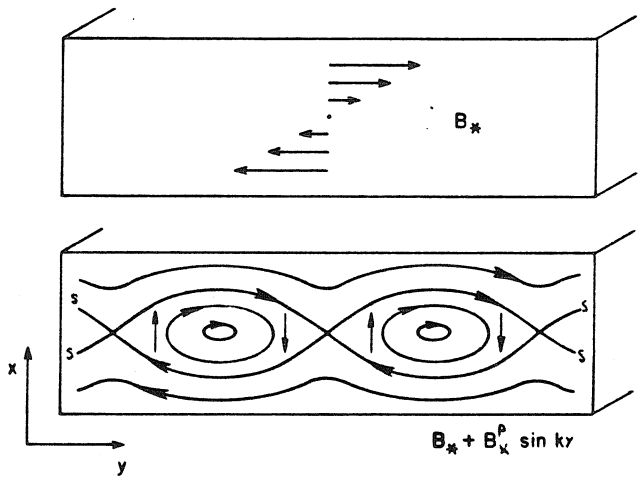

Fig. 32 (adapted from Ref. 27)

above: Plasma slab with shear field B_*.

below: Superposition of perturbation fields on B_* gives characteristic island topology. The surface marked S is the magnetic separatrix.

and there is no z-component of perturbed velocity or magnetic field. The validity of the assumption of incompressibility has been established in the complete derivation. For purposes of this discussion, it is claimed that the growth of the instability proceeds on time scales much longer than the characteristic hydromagnetic time a/V_A where V_A is the Alfvén velocity and a is a characteristic length in the plasma, e.g., the width of the plasma slab or the radius of a plasma cylinder. That is, the fluid motion is subsonic, hence incompressible.

It is assumed that B_x^p and v_y^p vary as $e^{\gamma t}$ sin ky, while E_z^p, J_z^p, v_x^p, and B_y^p vary as $e^{\gamma t}$ cos ky (it is the superposition of B_x^p sin ky that gives the island topology in Fig. 32).

$$\nabla \cdot \underset{\sim}{B} = 0 \Longrightarrow \frac{\partial}{\partial x} B_x^p = kB_y^p \tag{5.8}$$

$$\nabla \times \underset{\sim}{B} = \mu_o \underset{\sim}{J} \Longrightarrow \mu_o J_z^p = \frac{\partial B_y^p}{\partial x} - \frac{\partial B_x^p}{\partial y} = \frac{1}{k} \frac{\partial^2 B_x^p}{\partial x^2} - kB_x^p \tag{5.9}$$

$$\text{eqs. (5.4) and (5.5)} \Longrightarrow \frac{\partial}{\partial t} B_x^p = -\frac{\partial}{\partial y}\left[v_x^p B_* + \eta_o J_z^p\right]$$

$$= -kv_x^p B_* + \eta_o k J_z^p$$

$$= -kv_x^p B_* + \frac{\eta_o}{\mu_o}\left(\frac{\partial^2 B_x^p}{\partial x^2} - k^2 B_x^p\right) \tag{5.10}$$

using equation (5.8) in the last step. The width of the resistive layer, ε, is assumed very small in comparison with the extent of the plasma in the x-direction and $2\pi/k$, the wavelength of the perturbation. The resistive region is treated as a boundary layer. The quantity Δ' is defined by (cf. equation (5.1))

$$\Delta' \equiv [B_x^{p'}(\tfrac{\varepsilon}{2}) - B_x^{p'}(-\tfrac{\varepsilon}{2})] / B_x^p(0) \tag{5.11}$$

and is the reciprocal of the scale length over which $B_x^{p'}$ changes across the boundary layer. Hence

$$\frac{\partial^2 B_x^p}{\partial x^2} \simeq \Delta' B_x^p/\varepsilon \tag{5.12}$$

and since $k\varepsilon << 1$ and $\Delta'/k \gtrsim 1$, equation (5.9) becomes

$$\mu_o J_z^p \simeq (\frac{\Delta'}{k\varepsilon} - k)B_x^p \simeq \frac{\Delta'}{k\varepsilon} B_x^p \tag{5.13}$$

The growth rate of the tearing mode may now be determined. Within the boundary layer the resistive term in Ohm's law becomes comparable in magnitude to the $\underset{\sim}{v} \times \underset{\sim}{B}$ and electric field terms, or

$$v_x^p B_* \sim \eta_o J_z^p \sim \frac{1}{k} \frac{\partial B_x^p}{\partial t} = \frac{\gamma}{k} B_x^p \tag{5.14}$$

Hence $\frac{\gamma}{k} B_x^p \sim \eta_o \frac{\Delta'}{k\varepsilon\mu_o} B_x^p$ (from (5.13) and (5.14))

or
$$\gamma \sim \frac{\eta_o \Delta'}{\varepsilon\mu_o} \tag{5.15}$$

From incompressibility $kv_y^p \simeq v_x^p/\varepsilon$. The rate of change of kinetic energy is

$$\gamma\rho_o \frac{1}{2}(v^p)^2 \simeq \gamma\rho_o \frac{1}{2} (v_x^p)^2/(k\varepsilon)^2 \tag{5.16}$$

Balancing the rates on which work is done on the fluid

$$\underset{\sim}{v}^p \cdot \underset{\sim}{F} \simeq v_x^p B_* J_z^p = \gamma\rho_o \frac{1}{2} (v_x^p)^2/(k\varepsilon)^2 \implies$$

$$\Longrightarrow \quad \gamma\rho_o v_x^p \simeq 2B_*(k\varepsilon)^2 J_z^p \simeq 2B_* \frac{\Delta'}{\mu_o} B_x^p k\varepsilon \tag{5.17}$$

From (5.14)

$$\gamma \sim k v_x^p \frac{B_*}{B_x^p} \simeq k \cdot \frac{B_*}{B_x^p} \cdot 2B_* \frac{\Delta'}{\mu_o} B_x^p \cdot \frac{1}{\gamma\rho_o} k\varepsilon$$

or

$$\gamma^2 \sim (2\varepsilon \frac{\Delta'}{\mu_o\rho_o}) B_*^2 k^2 \tag{5.18}$$

From equations (5.15) and (5.18)

$$\varepsilon \sim \frac{\gamma^2\rho_o}{k^2} \frac{\mu_o}{\Delta'} \frac{1}{2B_*^2} \simeq \frac{\rho_o}{k^2} \frac{1}{2B_*^2} \frac{\eta_o^2}{\varepsilon^2} (\frac{\Delta'}{\mu_o}) \tag{5.19}$$

Within the boundary layer $B_*' \simeq B_*/\varepsilon$ so from (5.19)

$$\varepsilon^5 \simeq \frac{\rho_o}{2} \frac{1}{(kB_*')^2} \frac{\eta_o^2 \Delta'}{\mu_o} \tag{5.20}$$

and from (5.18)

$$\gamma^2 \sim 2\varepsilon^3 \frac{\Delta'}{\mu_o\rho_o} (kB_*')^2 \tag{5.21}$$

hence

$$\gamma \sim [\frac{(kB_*')^2\eta_o^3}{2\sqrt{2}\ \rho_o} (\frac{\Delta'}{\mu_o})^4]^{1/5} \tag{5.22a}$$

$$= .81\ \tau_s^{-3/5}\ \tau_A^{-2/5} (\Delta' a)^{4/5}\ (a^2 \frac{kB_*'}{B_{\phi o}})^{2/5} \tag{5.22b}$$

where τ_s is the resistive skin time, τ_A the Alfvén time

$$\tau_s \equiv \frac{a^2\mu_o}{\eta_o} \quad , \qquad \tau_A = \frac{a\sqrt{\mu_o\rho_o}}{B_{\phi o}} \tag{5.23}$$

$B_{\phi o}$ is the toroidal field, and a is the characteristic plasma dimension.

In toroidal geometry a more elaborate calculation yields for the growth rate

$$\gamma = .55\ \tau_S^{-3/5}\ \tau_A^{-2/5}(\Delta' a)^{4/5}\ \left(\frac{a}{R}\ n\ \frac{aq'}{q}\right)^{2/5} \tag{5.24}$$

The width of the magnetic island is given by the largest excursion of the magnetic separatrix (surface S in Fig. 32) from the x = 0 plane. The following simple derivation is due to Matsuda and Yoshikawa[40] and is valid in the linear approximation.

The flux function for the magnetic field is given by

$$B_x = -\frac{\partial \psi}{\partial y} \quad , \quad B_y = \frac{\partial \psi}{\partial x} \tag{5.25}$$

From equation (5.3)

$$\psi = \psi_o + \frac{1}{2} B_*' x^2 + \frac{B_x^p}{k} \cos ky + O(x^3) \tag{5.26}$$

in the vicinity of x = 0. The x-dimension is assumed normalized to the width of the plasma so that the higher-order terms are negligible within the resistive boundary layer. The function takes the constant value ψ_S on the separatrix. In the x = 0 plane $\psi_S \simeq \psi_o - B_x^p/k$ is the expression valid on the lines $y = 2n\pi/k$, the locus of saddle points, and at the point of greatest separation from the x = 0 plane, at x = w/2 and $y = (2n+1)\pi/2k$, $\psi_S \simeq \psi_o + \frac{1}{2} B_*'(\frac{w}{2})^2 + B_x^p/k$. Eliminating $\psi_S - \psi_o$ gives

$$w = 4(B_x^p/kB_*')^{1/2} \tag{5.27}$$

In toroidal geometry this becomes

$$w \simeq 4r\left(\frac{B_r^p}{mB_\theta}\left|\frac{q}{rq'(r)}\right|\right)^{1/2} \tag{5.28}$$

where r and θ are the radial coordinate and poloidal angle, and m is the poloidal mode number. The salient result is that in the linear approximation the magnetic island width, which has been assumed to be smaller than the resistive boundary layer with ε, is inversely proportional to the square root of the magnetic shear.

Rutherford[41] showed that nonlinear growth results when the second order $\underset{\sim}{v} \times \underset{\sim}{B}$ term $v_y^p B_x^p$ becomes appreciable and changes the nature of the growth from exponential to linear; in a slab geometry

$$\frac{dw}{dt} \simeq 1.66\ \eta_o \frac{\Delta'}{k} \tag{5.29}$$

White, Monticello, Rosenbluth, and Waddell[42] showed that when the width of the island approaches that of the boundary layer the growth saturates according to

$$\frac{dw}{dt} \simeq 1.66\ \eta_o[\Delta'(w) - \alpha w]\, k \tag{5.30}$$

where $\Delta'(w)$ is the discontinuity in the derivative of the radial magnetic field perturbation from one edge of the island to the other, and α depends on the profile of the unperturbed current density, the magnetic shear B_*', and is also dependent on the radial eigenmode asymmetry in cylindrical geometry.

The velocity, magnetic field, and current density components for the derivation of the linear growth rate in slab geometry are shown in Fig. 33. The magnetic separatrix appears as well. The perturbation

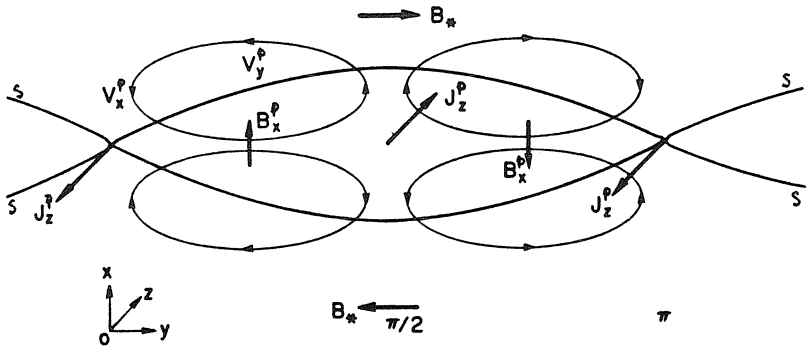

Fig. 33 (adapted from Ref. 27)

Fluctuation components of current (J_z^p), velocity (v_x^p and v_y^p) and magnetic field (B_x^p). Also shown, the shear field B_* and magnetic separatrix S.

fluid velocity is convective. A charged particle may make its way quite rapidly across the tearing-mode magnetic island by a sequence of convection into the island, a Coulomb collision impetus across the $x = 0$ surface, and flow outward through the opposite convection cell. Thus, closely spaced island structures or magnetic islands grown to considerable fractions of the minor toroidal radius by nonlinear mechanisms can enhance cross-field transport of energetic particles from the hotter center of the discharge to the cooler walls.

D. Recent Theory and Experiment

Subsequent to the FKR and FRS computations, the effects of the toroidal curvature have been carefully computed by Glasser, Greene, and Johnson;[43] the results are stabilization of the tearing modes if the current profile is made sufficiently flat but destabilization if the current profile contracts, and that elevated temperatures improve stability. Drake and Lee[44] are the most recent of several investigators into modifications to tearing modes by kinetic effects. They find that tearing mode growth rates and the boundary layer width are modified, although not to a great extent, in highly collisional devices like the Caltech Tokamak. They assert that the growth constant γ has an imaginary component equal to the diamagnetic drift frequency ω^* evaluated at the mode rational surface, and that this accounts for the observed nonzero phase velocity of Mirnov oscillations, providing that ω^* is sufficiently large.

Considerable research has gone into destruction and distortion of magnetic islands. Finn[45] has investigated the nonlinear interaction between $m = 2$, $n = 1$, and $m = 3$, $n = 1$ tearing modes; Stix[46] has looked into

the braiding of lines of force due to minute deviations from symmetry of the plasma current flow; and Kadomtsev and Pogutse[47] have considered certain nonlinear mechanisms that cause helical perturbations to grow into plasma-free inclusions or "bubbles." Detailed investigation has been made into the m = 1 oscillation, the physics of which is considerably more complex than the $m \geq 2$ modes. This mode has not yet been observed on the Caltech Tokamak, and is left out of this discussion.

Magnetic islands may be formed by driving mechanisms other than resistive MHD modes. Chrisman, Clarke, and Rome[48] point out that regardless of origin magnetic islands are "the result of having a harmonic component of the perturbed magnetic field in resonance with the unperturbed rational surface field lines in the presence of shear." Matsuda and Yoshikawa[49] have demonstrated that formation of magnetic islands may be driven by the spatial periodicity of the toroidal magnetic winding. The Caltech Tokamak has a nearly continuous winding and the ports are not distributed periodically, hence this effect is expected to be minimal.

Since insulating materials such as pyrex, quartz, and alumina are severely damaged by exposure to Tokamak discharges, it has not been until quite recently that sufficient courage was summoned to perform direct measurements on even relatively cool plasmas. Thus, nearly all measurements of Mirnov oscillations have been made with coils sensitive to the poloidal fluctuation field protected from the plasma by placement in the shadow of a limiter. Robinson and McGuire[50] in 1979 placed a probe consisting of 24 coils, 4 mm apart, in a 6 mm diameter quartz envelope into

the Tosca Tokamak. They were able to verify that the spatial distribution of radial and poloidal fluctuation fields of Mirnov oscillations with m = 3 was quite similar in form to the cylindrical eigenfunctions of Furth, Rutherford, and Selburg (Fig. 31). None of the researches of Mirnov and Semenov and of Robinson and McGuire considered plasmas altered by gas puffing.

VI. Magnetic Fluctuation Experiments

A. Introduction

This chapter will deal with some of the issues raised and claims made in the foregoing. Specifically, assumptions were made about the shrinkage of the current channel due to the influx of ancillary hydrogen and due to the time-evolution of the discharge. Furth, Rutherford, and Selburg's theoretical results on the stabilization of high m-number tearing modes with the level of magnetic shear were summarized. The sort of gas puff used to study particle confinement (Fig. 9) may be used to verify the coincidence of stabilization and destabilization of magnetic fluctuation modes with the presence and absence of gas feed and additionally, in the latter case, with the time-evolution of the discharge. As promised, the degradation in particle confinement seen near the Murakami-limit density will be shown to coincide with destabilization of an $m = 2$ fluctuation mode with a growth rate an order of magnitude longer than the classical tearing-mode growth rate. Finally, the analysis methods outlined in Chapter III afford an opportunity to examine the structure of the fluctuations.

B. Fluctuations during the density rise

A series of discharges was run with gas pulses giving density traces qualitatively similar to that of Fig. 9 and differing quantitatively only in that the peak particle density achieved by the puff was 9.0×10^{12} cm^{-3} rather than 6.7×10^{12} cm^{-3} (other

discharge parameters are summarized in the caption to Fig. 34). The fluctuation data were recorded in a 1.024 msec interval beginning at 4.15 msec into the shot, that is, at the foot of the density rise segment. Typical radial and poloidal fluctuation ($\dot{B}$) signals recorded from coils in a single probe inserted 2 cm into the discharge are shown in Fig. 34. The striking features of these signals are the near monochromaticity of the poloidal signal, the appearance of higher-frequency components in the radial signal, and the exponential growth and saturation of the dominant poloidal mode. Figs. 35 and 36 quantify the first two observations by showing the amplitude of the auto-power spectral density (apsd), defined in Chapter III, of the radial and poloidal ($\dot{B}$) signals. The principal differences are to be found in the dominant 17 kHz peak for which the poloidal apsd amplitude exceeds the radial apsd amplitude (1.28 and 0.42 Gauss^2/μsec, respectively) and in the higher frequency range for which the radial apsd amplitudes are generally larger than their poloidal counterparts (e.g., evaluated at the peak near 52 kHz the radial apsd amplitude is 0.86 Gauss^2/μsec while the poloidal apsd amplitude is 0.53 Gauss^2/μsec). It is characteristic of all the fluctuation data analyzed in this study that the radial spectra display more prominent high-frequency activity than do the corresponding poloidal spectra. It is characteristic only of the density rise of a gas puff that a single low-frequency mode has been seen to dominate the radial fluctuation spectra. The reader is reminded that the Furth, Rutherford, and Selburg[39] theory states that in a low limiter-q discharge like those considered herein

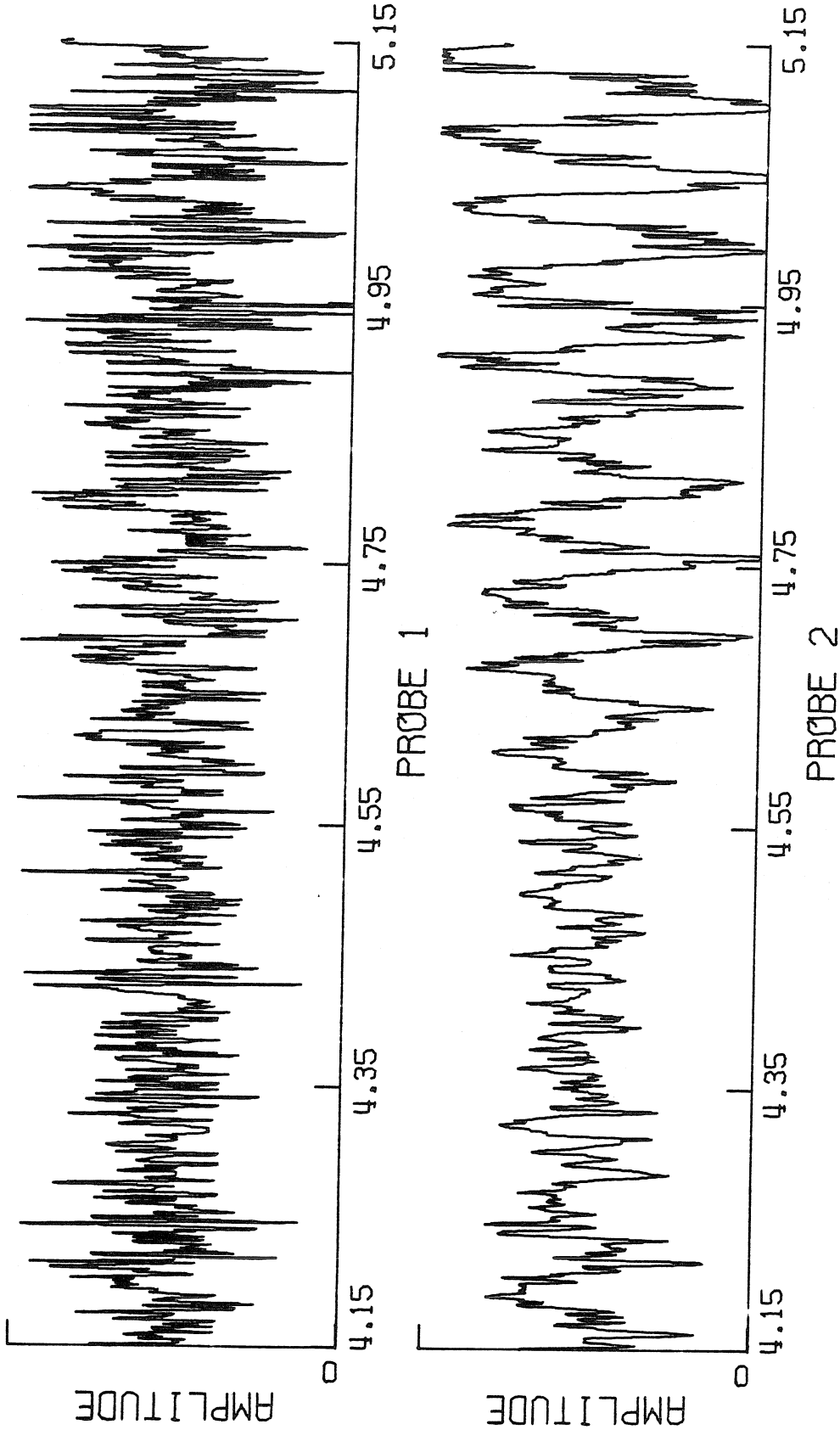

Figure 34. Radial (above) and poloidal (below) fluctuation signals. Discharge parameters: B_ϕ = 4.1 kG, OHFB = 1 kV, OHSB = 360v, VFFB = 130v, VFSB = 55v, filling pressure = 1.35 x 10^{-4} torr, puff reservoir pressure = 970 Torr, 125v pulse lasting 0.44 msec. Full scale = 10 mV both traces.

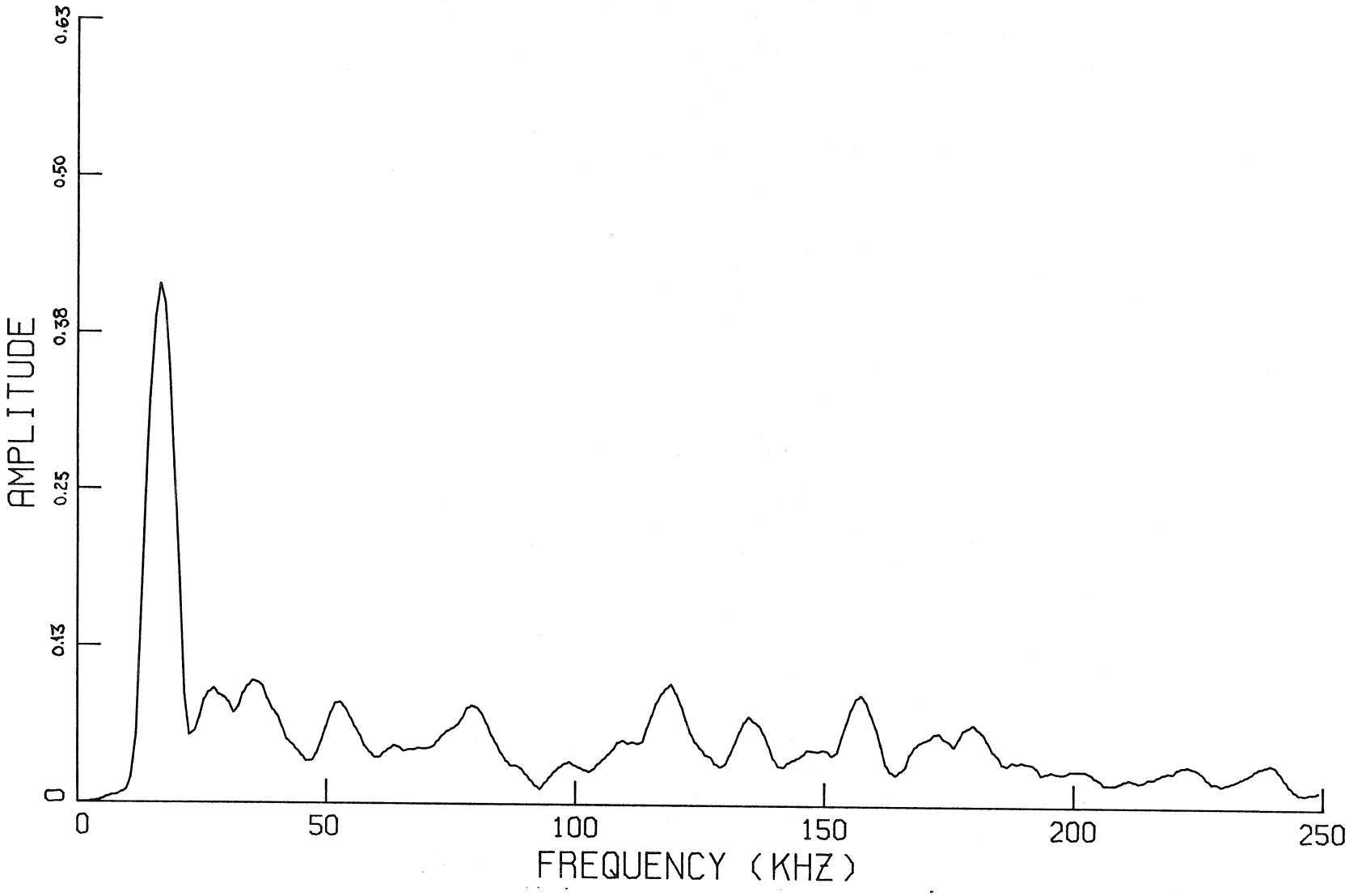

Figure 35. Auto-power spectral density of the radial fluctuations (upper trace) of Figure 34. Note dominant 17 kHz peak, smaller amplitude higher frequency peaks. Amplitude in units of Gauss^2/μsec.

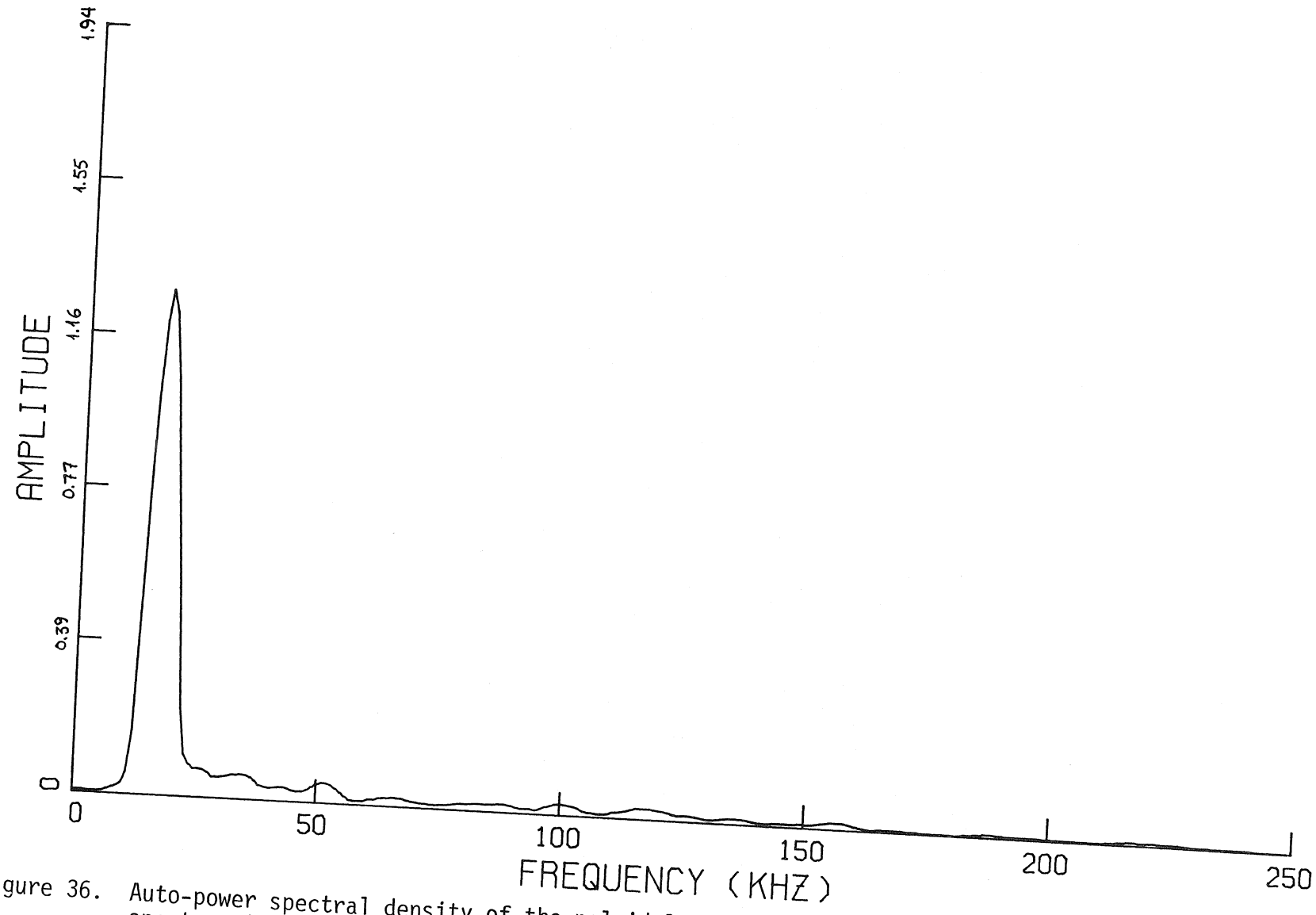

Figure 36. Auto-power spectral density of the poloidal fluctuations (lower trace) of Figure 34. The spectrum is monomodal. Amplitude in units of Gauss^2/μsec.

(q(a)=3.8) high magnetic shear stabilizes all but the m=2 tearing mode. The determination of the fluctuation mode numbers from the modal frequencies (assuming solid-body rotation) and from the phase of the cross-power spectral-density (cpsd) function is deferred until the next section in which the fluctuation spectra will show many prominent modes. The mode corresponding to the dominant peak of Figs. 35 and 36 will then be identified as having poloidal number m=2.

The growth time of the dominant mode of poloidal signals similar to those of Fig. 34 may be determined by a linear least-squares fit to the natural logarithm of the absolute value of the extrema of the Gaussian-averaged signal (Gaussian averaging in the time domain is equivalent to low-pass filtering in the frequency domain; a half-width of N=3 was used as in Figs. 10 and 11). Growth times determined in this fashion are typically $\tau_g \hat{=} 0.4$ msec. The theoretical growth rate of the tearing mode is given by equation (5.24). Neglecting factors of order unity depending on the magnetic shear length (q/q') and the jump in the radial derivative of the radial magnetic field across the resistive boundary layer (Δ') this rate is

$$\tau_{tm} \sim \tau_s^{3/5} \tau_A^{2/5}$$

where the resistive skin time is defined in equation (5.23) and repeated here for convenience

$$\tau_s = a^2\mu_o/\eta$$

and the Alfvén, or hydromagnetic, time is

$$\tau_A = a/v_A = a\sqrt{\mu_o\rho_o}/B_\phi$$

where the characteristic dimension of the plasma a is taken to be the minor radius, ρ_o is the mass density, and the plasma resistivity η was defined in connection with equation (2.7). For a particular discharge giving $\tau_g = 0.38$ the average particle density during the period of exponential growth was determined from microwave interferometer measurements to be 8.55×10^{12} cm^{-3} (4 3/4 fringes). Assuming $Z_{eff} = 1.5$ and taking $T_e = 100$ eV and $B_\phi = 4.1$ kG one has $\eta = 7.1 \times 10^{-5}$ ohm-cm, which is extraordinarily close to the resistivity of stainless steel, and $\tau_s = 40$ msec, $\tau_A = 4.9 \times 10^{-5}$ msec, hence $\tau_{tm} \sim 0.2$ msec. Thus, this low-frequency fluctuation mode grows on the time-scale expected from tearing-mode theory; this is roughly four orders of magnitude slower than the hydromagnetic (kink-mode) time.

The magnetic Reynolds number for the above is $S = \tau_s/\tau_A = 8.1 \times 10^5$. In the full calculation of tearing-mode growth rates by Furth, Killeen, and Rosenbluth[38] the full set of MHD equations is solved in the limit $S \to \infty$ to obtain equation (5.22).

Figures 37 and 38 show respectively the amplitude and phase of the cross-power spectral density (cpsd) of the same-probe radial

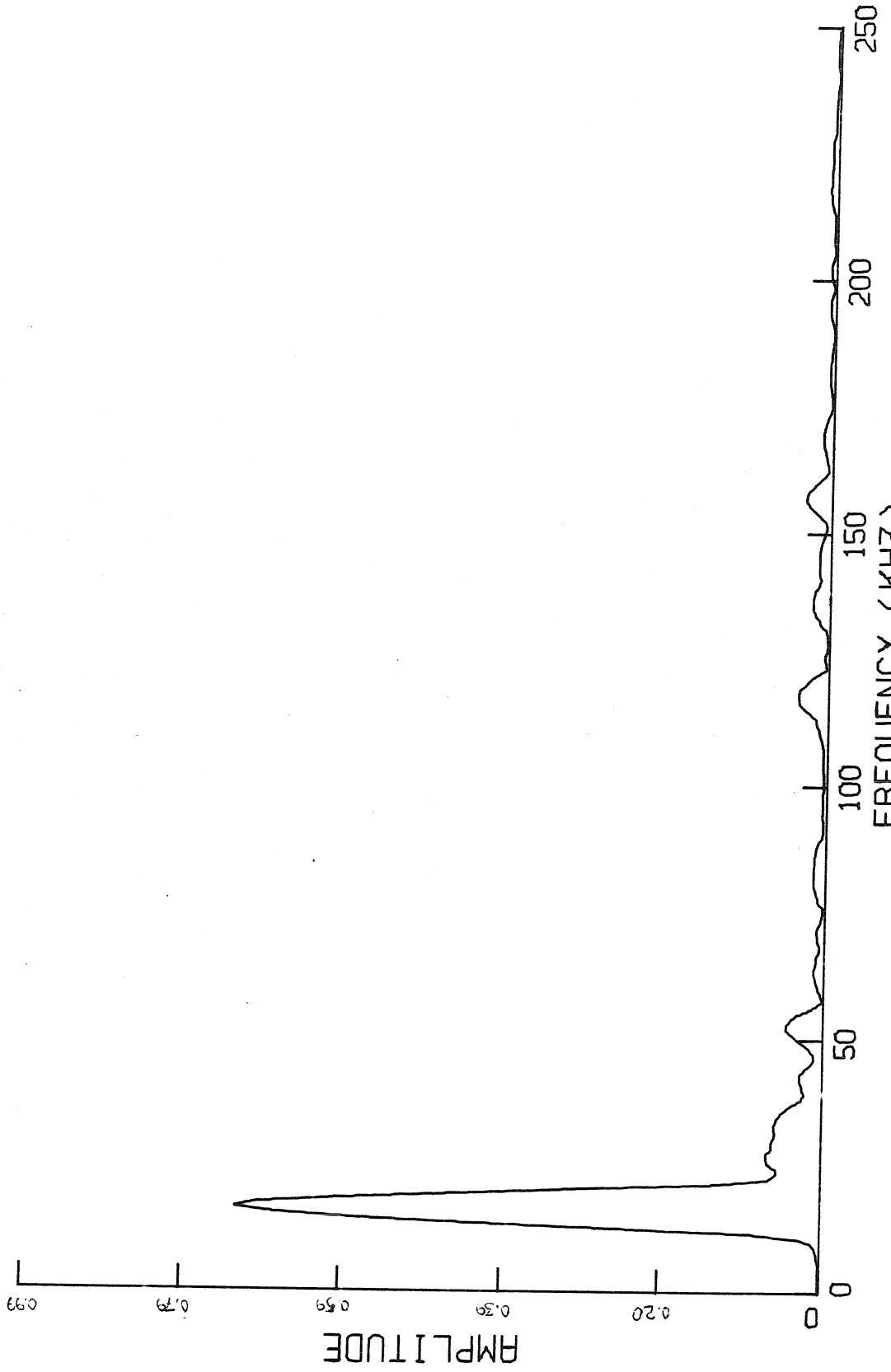

Figure 37. Amplitude of cross-power spectral density for the radial and poloidal signals of Figure 34. Amplitude in units of Gauss^2/μsec.

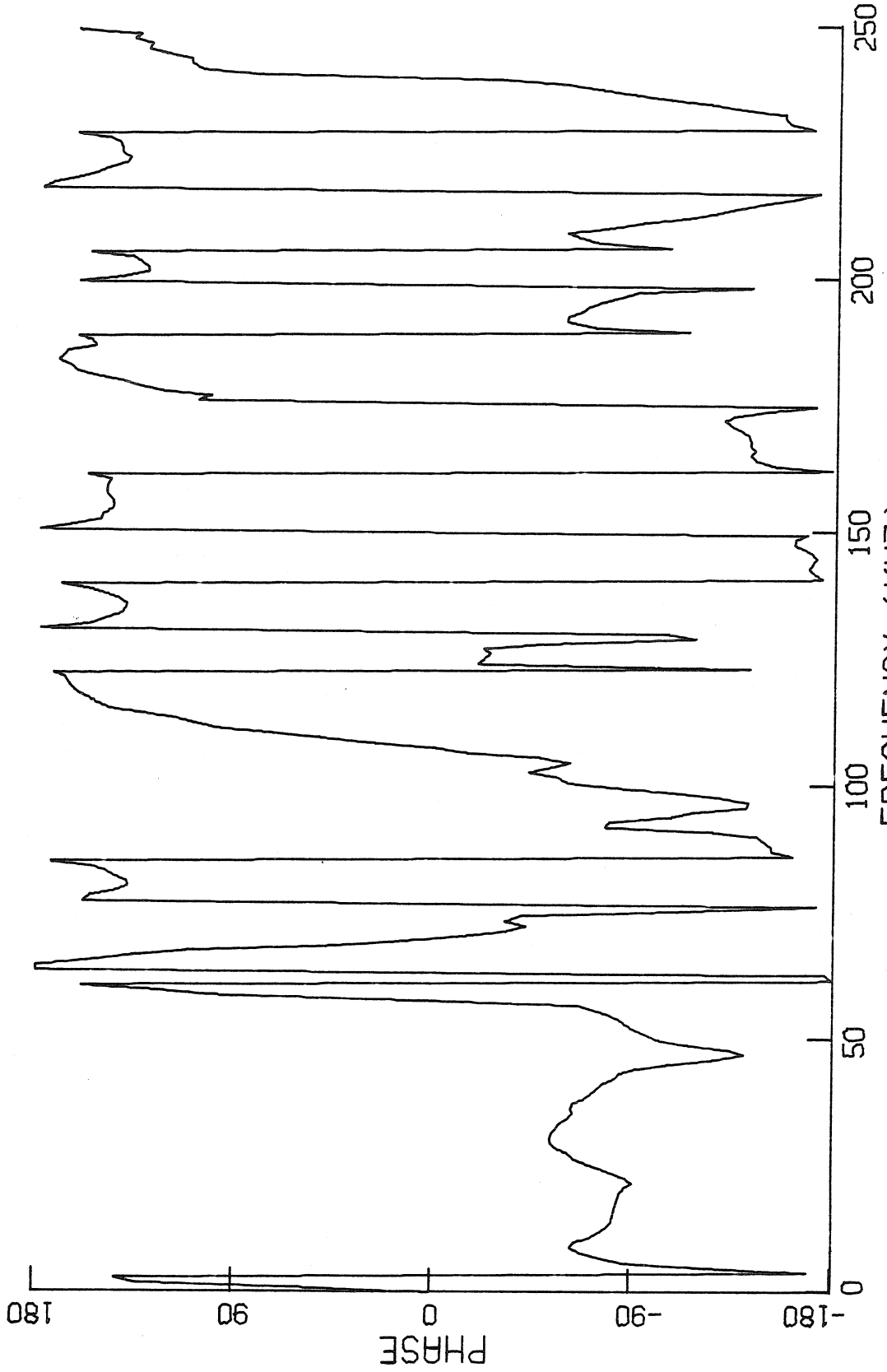

Figure 38. Phase of cross-power spectral density for the radial and poloidal signals of Figure 34.

and poloidal signals of Fig. 34. The radial fluctuations are seen to lead the poloidal fluctuations by nearly 90° over the frequency range of significant model structure, i.e., the range of appreciable cpsd amplitude. This phase shift is consistent with that deduced from $\nabla\cdot\underset{\sim}{B}=0$ and $B_r \sim \sin m\theta$ and $B_\theta \sim \cos m\theta$ in Chapter III.

Figure 39 shows the normalized cross-correlation amplitude for poloidal signals originating from coils in probes separated by 4.5 cm in arc length and inserted 2 cm into the discharge (i.e., the coils lie on a circle of radius 13 cm with center on the magnetic axis (Fig. 40)) from which Figs. 34-39 are derived. The large peak value ($\sim$0.8) suggests strong coherence of the poloidal signals. Fig. 41 shows the normalized cross-correlation amplitude for the same-probe radial and poloidal signals of Fig. 34. The peak value ($\sim$0.4) is smaller than that for widely separated poloidal signals. This smaller value is simply a consequence of correlating two signals with dissimilar spectra as may be seen from direct substitution, as in equation (3.15), of $x(t) = \sum_{m,n} f_{mn}(r)\cos(\omega_m t - m\theta - n\phi)$ and $y(t) = \sum_{m,n} g_{m,n}(r)\sin$

$(\omega_m t - m(\theta+\theta_o) - n\phi)$ where $f_{mn} \neq g_{mn}$ for some m and n.

The root-mean-square poloidal magnetic fluctuation field measures, typically, 2 to 8 (2.6 for lower trace, Fig. 34) Gauss over the 1.024 msec sampling time. The wide spread in values comes from the randomness of the onset of exponential growth of the dominant fluctuation mode within the sampling interval. The root-mean-square radial fluctuation field typically measures 0.5 to 1.2 (0.7 for upper

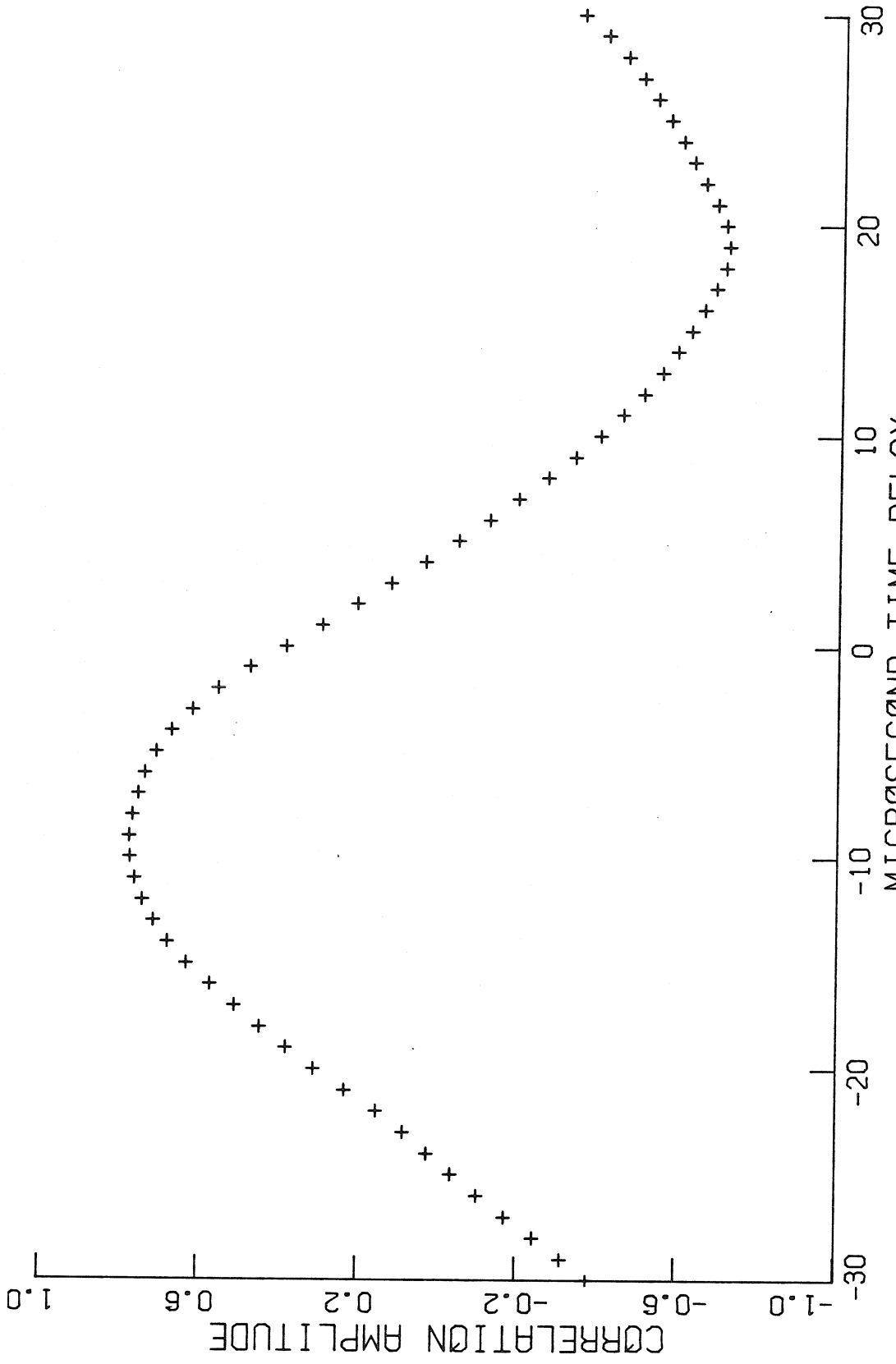

Figure 39. Normalized cross-correlation amplitude of signals from two poloidal coils 4.5 cm apart in arc length and inserted 2 cm into the plasma. One signal was the lower trace of Figure 34.

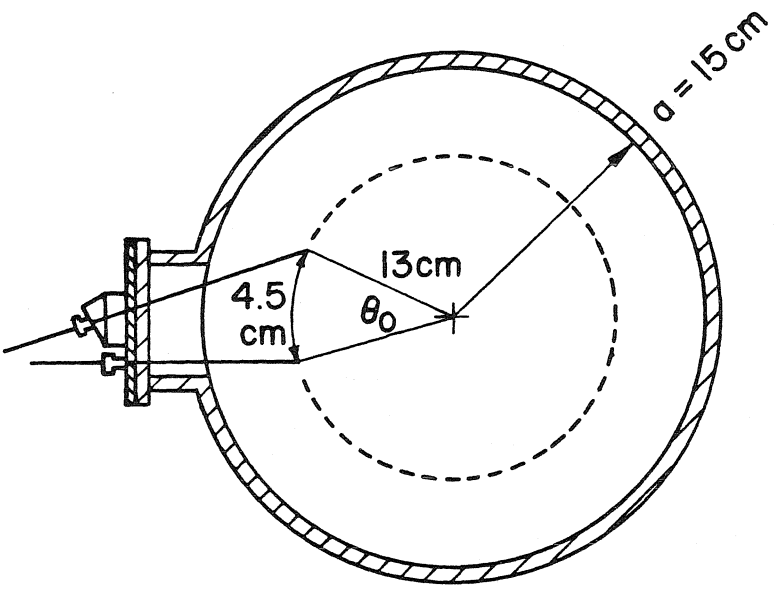

Fig. 40 Orientation of probes used to obtain θ-θ normalized cross-correlation amplitude of Fig. 39. θ_0 = 4.5/13 = 0.35 rad = 19°.

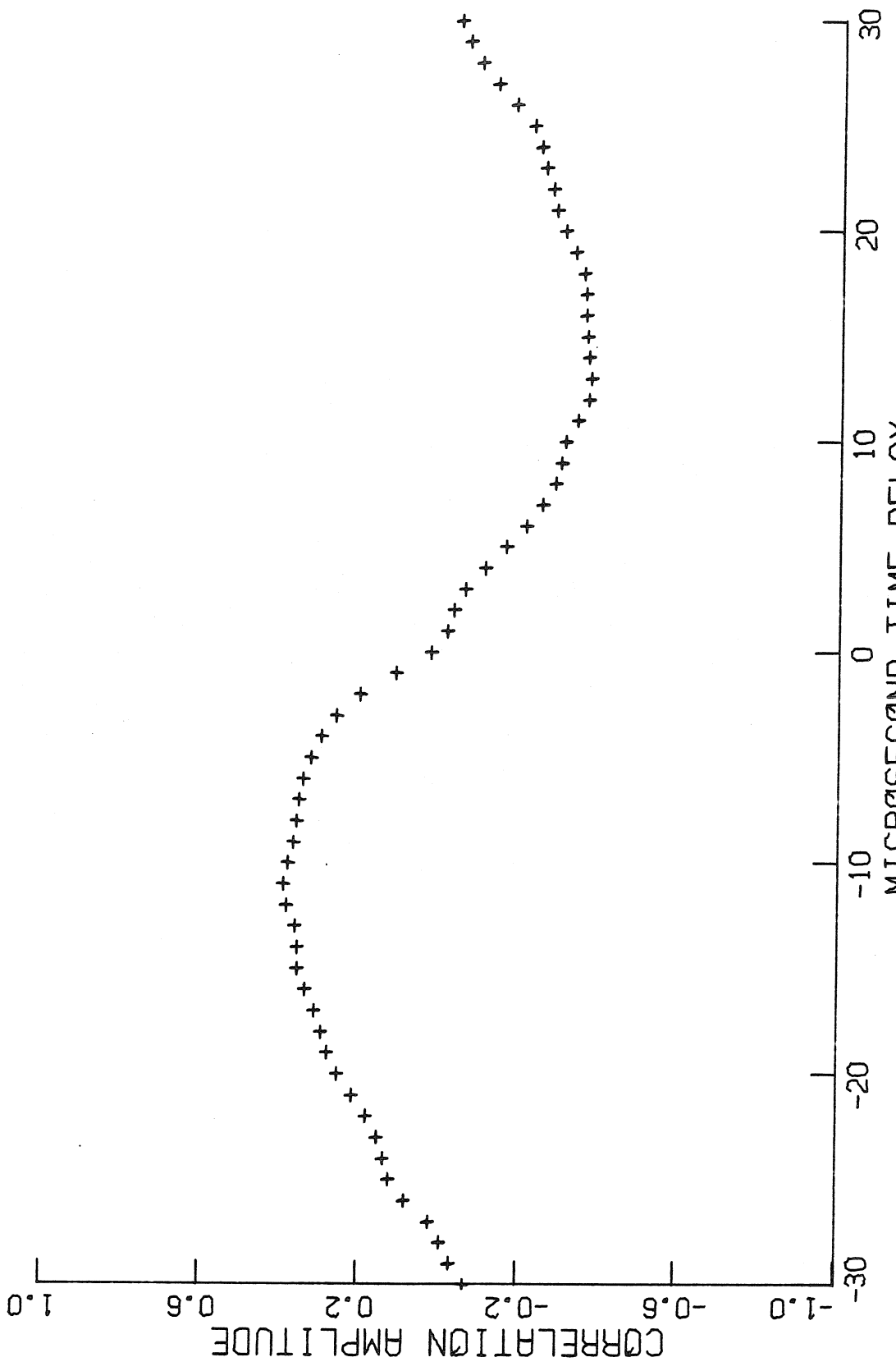

Figure 41. Normalized cross-correlation amplitude of signals of Figure 34.

trace, Fig. 34) Gauss and appears to increase monotonically with increasing penetration (up to 3 cm) of the plasma by the probes. These values may be used to estimate the width of the magnetic island via equation (5.28). This quantity has been evaluated numerically by consideration of a series of temperature profiles $T\propto(1-.9r^2/a^2)^p$ where a is the toroidal minor radius and the parameter p takes the values 1.0, 1.5, 2.0 to successively represent increasing amounts of magnetic shear; the extreme values of p represent rather broad and peaked, respectively, temperature profiles in comparison with Thomson-scattering measurements from other Tokamaks. The current-density profile is then modeled by $J\sim T^{+3/2}$ and knowledge of the total plasma current, hence $B_\theta(r)$ may be computed from $B_\theta(r)\sim \mu_o [\int_o^r dr\, J(r)]/2\pi r$. Knowledge of the toroidal field allows the program to work backwards from the poloidal and toroidal mode numbers m and n to compute the radius $r_s(=q^{-1}(m/n))$ of the mode-rational surface and the magnetic shear at r_s. Now, assuming m=2, n=1, and B_r^p = 1.8 Gauss (i.e., 1.25 Gauss rms) and taking I_p = 24 kA and B_ϕ = 4.1 kG (experimental values for the discharge during which the signals of Fig. 34 were recorded) the respective widths, for p = 1.0, 1.5, and 2.0, are 3.2, 2.0, and 1.7 cm and $\delta B_\theta/B_\theta$ values (for $(\delta B_\theta)_{rms}$ = 8 Gauss) are 5.0, 3.0, and 2.7%. For purposes of comparison, the Tosca Tokamak group[50] have reported an m=2 width of 3.0 cm for $\delta B_\theta/B_\theta$ = 3% just prior to disruption of a non-gas-puffed discharge. These measurements were made with probes comparable to those used in this study.

C. Fluctuations early in the density decay

One expects that if the lack of high-frequency (presumably high m-number) magnetic fluctuation activity during the density rise is the result of increased levels of magnetic shear brought about by edge-coding of the plasma by neutral-gas feed, then cessation of this feed might destabilize these modes. That is, the magnetic shear may relax back to smaller levels when the external source of neutrals is gone. The temporal region in which to look for these modes is during the density decay of a short gas puff (Fig. 9).

1. Levels of fluctuation components

Unless otherwise stated the discharges considered in this section are identical to those of the previous section: the density traces are qualitatively similar to that of Fig. 9 differing quantitatively only in that the peak particle density attained each shot was approximately 9.0×10^{12} cm^{-3} (5 microwave fringes); other parameters are summarized in the caption to Fig. 42. The fluctuation data were recorded in a 1.024 msec interval beginning at 6.15 msec into the shot, that is, just after the peak puff density. Fluctuation signals from two different probes each inserted 3 cm into the discharge were used in the analysis to follow. To prevent confusion about the placement of the probes the reader is requested to refer to Fig. 40. These two probes were separated by 4.5 cm in arc length, hence the coils lay on a toroidal surface of minor radius 12 cm and the poloidal angle of separation was thus $\theta_o = 4.5/12 = 0.375$ rad $= 21.5^o$. The radial and poloidal signals from the upper probe and the poloidal

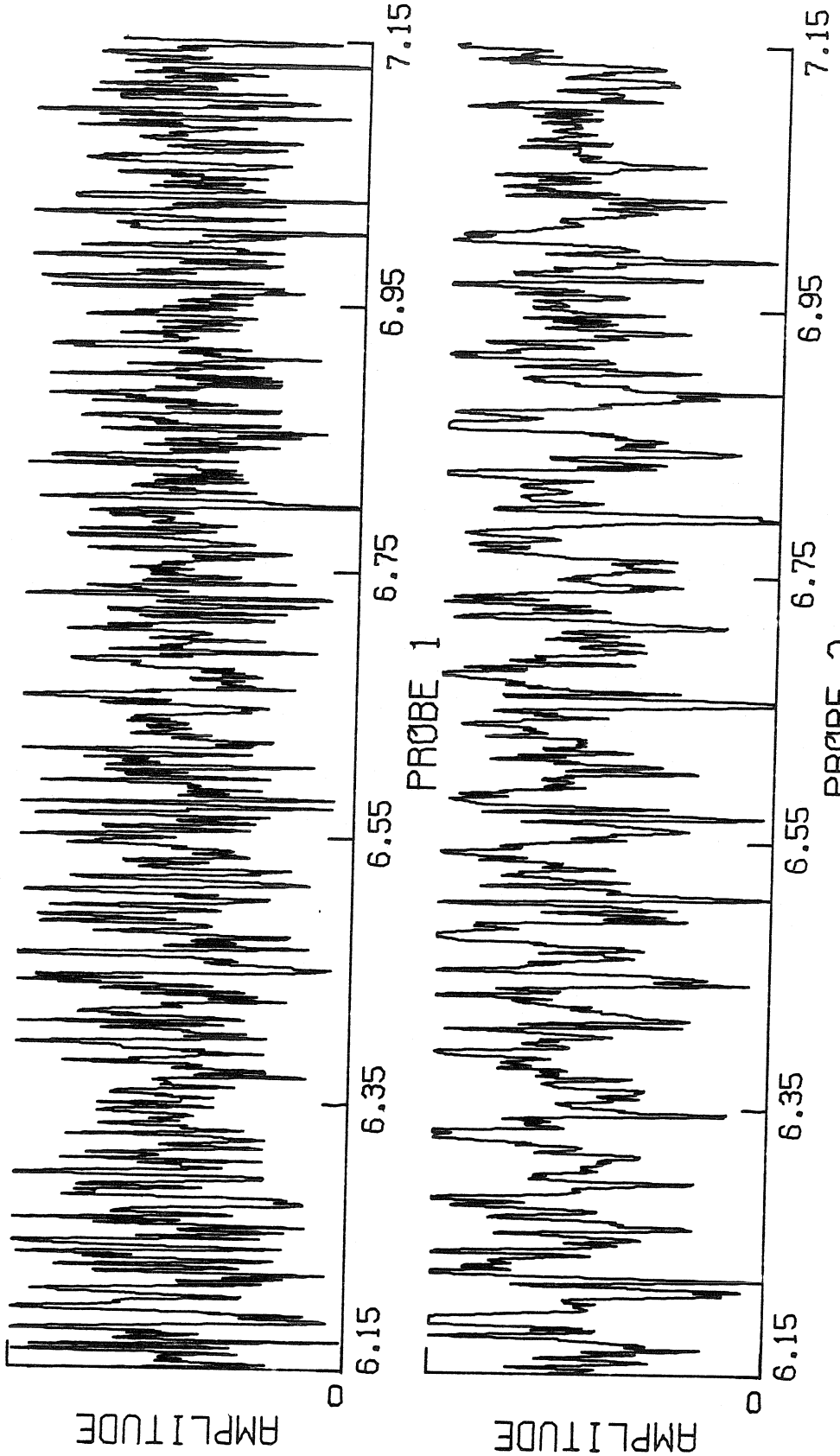

Figure 42. Radial (above) and poloidal (below) fluctuation signals. Discharge parameters: B_ϕ = 4.1 kG, OHFB = 1 kV, OHSB = 360v, VFFB = 130v, VFSB = 55v, filling pressure = 1.35 x 10^{-4} Torr, puff reservoir pressure = 970 Torr, 125v pulse lasting 0.44 msec. Full scale = 20 mV upper trace, 14 mV lower trace.

signal from the lower probe were recorded. Hence, same-probe radial-poloidal correlations come from the upper probe, etc.

Figure 42 shows the fluctuation signals from the radial (upper trace) and poloidal (lower trace) coils in the upper probe. In comparison to the poloidal signal of Fig. 34, the poloidal signal of Fig. 42 shows higher frequency content. Figs. 43 and 44 show the auto-power spectral densities (apsd's) of, respectively, the radial and poloidal signals of Fig. 42. The reader is reminded that these are aspd's of the temporal derivative of the particular magnetic field components, hence the unit of amplitude is $Gauss^2/\mu sec$; the apsd's of the magnetic field components themselves may be obtained by division of the $\dot{B}$ apsd's of Figs. 43 and 44 by ω^2 since the Fourier transform of $\dot{B}$ is ω times the Fourier transform of B (the $\dot{B}$ apsd's and cpsd's are always shown because they are directly deduced from the measurement and any higher-frequency modal structure shows up more clearly than in plots of the B apsd's and cpsd's).

In qualitative comparison to Fig. 35 the radial fluctuation apsd of Fig. 43 shows a lack of domination by the lowest frequency mode, in fact, numerous modes at frequencies less than 200 kHz have comparable amplitudes. The poloidal fluctuation apsd of Fig. 44 is qualitatively similar to that of Fig. 36 in that the lowest frequency mode still dominates the spectrum but clearly Fig. 44 shows the increased presence of higher-frequency activity seen in the lower trace of Fig. 42. Quantitatively, the amplitudes of the lowest-frequency modal (B apsd) activity in the early density decay

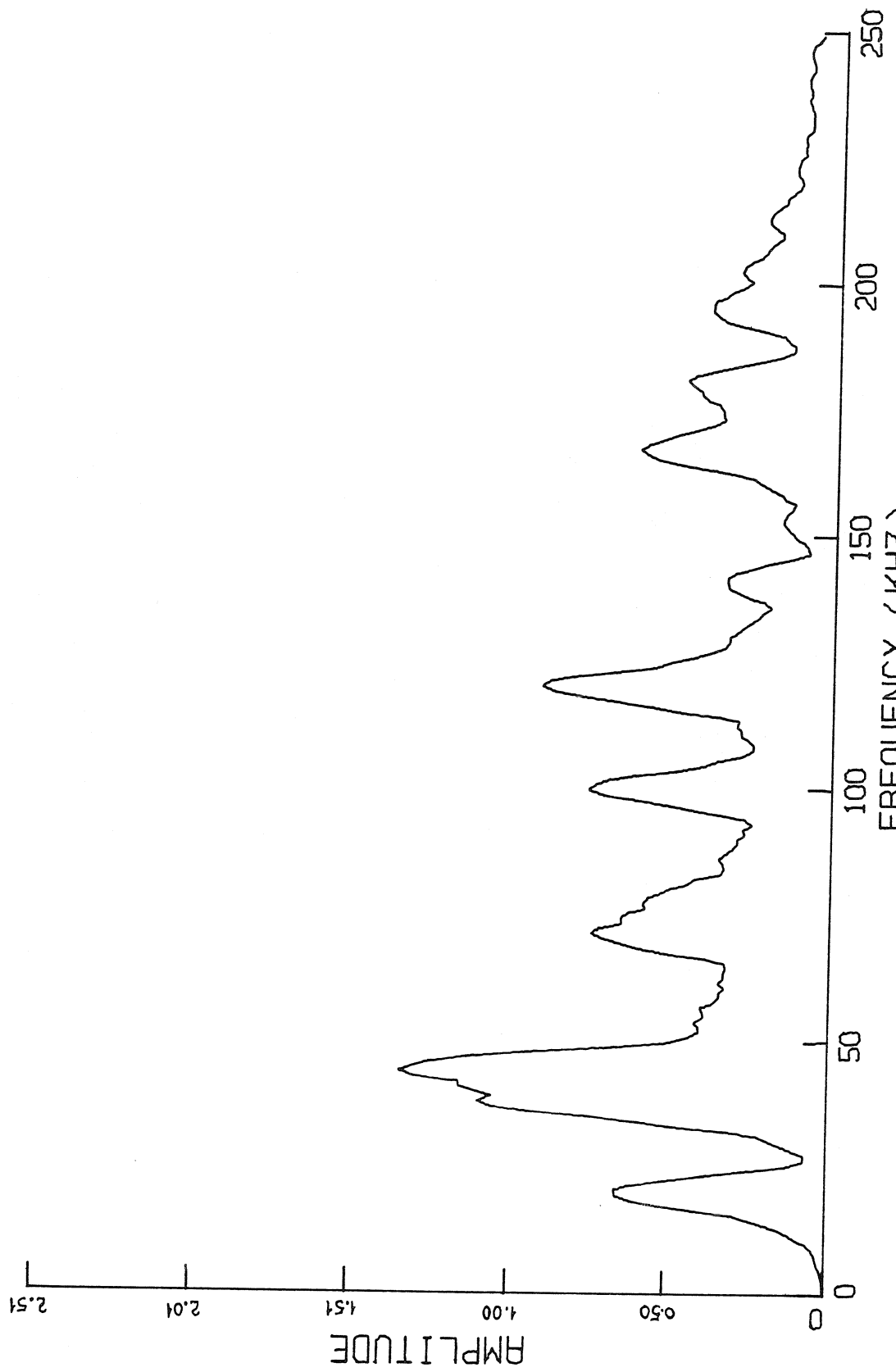

Figure 43. Auto-power spectral density of the radial fluctuations (upper trace) of Figure 42. Numerous peaks at frequencies <200 kHz have comparable amplitudes. Amplitude in units of Gauss^2/μsec.

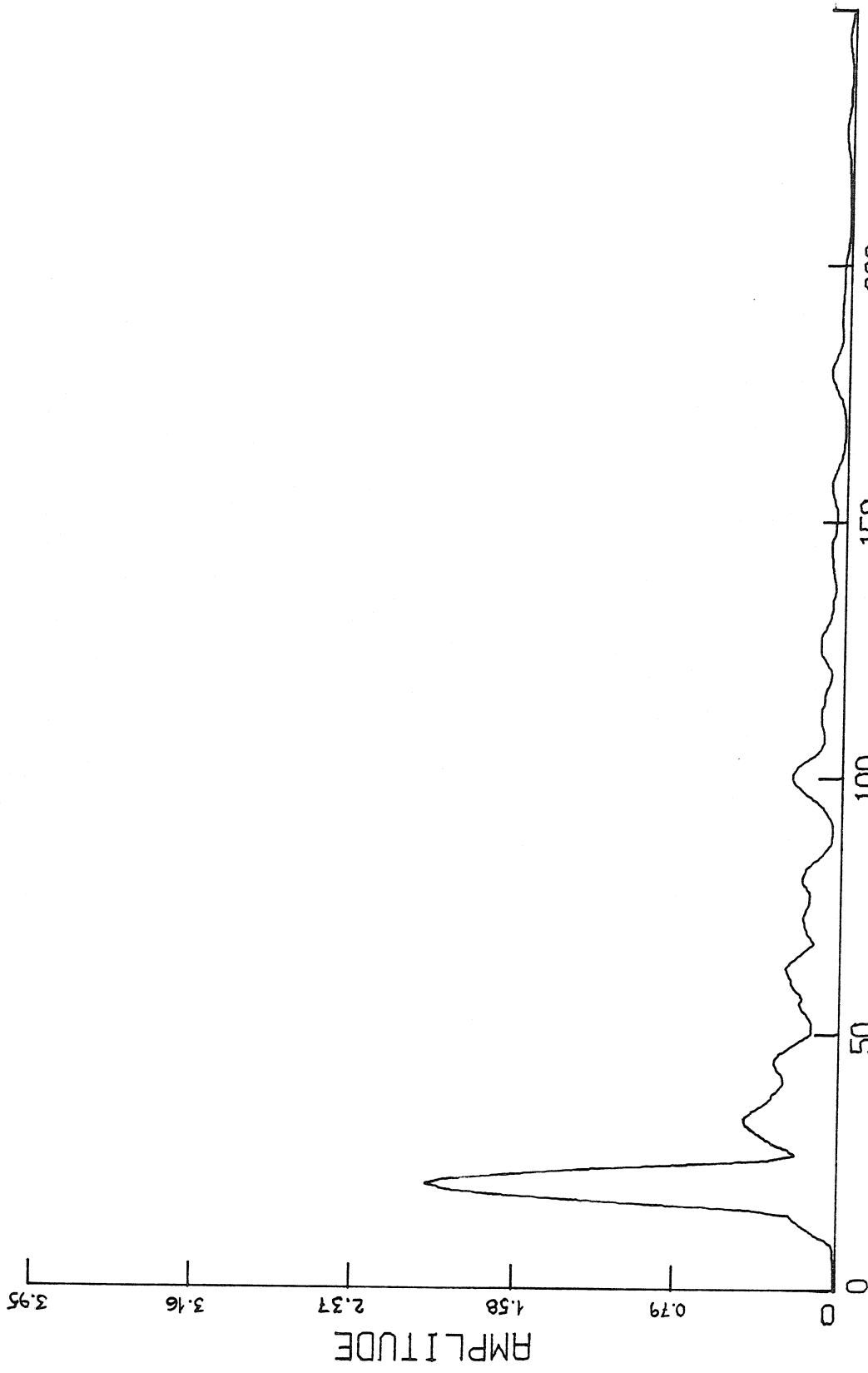

Figure 44. Auto-power spectral density of the poloidal fluctuations (lower trace) of Figure 42. A single mode dominates the spectrum. Amplitude in units of Gauss^2/μsec.

are comparable (poloidal to poloidal and radial to radial) to those in the density rise: the lowest-frequency poloidal mode of Fig. 36 achieves a peak amplitude of 1.28 Gauss^2/μsec at 17 kHz, hence the B apsd is about 1.12 x 10^{-4} Gauss^2-sec; for the corresponding peak of Fig. 44 the peak amplitude is 2.01 Gauss^2/μsec at 21 kHz, hence this B apsd is about 1.15 x 10^{-4} Gauss^2-sec. Since the poloidal spectra of Figs. 36 and 44 are nearly monomodal and the peak B apsd amplitudes are the same one would expect the root-mean-square poloidal B's to be comparable, with the value for Fig. 44 slightly larger because of its high-frequency content; in fact, the density rise B_{rms} of the lower (poloidal) trace in Fig. 34 is 2.6 Gauss while the corresponding early-decay poloidal B_{rms} from Fig. 44 is 2.9 Gauss. The poloidal B_{rms} values from the early decay are quite reproducible from shot to shot, while in the density rise, the poloidal B_{rms} values (and the apsd and cpsd amplitudes) vary depending on when in the sampling window the low-frequency mode is destabilized. A comparison of the peak amplitudes of the lowest-frequency mode of the radial apsd's of Figs. 35 and 43 show similar correspondance: from Fig. 35 the peak apsd is 0.42 Gauss^2 at 17 kHz so that the density-rise B apsd is about 3.6 x 10^{-5} Gauss^2-sec while from Fig. 43 the peak apsd is 0.67 Gauss^2 at 21 kHz, hence the early-decay B apsd is about 3.8 x 10^{-5} Gauss^2-sec. The level of high-frequency activity of Fig. 43 greatly exceeds that of Fig. 35; this shows up in the root-mean-square radial magnetic fields: 0.7 Gauss in the density rise and 1.2 Gauss in the early decay. Inserting probes in the range of 1 to 3 cm into

the discharge shows that the root-mean-square level of poloidal magnetic fluctuations stays at roughly 2.5 Gauss independent of position while the root-mean-square level of radial magnetic fluctuations increases monotonically from about 0.6 Gauss 1 cm in to about 1.25 Gauss 3 cm in.

Figs. 45 and 46 show, respectively, the amplitude and phase of the cross-power spectral density (cpsd) for correlation between the single- (upper-) probe radial and poloidal magnetic fluctuation signals of Fig. 42. Comparison of these figures showsthat the radial fluctuations lead the poloidal fluctuations by about 90° near frequencies with strong modal activity, i.e., high cpsd amplitude. The closeness to 90° varies from shot to shot and occasionally the cpsd phase comes out much flatter, and closer to 90°, than Fig. 46.

2. Apparent poloidal rotation rate and determination of mode numbers

Fig. 47 shows the normalized cross-correlation amplitude derived from two poloidal fluctuation signals coming from coils separated by poloidal angle $\theta_0 = 21.5^{\circ}$ as detailed above. One signal is, of course, the lower trace of Fig. 42 and the other comes from the lower probe (Fig. 40). The peak normalized cross-correlation amplitude occurs at $\tau = 6$ μsec (±1 μsec sampling error). It was shown in the discussion preceding equation (3.16) that, in principle, a magnetic spectrum having origin in the poloidal solid-body rotation at angular frequency ω_0 of a plasma containing an arbitrary number of magnetic islands would display its peak normalized cross-correlation amplitude at a time delay $\tau = \theta_0/\omega_0$ where θ_0 is the poloidal angle of separation of the points at which the spectrum is sampled. Hence, the fluctuations

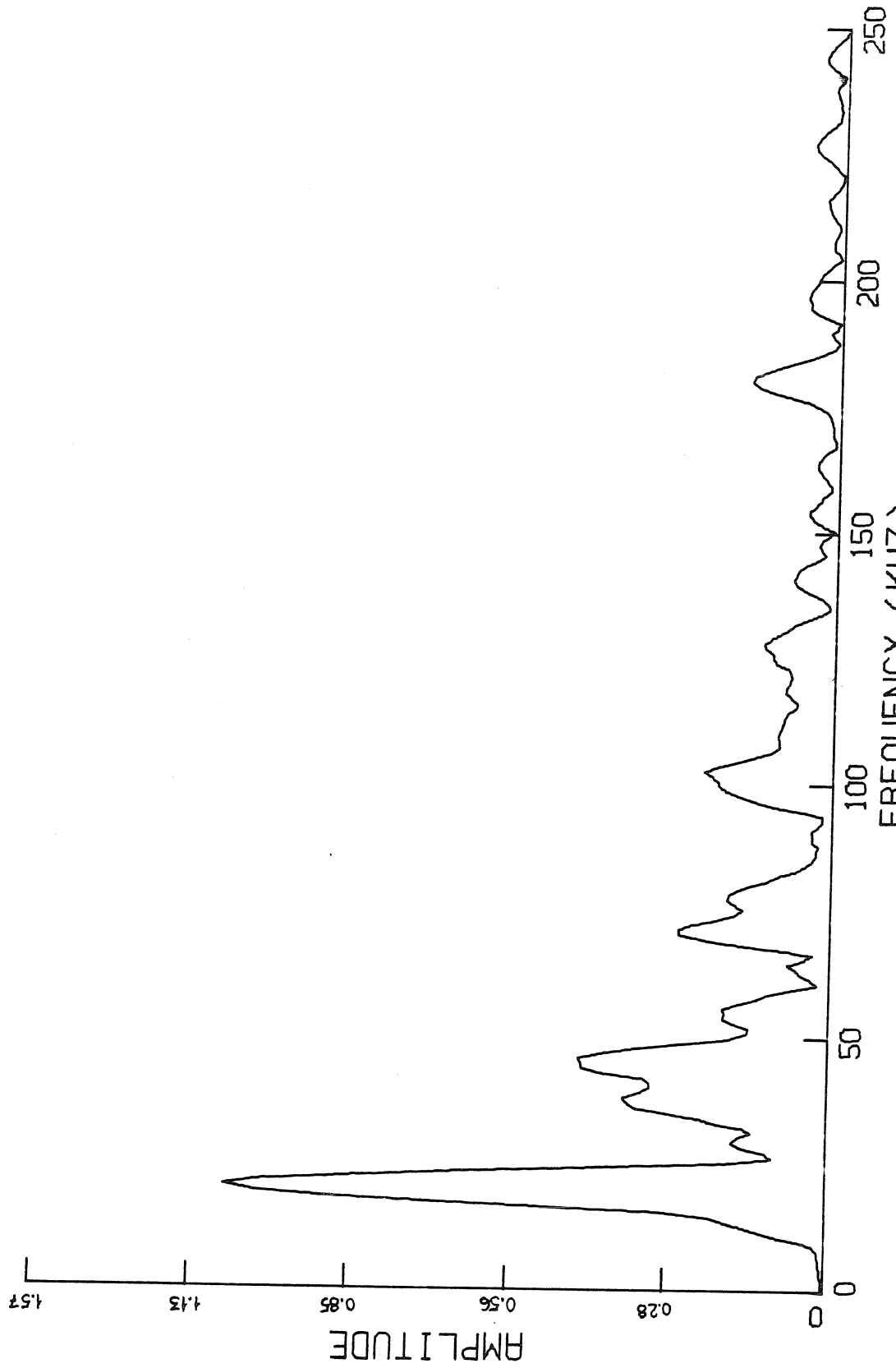

Figure 45. Amplitude of cross-power spectral density for correlation of the two traces of Figure 42. Amplitude in units of Gauss^2/μsec.

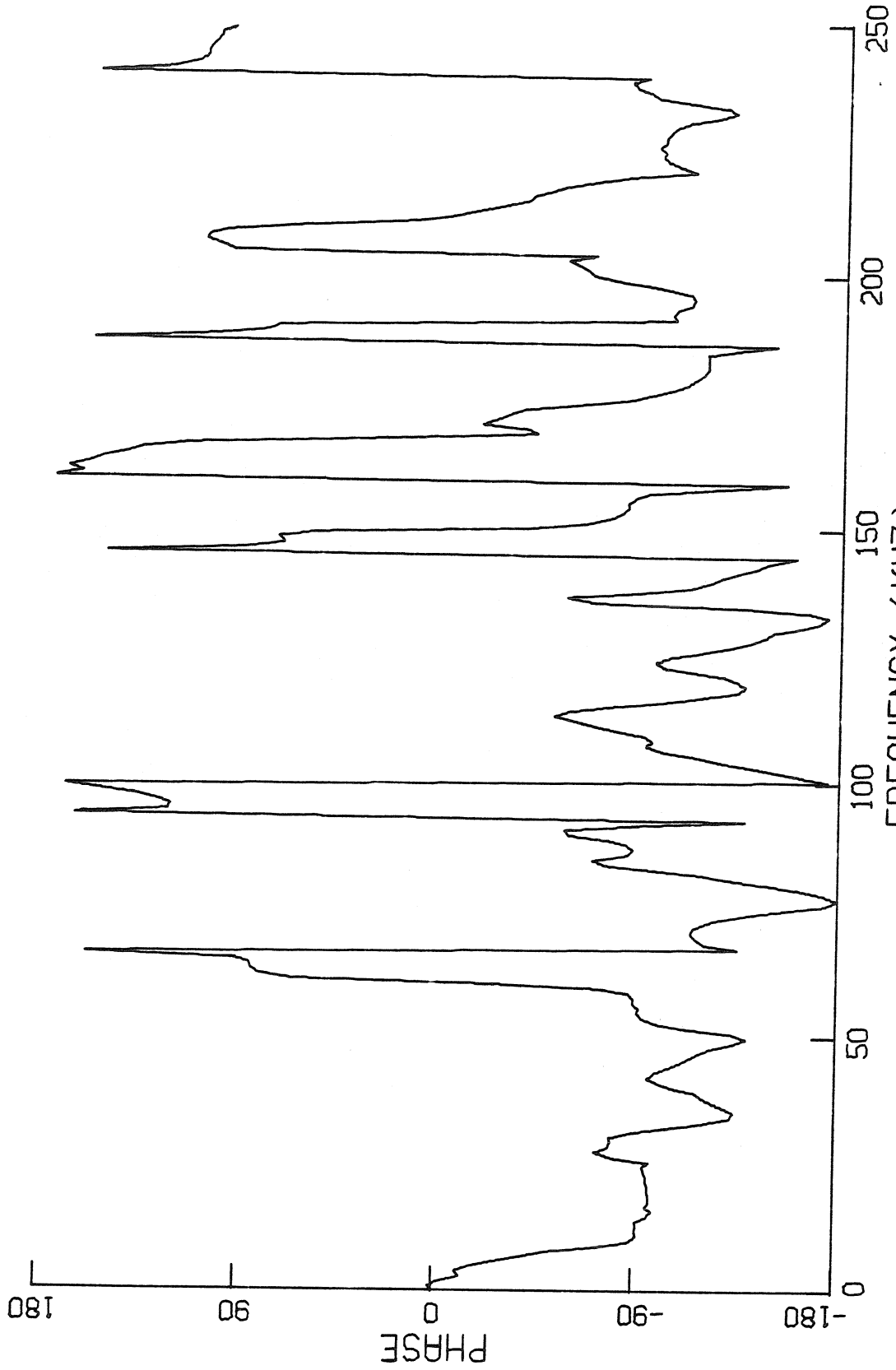

Figure 46. Phase of cross-power spectral density for correlation of the two traces of Figure 42.

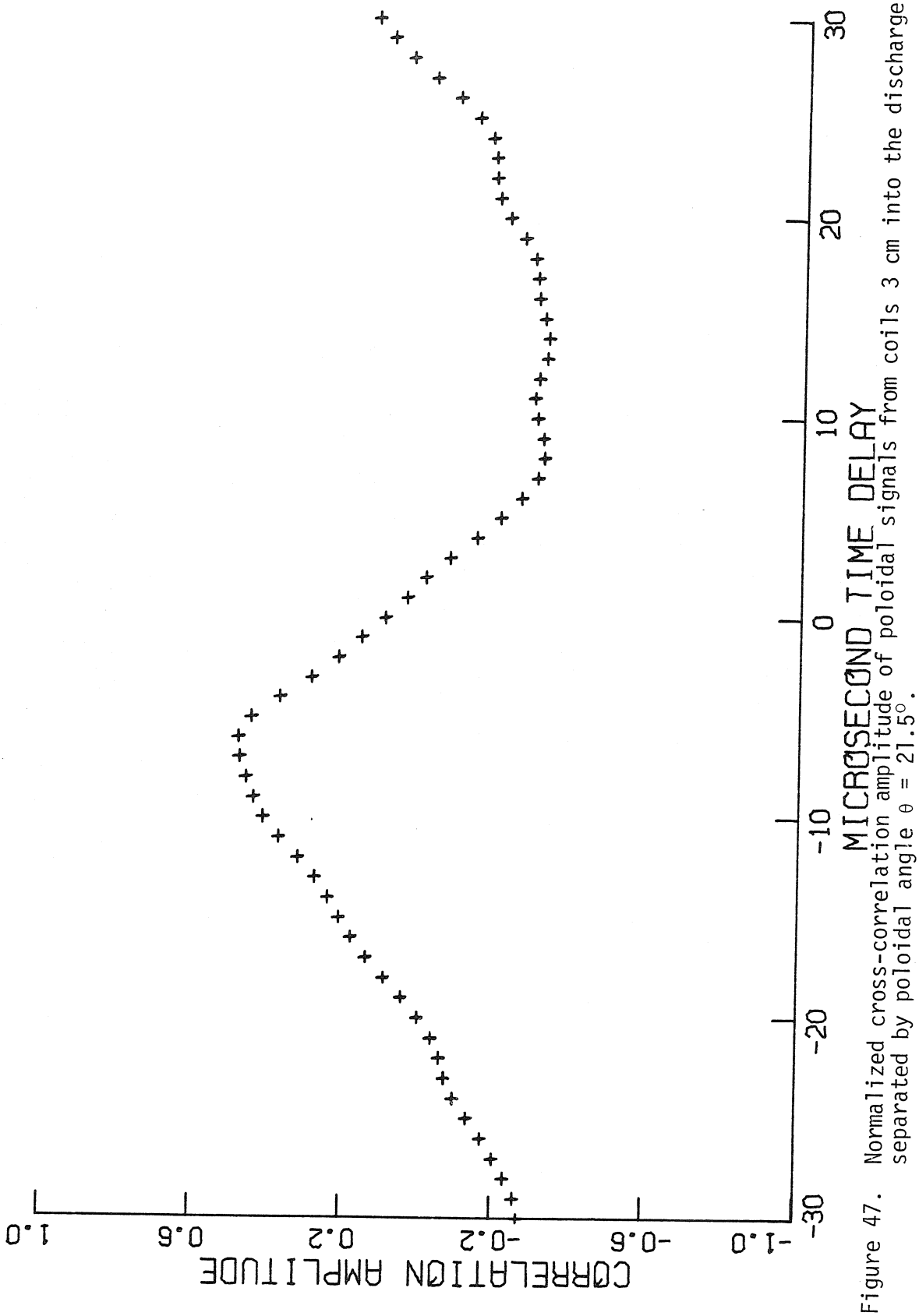

Figure 47. Normalized cross-correlation amplitude of poloidal signals from coils 3 cm into the discharge separated by poloidal angle $\theta = 21.5^{\circ}$.

of the discharge presently under consideration appear to rotate with poloidal angular velocity $\omega_o = \theta_o/\tau = 0.375$ rad/(6±1 μsec) = $(6.3^{+1.2}_{-0.9}) \times 10^4$ rad/sec. The expected solid-body frequency of a magnetic structure having m-fold poloidal symmetry is $m\omega_o/2\pi = m(10^{+2.0}_{-1.4})$kHz; that is, these are the frequencies one would expect to have appreciable amplitude in the cross-power spectral density (cpsd) obtained from the poloidal traces generating Fig. 47.

Figs. 48 and 49 show, respectively, the cpsd amplitude and phase for the two poloidal signals that gave Fig. 47. Figs. 50 and 51 show, respectively, the cpsd amplitude and phase from correlation of the radial signal from the upper probe and the poloidal signal from the lower probe in the geometry used throughout this section. The set of frequencies corresponding to the local peak (poloidal-poloidal) cpsd amplitudes of Fig. 48 is summarized in the first column of Table III. The second column shows that these frequencies are nearly integer multiples of 11 kHz. Columns five and six repeat this for the set of frequencies corresponding to the local peak (radial-poloidal) cpsd amplitudes of Fig. 50. This same information is shown graphically in Fig. 52: the modal peak frequencies f_m are plotted against the integer closest to $f_m/11$ kHz. The frequencies barely budge from a straight line through the origin. This behavior is consistent with the idea of solid-body rotation; it appears that poloidal modes m=2, 3, 4, 5, 6, 7, 9, and 10 are present (neither Fig. 48 nor Fig. 50 has significant amplitude above the background

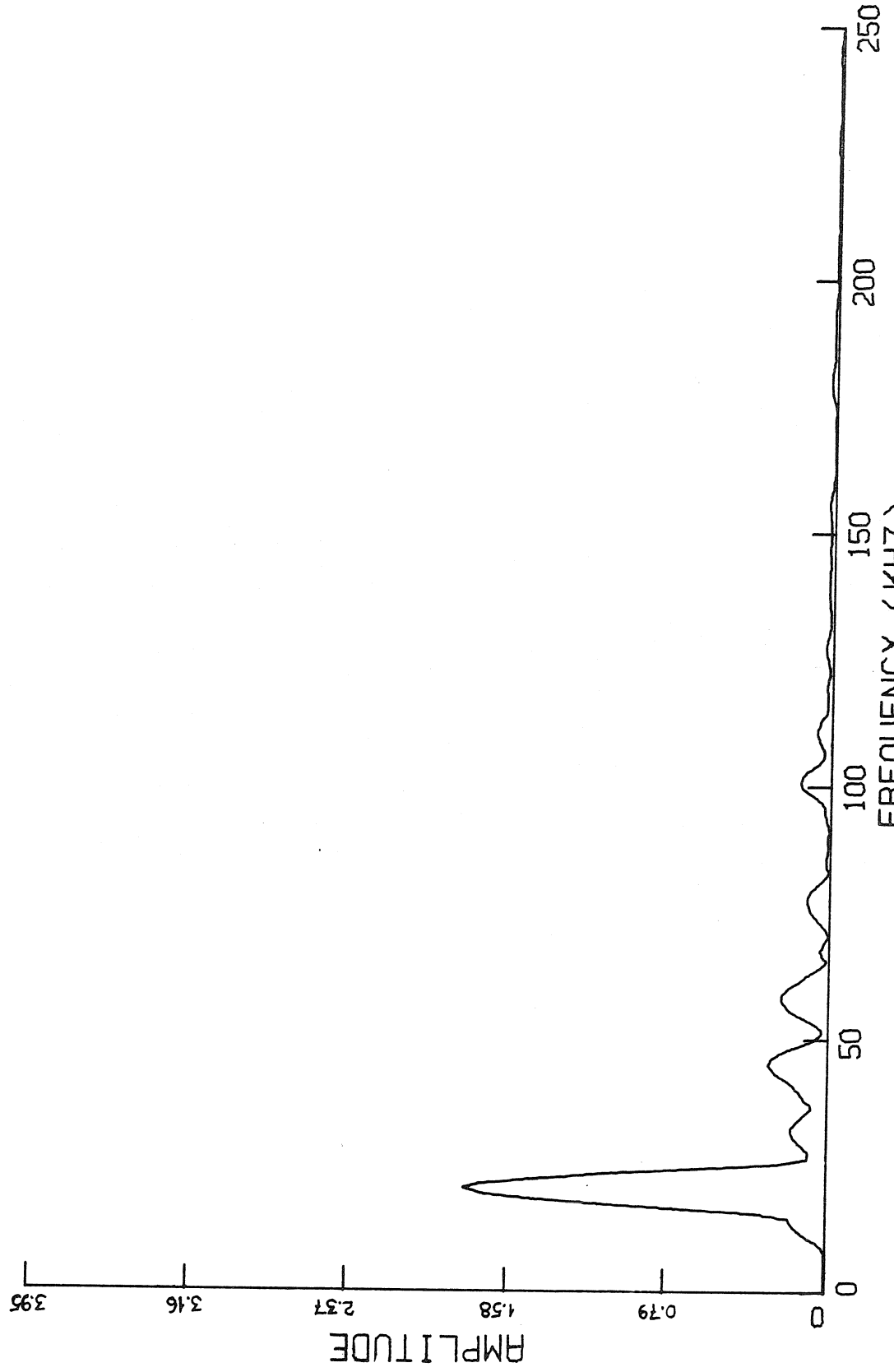

Figure 48. Amplitude of the cross-power spectral density of the signals used to generate Figure 47. Amplitude in units of Gauss^2/μsec.

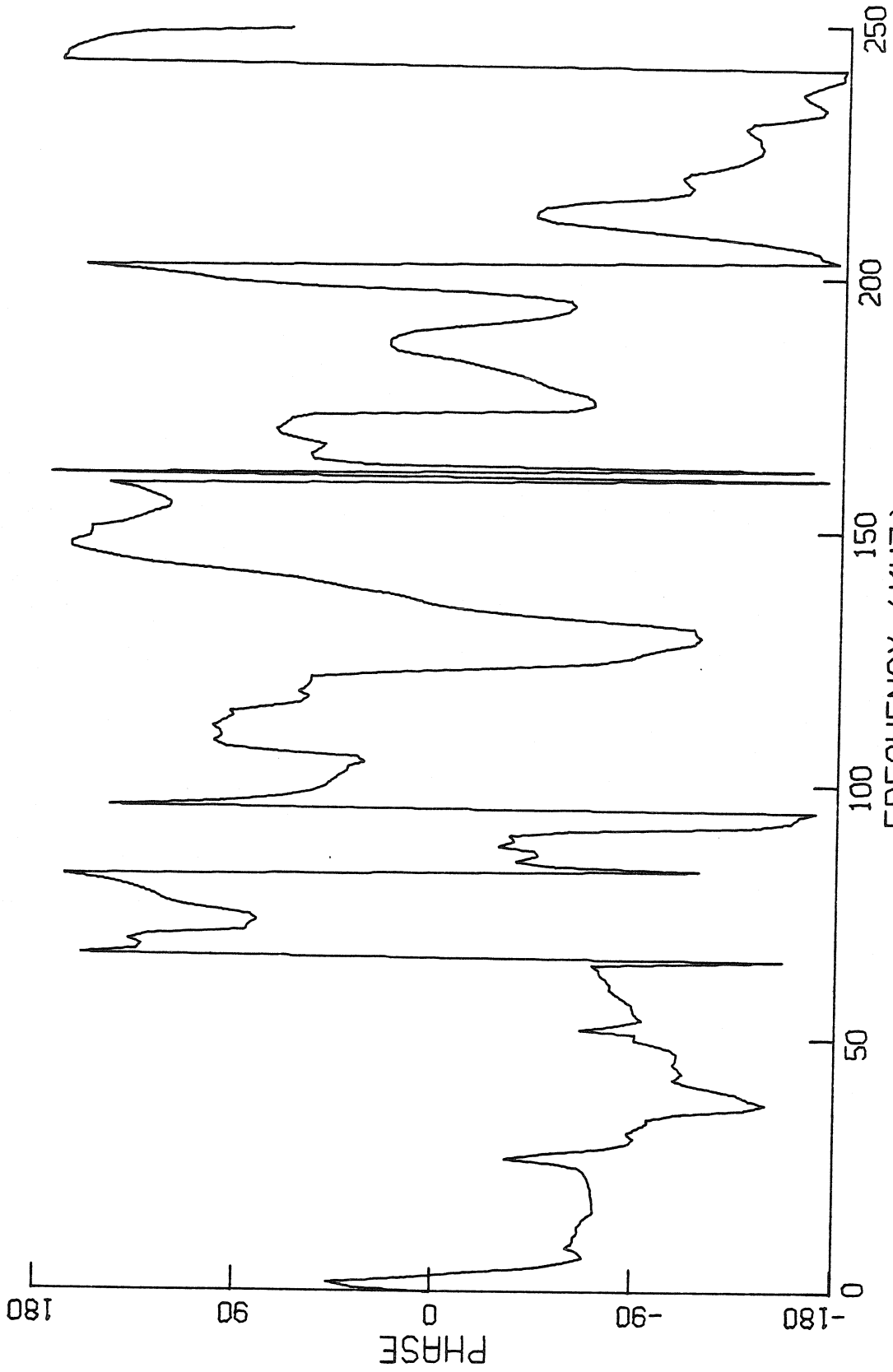

Figure 49. Phase of cross-power spectral density corresponding to Figure 48.

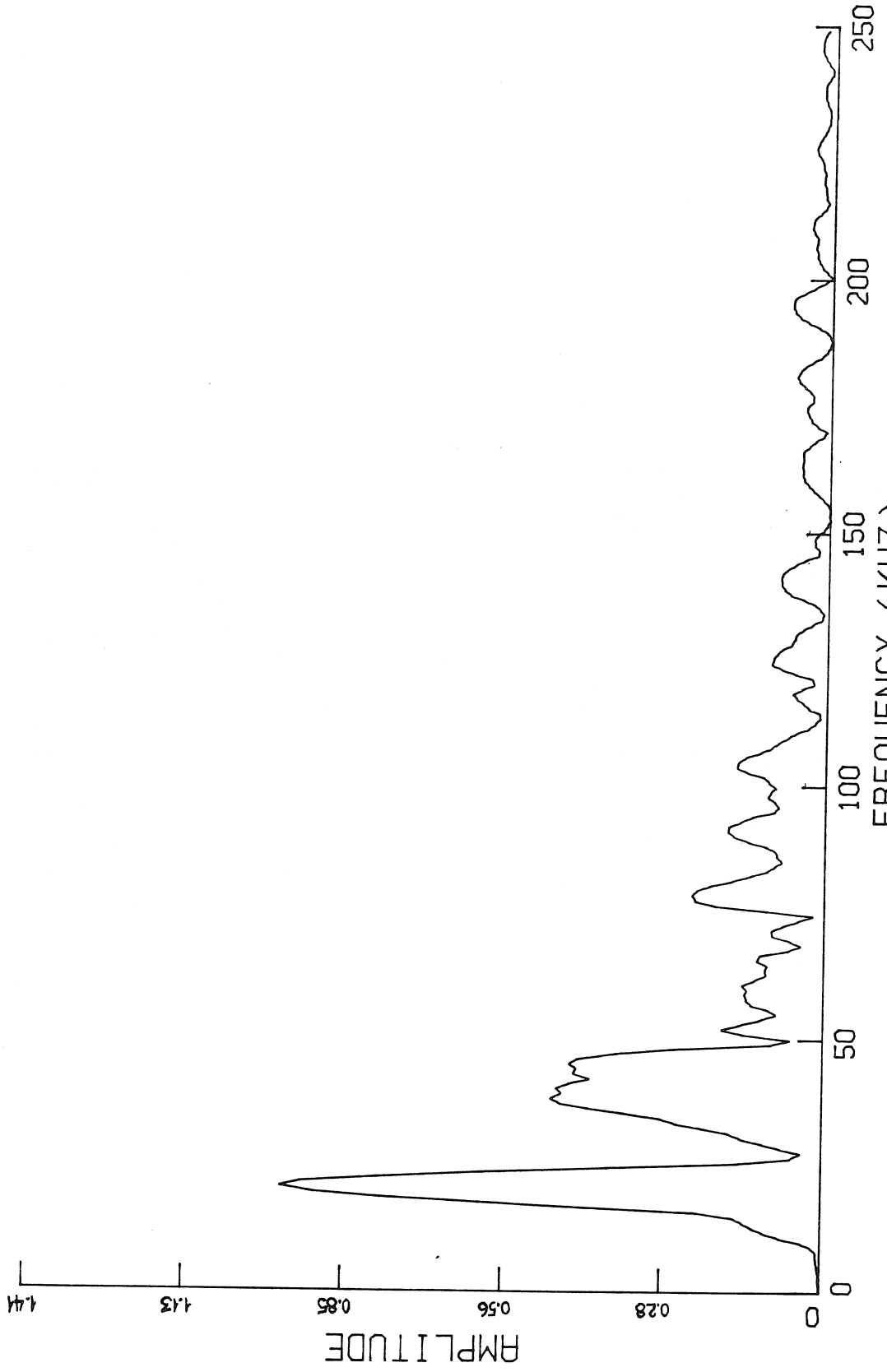

Figure 50. Amplitude of cross-power spectral density of radial and poloidal signals from coils 3 cm into the discharge and separated by poloidal angle $\theta = 21.5^{o}$. Amplitude in $Gauss^2/\mu sec$.

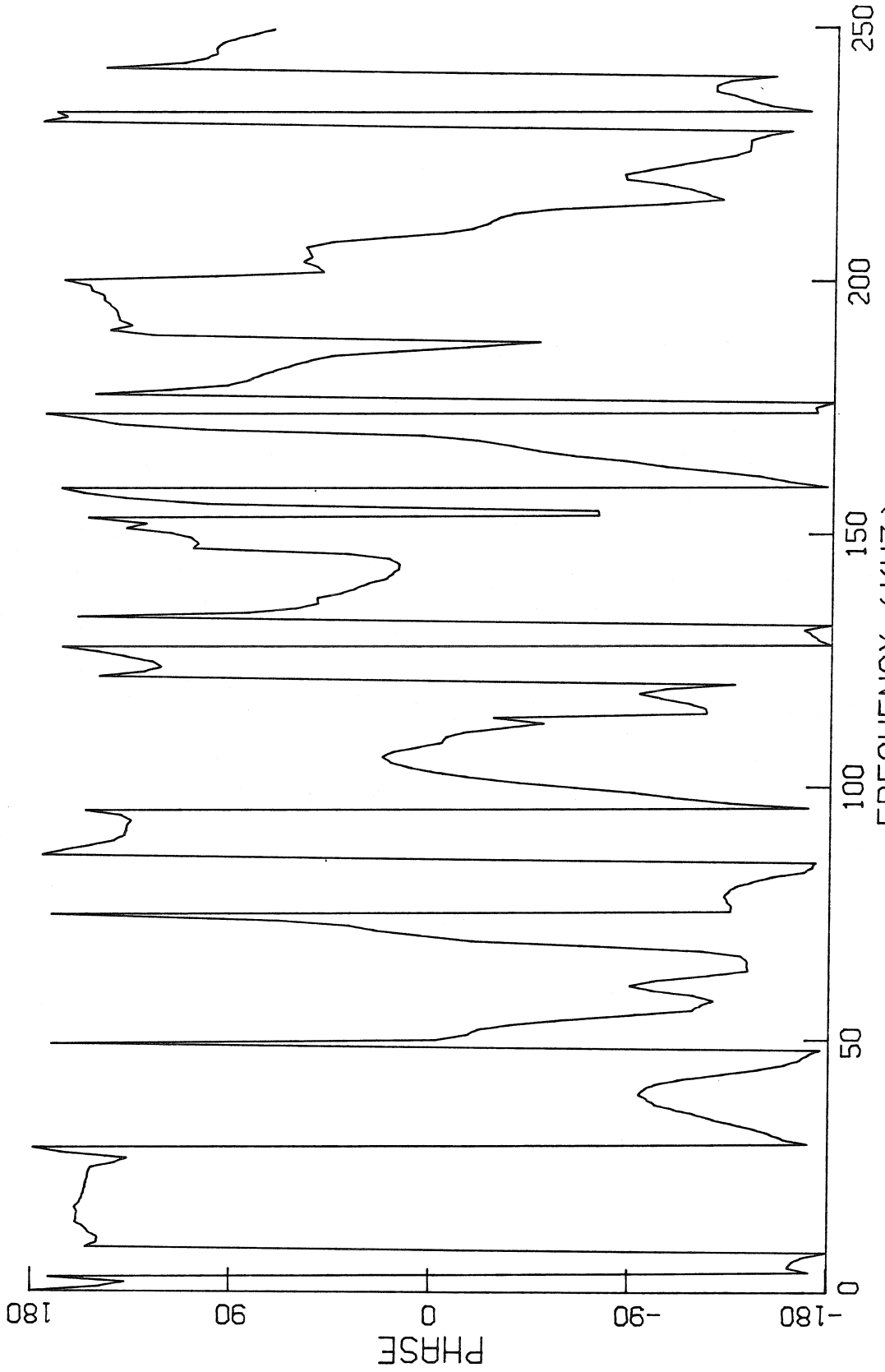

Figure 51. Phase of the cross-power spectral density corresponding to Figure 50.

TABLE III

$f_{\theta\theta}$(kHz)	$f_{\theta\theta}$/11 kHz	$\phi_{\theta\theta}$(deg)	$\phi_{\theta\theta}/\theta_o$	$f_{r\theta}$(kHz)	$f_{r\theta}$/11 kHz	$\phi_{r\theta}-90^o$	$(90^o-\phi_{r\theta})/\theta_o$
21	1.9	64	3.0±0.3	24	1.9	65	3.0±0.3
32	2.9	80	3.7±0.5	38	3.5	171	8.0±0.6
44	4.0	92	4.3±0.8	45	4.1	110	5.1±0.8
59	5.4	60	2.8±1.0	52	4.7	249	11.6±0.9
67	6.1	201	9.3±1.1	65	5.9	130	6.0±1.1
77	7.0	210	9.7±1.3	78	7.1	138	6.4±1.3
101	9.2	275	12.8±1.7	98	8.9	161	7.5±1.6
110	10.0	221	10.3±1.8	104	9.5	281	4.8±1.7

NOTES:

$f_{\theta\theta}$ and $\phi_{\theta\theta}$ are modal peak frequencies and phases from Figs. 48 and 49.

$f_{r\theta}$ and $\phi_{r\theta}$ are modal peak frequencies and phases from Figs. 50 and 51.

θ_o is the poloidal angle of coil separation (21.5^o).

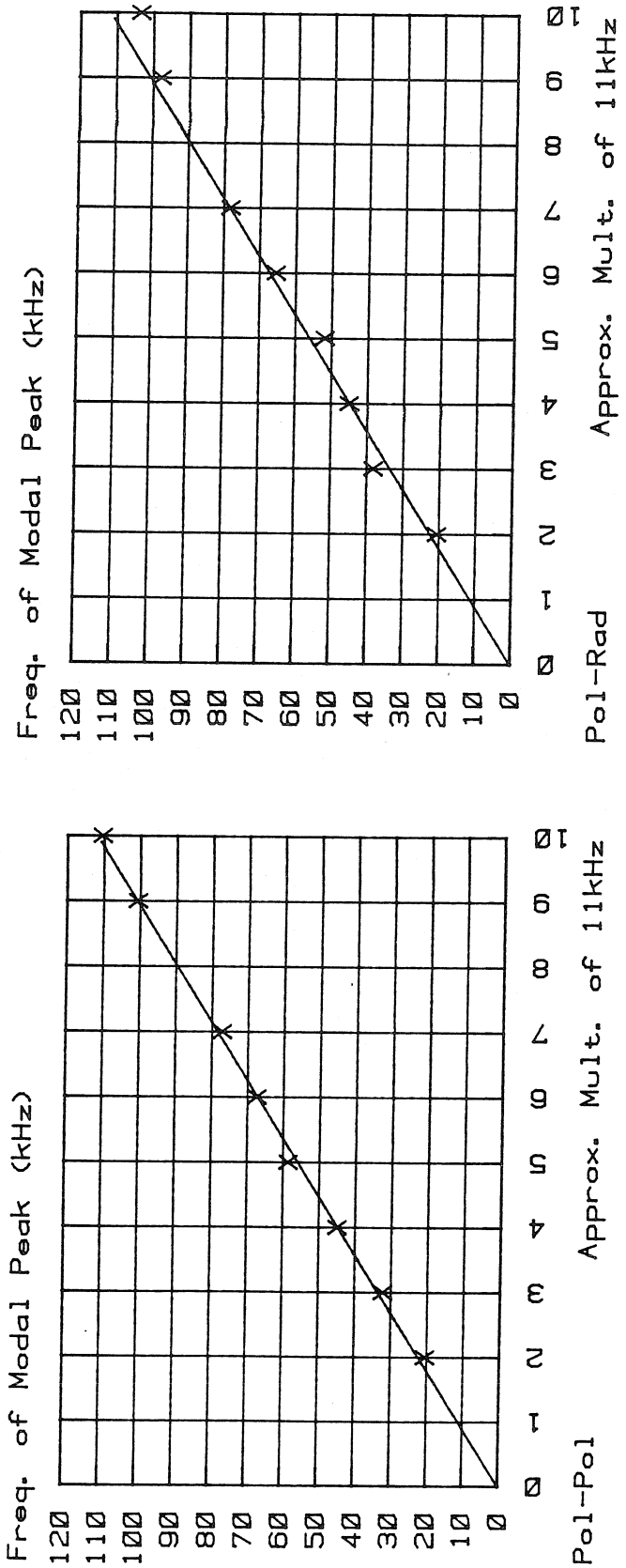

Figure 52. Frequencies f_m at cpsd modal peaks from Figure 48 (left) and Figure 50 (right) are plotted against integer closest to $f_m/11$ kHz. The closeness to a straight line suggests solid-body rotation of magnetic islands with m=2, 3, 4, 5, 6, 7, 9, 10.

level near 88 kHz where the m=8 would be expected). It should be noted that the Gaussian averaging used to smooth the cpsd phase function may also shift the frequency peaks in the cpsd amplitude, additionally only discrete frequencies separated by 977 Hz are available from the Fast Fourier Transform program. Hence, there is some lack of precision in specifying the peak frequency of a mode. Nonetheless, the apparent poloidal rotation frequency of 11 kHz falls within the bounds of the apparent poloidal rotation frequency deduced above from the peak value of the normalized cross-correlation amplitude. Note also that the mode number deduced for the lowest frequency peak is m=2. The mode closest to this in frequency in the spectra of Figs. 35-37 is, of course, the only mode not stabilized during the density rise which, from tearing-mode theory, was anticipated to be the m=2.

It remains to apply the relations summarized in Table I to the cpsd phases of Figs. 49 and 51 associated with the modal peak frequencies of Figs. 48 and 50. This information is summarized in Table III in columns three, four, seven, and eight. First of all, the phases produced by the Fast Fourier Transform program are, of course, unique up to addition of an integral multiple of 2π. This accounts for the values of phase in Table III greater than 180° and also explains why the tabulated phases have the same sign while the phase traces of Figs. 49 and 51 change sign numerous times. Secondly, the reader is reminded of the discussion in Chapter II that showed that if one transient-recorder channel triggers one clock cycle (1 μsec) later than the other a frequency-dependent phase shift

$\delta\phi = 2\pi f \times (1\ \mu\text{sec})$ radians is introduced into the cpsd phase. The phases in column three of Table III have been arbitrarily adjusted for such an error. The phases in column seven have been left alone. The mode numbers deduced from these phases and the relations of Table I are tabulated in columns four and eight of Table III, the error in the mode number δm corresponding to $\delta\phi/\theta_o$ is indicated. The mode numbers deduced from the poloidal-poloidal cpsd do not disagree too badly with the solid-body rotation-deduced mode numbers for m=2, 3, 4, and 10. The mode numbers deduced from the radial-poloidal cpsd phase do not disagree too badly with the solid-body rotation-deduced mode numbers for m=2, 4, 6, 7, and 9. Otherwise the agreement is abysmal. The motivation for assuming a byte was dropped and correcting the phases of column three was an upward skewing in a plot of the cpsd phase-deduced mode numbers versus the solid-body rotation-deduced mode numbers; there is no certainty that one channel did indeed trigger one clock cycle later than the other.

The failure to consistently obtain mode numbers from cpsd phases to match closely solid-body rotation mode numbers is simply not understood. The agreement is generally best at the lowest frequency modes, m=2, 3, and 4, but this varies from shot to shot. Particularly puzzling is the common case of good agreement of the solid-body rotation mode number with the poloidal-poloidal (or poloidal-radial) mode number and simultaneous disagreement with the poloidal-radial (or poloidal-poloidal) mode number.

3. The origin of higher m-number fluctuation modes

It is appropriate to pause at this point, now that the existence of magnetic fluctuation modes having poloidal mode numbers $m \geq 4$ is established, to inquire into the nature of them. As mentioned in the last chapter, Chrisman, Clarke, and Rome[48] showed that a necessary condition for the formation of magnetic islands is the existence of a perturbation component of magnetic field at a (unperturbed) mode-rational surface in the presence of magnetic shear. As previously discussed, for a realistic current-density profile this means that only magnetic islands with poloidal mode number m and toroidal mode number n such that $m/n < q(a)$ may be formed. Magnetic fluctuations observed in numerous Tokamaks are identified as having poloidal mode numbers m=2, 3, and 4 and are generally believed to have toroidal mode number n=1. Since the limiter q of the discharges considered herein is nominally 3.8 (Fig. 14) it is unlikely that the modes identified in Table III as having $m \geq 5$ can have n=1. In the research presently to be described it is shown that the majority of high m-number peaks in the cross-power spectral density are associated with the distortion of the shape of the magnetic islands, that is, they are harmonic distortion products and their m and n numbers are simply related to the m and n numbers of the undistorted islands.

It is convenient to adopt the convention of identifying the tearing mode with poloidal mode number m and toroidal mode number n by the ordered pair (m,n). The degenerate, or harmonic, mode (m,n) where m and n have greatest common divisor (gcd) $\ell > 1$, may coexist on

the mode-rational surface determined by $q(r) = m/n = m_o/n_o$, where $m=\ell m_o$ and $n=\ell n_o$, with the mode (m_o,n_o). For example, modes (4,2) and (2,1) may coexist on the q=2 surface. The (4,2) mode makes four turns the short way around the torus for every two it makes the long way. It is not difficult to visualize this mode as two coaxial and disjoint helices. In fact, the (m,n) mode consists of $\ell=\gcd(m,n)$ coaxial and disjoint helices. The superposition of a harmonic radial magnetic field distorts the magnetic island shape associated with the fundamental (cf. Fig. 32). If the magnetic island (m,n) were to rotate in the poloidal direction with angular frequency ω then poloidal magnetic probes would detect a frequency component $m\omega$; if the ℓth harmonic distortion product $(\ell m,\ell n)$ were to owe its existence to a static (in comparison to the sampling interval) deformation of the (m,n) magnetic islands then the frequency component $\ell m\omega$ would be detected and would be in strict phase relation to the fundamental component. This phase relation manifests itself as the equality of the delays in time (ϕ/ω) of the modes in travelling from one probe to the other. If there be velocity shear, then the harmonics resulting from distortion of one set of magnetic islands would be distinguishable from the distortion products of another system on a different mode-rational surface. In particular, the m=6, which may be either a(6,3) or a(6,2) mode, could have its origin determined by comparison of its time delay with those of the (3,1) and the (2,1).

Table IV contains data recorded during the initial portion of the density decay of a gas puff and is organized according to the time

TABLE IV

Probes containing coils sensitive to poloidal magnetic-field fluctuations are placed 1 cm into the discharge and are separated by 6 cm in arc length, hence the poloidal angle of separation is $\theta_o = 6/14 = 0.43$ rad = 24.6 deg. The peak puff particle density attained this shot was 1.6×10^{13} cm^{-3}. The frequencies and phases come from the cpsd modal peak values, and the m numbers are derived from the multiplicity of the apparent poloidal frequency of rotation.

Freq (kHz)	Phase (deg)	Delay (μsec)	m
23	66	7.9	2
49	127	7.2	4
88	266	8.4	8
104	290	7.8	10

Average delay between probes = 7.8 μsec.

37	169	12.8	3
64	247	10.8	6
130	515	11.0	12
150	624	11.5	15

Average delay between probes = 11.5 μsec.

77	262	9.4	7

delay of the mode. Naturally, the phases are unique up to the addition of integer multiples of 2π. For the particular shot tabulated it is found that the m=2, 4, 8, and 10 modes (m-numbers determined from the solid-body rotation frequencies) are subject to equal, within the precision of the experiment (± 1 μsec), delays in time, or they may be said to be locked in phase. Similarly, there is a natural grouping in terms of time delay of the m=3, 6, 12, and 15 modes. These modes are therefore identified as fundamentals, m=2 and 3, and harmonics originating with magnetic island deformation. The m=5, 9, 11, 13, 14, 16, and above modes are not of amplitude sufficient to be resolved from the background noise of the cross-power spectral-density function.

Fig. 53 shows the cpsd amplitude for the two poloidal signals from which Table IV is obtained. The bar chart, Fig. 54, is obtained from Fig. 53 in the following way. First, the amplitude of the B cpsd is obtained from the amplitude of the $\dot{B}$ cpsd by division by ω^2. Then the square root at each modal peak frequency is taken. This result, in units of Gauss-sec$^{\frac{1}{2}}$, is a measure of the strength of the poloidal magnetic-field fluctuation frequency component at the probes (the positions of which are described in Table IV). Next the set of these values corresponding to the m=2 island fundamental and harmonics is normalized to make the value of the fundamental unity. Likewise the m=3 fundamental and harmonics. Since the magnetic field seen by a probe is the result of perturbation currents (in Fig. 33 $J_z^p \sim \cos ky$; in cylindrical geometry this becomes $J_z^p \sim \cos m\theta$)

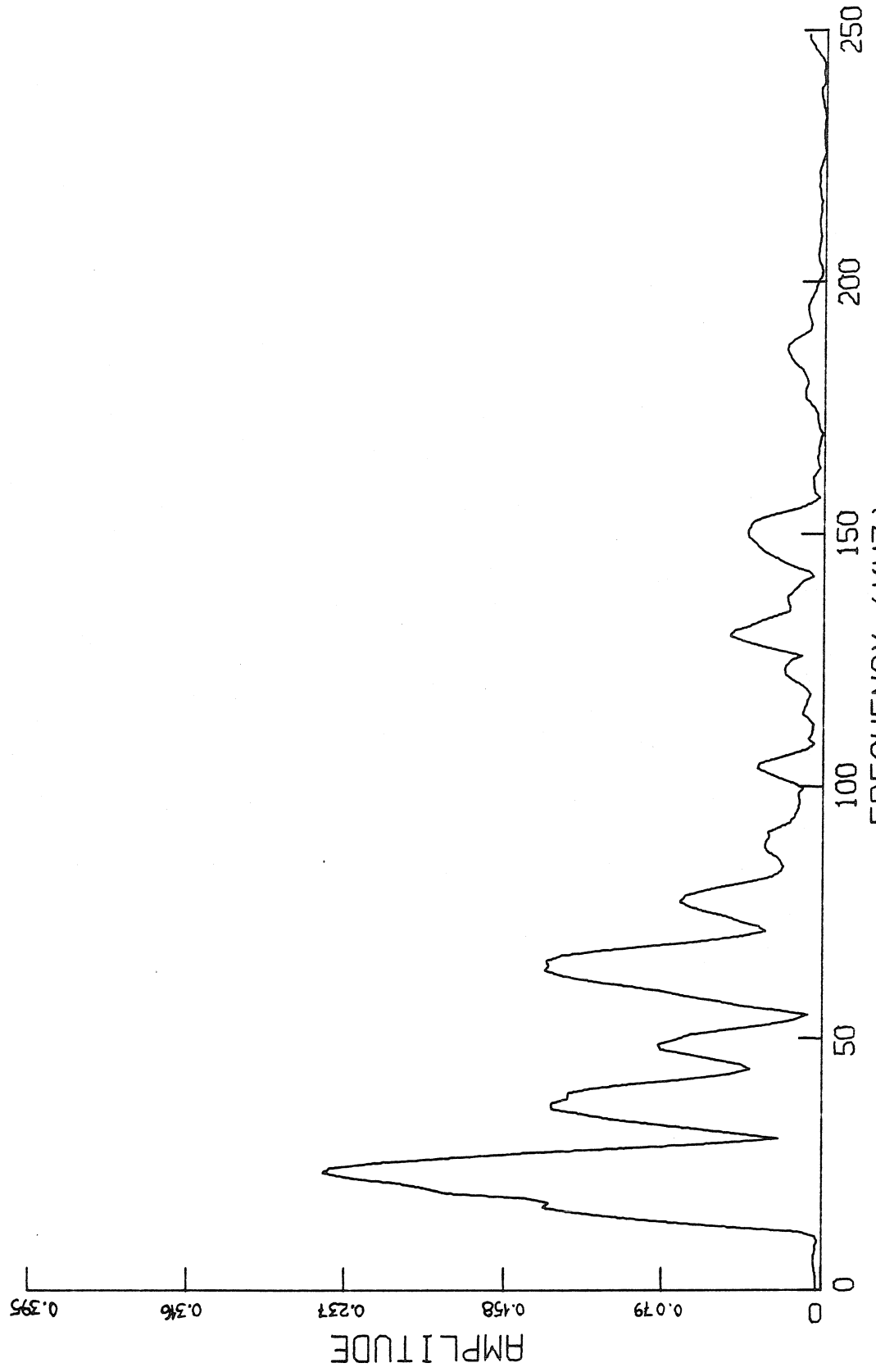

Figure 53. Amplitude of cpsd from which Table IV is obtained. Discharge parameters are the same as in Figure 42. Amplitude in $Gauss^2/\mu sec$.

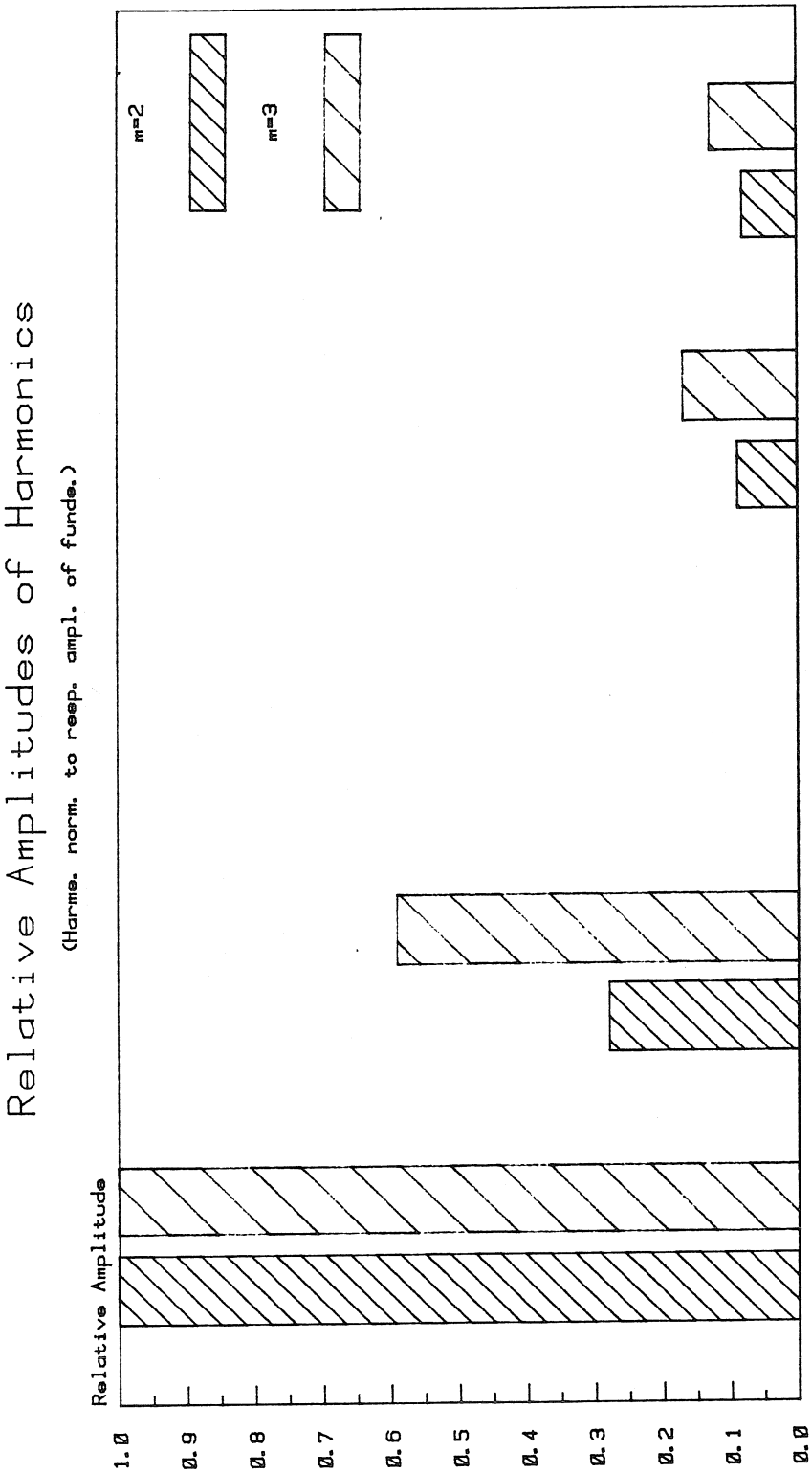

Figure 54. Comparison of modal peak $(Bcpsd)^{\frac{1}{2}}$ for the two families of harmonics of Table IV. Each family is normalized to the $(Bcpsd)^{\frac{1}{2}}$ of its fundamental.

having m-fold poloidal symmetry, the probes see essentially a sum of multipole fields. The higher the m-number of the magnetic island the higher the order of the multipole. The fall-off of $(B\ \mathrm{cpsd}(\omega))^{1/2}$ with increasing order of the harmonic is consistent with multipole fields and the less rapid fall-off of the m=3 harmonics than the m=2 harmonics is consistent with the smaller distance from the probes to the m=3, n=1 mode rational surface than to the m=2, n=1 mode rational surface (recall that a current-density profile that decreases monotonically with increasing r gives a safety-factor profile that increases monotonically with increasing r). It may be of interest that the m=2 family of amplitudes in Fig. 54 falls off roughly as frequency to the minus seven-fourths while the m=3 family falls off roughly as frequency to the minus three-halves.

The neat organization of Table IV is rather fortuitous; in general, about one-half of the higher-order cpsd peaks can be shown to be locked to fundamentals. A magnetic island undergoing modification of shape may generate harmonics with changing phase relations to the fundamental. There is experimental and theoretical evidence that magnetic island shapes may be modified by various physical processes. For example, proximity to the wall or to other island chains on other mode-rational surfaces may alter the structure. It must be kept in mind that the plasma in the Caltech Tokamak is probably continuously changing in current-density profile, hence in distribution of mode-rational surfaces, and moving upward and outward to the wall. Those harmonic modes so identified through time delay

measurements are thus thought to represent relatively stable ($\gtrsim$ 1 msec) structures.

It may be of interest to point out that both the (6,2) and (6,3) modes have been identified from measurements made during different discharges.

4. The m=7 mode

Standing alone in Table IV is a 77 kHz magnetic fluctuation mode. It is not correlated in time delay with either the m=2 or m=3 families of oscillations as one might expect given the fact that 7, 2, and 3 are relatively prime. If this mode were an m=7, n=2 it should have maximum amplitude of perturbation fields near the $r_s = q^{-1}(3.5)$ mode-rational surface. Since q(a) = 3.8 for the discharges presently under consideration the possibility arises that the cpsd amplitude might peak near the limiter. Figure 55 shows values of poloidal-radial cpsd amplitude for a sequence of 9 discharges identical to the one summarized in Table IV and Figs. 53 and 54. It is seen that the maximum falls roughly at 2 centimeters probe insertion distance. The scatter in the data is rather large, however, comparisons with the m=2 and m=3 cpsd amplitudes were made for these same discharges and these latter profiles are strongly monotonically increasing with increasing penetration.

The m=7 spectral peak is ubiquitous throughout the puff density decay, unlike the other prime number oscillations m=5 and m=11 which are rarely discernible from the noise. Identification of the m=5 improves considerably at 3 cm probe penetration, presumably

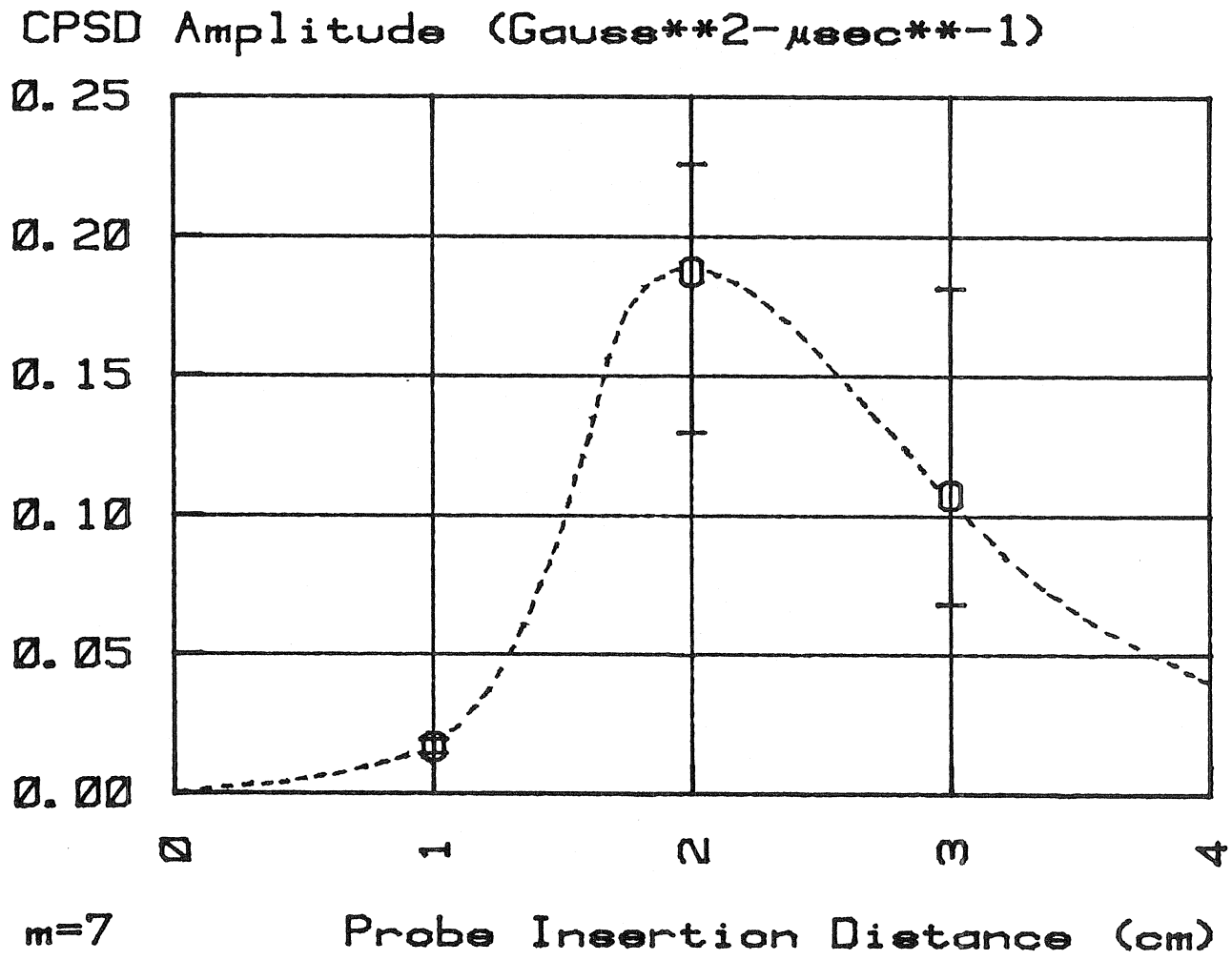

Figure 55. Values of poloidal-radial m=7 (nom. 77 kHz) cpsd amplitude versus distance probes are pushed into the plasma (cf. Furth, Rutherford, and Selburg[39] eigenmodes, Figure 31). q(a) = 3.8 hence this mode is identified as the m=7, n=2. Both poloidal and radial signals come from the same probe. Peak puff particle density = 9.0×10^{12} cm^{-3}.

because of the closer proximity of the $r_s = q^{-1}(2.5)$ surface. The level of the m=7 as indicated by the amplitude of the cross-power spectral-density function is very small (cf. Figs. 36 and 44) during the density rise.

As of this writing, the analysis of the stability of high mode-number ($m \geq 4$) resistive instabilities is still in development[51]; it is speculated that these modes may be unstable in the vicinity of the plasma surface given the proper boundary conditions for the governing differential equation[52].

D. Fluctuations later in the decay

One anticipates that the magnetic shear in the plasma increases during neutral gas feed and decreases upon termination of the feed. One sees stabilization of high poloidal mode-number fluctuations in the presence of neutral gas feed and destabilization of higher-order modes immediately upon cessation of the feed. Earlier it was suggested that, as in other Tokamaks, the current channel may shrink as the discharge evolves in time, hence the magnetic shear may again become a stabilizing factor for the higher-order modes later on in the decay. It turns out that unlike the early portion of the decay the nature of the magnetic fluctuations in the later stages of the density decay is highly dependent on the intensity of the gas puff, that is, on the duration of the gas pulse. For this reason the first portion of the discussion to follow will deal with discharges identical to those considered in the foregoing material of this chapter and the next portion will consider the effects of the systematic prolongation of the auxiliary gas feed.

1. Moderate intensity gas puffs

Again, a sequence of discharges was run for which the density traces were qualitatively similar to that of Fig. 9 differing quantitatively in that the peak density each shot was approximately 9.0×10^{12} cm^{-3}; other parameters are summarized in the caption to Fig. 56. The fluctuation data for all shots in this and the following sections were recorded in a 1.024 msec interval beginning 8.15 msec into the shot, that is, 1.0 msec after the end of the "early decay" sampling interval. Radial and poloidal fluctuation signals from a single probe inserted 3 cm into the discharge are shown in Fig. 56. The amplitude of the autopower spectral density (apsd) is shown in Fig. 57 for the radial signal (upper trace Fig. 56) and in Fig. 58 for the poloidal signal (lower trace Fig. 56). The reader will note upon comparing Figs. 57 and 58 to Figs. 43 and 44 that the auto-power spectra are similar in the early and later decay sampling periods. A large number of discharges with successive probe insertion distances of 1, 2, and 3 cm were compared and the following general trends were noted:

(a) Both the radial and poloidal root-mean-square fluctuation fields decline from the early sampling interval to the later sampling interval on the average by less than 50%.

(b) The peak normalized cross-correlation amplitudes are nearly identical ($\sim$0.6).

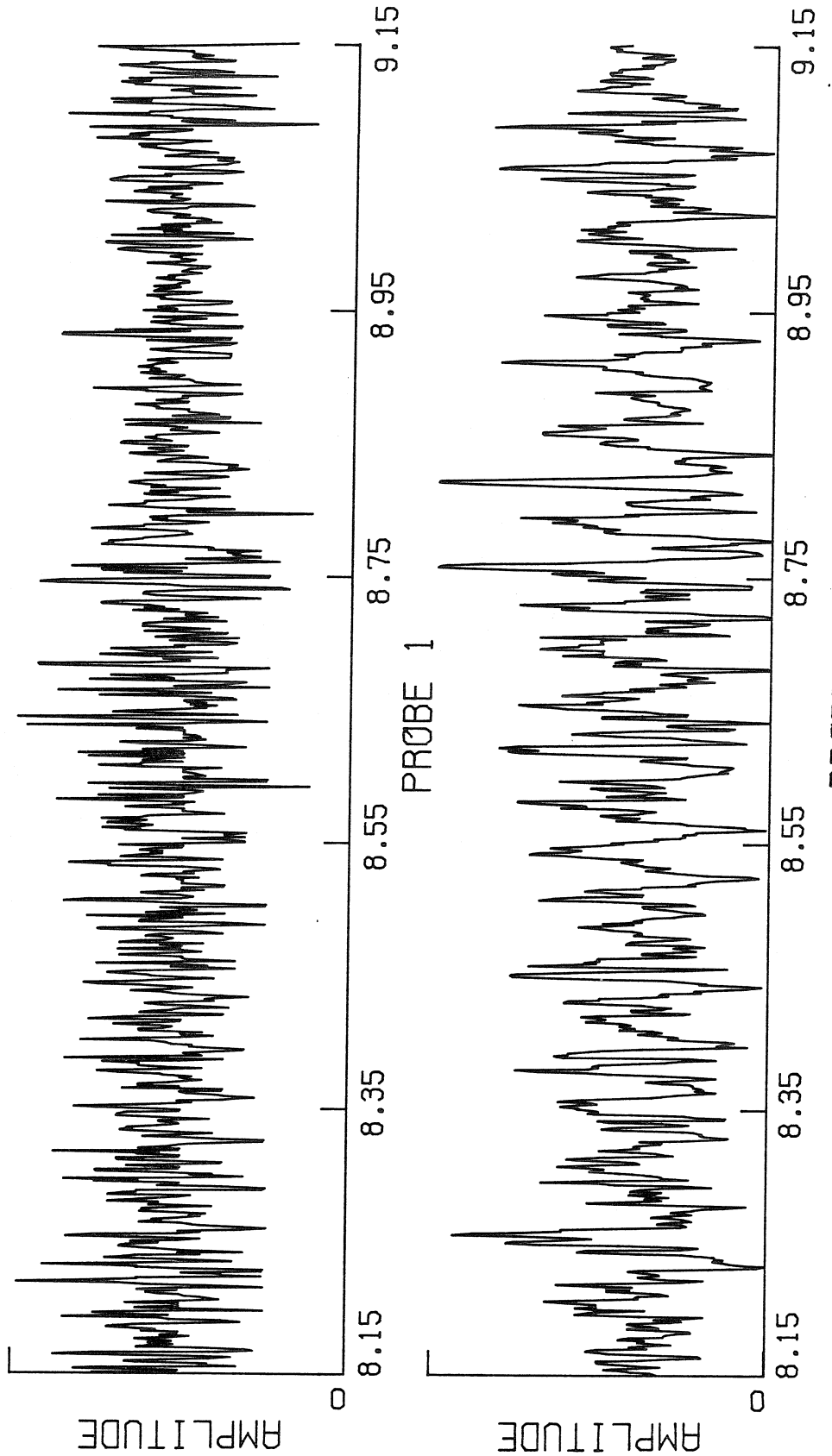

Figure 56. Radial (above) and poloidal (below) fluctuation signals. Discharge parameters: B_ϕ = 4.1 kG, OHFB = 1 kV, OHSB = 360v, VFFB = 130v, VFSB = 55v, filling pressure = 1.35 x 10^{-4} Torr, puff reservoir pressure = 970 Torr, 125v pulse lasting 0.43 msec. Full scale = 20 mV upper trace, 14 mV lower trace.

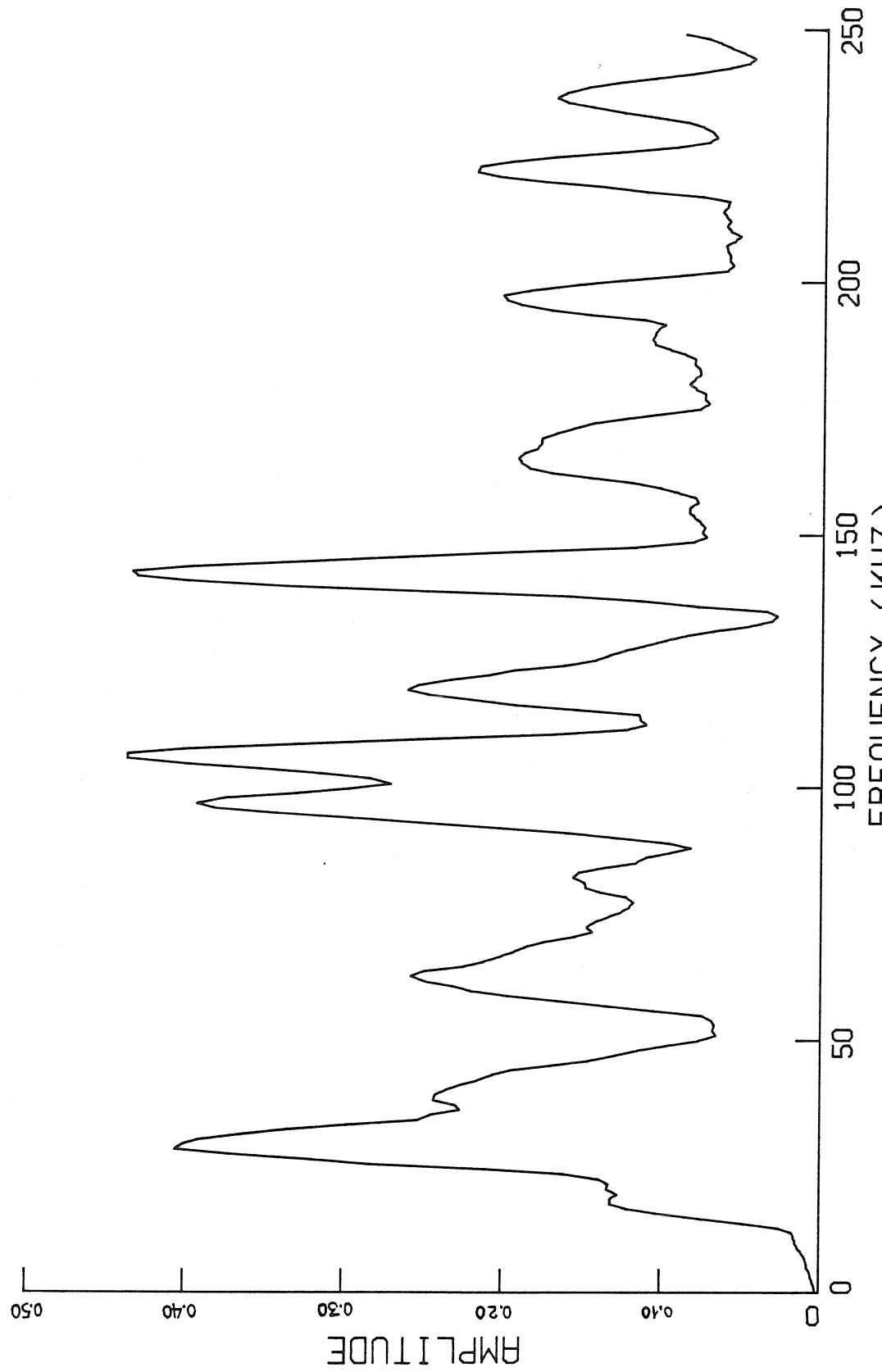

Figure 57. Auto-power spectral density of the radial fluctuations (upper trace) of Figure 56. Cf. Figure 43. Amplitude in units of Gauss^2/μsec.

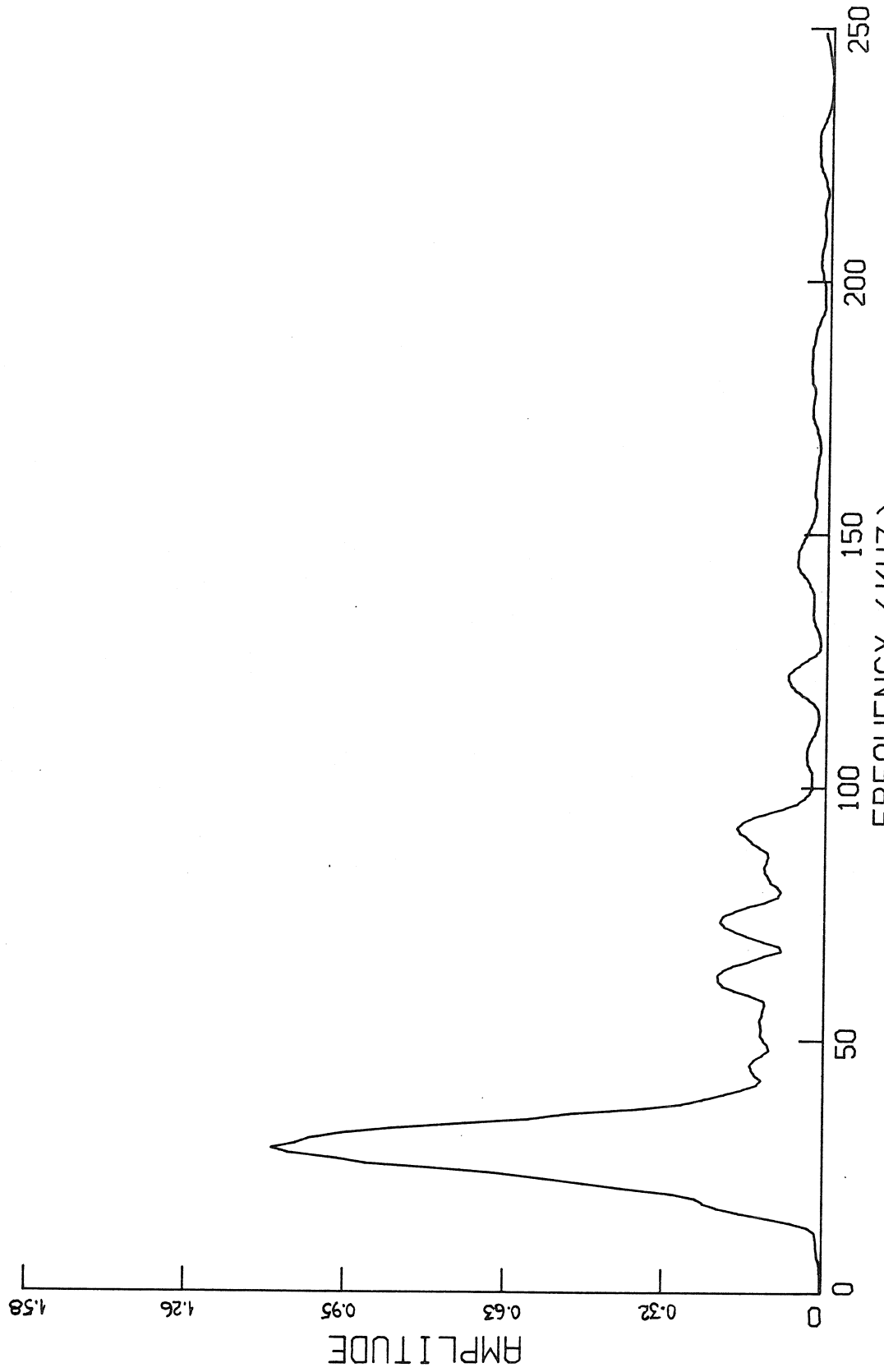

Figure 58. Auto-power spectral density of the poloidal fluctuations (lower trace) of Figure 56. Cf. Figure 44. Amplitude in units of Gauss^2/μsec.

(c) On the average the poloidal-poloidal cpsd amplitude of the m=2 fluctuation mode declines on the order of 50%. There is considerable shot-to-shot scatter in a collection of these data at a single insertion distance into the plasma. The cpsd amplitudes of the m=3, 4, and 7 modes decline as well, again with considerable scatter.

(d) One finds in the later decay interval, occasionally, the m=3 and certain higher-order modal peaks missing from poloidal-poloidal cpsd's. The m=3 peak has never been found to be missing from early sampling interval spectra. It is interesting to note that the m=9 peak was missing from the spectra for which the m=3 peak was missing. This is consistent with the idea that the m=9 peak originates in deformation of the m=3 magnetic island. The infrequent loss of the m=3 mode from the cross-power spectra suggests that the magnetic shear may, from the early to the later sampling intervals, increase sufficiently to approach the level necessary to stabilize the m=3 mode.

2. Prolongation of the duration of the gas puff

Motivated by the observed degradation of particle confinement with increasing gas-puff intensity and the intensity-dependent

appearance of minor disruptions characterized by negative spikes on the one-turn voltage trace, the effects on magnetic fluctuations caused by a systematic increase in the duration of the neutral gas feed were investigated. A sequence of discharges similar to that producing Figs. 26-28 was run; discharge parameters are summarized in the caption to Fig. 59.

Figs. 59a and 59b show the root-mean-square poloidal magnetic fluctuation field plotted against the intensity of the gas puff as measured by the maximum line-averaged particle density attained during the puff; Fig. 59a displays data from the early portion of the decay (sampling interval 6.15 to 7.15 msec in the shot, i.e., just after the density peak) while Fig. 59b shows data taken later in the decay (8.15 to 9.15 msec into the shot). Each of Figs. 59a and 59b is composed of two traces, each trace being comprised of values measured from one of a pair of poloidal probes inserted 1 cm into the discharge and separated by 6 cm in circular arc length, that is, the probes intercept poloidal angle $\theta_o = 6/14 = 0.43$ rad = 24.6^o (cf. Fig. 40). A comparison of these two figures shows that for puffs attaining peak densities in excess of about 1.5×10 cm^{-3} the rms level of poloidal magnetic fluctuations undergoes significant growth from one sampling interval to the next. This growth is sufficiently slow that no real change in the level of the fluctuations is seen during either the early or the late decay sampling intervals.

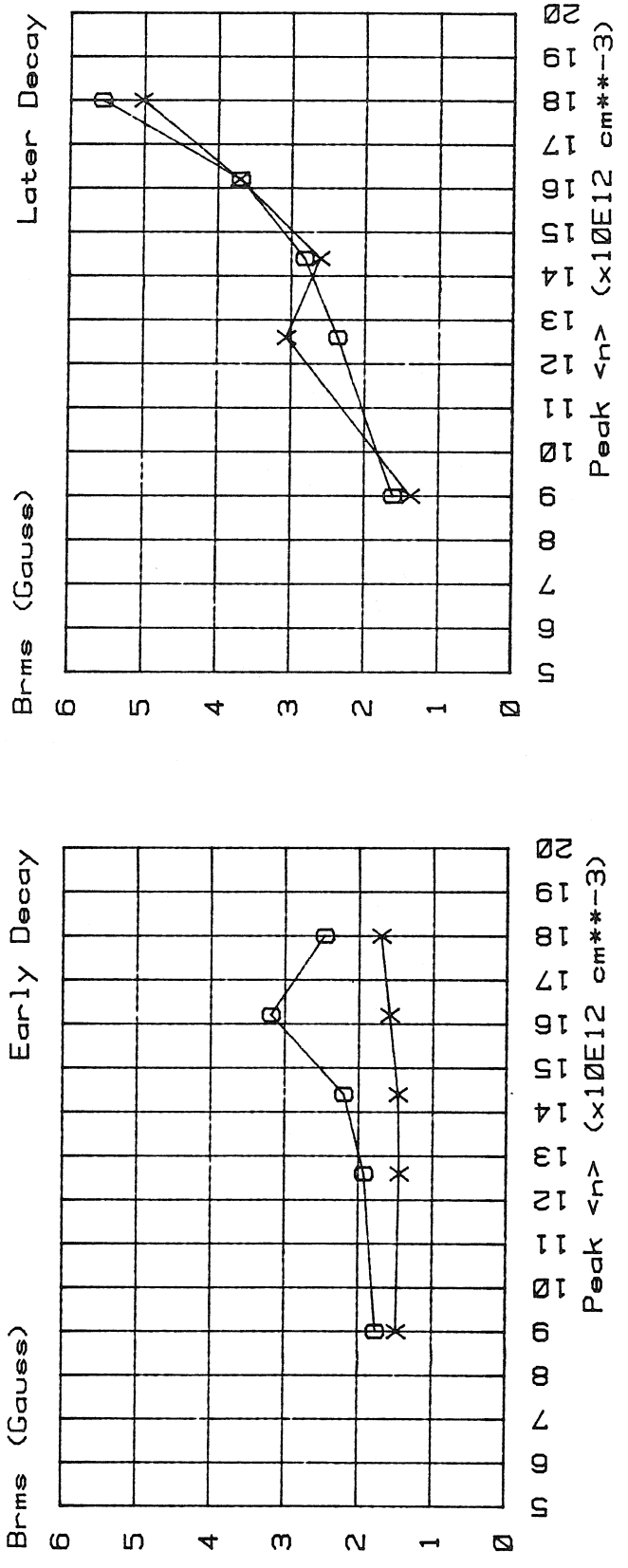

Figure 59. Variation of gas-puff intensity (duration of short pulse). The circles represent values recorded from upper, crosses from lower, of pair of poloidal probes separated by 24.6° in poloidal angle. Growth in rms poloidal B from early sampling interval (Figure 59a) to later sampling interval (Figure 59b) is apparent for those puffs attaining in excess of about 1.5×10^{13} cm^{-3} peak density.

Figs. 60a and 60b show the peak value of the normalized cross-correlation amplitude of these pairs of signals in the early and late decay sampling intervals, respectively. The trend is towards higher values of this quantity as a discharge of a given gas-puff intensity evolves and as the puff is intensified (as the gas pulse is made longer). An examination of the fluctuation spectra shows that with increasing puff intensity the m=2 mode comes to dominate the cross-power spectral density (cpsd) to the exclusion of other modal peaks in the later decay. In the early decay the spectra are qualitatively alike and a full spectrum of modal peaks (out to about 150 kHz) shows up regardless of puff intensity.

Figs. 61a and 61b show the poloidal-poloidal cpsd peak m=2 modal amplitudes for these same discharges. Fig. 61a shows that the level of m=2 fluctuations in the early decay is relatively independent of puff intensity while Fig. 61b shows that the m=2 cpsd peak modal amplitude increases with increasing puff intensity. The small value at 1.53×10^{13} cm^{-3} is deceptive: the m=2 modal peak was unusually broad for this discharge accounting for the rms poloidal magnetic fluctuation field level in Fig. 59b. Negative spikes on the one-turn voltage appeared for those discharges meeting or exceeding 1.62×10^{13} cm^{-3} peak particle density.

To put these results into perspective, it is found that in the first millisecond after a gas-puff of arbitrary intensity attains its peak density the fluctuation spectra are similar in number of modes present and their cpsd amplitudes, and the root-mean-square

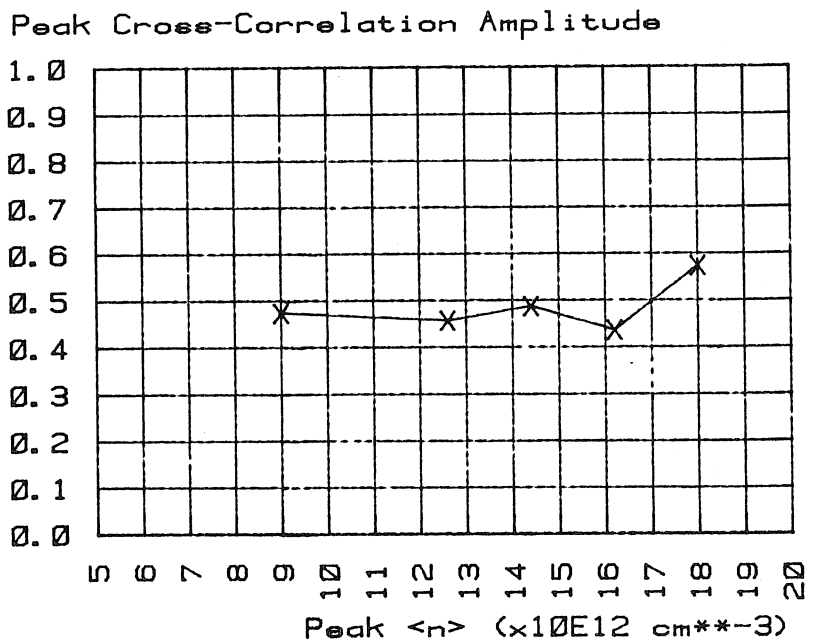

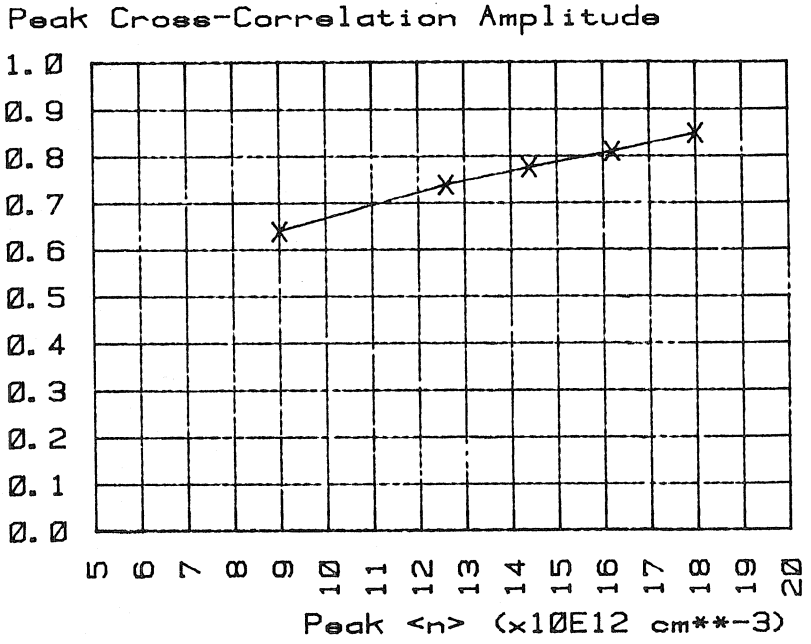

Figure 60. Peak normalized cross-correlation amplitudes for discharges of Figure 59. The trend is towards higher values as a discharge of given gas-puff intensity evolves and as the puff is intensified (longer pulse) in a given sampling interval.

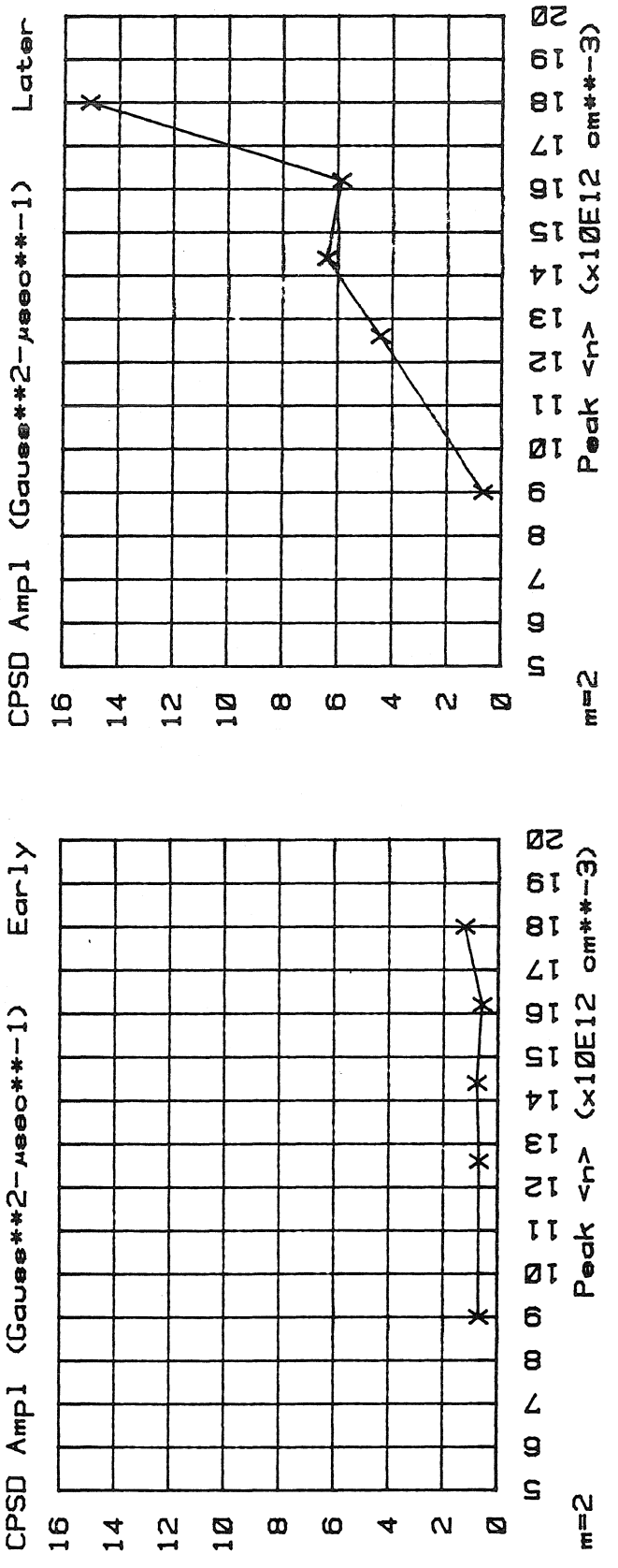

Figure 61. Amplitude of the poloidal-poloidal cross-power spectral density m=2 peak for discharges of Figure 59. The growth in rms poloidal B in Figure 59 is accounted for in the m=2 fluctuation mode.

level of fluctuations is independent of the gas-puff intensity. For gas puffs attaining peak densities of 9.0×10^{12} cm^{-3} or less one finds that as the puff density decay evolves in time the rms level of poloidal magnetic-field fluctuations generally declines slightly while higher-order modes (m=3, 5, etc.) may stabilize. For gas puffs attaining peak particle densities in excess of about $9.0 \times 10^{12} cm^{-3}$ one finds that the m=2 poloidal-poloidal cpsd level grows (slowly compared with the classical tearing mode result) during the decay. For puffs with peak densities in excess of about 1.5×10^{13} cm^{-3} the m=2 mode grows sufficiently that the root-mean-square poloidal magnetic fluctuation field measured in the later sampling period substantially exceeds the earlier level. At these puff intensities the poloidal-poloidal cpsd spectra are completely monomodal and the total magnetic fluctuation energy is in the m=2 mode (one must bear in mind that increased fluctuation levels may imply either wider magnetic islands (eqn. 5.28) or outward movement of the islands or both). The reader is reminded of the degradation in particle confinement for discharges with peak puff densities in excess of about 1.3×10^{13} cm^{-3}. Finally, it is noted that the puff intensity threshold for the appearance of negative voltage spikes and glitches in the plasma current trace (minor disruptions) is of the order of 1.6×10^{13} cm^{-3}.

The stabilization of higher-order magnetic fluctuation modes as the density decay evolves in time is consistent with the view that the magnetic shear in the plasma increases as the shot evolves because

of current-channel shrinkage due to thermal instabilities[30]. The increasing monomodality of the fluctuation spectra as the intensity of the gas-puff is elevated also makes one suspicious that the magnetic shear may be important. Some recent theoretical results suggest this as well and the parallels to the experimental phenomenology are quire interesting.

White, Monticello, and Rosenbluth[53] have developed a numerical code that uses an approximation to the full set of non-linear resistive MHD equations, the coupling between modes of different helicities being ignored, in an attempt to explain aspects of disruptions and their precursor MHD oscillations in the PLT Tokamak plasma. The PLT experimenters observed elimination of the m=1 X-ray node followed by a growing m=2 oscillation which culminated in a disruption. The code predicts that the presence of an m=2 island can increase radial thermal conductivity; this may account for the disappearance of the PLT m=2 X-ray node -- the increased thermal conductivity may make $q(0)>1$ (certainly there is yet no evidence that the q=1 mode-rational surface exists in the Caltech Tokamak. However, this code predicts non-linear growth of the m=2 magnetic island which may be of considerable significance). White et al. maintain that the PLT m=2 precursor oscillations coincide phenomenologically with the existence of an m=2 magnetic island of some critical size in their numerical simulation. Further, they declare that the increasing radial thermal conductivity due to the island itself, from the magnetic island width saturation theory of White, Monticello, Rosenbluth,

and Waddell[42] which regards magnetic island growth as a quasi-linear development of a single uncoupled mode, thus increases the island saturation width (that is, transport of energetic particles across the magnetic island decreases the magnetic shear in the vicinity of the island which in turn increases the island width; cf. eqn. (5.28) valid in the linear approximation). The wider island having continued access to the hotter central plasma may progressively grow by this mechanism. Further, when the magnetic island grows wider than the thin resistive boundary-layer non-linear $\underset{\sim}{J} \times \underset{\sim}{B}$ terms in the equations of motion dominate the $\rho d\underset{\sim}{v}/dt$ terms[44]. These non-linear terms are stabilizing and slow down the growth of the island below linear tearing mode theoretical rates. The White, Monticello, and Rosenbluth code requires for this m=2 island non-linear growth that the magnetic shear in the neighborhood of the q=2 mode-rational surface initially be very large. The code also predicts that as the magnetic island grows it eventually comes into contact with the limiter. Kadomtsev and Pogutse[47] suggest such wall contact as a mechanism for the generation of negative voltage spikes.

On the basis of the slow growth of the m=2 fluctuation mode and, at the highest levels of gas-puff intensity, the degradation of particle confinement and the culmination of m=2 growth in a disruption, it appears that the White, Monticello, and Rosenbluth[53] code closely describes the observed phenomena. The gas-puff intensity levels required for degradation of particle confinement (peak puff density in excess of $\sim 1.3 \times 10^{13}$ cm^{-3}) and for growth during the density

decay of the root-mean-square level of m=2 magnetic field fluctuations (peak puff density in excess of $\sim 1.5 \times 10^{13}$ cm^{-3}) may be associated with the code's requirement of sufficient steepness of the current density profile in the neighborhood of the q=2 mode rational surface for the evolution of the m=2 magnetic island to a very large size.

In closing this section, it is noted that the White, Monticello, and Rosenbluth[53] code predicts an increase in the plasma minor radius as the m=2 island reaches maximum size; this expansion may cause the plasma to contact the limiter. There is some indirect experimental evidence of an expansion of the plasma minor radius during those shots which disrupt. Recall that the position-coil systems show that the plasma steadily moves upwards and outwards as the discharge evolves in time. It is found that at the highest gas-puff intensities, that is, for those shots that disrupt, a well-centered discharge requires significantly higher vertical field levels than those required for non-disrupting discharges (the poorly-centered discharges prematurely terminate just after the density peak). The larger vertical field, of course, pushes the plasma inwards.

VII. Summary and Suggestions for Future Research

A. Particle Confinement Experiments

1. The decay of particle density resulting from a short gas puff in a well-centered discharge is linear in time. This result is consistent with Alcator scaling.
2. The confinement of particles is independent of variation of the plasma current and toroidal field.
3. The confinement of particles becomes progressively poorer as the gas pulse is delayed from the beginning of the discharge.
4. The confinement of particles fails to improve as the gas pulse is prolonged, a result not expected from Alcator scaling.
5. The confinement of particles becomes significantly degraded for gas-puffed discharges attaining peak densities near the Murakami limit ($n_e \gtrsim 1.3 \times 10^{13} cm^{-3}$ for B_ϕ = 4.1 kG).

B. Magnetic Fluctuation Experiments

1. Density rise of gas puff
   a. The radial and poloidal spectra are monomodal ($m = 2$ at approximately 17 kHz). This result is consistent with the predictions of the Furth, Rutherford, and Selburg theory for the stability of tearing modes in a plasma with strong magnetic shear.
   b. The fluctuation signals grow exponentially on classical tearing mode time scales.
   c. The estimated width of the $m = 2$ magnetic island is 2 to 3 cm and $\delta B_\theta / B_\theta \sim 3$ to 5%.

2. Early density decay

   a. The fluctuation spectra are not monomodal. This is consistent with the Furth, Rutherford, and Selburg theory for the stability of tearing modes in a plasma with weak magnetic shear. The m = 2 mode (21 kHz) dominates the poloidal spectra but the radial spectra are broader.

   b. The level of m = 2 radial and poloidal auto-power spectral-density is about the same as in the density rise. The root-mean-square poloidal and radial magnetic fluctuation fields are about 2.9 and 1.2 Gauss, respectively, near the limiter.

   c. From normalized cross-correlation amplitude measurements the plasma appears to rotate in the poloidal direction with the sense of the electron diamagnetic drift at angular velocity $\omega_o \sim 6.3 \times 10^4$ rad/sec.

   d. Spectral peak frequencies are nearly integer multiples of 11 kHz. Typically m = 2 through 15 modes are identified.

   e. The phase of the cross-power spectral density gives mode numbers that sometimes agree with the solid-body rotation mode numbers, but in general the agreement is poor.

   f. Time-delay measurements for modal peaks suggests that many of the higher-order modes (m > 3 in a q(a) = 3.8 plasma) may come from deformation of the m = 2 and m = 3 islands.

   g. A strong m = 7 (77 kHz) mode is observed peaking (in radial-poloidal cross-power spectral density) near the limiter in a q(a) = 3.8 plasma. This mode is identified as the m = 7, n = 2. High m-number tearing modes are the subject of current

theoretical investigation. The Furth, Rutherford, and Selburg theory suggests that such modes must be stable, but Wesson claims that proximity to the walls may destabilize such modes.

3. Later density decay

   a. Unlike the early decay, the results are highly dependent on the amount of gas admitted.

   b. For low to moderate intensity (peak $n_e \lesssim 9 \times 10^{12} cm^{-3}$) puffs:

      i. The fluctuation spectra are qualitatively the same as in the early decay.

      ii. The $m = 2$ and B_{rms} levels decline slightly from those measured during the early decay.

      iii. Occasionally the $m = 3$ is stabilized, unlike the early decay when it is always unstable. This is consistent with the Furth, Rutherford, and Selburg theory, provided the magnetic shear increases as the discharge evolves in time.

   c. For higher intensity ($9 \times 10^{12} cm^{-3} \lesssim$ peak $n_e \lesssim 1.5 \times 10^{13} cm^{-3}$) puffs:

      i. The poloidal fluctuation spectra become increasingly monomodal ($m = 2$) as the gas pulse is prolonged.

      ii. The peak normalized cross-correlation amplitude and $m = 2$ spectral amplitude increase with respect to values measured in the early decay; these amplitudes also

increase over the same sampling interval as the gas pulse is prolonged.

c. For very high intensity (peak $n_e \gtrsim 1.5 \times 10^{13} cm^{-3}$) puffs:

i. The poloidal fluctuation spectra are monomodal, the peak normalized cross-correlation amplitude is very high (~ 0.85), the root-mean-square poloidal magnetic fluctuation field levels are elevated with respect to those of the early decay, as are the $m = 2$ spectral levels.

ii. The rate at which the rms B level grows, from the early sampling interval to the late sampling interval, is much slower than the classical tearing-mode growth rate. This is consistent with the theory of the nonlinear destabilization of the $m = 2$ tearing mode deduced by White, Monticello, and Rosenbluth.

iii. For puffs attaining peak densities in excess of about $1.6 \times 10^{13} cm^{-3}$ minor disruptions occur.

4. General observations

a. The fluctuations always appear to rotate in the direction of electron diamagnetic drift.

b. The radial fluctuation spectra have more high-frequency modal content than do the poloidal spectra.

c. The $m = 2$ peak in the poloidal auto-power spectral density always has larger amplitude than that of the radial $m = 2$ peak.

d. The apparent angular velocity of poloidal rotation of the

plasma increases from density rise to early decay and from early decay to later decay sampling intervals.

C. Suggestions for Future Research

1. The $m = 7$, $n = 2$ mode could be studied with multiple loop probes, i.e., probes containing regularly spaced poloidal and radial coils. The radial profiles of the fluctuation components could be measured simultaneously in a single discharge and so avoid the problem of shot-to-shot scatter. Integration of the poloidal coil signals from the beginning of the discharge would allow computation of the magnetic shear at the $q = 3.5$ surface.
2. Kadomtsev and Pogutse have proposed that prior to a disruption the plasma grows in minor radius by formation of a "vacuum bubble" (plasma-free inclusion). The presence of such a bubble might be detected with Langmuir probes inserted into Caltech Tokamak discharges with gas puffs taking the density to the Murakami limit.

APPENDIX I

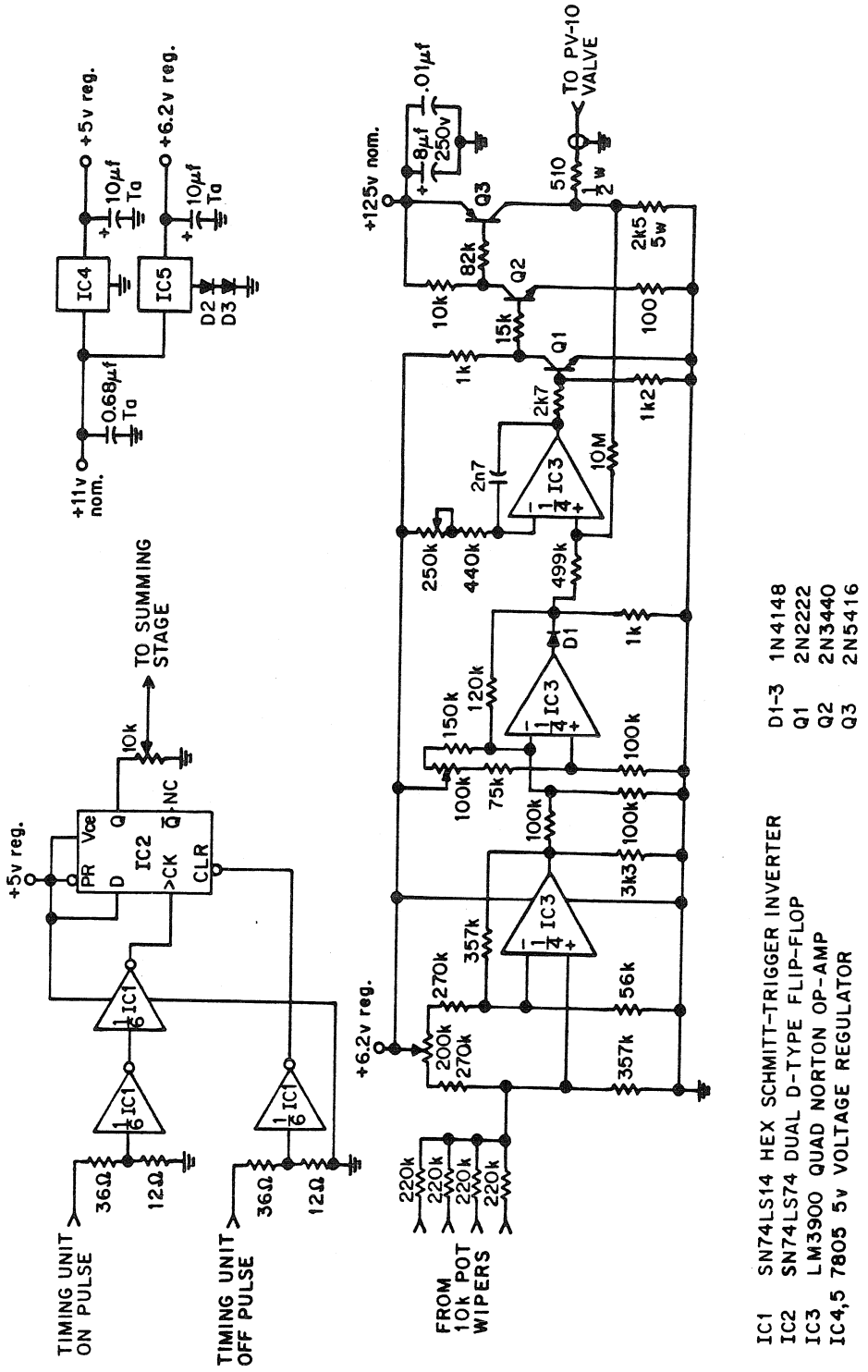

Fig. 62 Gas-puff valve voltage programming circuit

APPENDIX II: Gaussian averaging of the cpsd

Figure 63 shows the amplitudes of the Fast Fourier Transform (FFT) for two poloidal signals recorded in the early decay sampling interval of a typical discharge with gas puffing. Recall that the FFT routine yields amplitudes and phases at 1024 integer multiples of 977 Hz; these traces show the points connected. The amplitude of the approximation to the cross-power spectral density (cpsd) given by Eq. (3.5) is plotted in the upper trace of Fig. 64. Gaussian averaging, as described in the discussion of the microwave interferometer, is applied to these data to give the lower trace of Fig. 64. A gaussian with full-width at half-maximum of 6.5 kHz was used. This averaging may be seen to smooth the spectrum, while preserving its main features. The cpsd phases corresponding to Fig. 64 are shown in Fig. 65.

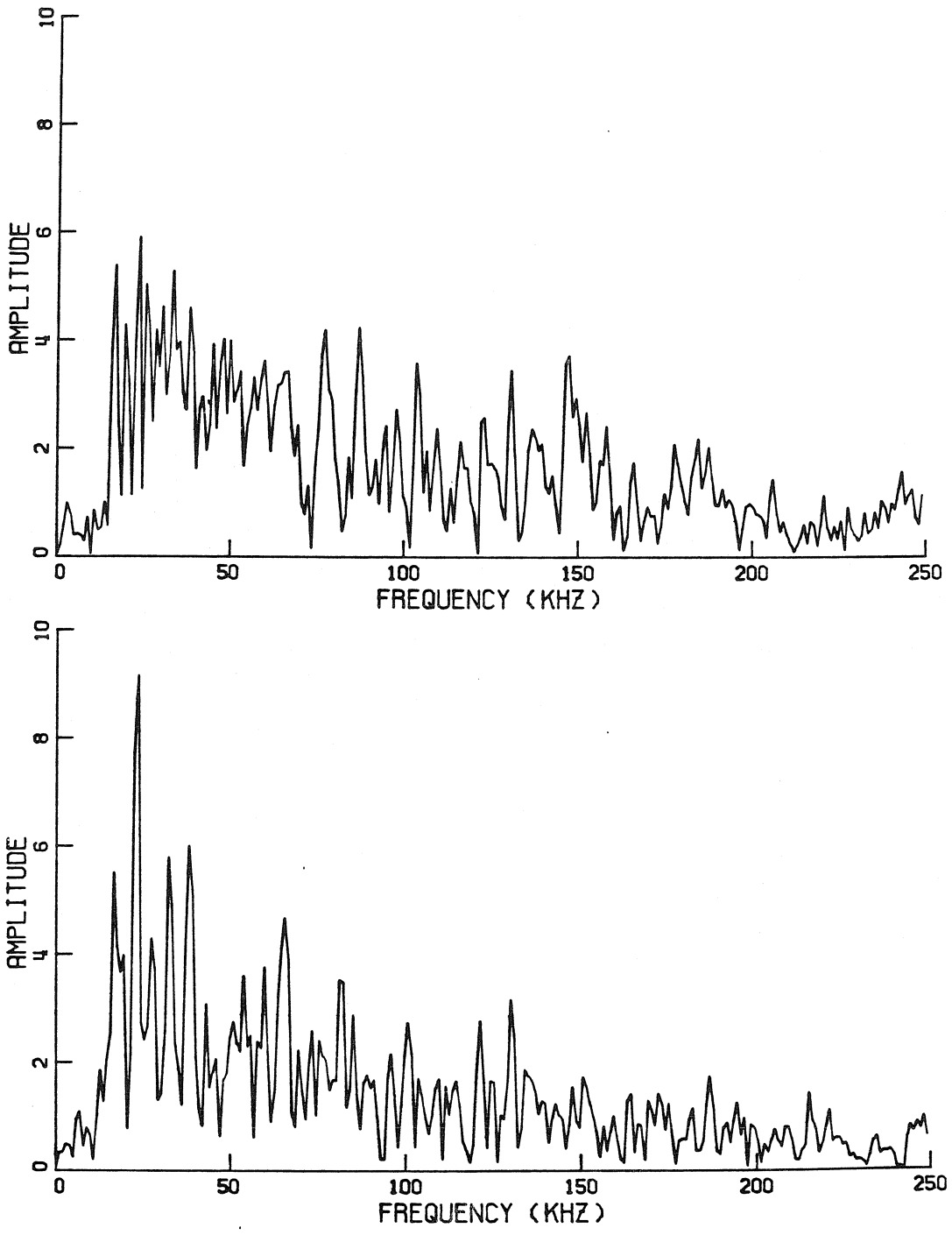

Fig. 63. Amplitudes of the Fast Fourier Transforms of two poloidal signals.

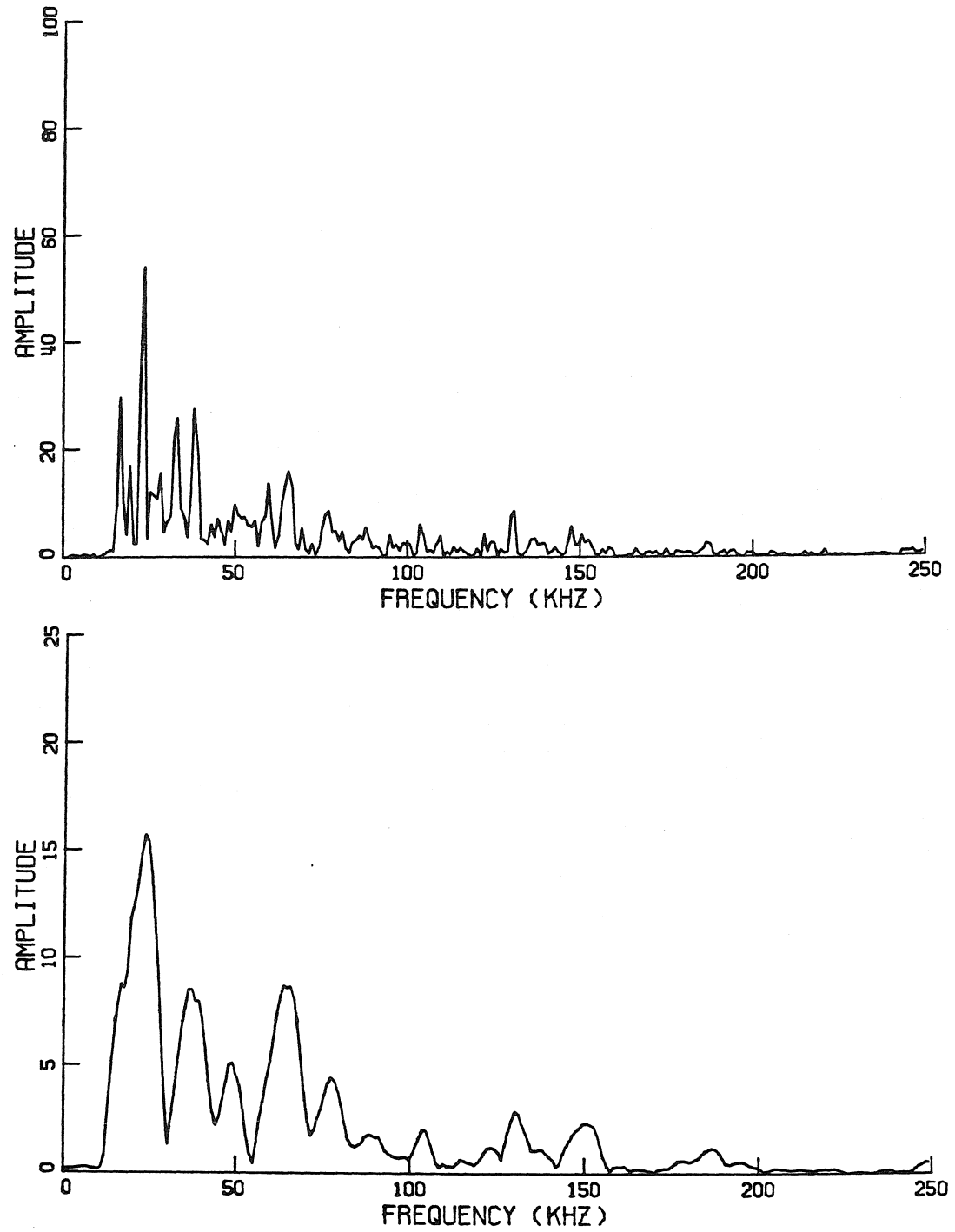

Fig. 64 Top: unaveraged cpsd amplitude for the two FFT's of Fig. 63.
Bottom: Gaussian-average of top trace. The FWHM of the gaussian is 6.5 kHz, i.e., N = 4 in Eq. (2.4).

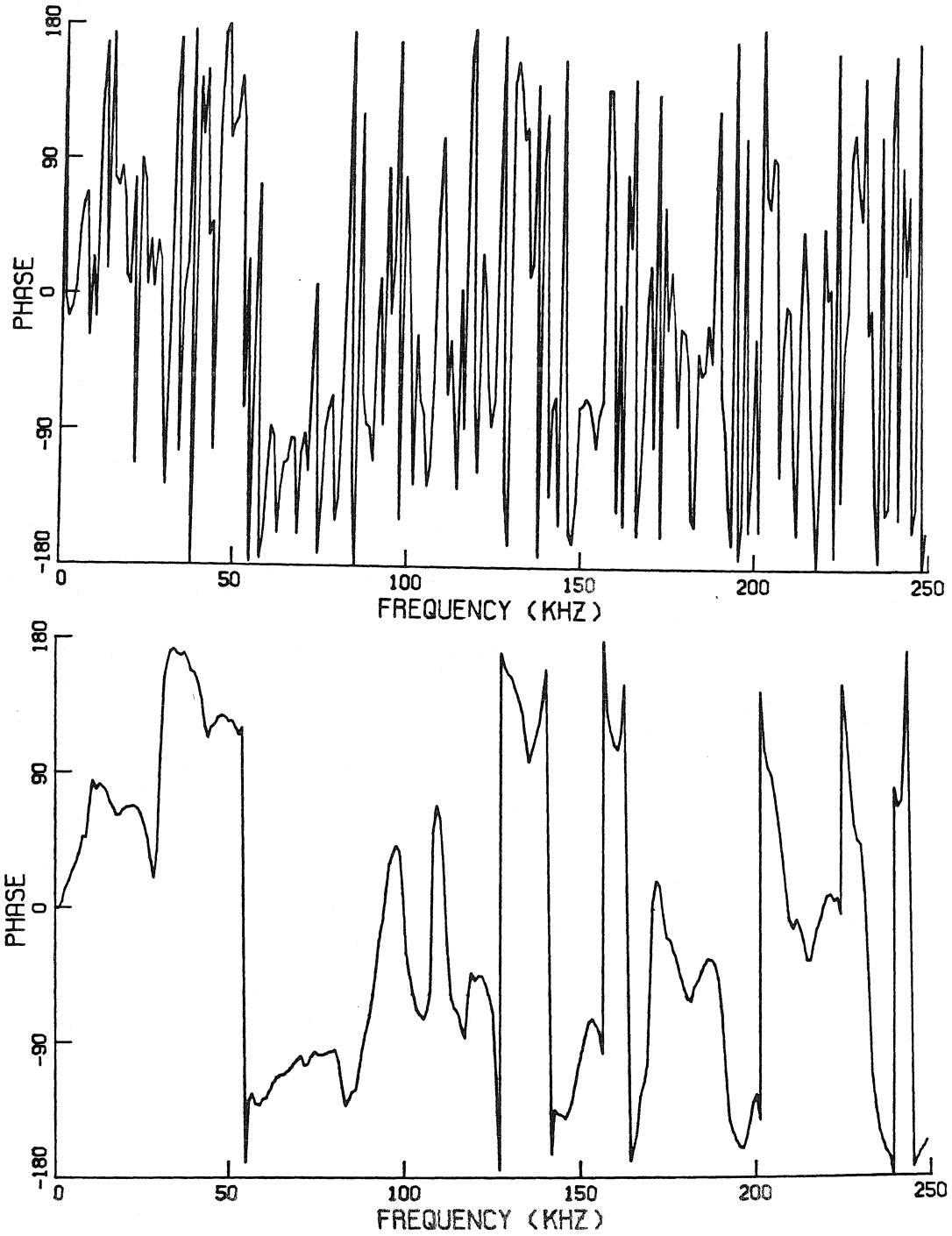

Fig. 65 Phases of the cpsd corresponding to Fig. 64

APPENDIX III: Focusing Resonance Cones

Focusing resonance cones

B. Levine, G. J. Greene, and R. W. Gould

California Institute of Technology, Pasadena, California 91125
(Received 7 November 1977)

The potential for an oscillating ring source immersed in cold, magnetized, collisionless plasma in the resonance cone regime ($K_\parallel/K_\perp<0$) is evaluated exactly and asymptotically, giving insight into the gross spatial behavior of the focusing resonance cones. The nature of the singularity in potential is clarified by the introduction of a noninfinitesimal collision frequency. Thermal effects are considered numerically, revealing an interesting interference structure in potential as well as a density depression near the focus of the cone due to the ponderomotive force.

I. INTRODUCTION

Resonance cones[1,2] emanating from ring sources have recently been studied in experiments with the objectives of focusing in order to observe ponderomotive force effects[3,4] and exciting a single axial wavenumber by means of a phased array of these sources.[5] In this paper an exact expression for the potential of an oscillating ring charge in a highly-magnetized, cold, collisionless plasma in the resonance cone regime ($K_\parallel/K_\perp<0$) is derived. The character of the singularity in the potential is clarified by introduction of a noninfinitesimal collision frequency; likewise, the focusing nature of the cones becomes apparent. First-order warm plasma effects are considered in numerical evaluation of the electric potential which displays the thermal interference structure. Lastly, an approximation to the ponderomotive force-induced density modification for weak fields is evaluated. Ion terms and sheath effects around the probe are neglected, and the plasma is assumed to be spatially uniform.

II. THE POTENTIAL

A. Collisionless theory

The volume charge density

$$\rho_{ext}(\mathbf{r},t)=(S/2\pi\rho)\delta(\rho-\rho_0)\delta(z)e^{-i\omega t} \tag{1}$$

describes an oscillating ring charge of radius ρ_0 centered in the $z=0$ plane (Fig. 1) having total charge magnitude S and oscillation frequency ω. The Fourier transform with respect to the spatial variables being taken, Eq. (1) yields

$$\hat{\rho}_{ext}(\mathbf{k},t)=Se^{-i\omega t}J_0(k_\perp\rho_0). \tag{2}$$

Since the quasi-static approximation $\mathbf{E}=-\nabla\phi$ is appropriate for determination of the near-field solution, there results

$$\rho_{ext}=\nabla\cdot\mathbf{D}=\nabla\cdot\epsilon_0\mathbf{K}\cdot\mathbf{E}=-\epsilon_0\nabla\cdot\mathbf{K}\cdot\nabla\phi\ , \tag{3}$$

where $\mathbf{K}$, the plasma dielectric tensor, has components $K_{xx}=K_{yy}=K_\perp$, $K_{xy}=-K_{yx}=K_H$, $K_{yz}=K_{zy}=0$, and $K_{zz}=K_\parallel$. Fourier transforming Eq. (3) with respect to the spatial variables and utilizing Eq. (2) yields

$$\hat{\phi}(\mathbf{k},t)=(S/\epsilon_0)e^{-i\omega t}[J_0(k_\perp\rho_0)/(k_\perp^2K_\perp+k_\parallel^2K_\parallel)]. \tag{4}$$

It is readily verified (Ref. 6, p. 679) that evaluation of the inverse Fourier transform of Eq. (4) gives

$$\phi(\mathbf{r},t)=\frac{Se^{-i\omega t}}{2\pi^2\epsilon_0K_\perp}\int_{k_\parallel=0}^{\infty}dk_\parallel\cos k_\parallel z\begin{cases}I_0[\rho k_\parallel(K_\parallel/K_\perp)^{1/2}]K_0[\rho_0k_\parallel(K_\parallel/K_\perp)^{1/2}], & \rho<\rho_0\\ I_0[\rho_0k_\parallel(K_\parallel/K_\perp)^{1/2}]K_0[\rho k_\parallel(K_\parallel/K_\perp)^{1/2}], & \rho>\rho_0\end{cases} \tag{5}$$

provided

$$\mathrm{Re}(K_\parallel/K_\perp)^{1/2}>0. \tag{6}$$

The inequality given by Eq. (6) holds upon inclusion of a small, nonzero collision frequency ν into the cold, magnetized plasma dielectric tensor expression. The integral in Eq. (5) is expressible in terms of a Legendre function of the second kind (Ref. 6, p.732), a so-called conical function, to wit

$$\phi(\mathbf{r},t)=\frac{Se^{-i\omega t}}{4\pi^2\epsilon_0(\rho\rho_0K_\perp K_\parallel)^{1/2}}Q_{-1/2}\left[\frac{z^2+(\rho^2+\rho_0^2)K_\parallel/K_\perp}{2\rho\rho_0K_\parallel/K_\perp}\right], \tag{7}$$

again, provided Eq. (6) holds and $z\neq0$. $Q_{-1/2}(\zeta)$ is singular for arguments $\zeta=\pm1$, hence the surfaces on which the potential is singular are

$$z=\pm(\rho-\rho_0)(-K_\parallel/K_\perp)^{1/2},\quad z=\pm(\rho+\rho_0)(-K_\parallel/K_\perp)^{1/2}. \tag{8}$$

These are two cones of half-angle $\mathrm{arccot}(-K_\parallel/K_\perp)^{1/2}$ which intersect on the source ring and whose vertices are given by $z_c=\pm\rho_0(-K_\parallel/K_\perp)^{1/2}$. There are no singularities for the case $K_\parallel/K_\perp>0$.

The nature of the singularity for $\arg Q_{-1/2}=1$ (the discussion for $\arg Q_{-1/2}=-1$ is similar) can be made manifest by consideration of the identity[7]

$$Q_n(\mu)=\frac{1}{2}\left(\log\frac{\mu+1}{\mu-1}\right)F[-n,n+1;\ 1;\ (1-\mu)/2]$$

 0031-9171/78/2107-1116$00.90 © 1978 American Institute of Physics

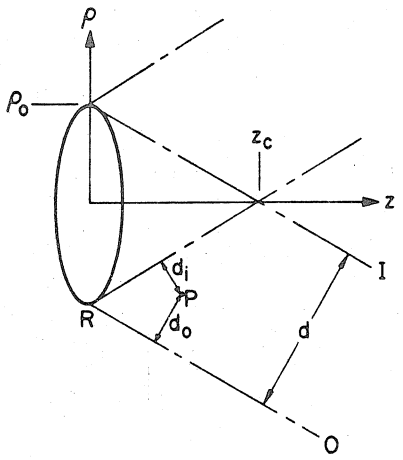

FIG. 1. Geometry of the problem. R denotes the ring source in the $z=0$ plane, centered on $\rho=0$. I and O denote the inner and outer cones of cold plasma theory, d_i and d_o are the distances from an arbitrary point P to the inner and outer cones, and d is the distance from a vertex to the outer cone. The static magnetic field is along the z axis, and the vertex of the inner cone is at z_c.

$$+\sum_{p=0}^{\infty}\frac{(n+p)!}{(n-p)!}\frac{[(\mu-1)/2]^p}{(p!)^2}[\psi(p)-\psi(n)], \tag{9}$$

where n is an arbitrary real number, $\psi(z)=d/dz \times \log\Gamma(z+1)$, and it is implicit that $\log(1+\mu/1-\mu)$ is taken for $\mu<1$. For $n=-1/2$ and $\mu=1+\epsilon$, $\epsilon \ll 1$, there results

$$Q_{-1/2}(1+\epsilon)\sim\frac{1}{2}\log\frac{2}{|\epsilon|} \text{ as } \epsilon\to 0, \tag{10}$$

where

$$\epsilon=\frac{(\rho-\rho_0)^2(K_\parallel/K_\perp)+z^2}{2\rho\rho_0(K_\parallel/K_\perp)}. \tag{11}$$

If one defines d_i, d_o, and d as the respective distances from (ρ,z) to the inner cone [for $|z|\le\rho_0(-K_\parallel/K_\perp)^{1/2}$], from (ρ,z) to the outer cone, and from either vertex to the outer cone, then

$$d_{i,o}=\left|\frac{z\pm(\rho-\rho_0)(-K_\parallel/K_\perp)^{1/2}}{(1-K_\parallel/K_\perp)^{1/2}}\right|, \quad d=\frac{2\rho_0(-K_\parallel/K_\perp)^{1/2}}{(1-K_\parallel/K_\perp)^{1/2}}, \tag{12}$$

and thus

$$\frac{2}{|\epsilon|}=\frac{(\rho/\rho_0)}{(d_i/d)(d_o/d)}. \tag{13}$$

Hence, $d_i\to 0$ or $d_o\to 0$ implies $\epsilon\to 0$, unless d_i/ρ or d_o/ρ is kept constant as the limit is taken; that is, the vertices themselves are not in the domain of validity of Eq. (10). Allowing, with no loss of generality, $d_i\to 0$, the asymptotic expression for the potential on the inner cone becomes

$$\phi(\mathbf{r},t)\sim\frac{S e^{-i\omega t}}{4\pi^2\epsilon_0\rho_0(K_\parallel K_\perp)^{1/2}} \times\left[\frac{\log(\rho/\rho_0)^{1/2}-\log(d_i/d)^{1/2}}{(\rho/\rho_0)^{1/2}}\right] \text{as } d_i\to 0, \tag{14}$$

where $\mathbf{r}=(\rho,z)$ and $0<|z|<\rho_0(-K_\parallel/K_\perp)^{1/2}$.

B. Collisional effects

The $\log(d_i/d)^{1/2}$ term speciously dominates expression (14), since d_i may be made arbitrarily small, whereas ρ is constrained to be positive by exclusion of the vertices from the domain of validity. However, inclusion of a small, nonzero collision frequency ν makes it impossible for the expression for d_i given by Eq. (12) to vanish, making it mandatory to retain the $\log(\rho/\rho_0)^{1/2}$ term, particularly near the vertices. For a highly magnetized, cold plasma, neglecting terms of order (m_e/m_i) and following Allis *et al.*,[8]

$$K_\perp\simeq 1, \quad K_\parallel\simeq-\frac{\omega_{pe}^2}{\omega^2}\left(1-i\frac{\nu}{\omega}\right), \tag{15}$$

where m_e and m_i are the electron and ion masses, respectively, and ω_{pe} is the electron plasma frequency.

Simple algebra shows that on the surface $z+(\rho-\rho_0)\times(\omega_{pe}/\omega)=0$

$$d_i/d\simeq\tfrac{1}{4}(1-\rho/\rho_0)(\nu/\omega)\exp(i\pi/2). \tag{16}$$

The $\log(\rho/\rho_0)^{1/2}$ term is the sole term retained when

$$\rho/\rho_0\ll\nu/4\omega \text{ or } |z-\rho_0(\omega_{pe}/\omega)|\ll\tfrac{1}{4}(\nu/\omega)(\rho_0\omega_{pe}/\omega). \tag{17}$$

Thus, there exists $\delta>0$ such that in two limiting cases

$$\phi(\mathbf{r},t)\sim\frac{-S\exp[-i(\omega t\pm\pi/2)]}{8\pi^2\epsilon_0\rho_0(\omega_{pe}/\omega)}\frac{\log[(1-\rho/\rho_0)(\nu/\omega)]}{(\rho/\rho_0)^{1/2}}, \quad \text{for } 0<|z|<\rho_0(\omega_{pe}/\omega)-\delta, \tag{18a}$$

$$\phi(\mathbf{r},t)\sim\frac{S\exp[-i(\omega t\pm\pi/2)]}{8\pi^2\epsilon_0\rho_0(\omega_{pe}/\omega)}\frac{\log(\rho/\rho_0)}{(\rho/\rho_0)^{1/2}}, \quad \text{for } (1-\tfrac{1}{4}\nu/\omega)\rho_0(\omega_{pe}/\omega)\ll|z|<\rho_0(\omega_{pe}/\omega), \tag{18b}$$

where $z\sim(\rho-\rho_0)(\omega_{pe}/\omega)$. For all intents and purposes, Eq. (18a) characterizes the singularity. The focusing nature of the cones is readily seen in either case.

C. Warm plasma effects

Inclusion of nonzero temperature gives rise to an interference structure on the inside of the resonance cone emanating from an oscillating point charge.[2] Hence, for a ring source an interference structure would be expected to appear outside the cone for $z<z_c$ and both inside and outside for $z>z_c$. (Observation of the interference structure within the cone for the case $z>z_c$ has been reported in Ref. 3, p. 111). To ascertain the main features of this structure, we have evaluated Eq. (5) numerically using the warm plasma dielectric functions

$$K_\parallel\simeq 1-\frac{\omega_{pe}^2}{k_\parallel^2 v_{th}^2}Z'\left(\frac{\omega}{k_\parallel v_{th}}\right) \text{ and } K_\perp\simeq 1. \tag{19}$$

Z' is the derivative of the plasma dispersion function and $v_{th}^2=2\kappa T_e/m_e$, where κ is Boltzmann's constant and T_e is the electron temperature. Here, we have assumed $\omega_{ce}^2>\omega^2$, ω_{pe}^2 where ω_{ce} is the electron cyclotron frequency.

The integrand of Eq. (5) has a logarithmic singularity at $k_\parallel=0$. For purposes of numerical evaluation, it is

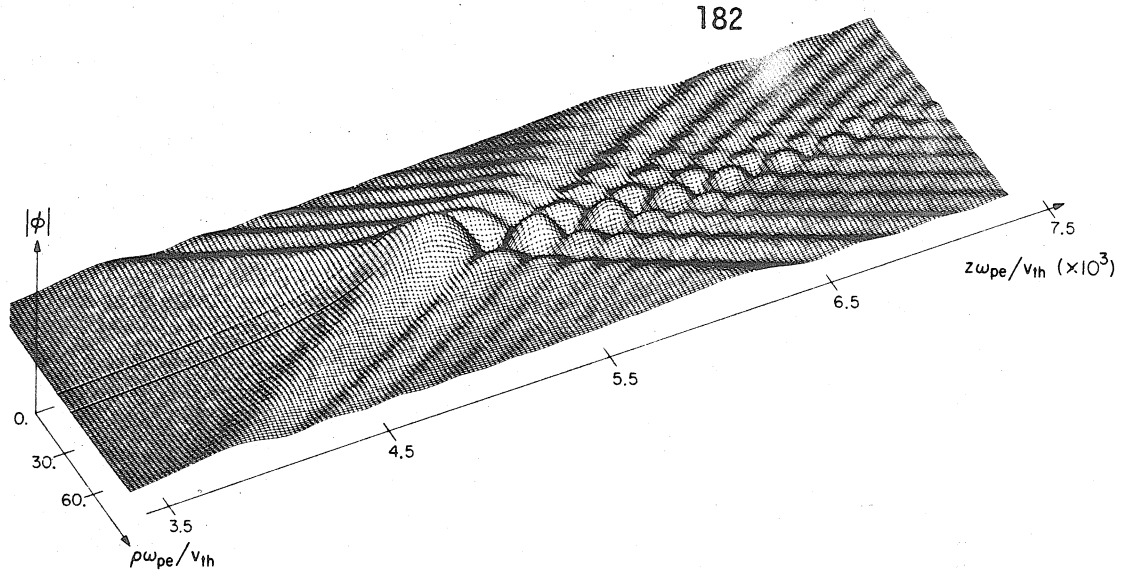

FIG. 2. Magnitude of the complex potential for a part of the inner cone, displaying the interference structure due to thermal effects. The ring source is located as in Fig. 1; the dimensionless parameters are $\omega/\omega_{pe}=0.02$ and $\rho_0\omega_{pe}/v_{th}=270$. The resonance cone focus occurs at $z\omega_{pe}/v_{th}=4.93\times10^3$; the vertex given by cold plasma theory is at $z_c\omega_{pe}/v_{th}=4.83\times10^3$.

convenient to treat the singularity separately. Let the integrand in Eq. (5) be defined as $f(k_\parallel)$. Then, the potential may be written

$$\phi(\mathbf{r},t)=\frac{Se^{-i\omega t}}{2\pi^2\epsilon_0}\left(\int_0^\eta dk_\parallel\left\{f(k_\parallel)+\cos(k_\parallel z)\times\log\left[\frac{1}{2}\rho_0 k_\parallel\left(\frac{\omega_{pe}^2}{\omega^2}-1\right)^{1/2}\right]\right\}-\int_0^\eta dk_\parallel\cos(k_\parallel z)\times\log\left[\frac{1}{2}\rho_0 k_\parallel\left(\frac{\omega_{pe}^2}{\omega^2}-1\right)^{1/2}\right]+\int_\eta^\infty dk_\parallel f(k_\parallel)\right) \quad (20)$$

for arbitrary η. The singularity now appears only in the second integral which may be evaluated exactly in terms of the sine integral $\mathrm{Si}(x)$. For an appropriate choice of $\eta\{$i.e., $\eta<1/[\rho(\omega_{pe}^2/\omega^2-1)^{1/2}]$, $1/z$, $\omega/v_{th}\}$, the second integrand is a slowly varying function of $k_\parallel$, and the integral may be evaluated by Simpson's rule, while the last integral may now be computed using the fast Fourier transform algorithm.[9]

Dimensionless variables appropriate for the evaluation of Eq. (5) are: frequency, $f\equiv\omega/\omega_{pe}$; distance along the ρ direction, $\mathcal{R}\equiv(\omega_{pe}/v_{th})\rho$; radius of the ring source, $\mathcal{R}_0\equiv(\omega_{pe}/v_{th})\rho_0$; and distance along the z direction, $\mathcal{z}\equiv(\omega_{pe}/v_{th})z$. The potential was evaluated for typical

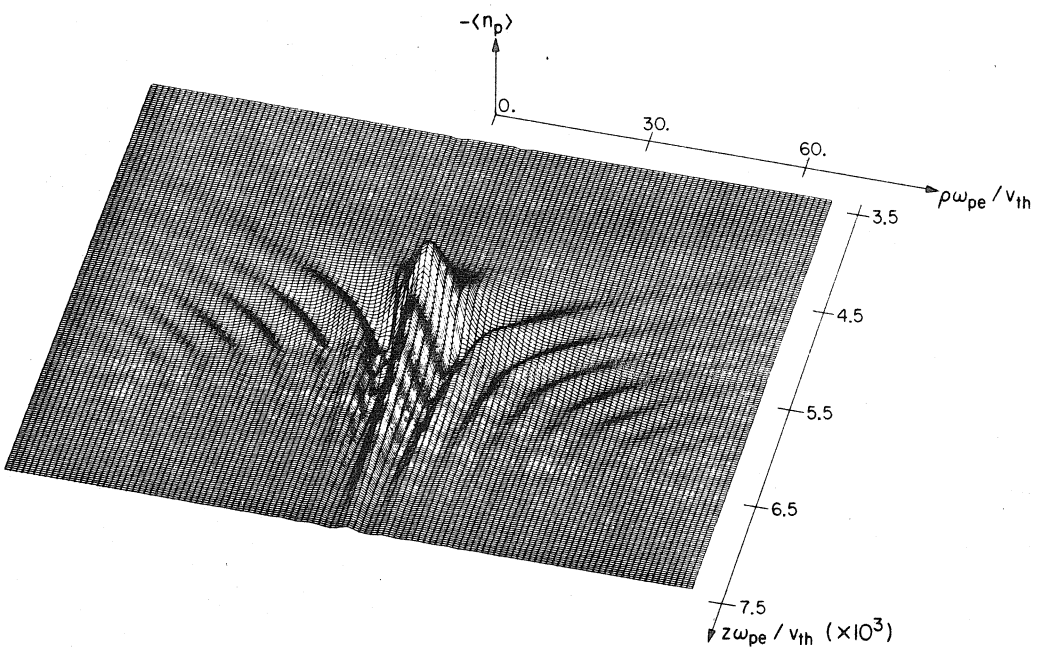

FIG. 3. First-order density depression due to the pondermotive force for $\omega/\omega_{ce}=0.02$. The location of the ring source and the dimensionless parameters are as in Fig. 2; note change in orientation of axes. The peak density depression occurs at $z\omega_{pe}/v_{th}=5.15\times10^3$.

parameters $f=0.056$ and $\mathcal{R}_0=270$, which may correspond, for example, to a laboratory plasma with $n_e=10^{10}$ cm^{-3}, $T_e=2$ eV, $\rho_0=4$ cm, and $\omega/2\pi=50$ MHz.

A plot of the magnitude of the complex potential clearly shows the converging cone-like structure expected from cold plasma theory (Fig. 2). The focus of the cone ($\vartheta=4.93\times10^3$) is shifted slightly from the cold plasma vertex ($\vartheta_c=4.83\times10^3$). A simple interference structure is found outside the cone, while a complicated pattern appears inside the cone for $\vartheta>\vartheta_c$, resembling a series of diverging cones with vertices along the z axis. The magnitude of the potential is found to be approximately proportional to $\xi^{-1/2}$, where $\xi=[R^2+(\vartheta_c-\vartheta)^2]^{1/2}$ represents the distance along the surface of the cone for $\vartheta<\vartheta_c$, provided we are not too close to the vertex ($\xi\gtrsim135$).

The ponderomotive force causes density modifications which, in turn, change ω_p and hence the structure of the cone. As a first-order approximation for small density perturbations we evaluate the ponderomotive force which arises from the fields obtained from linear theory.

The ponderomotive force may be derived by time-averaging the momentum transport fluid equations for each species over a period $2\pi/\omega$.[10] Let the density of a species be n_0+n_p, where n_p is the perturbation caused by the ponderomotive force, and assume $n_p\ll n_0$. The averaged fluid equation for one species in the quasi-static approximation is

$$\frac{\langle\nabla p\rangle}{n_0}-q(\mathbf{E}_a+\mathbf{v}_d\times\mathbf{B}_0)=-\frac{m}{2}\,\mathrm{Re}\{[(\mu\cdot\mathbf{E})^*\cdot\nabla](\mu\cdot\mathbf{E})\}, \tag{21}$$

where p is the pressure, $\mathbf{E}_a$ is an ambipolar electric field, $\mathbf{v}_d$ is a drift velocity, μ is the mobility tensor, and $\mu\cdot\mathbf{E}$ will be evaluated using results from linear theory. Equation (21) represents a pressure balance, and the right-hand side may be identified as the ponderomotive force density. The particle density is assumed to reach an equilibrium where an equation of state for a species may be approximated by $\nabla p=\gamma\kappa T\nabla n_p$, where γ is the coefficient of adiabatic expansion. Neglecting thermal corrections to the mobility, assuming $T_i\ll T_e$ and $n_i\simeq n_e$, summing the z component of Eq. (21) over species and integrating, we find

$$\left\langle\frac{n_p}{n_0}\right\rangle\simeq\frac{-\pi\epsilon_0}{\gamma_e\kappa T_e}\sum_{\alpha=i,e}\left(\frac{q_\alpha^2}{m_\alpha}\right)\left(\frac{|\mathbf{E}_p|^2}{\omega^2-\omega_{c\alpha}^2}+\frac{|\mathbf{E}_z|^2}{\omega^2}\right), \tag{22}$$

where q_α is the charge of species α and the fields are those obtained from linear theory. Numerical evaluation for an argon plasma with $\omega/\omega_{ce}=0.02$, using the parameters given here, shows that the density depression is sharply peaked near the resonance cone focus (Fig. 3). The thermal effects cause an interference structure in density whose phase fronts lie roughly parallel to the surface of the cone for $\vartheta<\vartheta_c$ and parallel to the z axis for $\vartheta>\vartheta_c$.

ACKNOWLEDGMENT

This research was supported by the U. S. Department of Energy under Contract E(04-3)-767.

[1]H. H. Kuehl, Phys. Fluids 5, 1095 (1962).
[2]R. K. Fisher and R. W. Gould, Phys. Fluids 14, 857 (1971).
[3]R. L. Stenzel and W. Gekelman, Phys. Fluids 20, 108 (1977).
[4]W. Gekelman and R. L. Stenzel, Phys. Fluids 20, 1316 (1977).
[5]P. M. Bellan and M. Porkolab, Phys. Fluids 19, 995 (1976).
[6]I. S. Gradshteyn and I. M. Ryzhik, *Tables of Integrals, Series and Products* (Academic, New York, 1965), 4th ed.
[7]L. Robin, *Fonctions Sphériques de Legendre* (Gauthier-Villars, Paris, 1957), Tome II, p. 137.
[8]W. P. Allis, S. J. Buchsbaum, and A. Bers, *Waves in Anisotropic Plasmas* (M.I.T. Press, Cambridge, Mass. 1963), p. 91.
[9]J. W. Cooley, P. A. W. Lewis, and P. D. Welch, IEEE Trans. Audio Electroacoust. AU-15, 79 (1967).
[10]H. H. Kuehl, Phys. Fluids 19, 1972 (1976).

BIBLIOGRAPHY

1. Lawson, J. D., "Some Criteria for a Power Producing Thermonuclear Reactor," Proc. Phys. Soc. (London) B70, 6 (1957).
2. Dean, S. O., et al., "Status and Objectives of Tokamak Systems for Fusion Research," U.S. Atomic Energy Comm., Report WASH-1295 (1974).
3. Pfirsch, D. and Schluter, A., Max-Planck-Institut, Report MPI/PA/7/62 (1962).
4. Furth, H. P., "Progress toward a Tokamak Fusion Reactor," Sci. Amer. 241, 2 (1979).
5. Apgar, E., et al., "High Density and Collisional Plasma Regimes in the Alcator Programme," Plasma Physics and Controlled Fusion Research, Sixth Conf. Proc., IAEA, Vienna, Vol. I, 247 (1976).
6. Daughney, C., "Empirical Scaling for Present Ohmically Heated Tokamaks," Nuc. Fusion 15, 967 (1975).
7. Hutchinson, I. H. and Strachan, J. D., "Particle Drifts and the Transition to Containment in the LT-3 Tokamak," Nuc. Fusion 14, 649 (1974).
8. Abramov, V. A., Pogutse, O. P., and Yurchenko, E. I., "Gas Breakdown in a Tokamak," Sov. J. Plasma Phys. 1, 297 (1976).
9. Abramov, V. A., Vikhrev, V. V., and Pogutse, O. P., "Initial Stage of the Discharge in a Tokamak," Sov. J. Plasma Phys. 3, 288 (1977).
10. Papoular, R., "The Genesis of Toroidal Discharges," Nuc. Fusion 16, 37 (1976).
11. Rose, D. J. and Clarke, M., Plasmas and Controlled Fusion, MIT Press, Cambridge, Mass., 1961
12. Equipe TFR, "Line Radiation in the Visible and in the Ultraviolet in TFR Tokamak Plasmas," Nuc. Fusion 15, 1053 (1975).

13. Gorelik, L. L., et al., "Radiation Power of a Plasma as a Function of the Discharge Parameters in the Tokamak-3 Device," Nuc. Fusion 12, 185 (1972).

14. Gibson, A., "Radiation Limits to Tokamak Operation," Nuc. Fusion 16, 546 (1976).

15. Stott, P. E. Daughney, C. C., and Ellis, R. A., "Control of Recycling and Impurities in the ATC Tokamak by Means of Gettered Surfaces," Nuc. Fusion 15, 431 (1975).

16. Fielding, S. J., et al., "High-Density Discharges with Gettered Torus Walls in DITE," Nuc. Fusion 17, 1382 (1977).

17. Oren, L. and Taylor, R. J., "Trapping and Removal of Oxygen in Tokamaks," Nuc. Fusion 17, 1143 (1977).

18. Murakami, M., Callen, J. D., and Berry, L. A., "Some Observations on Maximum Densities in Tokamak Experiments," Nuc. Fusion 16, 347 (1976).

19. Burrell, K. H., "A Fast Hydrogen Gas Injection System for Plasma Physics Experiments," General Atomic Co. Report GA-A14604 (1977).

20. Cross, R. C., "Construction of Diagnostic Equipment for the Texas Tech Tokamak," Tech. Report No. 2, Plasma Laboratory, Texas Tech University, Lubbock, Texas (1977).

21. Dimock, D. L., et al., "The Ontogeny of a Tokamak Discharge, Nuc. Fusion 12, 271 (1973).

22. Artsimovich, L. A., "Tokamak Devices," Nuc. Fusion 12, 215 (1972).

23. Spitzer, L., Physics of Fully Ionized Gases (Interscience--J. Wiley & Sons, New York, 1962), p. 139.

24. Shafranov, V. D., "Hydromagnetic Stability of a Current-Carrying Pinch in a Strong Longitudinal Magnetic Field," Sov. Phys.--Tech. Phys. 15, 175 (1970).

25. Ware, A. A., "Instability Waves in Magnetically Confined Plasmas," J. Nucl. Energy, Part C: Plasma Physics 3, 93 (1961).

26. Ware, A. A., "Comparison between Theory and Experiment for the Stability of the Toroidal Pinch Discharge," Nuc. Fusion: 1962 Supplement, Part 3, 869.

27. Bateman, G., MHD Instabilities (MIT Press, Cambridge, Mass., 1978), passim.

28. Meisel, D., et al., "General Properties and Stability Behavior of High-Density Tokamak Plasmas in Pulsator I," Plasma Physics and Controlled Fusion Research, Sixth Conf. Proc. IAEA, Vienna, Vol. I, (1976), p. 259.

29. Scaturro, L. S. and Kusse, B., "Electric Probe Measurements Near the Plasma Edge in Alcator," Nuc. Fusion 18, 1717 (1978).

30. Furth, H. P., Rosenbluth, M. N., Rutherford, P. H., and Stodiek, W., "Thermal Equilibrium and Stability of Tokamak Discharges," Phys. Fluids 13, 3020 (1970).

31. Kluber, O., et al., "High Density Tokamak Discharges in the Pulsator Device with $\beta_p > 1$," Nuc. Fusion 15, 1194 (1975).

32. Ware, A. A., "Pinch-Effect Oscillations in an Unstable Tokamak Plasma," Phys. Rev. Lett. 25, 916 (1970).

33. Ware, A. A., "The Importance of the Trapped-Particle Pinch Effect in Tokamak Plasmas," Plasma Physics and Controlled Fusion Research, Fourth Conf. Proc. IAEA, Vienna, Vol. I (1971), p. 411.

34. Coppi , B. and Spight, C., "Ion Mixing Mode and Model for Density Rise in Confined Plasmas," Phys. Rev. Lett. 41, 551 (1978).

35. Antonsen, T., Coppi, B., and Englade, R., "Inward Particle Transport by Plasma Collective Modes," Nuc. Fusion 19, 641 (1979).

36. Mirnov, S. V. and Semenov, I. B., "Investigation of the Instabilities of the Plasma String in the Tokamak-3 System by Means of a Correlation Method," Sov. J. Atomic Energy 30, 22 (1971).

37. Mirnov, S. V. and Semenov, I. B., "The Nature of the Large-Scale Instabilities in the Tokamak," Sov. Phys. JETP 33, 1134 (1971).

38. Furth, H. P., Killeen, J., and Rosenbluth, M. N., "Finite-Resistivity Instabilities of a Sheet Pinch," Phys. Fluids 6, 459 (1963).

39. Furth, H. P., Rutherford, P. H., and Selburg, H., "Tearing Mode in the Cylindrical Tokamak," Phys. Fluids 16, 1054 (1973).

40. Matsuda, S. and Yoshikawa, M., unpublished.

41. Rutherford, P. H., "Nonlinear Growth of the Tearing Mode," Phys. Fluids 16, 1903 (1973).

42. White, R. B., Monticello, D. A., Rosenbluth, M. N., and Waddell, B. V., "Saturation of the Tearing Mode," Phys. Fluids 20, 800 (1977).

43. Glasser, A. H., Greene, J. M., and Johnson, J. L., "Resistive Instabilities in a Tokamak," Phys. Fluids 19, 567 (1976).

44. Drake, J. F. and Lee, Y. C., "Kinetic Theory of Tearing Instabilities," Phys. Fluids 20, 1341 (1977).

45. Finn, J. M., "The Destruction of Magnetic Surfaces in Tokamaks by Current Perturbations," Nuc. Fusion 15, 845 (1975).

46. Stix, T. H., "Magnetic Braiding in a Toroidal Plasma," Phys. Rev. Lett. 30, 833 (1973).

47. Kadomtsev, B. B. and Pogutse, O. P., "Nonlinear Helical Perturbations of a Plasma in the Tokamak," Sov. Phys. JETP 38, 283 (1974).

48. Chrisman, P., Clarke, J., and Rome, J., "Magnetic Island Formation in a Tokamak Plasma from Helical Perturbations of the Plasma Current," Oak Ridge Natl. Lab Report ORNL-TM-4501 (1974).

49. Matsuda, S., and Yoshikawa, M., "Magnetic Island Formation Due to Error Field in the JFT-2 Tokamak," Jap. J. Appl. Phys. 14, 87 (1975).

50. Robinson, D. C. and McGuire, K., "Magnetic Islands and Disruptions in the Tosca Tokamak," Nuc. Fusion 19, 115 (1979).

51. Wesson, J. A., private communication.

52. Wesson, J. A., "Hydromagnetic Stability of Tokamaks," Nuc. Fusion 18, 87 (1978).

53. White, R. B., Monticello, D. A., and Rosenbluth, M. N., "Simulation of Large Magnetic Islands; A Possible Mechanism for a Major Tokamak Disruption," Phys. Rev. Lett. 39, 1618 (1977).